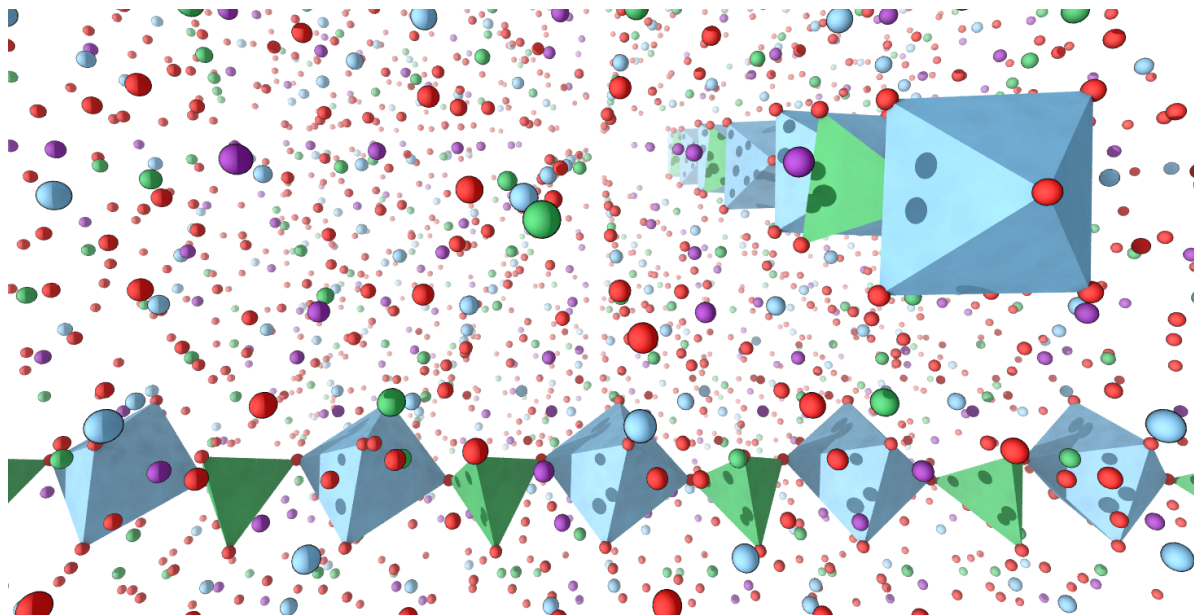


# Optical response and surface properties of $\text{KTiOPO}_4$ and related materials



## Dissertation

zur Erlangung des akademischen Grades

**Dr. rer. nat.**

vorgelegt dem Department Physik der Fakultät für Naturwissenschaften  
an der Universität Paderborn

von

**SERGEJ NEUFELD**

Tag der Abgabe  
Tag der mündlichen Prüfung

17. November 2022  
23. Februar 2023

**Promotionskommission**

Vorsitzender

Prof. Dr. Tim Bartley

*Universität Paderborn*

Gutachter

Prof. Dr. Wolf Gero Schmidt

*Universität Paderborn*

Gutachter

Prof. Dr. Simone Sanna

*Justus-Liebig-Universität Gießen*

Vertreter des Mittelbaus

Dr. Christof Eigner

*Universität Paderborn*

# Erklärung

Ich, Sergej Neufeld, geboren am 28. März 1990 in Wosnessenowka (Kasachstan), versichere, dass ich die vorliegende Arbeit ohne fremde Hilfe und ohne Benutzung anderer als der angegebenen Quellen angefertigt habe und dass die Arbeit in gleicher oder ähnlicher Form noch keiner anderen Prüfungsbehörde vorgelegen hat und von dieser als Teil einer Prüfungsleistung angenommen worden ist. Alle Ausführungen, die wörtlich oder sinngemäß übernommen worden sind, sind als solche gekennzeichnet.

---

Ort, Datum

---

Unterschrift





## Abstract

The ferroelectric potassium titanyl phosphate ( $\text{KTiOPO}_4$ , KTP) along with its isomorphs rubidium titanyl phosphate ( $\text{RbTiOPO}_4$ , RTP) and potassium titanyl arsenate ( $\text{KTiOAsO}_4$ , KTA) are used extensively within linear and nonlinear optics, in particular for frequency-conversion devices and waveguide structures. Despite this frequent use, many bulk and surface-related properties of the KTP crystal family are still either poorly understood or have not yet been investigated at all.

On the footing of the density-functional theory (DFT), this study aims at addressing a number of open questions regarding the (i) spectroscopic signatures of KTP, RTP and KTA and (ii) surface terminations of the [001] and [010] surfaces of KTP. In the first step, the influence of quasiparticle and excitonic effects on the dielectric response function of all three materials is investigated stepwise by performing DFT calculations utilizing the  $GW$  approximation and solving the Bethe-Salpeter equation. A comparison between the spectra subsequently allows to estimate the influence of alkali and group-V elements on the optical response of the KTP crystal family. In the next step, phononic densities of states and Raman susceptibilities of all three materials are evaluated on the basis of density-functional perturbation theory, allowing for a nonphenomenological mapping between experimental Raman bands and individual vibrational modes. Modes involving the displacement of O(9) and O(10)-type ions are highlighted as particularly important in the interpretation of the highest-intensity Raman bands. In addition, computational limitations of the present approach are identified. Lastly, thermodynamically stable reconstructions of the KTP [001] and [010] surfaces for typical chemical environments are determined using total-energy DFT calculations. Rebonding processes and changes in the surface stoichiometries, including a depletion of Ti and accumulation of O, are shown to induce the formation of occupied surface states and thus a pronounced shrinkage of the KTP band gap.



## Zusammenfassung

Das Ferroelektrikum Kaliumtitanylphosphat ( $\text{KTiOPO}_4$ , KTP) und seine beiden Isomorphen Rubidiumtitanylphosphat ( $\text{RbTiOPO}_4$ , RTP) und Kaliumtitanylarsenat ( $\text{KTiOAsO}_4$ , KTA) werden in großem Umfang in der linearen und nichtlinearen Optik, insbesondere in Bauelementen zur Frequenzumwandlung und Wellenleiterstrukturen eingesetzt. Trotz dieser verbreiteten Anwendungen sind eine Vielzahl von Volumen- und Oberflächeneigenschaften der KTP Kristallfamilie noch immer entweder unzureichend oder noch überhaupt nicht erforscht.

Auf der Grundlage der Dichtefunktionaltheorie (DFT) zielt diese Studie darauf ab, eine Reihe offener Fragen in Bezug auf (i) die spektroskopischen Signaturen von KTP, RTP und KTA und (ii) die Oberflächenterminierungen der [001]- und [010]-Oberflächen von KTP zu beantworten. Im ersten Schritt wird der Einfluss von Quasiteilchen- und exzitonischen Effekten auf die dielektrische Antwortfunktion aller drei Materialien schrittweise untersucht, indem DFT-Berechnungen unter Verwendung der  $GW$ -Näherung durchgeführt werden und die Bethe-Salpeter-Gleichung gelöst wird. Ein Vergleich zwischen den drei Spektren ermöglicht es anschließend, den Einfluss von Alkali- und Gruppe-V-Elementen auf die optische Antwort der KTP-Kristallfamilie zu evaluieren. Im nächsten Schritt werden die phononischen Zustandsdichten und Raman-Suszeptibilitäten aller drei Materialien auf der Grundlage der Dichtefunktionalstörungstheorie untersucht, was eine nichtphänomenologische Zuordnung zwischen experimentellen Raman-Banden und einzelnen Schwingungsmoden ermöglicht. Die besondere Rolle von Moden, welche die Auslenkung von Atomen des Typs O(9) und O(10) beinhalten, zur Interpretation von Raman-Banden hoher Intensität wird dabei hervorgehoben. Darüber hinaus werden die rechnerischen Grenzen des vorliegenden Ansatzes aufgezeigt. Schließlich werden thermodynamisch stabile Rekonstruktionen der [001]- und [010]-Oberflächen von KTP für typische chemische Umgebungen mit Hilfe von Berechnungen der DFT Gesamtenergien ermittelt. Es wird gezeigt, dass die Ausbildung neuer Bindungen und Änderungen der Oberflächenstöchiometrie, einschließlich einer Verarmung von Ti und einer Anreicherung von O, die Bildung besetzter Oberflächenzustände und damit eine deutliche Verkleinerung der KTP-Bandlücke bewirken.



# Contents

<b>1</b>	<b>Introduction</b>	<b>1</b>
<b>2</b>	<b>Fundamental Concepts</b>	<b>5</b>
2.1	Density-Functional Theory . . . . .	5
2.1.1	Hohenberg-Kohn Theorems . . . . .	5
2.1.2	Kohn-Sham Formalism . . . . .	7
2.1.3	Local-Density Approximation . . . . .	9
2.1.4	Generalized-Gradient Approximation . . . . .	10
2.1.5	Calculation of Forces . . . . .	11
2.1.6	The Band-Gap Problem in DFT . . . . .	12
2.2	The Self-Energy Concept . . . . .	14
2.2.1	Quasiparticle Picture and Green's Function . . . . .	14
2.2.2	Hedin's Equations and <i>GW</i> Approximation . . . . .	18
<b>3</b>	<b>Theoretical spectroscopy</b>	<b>23</b>
3.1	Dielectric Response Function . . . . .	24
3.1.1	The Independent-(Quasi-)Particle Approximation . . . . .	25
3.1.2	Local-Field Effects . . . . .	27
3.2	Two-Particle Effects and the Bethe-Salpeter Equation . . . . .	28
3.2.1	Generalization to Four-Point Operators . . . . .	28
3.2.2	The BSE Hamiltonian . . . . .	29
3.3	Raman Cross Section . . . . .	32
3.3.1	Ionic Contribution . . . . .	32
3.3.2	Electronic contribution . . . . .	35
<b>4</b>	<b>Ferroelectrics</b>	<b>37</b>
4.1	Ferroelectric-Paraelectric Phase Transition . . . . .	38
4.2	Technological Applications of Ferroelectrics . . . . .	40
4.3	The Potassium Titanyl Phosphate Crystal Family . . . . .	42
4.3.1	Crystal structure . . . . .	43
4.3.2	Curie temperature and crystal growth . . . . .	45
4.4	Polar Surfaces . . . . .	45

<b>5 Spectroscopic Signatures of KTP and Related Materials</b>	<b>49</b>
5.1 Band Structure and Dielectric Function of KTP . . . . .	49
5.1.1 Methodology . . . . .	49
5.1.2 Structural Properties . . . . .	51
5.1.3 Electronic Properties . . . . .	51
5.1.4 Linear Optical Properties . . . . .	55
5.2 Comparison to KTA and RTP . . . . .	59
5.2.1 Band Structure . . . . .	59
5.2.2 Dielectric Function . . . . .	60
5.3 Raman Cross Sections . . . . .	64
5.3.1 Computational Method . . . . .	65
5.3.2 Phonon Modes . . . . .	65
5.3.3 Raman Spectra . . . . .	68
5.4 Conclusions . . . . .	73
<b>6 Surface Reconstructions</b>	<b>75</b>
6.1 General Methodology . . . . .	75
6.2 Z Cut . . . . .	80
6.2.1 Structural Modelling . . . . .	81
6.2.2 Results . . . . .	84
6.3 Y Cut . . . . .	90
6.3.1 Structural Modelling . . . . .	91
6.3.2 Results . . . . .	92
6.4 Conclusions . . . . .	94
<b>7 Summary</b>	<b>97</b>
<b>Bibliography</b>	<b>100</b>
<b>A Lattice Vectors and Fourier Transformations</b>	<b>123</b>
<b>B Investigated K-Ti-P-O Phases</b>	<b>125</b>
<b>C Potential Energy Surfaces on KTP Z Cut</b>	<b>127</b>
<b>D Scientific Publications</b>	<b>131</b>

# 1

## Introduction

Modern digital communication relies strongly on the availability of high-quality optical devices to generate, manipulate and detect light. In these devices, crystals with ferroelectric properties have ever since played an important role as the active materials. Below a material-specific transition temperature, a ferroelectric is thereby characterized by the existence of a stable, internal (spontaneous) polarization  $P_s$ . Many interesting optical and structural properties of ferroelectrics can be traced back to the existence of this internal polarization, including the photovoltaic response [1] and electronic transport in ferroelectric field-effect transistors [2]. By applying an external electric field, the magnitude of  $P_s$  may be altered, effectively making the optical and structural properties of ferroelectrics externally tunable as well.

Among those tunable parameters, the second-order nonlinear optical coefficient is the most important quantity in the context of second-harmonic generation (SHG). Within a typical SHG setup, light of a fundamental frequency  $\omega$  is impinged onto a crystal. Nonlinear light-matter interaction leads to a partial conversion of the fundamental frequency to its second harmonic  $2\omega$ . This effect therefore allows to generate light with optical frequencies formally unaccessible through methods of conventional light generation. Within the last decades, SHG setups on the basis of periodically poled  $\text{KTiOPO}_4$  (KTP) [3–8], along with its isomorphs  $\text{KTiOAsO}_4$  (KTA) [3, 9] and  $\text{RbTiOKO}_4$  (RTP) [10, 11] emerged as alternatives to the conventionally used lithium niobate ( $\text{LiNbO}_3$ , LN) and lithium tantalate ( $\text{LiTaO}_3$ , LT). Due to their large transparency range along with high resistance to optical and mechanical damage, crystals of the KTP family are well suited for SHG applications in the visible wavelength regime [12]. Efficient conversion is thereby achieved by letting the impinged light propagate within a periodically grated crystal of alternating internal polarization state, preventing destructive interference between impinged and generated light (quasi-phase matching). The first periodic polarization reversal in KTP via the application of an electric field was realized by Chen *et al.* in 1994 [13]. In their experiment, the authors were able to fabricate periodic domains of widths as low as  $4\ \mu\text{m}$  by applying repeated pulses of  $2\ \text{kV}$  of voltage along the ferroelectric  $c$ -axis. With a value of  $\sim 2\ \text{eV/mm}$ , the electric field required to achieve domain inversion (coercitive field) was thereby one magnitude lower compared to LN ( $\sim 24\ \text{eV/mm}$ ). This advantage of low coercitive field strength, however, is partially offset by a high and spatially inhomogeneous value of  $\text{K}^+$  ionic conductivity along the fer-

roelectric  $c$ -axis [14]. This ionic conductivity quickly neutralizes surface charges induced by the poling process, counteracting the polarization reversal and giving rise to a higher susceptibility to optical damage. Transport of  $K^+$  ions is mainly governed by a vacancy mechanism [7], rendering the value of ionic conductivity highly dependent on the growth technique, sample quality, doping, as well as homogenization treatment [12, 14, 15]. In general, a low  $K^+$  deficiency, introduction of alkali metal defects (Rb, Cs) or a lowering of the temperature thereby results in a lower conductivity and higher domain quality.

Assessing the quality of SHG gratings and their physical properties requires techniques to thoroughly visualize ferroelectric domain structures in a noninvasive way. In this context, Raman spectroscopy provides a powerful tool to map structural changes within the domains, induced by the polarization reversal, onto frequency and intensity shifts of individual phonon modes, as has been shown successfully for periodically poled waveguides on the basis of KTP, LN and LT [16, 17]. Especially in the case of Rb-exchanged KTP, Raman analysis showed distinct modulations of modes close to the surface and domain walls, indicating the existence of stress fields caused by the larger Rb atomic radius compared to K.

For all discussed applications and characterization techniques, a precise knowledge about the materials electronic and optical properties is of fundamental interest. Especially the electronic band structure and dielectric response to external electric fields via the dielectric function  $\varepsilon(\omega)$  are key ingredients for the design of optical devices, because they give insights into the materials ability to absorb and refract light at optical frequencies  $\omega$ . Additionally, knowledge about the atomic arrangement of specific material surfaces (reconstructions) helps to determine structural effects of external perturbations, e.g., adsorption of molecules and electric poling. To assess these quantities, *ab initio* calculations on the basis of density-functional theory (DFT) are particularly suited. The main principle behind DFT, as initially formulated in 1964 by Hohenberg and Kohn [18], is a unique functional dependency of the ground-state energy  $E[\rho]$  on the electron density  $\rho$  of a many-electron system. Using the scheme proposed by Kohn and Sham [19], the ground-state energy as well as one-particle energies (band structures) may be evaluated via the self-consistent solution of the Kohn-Sham equations. Since its initial formulation, DFT has emerged as a standard method to determine ground-state properties of molecular and crystalline systems. Among others, these properties include total-energy differences, electronic band dispersions and the principle shape of the dielectric function, which are predicted with reasonable accuracy at feasible computational cost, even for systems containing several hundred atoms.

The Kohn-Sham scheme, however, suffers from an undesired effect: If the Kohn-Sham energy eigenvalues are interpreted as true excitation energies, the fundamental band gap, as the difference between ionization energy and electron affinity, is systematically underestimated [20–22]. This underestimation, in turn, gives rise to unreasonably low predictions regarding the onset of  $\varepsilon(\omega)$ . Additionally, the classification of certain materials into categories insulator, semiconductor and metalloid is rendered challenging. Corrections to the size of the fundamental band gap and dielectric function may be achieved by additionally including quasiparticle and excitonic effects, respectively. Their inclusion, however, comes at the prize of extraordinary computational cost.

In the case of the KTP crystal family, a number of the aforementioned quantities are yet theoretically unexplored. The general aim of this thesis is therefore to address the following open questions:

---

**1. What is the true dielectric response function of KTP, RTP and KTA?**

The dielectric function of all materials belonging to the KTP crystal family has yet been only determined using the independent-particle approximation (IPA), suffering from the systematic redshift in DFT and leaving the localization and characterization of electron-hole pairs during optical excitations (excitons) as an open question. Excitonic effects have been shown to noticeably affect the shape as well as position of the dielectric function, e.g., in LN [23] and KNbO<sub>3</sub> [24]. The first aim of this thesis is therefore to shed light onto the linear dielectric response of KTP, RTP and KTA by systematically calculating  $\varepsilon(\omega)$  on three levels of theory: (i) IPA, (ii) including self-energy corrections via the *GW* approximation (IQPA) and (iii) including excitonic effects by solving the Bethe-Salpeter equation. The shapes of  $\varepsilon(\omega)$  as well as differences between the response functions of the respective materials are discussed on the basis of transition characteristics.

**2. What is the correct assignment between phonon modes and observed Raman bands in bulk KTP, RTP and KTA?**

Although modulations in specific Raman bands of KTP type materials have been used to visualize domain walls for a long time, the macroscopic origin of those bands has never been quantitatively investigated. For KTP, a qualitative analysis was published by Kugel *et al.* in 1988 [25]. Using symmetry arguments, the most intense Raman peaks were mapped onto the fundamental vibrational modes of the KTP substructures, namely PO<sub>4</sub> tetrahedra and TiO<sub>6</sub> octahedra. Although widely accepted as the standard publication for mode assignments in KTP, this study stands on a phenomenological footing for the most part, limiting further analyses of the real KTP crystal structure. The aim is therefore to calculate the phonon density of states and Raman spectra of bulk KTP, RTP and KTA crystals, based on the polarizability theory of Raman scattering by Placzek [26, 27] in addition to density-functional perturbation theory. Similarities and pronounced differences between theoretical and experimental Raman spectra are discussed based on the displacement patterns of the involved atoms.

**3. What are the thermodynamically most stable reconstructions of [010] and [001] surfaces of KTP?**

Surfaces of polar materials are utilized in a number of technological applications, e.g., nitrate removal [28], water splitting [29] or the growth of high-quality III-nitrides [30, 31]. In the context of domain inversion, surface reconstructions of ferroelectric materials play a particularly important role. Due to the internal polarization, the two ferroelectric end facets of the crystal are not equivalent. A redistribution of charge during poling is therefore screened by a charge transport mechanism, either via mobile charges or a change in the surface stoichiometry. In the case of LN, the formation of two nonequivalent ferroelectric surfaces (Z<sup>+</sup> and Z<sup>-</sup>) was found to be accompanied by an accumulation of O and Li on the positive Z<sup>+</sup> surface [32, 33]. For KTP, only a small number of experimental studies have been performed to characterize the surface reconstructions. In particular, two studies by Atuchin *et al.* indicate the existence of an amorphous layer on top of the as-grown [001] surface, depleted of elements P and K [34, 35]. Treating the surface by mechanical polishing, the formation of nanosized islands was observed. These decompose into TiO<sub>2</sub> nanocrystals upon heating above

550 °C. However, the microscopic reconstruction mechanisms of the two technologically most important KTP surfaces, [001] (Z cut, polar) and [010] (Y cut, nonpolar), are still unknown. The third aim of this thesis is therefore the determination of the thermodynamically most stable surface reconstructions of Z and Y-cut KTP by means of DFT total-energy calculations. In the case of the polar Z cut, surfaces of opposing polarity ( $Z^-$  and  $Z^+$ ) are thereby treated separately, allowing different reconstructions to take place on either surface. Similarities and differences between stable terminations of all surfaces are identified, regarding structural motifs of the reconstructed layers as well as the influence of the reconstruction on the formation of electronic surface states.

This thesis is structured in the following way: First, the methodological background of this thesis is elaborated, starting with an introduction into DFT, the quasiparticle picture and the  $GW$  approximation in Chapter 2. The three theoretical methods to determine the linear dielectric function (IPA, IQPA, Bethe-Salpeter equation), used in this work, are systematically elaborated in Chapter 3. Additionally, a method to evaluate the Raman intensity within density-functional perturbation theory is introduced.

Chapter 4 serves as a review regarding the definition and technological importance of ferroelectric materials in general, along with the physical background of ferroelectric–paraelectric phase transitions. In particular, materials of the KTP family are introduced and discussed regarding their crystallographic and optical properties. An introduction into the methodology behind the modeling of polar surfaces concludes the chapter.

The results of this thesis are presented in the subsequent two chapters, starting with a comparison between optical responses as well as Raman spectra of KTP, RTP and KTA in Chapter 5. The determination of stable Y and Z-cut surfaces of KTP follows in Chapter 6. A summary and discussion of all results in Chapter 7 concludes this thesis.

# 2

## Fundamental Concepts

Within this thesis, total energies, band structures and optical properties of KTP (KTA, RTP) and its surfaces are determined numerically by solving the many-body Schrödinger equation. This chapter therefore aims at elaborating the fundamental aspects of the used methodology to treat the complex electron-electron interaction on an approximative footing. First, the density-functional theory as a general method to reformulate and solve the many-body Schrödinger equation is introduced, before the influence of quasiparticle (QP) effects on the electronic states is discussed. As a method to incorporate those quasiparticle effects into DFT, the self-energy concept within the *GW* approximation is thereby introduced.

In order to keep the notation simple and because electron spins are considered collinear within the body of this thesis, an explicit inclusion of a spin variable is neglected in the following. For a more in depth discussion of all topics covered in this chapter, the reader is referred to a variety of literature, in particular [36–39].

### 2.1 Density-Functional Theory

Every attempt to solve the quantum mechanical equations of motion of a many-electron system (e.g., a solid) inevitably runs into the „curse of dimensionality“: The sheer number of involved electrons, in addition to the mutual Coulomb interaction between each electron pair, renders the many-body wave function  $\Psi$  as the quantity of interest far too complex to handle, both analytically and numerically. Within DFT, a different way to tackle the many-electron problem is introduced by realizing that ground-state properties of the many-electron system (the total energy in particular) are actually unique functionals of the electron density  $\rho$  (Hohenberg-Kohn theorems) [18]. The futile direct search for  $\Psi$  can therefore be replaced by an algorithm to self-consistently determine  $\rho$ , which in turn determines the total energy of the system (Kohn-Sham equations) [19].

#### 2.1.1 Hohenberg-Kohn Theorems

Consider a system of  $N$  interacting electrons (mass  $m$  and charge  $e$ ) within an external, local and time-independent potential  $V_{\text{ext}}$  (e.g., an ionic background). The position and

momentum of the  $i$ -th electron shall be indicated by  $\mathbf{r}_i$  and  $\mathbf{p}_i$ <sup>1</sup>, respectively. This system is fully described by the following hamiltonian<sup>2</sup>

$$\mathbf{H} = \mathbf{T} + \mathbf{V}_{\text{ee}} + \mathbf{V}_{\text{ext}}, \quad (2.1)$$

where

$$\mathbf{T} = \sum_i \frac{\mathbf{p}_i^2}{2m} , \quad \mathbf{V}_{\text{ee}} = \sum_{i,j < i} \frac{e^2}{|\mathbf{r}_i - \mathbf{r}_j|} \quad \text{and} \quad \mathbf{V}_{\text{ext}} = \sum_i v_{\text{ext}}(\mathbf{r}_i) \quad (2.2)$$

denote the total kinetic energy, the nonlocal electronic Coulomb potential and the external potential, respectively. For later use, we note that  $\mathbf{T}$  and  $\mathbf{V}_{\text{ee}}$  are general quantities for any  $N$ -electron system, regardless of the particular ionic environment. In theory, the total energy of the electronic system may be determined by evaluating the expectation value of  $\mathbf{H}$  over the normalized many-body wave function  $\Psi$  as

$$E = \langle \Psi | \mathbf{H} | \Psi \rangle = \langle \mathbf{T} \rangle + \langle \mathbf{V}_{\text{ee}} \rangle + \langle \mathbf{V}_{\text{ext}} \rangle. \quad (2.3)$$

In practice, however, this idea is not practical, since the interaction term  $\mathbf{V}_{\text{ee}}$  prevents the factorization of  $\Psi$  into one-electron wave functions. Taking the fermionic character of electrons into account,  $\Psi$  is then, in general, given by a sum over Slater determinants of the form [40]

$$\psi(\mathbf{r}_1, \mathbf{r}_2, \dots, \mathbf{r}_N) = \frac{1}{\sqrt{N!}} \begin{vmatrix} \phi_1(\mathbf{r}_1) & \phi_1(\mathbf{r}_2) & \dots & \phi_1(\mathbf{r}_N) \\ \phi_2(\mathbf{r}_1) & \phi_2(\mathbf{r}_2) & \dots & \phi_2(\mathbf{r}_N) \\ \vdots & \vdots & \ddots & \vdots \\ \phi_N(\mathbf{r}_1) & \phi_N(\mathbf{r}_2) & \dots & \phi_N(\mathbf{r}_N) \end{vmatrix}, \quad (2.4)$$

where each entry  $\phi_i(\mathbf{r}_j)$  corresponds to the single-particle wave function of the  $i$ -th electron located at  $\mathbf{r}_j$ . The number of determinants thereby scales exponentially in  $N$ , rendering the storage of just a single many-body wave function nearly impossible, even for small atoms [40, 41]. Luckily, knowledge of the full wave function is neither desired nor needed. In many cases, the quantity of interest is not the entire spectrum of  $\mathbf{H}$ , but rather only the electronic ground-state energy  $E_0$  given by

$$E_0 = \min_{\Psi} \langle \Psi | \mathbf{H} | \Psi \rangle = \langle \Psi_0 | \mathbf{H} | \Psi_0 \rangle, \quad (2.5)$$

with  $|\Psi_0\rangle$  as the ground-state wave function. In 1964, Hohenberg and Kohn introduced two theorems [18], which give rise to a huge simplification in evaluating  $E_0$  via Eq. 2.5. At its core, the Hohenberg-Kohn theorems circumvent the problem of determining  $\Psi(\mathbf{r}_1, \mathbf{r}_2, \dots, \mathbf{r}_N)$  by proving that:

1. For a given external potential  $\mathbf{V}_{\text{ext}}$ , the total energy is in fact a unique functional of the electron density

$$\rho(\mathbf{r}) = \langle \Psi | \sum_i \delta(\mathbf{r} - \mathbf{r}_i) | \Psi \rangle. \quad (2.6)$$

<sup>1</sup>For the remainder of this thesis, operators as well as vectors are denoted in bold.

<sup>2</sup>The Born-Oppenheimer approximation is implicitly assumed here, i.e., the motion of the ionic and electronic system is considered to be decoupled.

The proof is indirect and establishes a bijective map between the set of all external potentials  $V_{\text{ext}}$  and the set of all electron densities  $\rho$  that (i) are normalized to  $N$  electrons and (ii) can be expressed as the ground-state density of a many-electron system under the influence of a given external potential (the set of „ $v$ -representable“ densities).<sup>3</sup> Due to condition (i), the terms  $\langle T_e \rangle$  and  $\langle V_{\text{ee}} \rangle$  are unique functionals of  $\rho$ . The bijective map  $\rho \leftrightarrow V_{\text{ext}}$  then ensures that  $\langle V_{\text{ext}} \rangle$ , as the last term in  $E$ , is a unique functional of  $\rho$  as well

2. The energy functional  $E[\rho]$  is subject to a variational principle in  $\rho$  and minimized by the ground-state density  $\rho_0 = \langle \Psi_0 | \sum_i \delta(\mathbf{r} - \mathbf{r}_i) | \Psi_0 \rangle$ . This statement follows directly from the first theorem, using the Releigh-Ritz variational principle.

It is thus possible to reformulate the searching scheme for the ground-state energy in Eq. 2.5 into

$$\begin{aligned} E_0 = \min_{\rho} E[\rho] &= \min_{\rho} \left\{ F[\rho] + \int v_{\text{ext}}(\mathbf{r}) \rho(\mathbf{r}) d\mathbf{r} \right\} \\ &= F[\rho_0] + \int v_{\text{ext}}(\mathbf{r}) \rho_0(\mathbf{r}) d\mathbf{r}. \end{aligned} \quad (2.7)$$

The sum of  $\langle T \rangle$  and  $\langle V_{\text{ee}} \rangle$  is thereby abbreviated as  $F[\rho]$ , i.e., the universal functional of an  $N$ -electron system. This new formulation is still, in principle, exact. However, apart from the trivial dependency of  $\langle V_{\text{ext}} \rangle$  on the electron density, the full shape of the functional  $E[\rho]$  is yet unknown.

### 2.1.2 Kohn-Sham Formalism

Without explicit knowledge of  $F[\rho]$ , the relation in Eq. 2.7 remains of no practical use. However, in 1965, Kohn and Sham proposed not only a theory to reformulate  $F[\rho]$  but also a scheme to determine the charge density  $\rho$  and total energy  $E$  in a self-consistent manner [19]. The key idea is the following: In the spirit of the Hartree-Fock theory, Kohn and Sham introduced a reference system of  $N$  noninteracting electrons under the influence of an effective mean-field potential. This reference system is then assumed to yield the exact charge density of the interacting system, which in turn yields the ground-state energy  $E_0$ .

In a noninteractive picture, the many-body wave function  $\Psi$  is given by a Slater determinant of the form 2.4, with one-particle (op) orbitals  $\phi_i(\mathbf{r})$ . The electron density in this case is given by

$$\rho_{\text{op}}(\mathbf{r}) = \sum_i |\phi_i(\mathbf{r})|^2. \quad (2.8)$$

The kinetic energy contribution  $T_{\text{op}}$  to the functional  $F[\rho]$  can then be written as

$$\begin{aligned} T_{\text{op}} &= \sum_i \langle \phi_i | \mathbf{T} | \phi_i \rangle = \sum_i \int \phi_i(\mathbf{r})^* \frac{\mathbf{p}^2}{2m} \phi_i(\mathbf{r}) d\mathbf{r} \\ &= -\frac{\hbar^2}{2m} \sum_i \int \phi_i(\mathbf{r})^* \nabla^2 \phi_i(\mathbf{r}) d\mathbf{r}. \end{aligned} \quad (2.9)$$

<sup>3</sup>The necessity of  $\rho$  to be  $v$ -representable can actually be dropped, as was shown, e.g., in an argument by Levy in 1982 [42].

Note that, at least implicitly,  $T_{\text{op}}$  is a functional of the density  $\rho_{\text{op}}$ . In a similar manner, another contribution to the universal functional  $F[\rho]$  is known explicitly, i.e., the electrostatic interaction energy  $E_{\text{H}}$  between two charge densities (Hartree energy) given by

$$E_{\text{H}}[\rho_{\text{op}}] = \frac{e^2}{2} \int \frac{\rho_{\text{op}}(\mathbf{r})\rho_{\text{op}}(\mathbf{r}')}{|\mathbf{r} - \mathbf{r}'|} d\mathbf{r} d\mathbf{r}'. \quad (2.10)$$

Evidently, the sum of  $T_{\text{op}}$  and  $E_{\text{H}}$  alone is only a rough estimate of the total functional  $F[\rho]$ . For one, the fermionic character of the electrons would be neglected, as it gives rise to an additional contribution, the exchange interaction. Additionally, all interactions that go beyond the Hartree picture and electronic exchange, commonly labeled as electronic correlation, are still missing. The existence of countless phenomena can thereby be attributed to electronic correlation, including van-der-Waals interaction and screening effects accompanying the creation of electron-hole pairs in a solid [40]. All exchange and correlation (XC) effects contributing to  $F[\rho]$  are now summarized in a (still unknown) functional  $E_{\text{xc}}[\rho]$ .

Assuming the electron density  $\rho$  of the interacting system to be equal to the density  $\rho_{\text{op}}$  of the noninteracting one, the ansatz for the energy functional 2.7 reads

$$\begin{aligned} E[\rho_{\text{op}}] &= F[\rho_{\text{op}}] + \int v_{\text{ext}}(\mathbf{r})\rho_{\text{op}}(\mathbf{r}) d\mathbf{r} \\ &= T_{\text{op}}[\rho_{\text{op}}] + E_{\text{H}}[\rho_{\text{op}}] + E_{\text{xc}}[\rho_{\text{op}}] + \int v_{\text{ext}}(\mathbf{r})\rho_{\text{op}}(\mathbf{r}) d\mathbf{r}. \end{aligned} \quad (2.11)$$

Apart from the assumption regarding the density, no approximation has yet been introduced, rendering the theory still exact up to this point.

For the ground-state density  $\rho_0$ , the variation of the functional  $E[\rho_{\text{op}}]$ , under the condition that  $\rho_{\text{op}}$  is normalized to  $N$  electrons, yields

$$\frac{\delta}{\delta \rho_{\text{op}}} \left\{ E[\rho_{\text{op}}] - \sum_{i=1}^N \epsilon_i \left( \int |\phi_i(\mathbf{r})|^2 d\mathbf{r} - 1 \right) \right\} \Big|_{\rho_0} = 0. \quad (2.12)$$

The constraint is enforced via the Lagrange multipliers  $\epsilon_i$ . Due to the explicit dependence of  $\rho_{\text{op}}$  on the one-particle orbitals  $\phi_i$ , the variation in 2.12 may be performed with respect to the orbitals  $\phi_i^*$ , considering

$$\frac{\delta}{\delta \phi_i^*} \{ \dots \} = \frac{\delta}{\delta \rho_{\text{op}}} \{ \dots \} \cdot \phi_i. \quad (2.13)$$

Combining Eqs. 2.9 – 2.13, the condition 2.12 reads

$$\begin{aligned} \frac{\delta}{\delta \phi_i^*} \left\{ E[\phi_i] - \sum_{i=1}^N \epsilon_i \left( \int |\phi_i(\mathbf{r})|^2 d\mathbf{r} - 1 \right) \right\} \Big|_{\rho_0} &= 0 \\ \Rightarrow \left( -\frac{\hbar^2}{2m} \nabla^2 + \underbrace{v_{\text{ext}}(\mathbf{r}) + e^2 \int \frac{\rho_{\text{op}}(\mathbf{r}')}{|\mathbf{r} - \mathbf{r}'|} d\mathbf{r}'}_{=v_{\text{eff}}} + v_{\text{xc}}[\rho_{\text{op}}] \right) \phi_i(\mathbf{r}) &= \epsilon_i \phi_i(\mathbf{r}) \end{aligned} \quad (2.14)$$

The term  $v_{\text{xc}} = \frac{\delta E_{\text{xc}}}{\delta \phi_{\text{op}}}$  thereby denotes the XC potential. This system of equations is known as the Kohn-Sham equations and describes an ensemble of  $N$  noninteracting electrons under the influence of an effective mean-field potential  $v_{\text{eff}}$ . Evidently,  $v_{\text{eff}}$  itself depends on the electron density  $\rho_{\text{op}}$ , making the Kohn-Sham equations (in principle) solvable via a self-consistency loop: The solutions  $\{\phi_i\}$  of 2.14 determine an electron density  $\rho_{\text{op}}$  via 2.8, which, in turn, fixes the effective potential  $v_{\text{eff}}$ , giving rise to another set of solutions  $\{\phi_i\}$ . By definition, self consistency is reached for the set of solutions yielding the true ground-state electron density  $\rho_0$ . By substituting  $T_{\text{op}}$  in Eq. 2.11 with its corresponding term within the Kohn-Sham equations 2.14, the total ground-state energy  $E_0$  may be expressed as

$$E_0 = \sum_{i=1}^N \epsilon_i - E_{\text{H}}[\rho_0] + E_{\text{xc}}[\rho_0] - \int v_{\text{xc}}[\rho_0] \cdot \rho_0 \, d\mathbf{r}. \quad (2.15)$$

An interpretation of the Kohn-Sham eigenvalues  $\epsilon_i$  to be true one-particle energies would thus underestimate the total energy by the Hartree energy and XC contributions. A further reason for the eigenvalues to not be misinterpreted as true excitation energies is the underestimation of the fundamental band gap, as later discussed in Sec. 2.1.6.

The Kohn-Sham equations thus provide an exact, systematic scheme to determine the ground-state energy. However, one essential problem remains, as  $v_{\text{xc}}$  and its dependence on the electron density remain unknown and have to be approximated.

### 2.1.3 Local-Density Approximation

Already in their original work, Kohn and Sham noted that if the spatial variation of  $\rho(\mathbf{r})$  was sufficiently small, the XC energy could be approximated as [19]

$$E_{\text{xc}}^{\text{LDA}}[\rho] = \int \rho(\mathbf{r}) \cdot \epsilon_{\text{xc}}^{\text{LDA}}[\rho(\mathbf{r})] \, d\mathbf{r} \quad \text{with} \quad \epsilon_{\text{xc}}^{\text{LDA}}[\rho] = \epsilon_{\text{x}}^{\text{LDA}}[\rho] + \epsilon_{\text{c}}^{\text{LDA}}[\rho]. \quad (2.16)$$

The term  $\epsilon_{\text{xc}}^{\text{LDA}}[\rho]$  in the integrand refers to the XC energy density of the homogenous electron gas. The magnitude of  $E_{\text{xc}}^{\text{LDA}}[\rho]$  is thus determined by the local value of the density  $\rho$  at position  $\mathbf{r}$  within this approximation, hence the naming „local-density approximation“ (LDA).

Within Hartree-Fock theory, the exchange part  $\epsilon_{\text{x}}^{\text{LDA}}$  is known exactly [36], namely

$$\epsilon_{\text{x}}^{\text{LDA}}[\rho] = -\frac{3e^2}{4\pi} \cdot k_{\text{f}} = -\frac{3e^2}{4\pi} (3\pi^2)^{\frac{1}{3}} \cdot \rho^{\frac{1}{3}}. \quad (2.17)$$

Neglecting correlation effects, a rescaled version of 2.17 is the basis of the XC energy within the  $X_{\alpha}$ -method by Slater and Johnson [43].

The shape of the correlation part  $\epsilon_{\text{c}}^{\text{LDA}}$  to  $\epsilon_{\text{xc}}^{\text{LDA}}$  is only accessible indirectly, e.g., via stochastic models [44]. On this basis, a number of parametrization have been published, including one by Vosko *et al.* [45], by Perdew and Wang [46] and by Perdew and Zunger [47]. The latter parametrization is thereby of the form

$$\epsilon_{\text{c}}^{\text{LDA}}[\rho] = \frac{\gamma}{1 + \beta_1 \sqrt{r_s[\rho]} + \beta_2 r_s[\rho]} \quad \text{with} \quad r_s[\rho] = \left( \frac{3}{4\pi\rho} \right)^{\frac{1}{3}}. \quad (2.18)$$

The constants  $\gamma$ ,  $\beta_1$  and  $\beta_2$  read

$$\gamma = -0.1423, \beta_1 = 1.0529 \text{ and } \beta_2 = 0.333. \quad (2.19)$$

Despite the fact that LDA is, per construction, only exact for sufficiently homogeneous systems, computed total energies and related quantities turned out to be surprisingly accurate also for strongly inhomogeneous crystals. Additionally, LDA is known to naturally fulfill the well-known sum rule

$$\int \rho_{\text{xc}}(\mathbf{r}, \mathbf{r}') d\mathbf{r}' = -1 \quad (2.20)$$

for the XC hole density, defined as the depletion of electrons at  $\mathbf{r}'$  due to the presence of another electron at  $\mathbf{r}$ . For this reason, LDA and its extension to spin polarized cases (LSDA) have sometimes been labeled „mother of all approximations“ [48].

However, LDA is also known to come with a number of drawbacks. For one, LDA tends to systematically overbind molecules and solids, resulting in an underestimation of lattice constants along with an overestimation of phonon frequencies and cohesive energies [49]. Additionally, LDA was shown to predict wrong energetic orderings of solid bulk phases as well as molecular confirmations, e.g., for molecular carbon [50].

## 2.1.4 Generalized-Gradient Approximation

As an extension to the LDA, the generalized-gradient approximation (GGA) yields an XC energy according to the semilocal form [51]

$$E_{\text{xc}}^{\text{GGA}}[\rho] = \int f[\rho, \nabla \rho] d\mathbf{r}, \quad (2.21)$$

with the kernel  $f$  as a function of the electron density and its gradient  $\nabla \rho$ . The best possible parametrization of  $f$  has been the subject of debate [40, 52]. One difficulty in finding adequate parametrizations lies in the fact that the XC-hole sum rule (see Eq. 2.20) is easily violated. Among the parametrizations that stood the test of time, the PBE formulation (named after their inventors Perdew, Burke and Ernzerhof) emerged as one of the most widely used to date [51]. PBE is thereby an extension and simplification of the formulation by Perdew and Wang (PW91) [46]. The full parametrization of  $f$ , including spin polarization<sup>4</sup>, reads

$$\begin{aligned} f[\rho, \nabla \rho] &= \rho \cdot (\varepsilon_x^{\text{PBE}}[\rho, \nabla \rho] + \varepsilon_c^{\text{PBE}}[\rho, \nabla \rho]), \\ \text{with } \varepsilon_x^{\text{PBE}}[\rho, \nabla \rho] &= \varepsilon_x^{\text{LDA}}[\rho] \cdot F_x[\rho, \nabla \rho] \\ \text{and } \varepsilon_c^{\text{PBE}}[\rho, \nabla \rho] &= \varepsilon_c^{\text{LDA}}[\rho] + H[\rho, \nabla \rho]. \end{aligned} \quad (2.22)$$

The two functions  $F_x$  and  $H$  are given by

$$\begin{aligned} F_x[\rho, \nabla \rho] &= 1 + \kappa - \frac{\kappa}{1 + \frac{\mu s^2}{\kappa}} \\ \text{and } H[\rho, \nabla \rho] &= \frac{e^2}{a_0} \gamma \phi^3 \ln \left( 1 + \frac{\beta}{\gamma} t^2 \left[ \frac{1 + At^2}{1 + At^2 + A^2 t^4} \right] \right), \end{aligned} \quad (2.23)$$

<sup>4</sup>If spin polarization is included, the entire charge density  $\rho$  is given as the sum of both spin channel contributions  $\rho^\uparrow$  and  $\rho^\downarrow$ .

with the generalized, dimensionless density gradients

$$s = \frac{|\nabla \rho|}{2k_F \rho} \quad \text{and} \quad t = \frac{|\nabla \rho|}{2\phi k_S \rho}, \quad (2.24)$$

a spin scaling factor

$$\phi = \frac{(1 + \xi)^{\frac{2}{3}} + (1 - \xi)^{\frac{2}{3}}}{2}, \quad \xi = \frac{\rho^\uparrow - \rho^\downarrow}{\rho^\uparrow + \rho^\downarrow}, \quad (2.25)$$

and a factor

$$A = \frac{\beta}{\gamma} \frac{1}{\exp\left(-\frac{\varepsilon_c^{\text{LDA}, a_0}}{\gamma \phi^3 e^2}\right) - 1}. \quad (2.26)$$

Further factors are  $a_0 = \frac{\hbar^2}{me^2}$ ,  $k_F = (3\pi^2)^{\frac{1}{3}} \cdot \rho^{\frac{1}{3}}$  and  $k_S = \sqrt{\frac{4k_F}{\pi a_0}}$ . The four remaining parameters  $\kappa$ ,  $\mu$ ,  $\gamma$  and  $\beta$  are obtained by considering a number of fundamental constraints regarding the slowly/rapidly varying limit and the high-density limit of  $\rho$  and are given by

$$\kappa = 0.804, \quad \mu = 0.220, \quad \gamma = 0.031, \quad \text{and} \quad \beta = 0.067. \quad (2.27)$$

While the PBE functional was shown to yield, on average, ground-state properties closer to experimental values (compared to the LSDA) [53], it also suffers from a shortcoming related to the systematic ambiguity of GGA functionals: It has been pointed out that, depending on how much weight is put on the gradient dependence of a given GGA XC functional, either the ground-state energy or bond lengths are described to a better degree, but never both at the same time [54, 55]. For this reason, PBE is known to overestimate lattice constants in solids while also drastically underestimating surface energies.

In this work, the PBEsol functional, an extension to PBE, is used [55]. In the spirit of the previously mentioned ambiguity regarding XC functionals, PBEsol has been specifically designed to yield accurate lattice constants in solids. The actual parametrization of the XC functional is identical to PBE (Eqs. 2.22–2.27), only the parameters  $\mu = \frac{10}{81}$  and  $\beta = 0.046$  are adjusted. Lattice constants obtained with PBEsol typically reproduce the respective experimental values with an accuracy of better than 0.5 % [56–58].

## 2.1.5 Calculation of Forces

In the absence of external fields, the external potential  $V_{\text{ext}}(\{\mathbf{r}_k\})$  entering into the general  $N$ -electron hamiltonian and the Kohn-Sham equations can be considered to arise from the bare Coulomb interaction between electrons and ions

$$V_{\text{ext}}(\{\mathbf{r}_k\}) = \sum_{k=1}^{N_e} v_{\text{ext}}(\mathbf{r}_k) = \sum_{k=1}^{N_e} \sum_{l=1}^{N_i} \frac{Z_l e^2}{|\mathbf{r}_k - \mathbf{R}_l|}, \quad (2.28)$$

where  $N_e$  denotes the number of electrons and  $N_i$  the number of ions with charge  $Z_l$  at position  $\mathbf{R}_l$ . The ionic geometry  $\{\mathbf{R}_l\}$  thus fixes the external potential, which, in turn, governs the electronic charge density and ground-state energy  $E_0$ , according to the Hohenberg-Kohn theorems. In most cases, it is therefore of crucial importance to determine the electronic

ground state at the ionic ground-state geometry, given by the arrangement  $\{\mathbf{R}_l\}$  which minimizes  $E_0$  or, alternatively, the total force

$$\mathbf{F} = - \sum_{l=1}^{N_i} \frac{\partial E_{\text{tot}}}{\partial \mathbf{R}_l}, \quad (2.29)$$

where  $E_{\text{tot}} = E_0 + \sum_{l,m < l}^{N_i} \frac{Z_l Z_m e^2}{|\mathbf{R}_l - \mathbf{R}_m|}$ .

The total energy  $E_{\text{tot}}$  is given by the sum of electronic ground-state energy 2.15 and ion-ion Coulomb interaction. The force acting on an individual ion  $l$ , given by the energy derivative in Eq. 2.29, may be deduced from a self-consistent DFT calculation using the Hellmann-Feynman theorem, stating that the derivative of the total energy  $E_{\text{tot}} = \langle \Psi | \mathbf{H} | \Psi \rangle$  with respect to an arbitrary parameter  $\lambda$  is given by<sup>5</sup>

$$\frac{\partial E_{\text{tot}}}{\partial \lambda} = \langle \Psi | \frac{\partial \mathbf{H}}{\partial \lambda} | \Psi \rangle. \quad (2.30)$$

For  $\lambda = \mathbf{R}_l$ , all terms in  $\mathbf{H}$  besides  $v_{\text{ext}}(\mathbf{r})$  and the ion-ion interaction term in Eq. 2.29 vanish, yielding

$$\frac{\partial E_{\text{tot}}}{\partial \mathbf{R}_l} = Z_l \int \rho(\mathbf{r}') \frac{\mathbf{r}' - \mathbf{R}_l}{|\mathbf{r}' - \mathbf{R}_l|^3} d\mathbf{r}' + \sum_{m \neq l}^{N_i} Z_m Z_l \frac{\mathbf{R}_m - \mathbf{R}_l}{|\mathbf{R}_m - \mathbf{R}_l|^3}. \quad (2.31)$$

From the individual forces, the ground-state geometry can be determined using a number of common optimization algorithms, including the residual minimization method/direct inversion in the iterative subspace (RMM-DIIS) [63, 64] and the conjugate gradient algorithm [65].

## 2.1.6 The Band-Gap Problem in DFT

In practical applications, the eigenvalues  $\{\epsilon_i\}$  obtained via the Kohn-Sham scheme 2.14 are often interpreted as true single-particle excitation energies of electrons in a solid, i.e., the energy gained (lost) by adding (removing) an electron. This is mostly mandated by a good agreement with experimental photoemission data as well as band dispersions for a number of systems [38, 41]. However, the values  $\epsilon_i$  do not bear a direct physical meaning<sup>6</sup> and an interpretation as excitation energies falls short in describing the fundamental band gap of semiconductors and insulators. In that context, the band gap is given by the difference between lowest unoccupied and highest occupied electronic state. For a large number of systems, their band gaps are underestimated by a large fraction of their value within Kohn-Sham theory [41, 67]. In the extreme case of the high-temperature superconductor  $\text{La}_2\text{CuO}_4$  (a Mott insulator), DFT-LDA calculations falsely predict metalicity (i.e., a vanishing band gap) [68]. Similarly, Ge is falsely predicted to be a metal within DFT-LDA [40, 69].

<sup>5</sup>Technically, the Hellmann-Feynman theorem only holds, if  $|\Psi\rangle$  is a true eigenstate of  $\mathbf{H}$ . However, in practice, the electronic wave functions are expanded in a finite basis set, giving rise to additional terms to Eq. 2.29, depending on the derivative of the wave function with respect to  $\lambda$  (Pulay forces) [59, 60]. These extra terms vanish, if the basis set is independent of the parameter  $\lambda$  (Hurley's condition) [61]. In the case of a plane-wave basis set, as used in this thesis, that condition is naturally fulfilled for  $\lambda = \mathbf{R}$  [62].

<sup>6</sup>Apart from the eigenvalue of the highest occupied state, which corresponds to the negative ionization energy for the true XC potential (DFT Koopmans' theorem) [66].

One reason for this underestimation can be traced to the sum of Hartree and XC contributions to the total energy in Eq. 2.11. The form of  $E_H$  implies a spurious interaction of an electron with itself that has to be compensated by  $E_{xc}$ . However, all local and semilocal approximations to  $v_{xc}$  (and thus to  $E_{xc}$ ) are known to compensate for this effect only partially, leaving a fraction of self-interaction in the Kohn-Sham scheme. Especially for one-electron systems, this error leads to a significant increase in both, total energy as well as Kohn-Sham eigenvalues. Within LDA, the total energy of the 1s electron in a hydrogen atom was shown to be overestimated by up to 5% [47, 70, 71]. With almost 50%, the overestimation of the 1s Kohn-Sham state is even higher [70]. Unoccupied states, however, are not affected by the lack of self-interaction compensation, since they do not contribute to the total charge density. The energy gap between highest occupied and lowest unoccupied state is therefore underestimated, regardless of the used approximation to  $v_{xc}$ .

Another fundamental reason why DFT eigenvalues fall short to accurately describe fundamental band gaps is related to the derivative discontinuity of the total energy  $E_0^N$  as a function of the electron number  $N$  and would persist even if the true XC functional was utilized. In a charge-neutral system, the band gap  $E_g$  equals the difference of the first ionization energy  $I_N$  and the first electron affinity  $A_N$  and is therefore related to  $E_0^N$  via

$$E_g = I_N - A_N \quad (2.32)$$

where  $I_N = E_0^{N-1} - E_0^N$  and  $A_N = E_0^N - E_0^{N+1}$ .

Extending DFT to account for fractional electron numbers enables the evaluation of  $E_0^N$  as a continuous function in  $N$ . It was thereby shown that  $E_0^N$  is composed of straight-line segments changing slope at integer values of  $N$  [66, 72, 73]. At these points, the total energy therefore features a derivative discontinuity. For  $N \rightarrow \infty$ , a change of  $N$  by  $\pm 1$  results in an infinitesimal variation  $\delta\rho$  of the charge density. Using the energy functional  $E_0[\rho]$  of the charge density, the band gap in Eq. 2.32 may thus be rewritten as

$$E_g = \lim_{\delta \rightarrow 0} \left\{ \frac{\delta E_0[\rho]}{\delta \rho} \bigg|_{N-\delta} - \frac{\delta E_0[\rho]}{\delta \rho} \bigg|_{N+\delta} \right\} > 0. \quad (2.33)$$

The derivative discontinuity (and thus the gap) is positive, since  $E_0^N$  is a convex function in  $N$  [66]. Both functional derivatives are evaluated at the  $(N \pm \delta)$ -electron ground-state charge densities. According to Eq. 2.11, two of the four contributions to  $E_0[\rho]$  are continuous in the density (external potential and Hartree contribution), leaving the derivative discontinuities

$$\Delta_T := \lim_{\delta \rightarrow 0} \left\{ \frac{\delta T[\rho]}{\delta \rho} \bigg|_{N-\delta} - \frac{\delta T[\rho]}{\delta \rho} \bigg|_{N+\delta} \right\} \quad (2.34)$$

$$\text{and } \Delta_{xc} := \lim_{\delta \rightarrow 0} \left\{ \frac{\delta E_{xc}[\rho]}{\delta \rho} \bigg|_{N-\delta} - \frac{\delta E_{xc}[\rho]}{\delta \rho} \bigg|_{N+\delta} \right\} \quad (2.35)$$

in the kinetic and XC energy as the only two terms building up the band gap. The former is thereby related to the  $N$ -electron Kohn-Sham eigenvalues  $\epsilon_i^N$  by the following argument: For noninteracting electrons<sup>7</sup>,  $E_g$  exactly equals  $\Delta_T$ . Using the theorem of Janak [74]

$$\frac{\partial E_0^N}{\partial f_i} = \epsilon_i^N, \quad (2.36)$$

<sup>7</sup>Or electrons within a local mean-field potential, e.g., the XC potential within LDA.

where  $f_i \in [0, 1]$  denotes the occupation number of the  $i$ -th Kohn-Sham state,  $I_N$  and  $A_N$  in Eq. 2.32 take the form

$$I_N = - \int_0^1 \epsilon_N^{N-1+f} df = -\epsilon_N^{N-\delta} \quad (2.37)$$

and  $A_N = - \int_0^1 \epsilon_{N+1}^{N+f} df = -\epsilon_{N+1}^{N+\delta}$ .

The right hand expressions thereby follow from the mean value theorem for  $N \rightarrow \infty$ , with  $\delta$  as a positive infinitesimal. The band gap  $E_g = \Delta_T$ , as the difference between  $I_N$  and  $A_N$  in the limit of  $\delta \rightarrow 0$ , is then exactly given by the Kohn-Sham gap  $\epsilon_{N+1}^N - \epsilon_N^N$ . It is therefore reasonable to assume that  $\Delta_T$  also denotes the Kohn-Sham gap if the true XC potential is used. In that case, the band gap reads

$$E_g = \epsilon_{N+1}^N - \epsilon_N^N + \Delta_{xc} \quad (2.38)$$

and evidently differs from the Kohn-Sham gap by the XC derivative discontinuity. For an arbitrary approximation to the XC potential, the band-gap discrepancy therefore originates from (i) a poor description of the Kohn-Sham gap due to shortcomings in the used XC potential and (ii) neglect of  $\Delta_{xc}$ . Studies for the materials Si, GaAs, AlAs and diamond thereby indicate that origin (ii) consistently accounts for about 80 % of the total band gap discrepancy with respect to LDA calculations [75].

## 2.2 The Self-Energy Concept

Since the band-gap underestimation in DFT is evidently related to the XC potential in general and would persist even for the true XC potential, the problem cannot be solved by introducing better approximations to  $\nu_{xc}$ . Instead, the aforementioned self-interaction of electrons within Kohn-Sham theory should be revisited.

### 2.2.1 Quasiparticle Picture and Green's Function

Within DFT, an electron is treated to be under the influence of an effective potential, given by the mean field created by the remaining electrons. A more fundamental way to directly describe the many-body problem can be introduced using second quantization. Within it, an electron is treated to be an excitation of the vacuum state  $|0\rangle$ , induced by the creation operator  $\psi^\dagger(\mathbf{r})$ . Both  $\psi^\dagger(\mathbf{r})$  and the adjoint annihilation operator  $\psi(\mathbf{r})$  thereby fulfill the anticommutator algebra

$$[\psi(\mathbf{r}), \psi(\mathbf{r}')]_+ = [\psi^\dagger(\mathbf{r}), \psi^\dagger(\mathbf{r}')]_+ = 0 \quad (2.39)$$

and  $[\psi(\mathbf{r}), \psi^\dagger(\mathbf{r}')]_+ = \delta(\mathbf{r} - \mathbf{r}')$ ,

with  $[A, B]_+ = AB + BA$ . An arbitrary base state of the  $N$ -electron Fock space may be created by successively applying  $\psi^\dagger(\mathbf{r})$  on the vacuum state:

$$|\mathbf{r}_1, \mathbf{r}_2, \dots, \mathbf{r}_N\rangle = \frac{1}{\sqrt{N!}} \psi^\dagger(\mathbf{r}_1) \psi^\dagger(\mathbf{r}_2) \dots \psi^\dagger(\mathbf{r}_N) |0\rangle. \quad (2.40)$$

An application of  $\psi^\dagger(\mathbf{r})$  on a  $N$ -electron state thus creates an electron at the position  $\mathbf{r}$ . The annihilation operator  $\psi(\mathbf{r})$ , on the other hand, removes an electron at the position  $\mathbf{r}$  from the system. Additionally,  $\psi(\mathbf{r})$  defines the vacuum state via the condition  $\psi(\mathbf{r})|0\rangle = 0$ .

An explicit time-dependence of  $\psi$  and  $\psi^\dagger$  is introduced within the Heisenberg picture via

$$\Psi(\mathbf{r}, t) = e^{\frac{i}{\hbar} \mathbf{H} t} \psi(\mathbf{r}) e^{-\frac{i}{\hbar} \mathbf{H} t} \quad \text{and} \quad \Psi^\dagger(\mathbf{r}, t) = e^{\frac{i}{\hbar} \mathbf{H} t} \psi^\dagger(\mathbf{r}) e^{-\frac{i}{\hbar} \mathbf{H} t}, \quad (2.41)$$

with the (time-independent) many-body hamiltonian  $\mathbf{H}$  given by 2.1. Using this field-operator formulation, all three fundamental operators in  $\mathbf{H}$  can be rewritten as

$$\begin{aligned} \mathbf{T}_e &= \sum_i -\frac{\hbar^2}{2m} \nabla_i^2 := \int \Psi^\dagger(\mathbf{r}, t) \left( -\frac{\hbar^2}{2m} \nabla^2 \right) \Psi(\mathbf{r}, t) d\mathbf{r}, \\ \mathbf{V}_{\text{ext}} &= \sum_i v_{\text{ext}}(\mathbf{r}_i) := \int \Psi^\dagger(\mathbf{r}, t) v_{\text{ext}}(\mathbf{r}) \Psi(\mathbf{r}, t) d\mathbf{r}, \\ \text{and} \quad \mathbf{V}_{\text{ee}} &= \sum_{i,j < i} v_{\text{ee}}(\mathbf{r}_i, \mathbf{r}_j) := \frac{1}{2} \int \Psi^\dagger(\mathbf{r}', t) \Psi^\dagger(\mathbf{r}, t) v_{\text{ee}}(\mathbf{r}, \mathbf{r}') \Psi(\mathbf{r}, t) \Psi(\mathbf{r}', t) d\mathbf{r} d\mathbf{r}', \end{aligned} \quad (2.42)$$

where  $v_{\text{ee}}(\mathbf{r}, \mathbf{r}') = \frac{e^2}{|\mathbf{r} - \mathbf{r}'|}$ . In the Heisenberg picture, the time evolution of  $\Psi$  is described by the Heisenberg equation

$$\frac{d\Psi}{dt} = \frac{1}{i\hbar} [\Psi, \mathbf{H}] + \frac{\partial \Psi}{\partial t}. \quad (2.43)$$

Inserting all three terms in 2.42 into  $\mathbf{H}$ , the equation of motion reads

$$\begin{aligned} i\hbar \frac{\partial}{\partial t} \Psi(\mathbf{r}, t) &= \mathbf{h}_0(\mathbf{r}) \Psi(\mathbf{r}, t) + \int \Psi^\dagger(\mathbf{r}', t) v_{\text{ee}}(\mathbf{r}, \mathbf{r}') \Psi(\mathbf{r}', t) \Psi(\mathbf{r}, t) d\mathbf{r}' \\ \text{where} \quad \mathbf{h}_0(\mathbf{r}) &= -\frac{\hbar}{2m} \nabla^2 + v_{\text{ext}}(\mathbf{r}). \end{aligned} \quad (2.44)$$

An electron created in this manner interacts with its surrounding via the naked Coulomb interaction  $v_{\text{ee}}$ , repelling electrons in its vicinity. The resulting Coulomb hole effectively leads to a decreased interaction of the electron with its surrounding (screening). Both the electron and its Coulomb hole thereby behave like a single entity with renormalized mass and charge: a quasiparticle. At temperature  $T = 0$ , the propagation of this quasiparticle is conveniently described using the corresponding time-ordered Green's function operating on the  $N$ -electron ground state  $|\Psi_0^N\rangle$ <sup>8</sup>

$$G(\mathbf{r}, t, \mathbf{r}', t') = -\frac{i}{\hbar} \langle \Psi_0^N | \mathcal{T}(\Psi(\mathbf{r}, t) \Psi^\dagger(\mathbf{r}', t')) | \Psi_0^N \rangle. \quad (2.45)$$

Here, the operator  $\mathcal{T}$  ensures an ascending ordering of the field operators according to their time variable, i.e.,

$$\mathcal{T}(A(t)B(t')) = \begin{cases} A(t)B(t') & \text{if } t' > t \\ -B(t')A(t) & \text{if } t' < t \end{cases}. \quad (2.46)$$

<sup>8</sup>For finite temperatures, the statistical operator within the grand canonical ensemble should be included in the expectation value in 2.45. By staying in the  $T \rightarrow 0$  limit, however, this statistical mean is identical to the expectation value over the  $N$ -electron ground state. A derivation of the Green's function and its Fourier transform at finite temperatures can be found, e.g., in [37].

Depending on the time ordering, the Green's function describes the propagation of (i) an electron created at the space-time position  $(\mathbf{r}', t')$  and removed at  $(\mathbf{r}, t)$  (if  $t > t'$ ) or (ii) a hole created at  $(\mathbf{r}, t)$  and removed at  $(\mathbf{r}', t')$  (if  $t < t'$ ). The connection between the Green's function and true excitation energies of the electronic system becomes evident by explicitly considering the transformation law between Heisenberg and Schrödinger picture for the field operators (see 2.41) and inserting the closure relation  $\mathbf{1} = \sum_i |\Psi_i^{N\pm 1}\rangle \langle \Psi_i^{N\pm 1}|$  of the  $(N \pm 1)$ -electron eigenstates between  $\Psi$  and  $\Psi^\dagger$ . Fourier transformation of  $\mathbf{G}(\mathbf{r}, \mathbf{r}', \tau)$ , with  $\tau := t - t'$ , then yields the compact Lehmann representation of the Green's function [37, 76]

$$\mathbf{G}(\mathbf{r}, \mathbf{r}', \omega) = \frac{1}{2\pi} \lim_{\gamma \rightarrow 0} \int \frac{A(\mathbf{r}, \mathbf{r}', \omega')}{\omega - \omega' + i\gamma \cdot \text{sgn}(\hbar\omega' - \mu)} d\omega'. \quad (2.47)$$

The spectral function

$$\begin{aligned} A(\mathbf{r}, \mathbf{r}', \omega) = & \sum_i \phi_i^{N-1}(\mathbf{r}) (\phi_i^{N-1}(\mathbf{r}'))^* \delta(\hbar\omega - \epsilon_i^{N-1}) \\ & + \sum_i \phi_i^{N+1}(\mathbf{r}) (\phi_i^{N+1}(\mathbf{r}'))^* \delta(\hbar\omega - \epsilon_i^{N+1}) \end{aligned} \quad (2.48)$$

is used here as a generalized density of states of the excited system, with the projections

$$\phi_i^{N-1}(\mathbf{r}) := \langle \Psi_i^{N-1} | \Psi(\mathbf{r}) | \Psi_0^N \rangle \quad \text{and} \quad \phi_i^{N+1}(\mathbf{r}) := \langle \Psi_0^N | \Psi(\mathbf{r}) | \Psi_i^{N+1} \rangle \quad (2.49)$$

between the  $N$ -electron ground state and the  $(N \pm 1)$ -electron excited states and their respective excitation energies

$$\epsilon_i^{N-1} = E_0^N - E_i^{N-1} \quad \text{and} \quad \epsilon_i^{N+1} = E_i^{N+1} - E_0^N. \quad (2.50)$$

Without electron-electron interaction,  $\phi_i^{N\pm 1}$  correspond to the respective  $i$ -th single-particle orbitals with energies  $\epsilon_i^{N\pm 1}$ . Note that the sign of the infinitesimal complex shift  $\gamma$ , required to ensure the causality of  $\mathbf{G}(\mathbf{r}, \mathbf{r}', \tau)$ , depends on the chemical potential  $\mu = \frac{\partial E_0^N}{\partial N}$ . As discussed in Sec. 2.1.6, the ground-state energy as a function of the electron number is convex and composed of line segments, changing slope at integer values of  $N$ . For this reason, the inequalities

$$\epsilon_i^{N-1} - \mu \leq 0 \quad \text{and} \quad \epsilon_i^{N+1} - \mu \geq 0 \quad (2.51)$$

hold, subsequently implying  $\epsilon_i^{N-1} \leq \epsilon_i^{N+1}$ . A many-electron system therefore loses more energy from removing one electron than it gains from adding one [76].

According to Eq. 2.47, the poles in the Green's function of an interacting many-electron system correspond to the true excitation energies  $\epsilon_i^{N\pm 1}$ , and thus encode the solution to the many-body problem in 2.3. Nevertheless, it is not immediately clear how  $\mathbf{G}(\mathbf{r}, \mathbf{r}', \omega)$  can be determined without explicit knowledge about the far too complex many-body wave function. As we will see, however, the many-body wave function is actually not required to determine the Green's function of the interacting system (similar to the ground-state energy in DFT).

Taking the partial time derivative of Eq. 2.45 and considering the time evolution of the field operators in Eq. 2.44, the time evolution of the Green's function  $\mathbf{G}(1, 2)$  reads<sup>9</sup>

$$\left( i\hbar \frac{\partial}{\partial t_1} - \mathbf{h}_0(\mathbf{r}_1) \right) \mathbf{G}(1, 2) + i\hbar \int v_{ee}(1, 3) \mathbf{G}(1, 3^+, 2, 3^{++}) d(3) = \delta(1-2), \quad (2.52)$$

where  $v_{ee}(1, 3) = v_{ee}(\mathbf{r}_1, \mathbf{r}_3) \cdot \delta(t_1 - t_3)$ .

Infinitesimal time shifts  $3^+ := (\mathbf{r}_3, t_3 + \eta)$  and  $3^{++} := (\mathbf{r}_3, t_3 + 2\eta)$ , with  $\eta \rightarrow 0^+$ , thereby ensure correct time ordering of the involved field operators. Determining the one-particle Green's function therefore requires to determine the two-particle Green's function  $\mathbf{G}(1, 2, 3, 4)$ , defined by

$$\mathbf{G}(1, 2, 3, 4) = -\frac{1}{\hbar^2} \langle \Psi_0^N | \mathcal{T}(\Psi(1)\Psi(2)\Psi^\dagger(4)\Psi^\dagger(3)) | \Psi_0^N \rangle, \quad (2.53)$$

which reflects the correlated propagation of two particles from coordinates 3 and 4 to 1 and 2. The time evolution of  $\mathbf{G}(1, 2, 3, 4)$  subsequently involves the three-particle Green's function, giving rise to an infinite coupling between  $\mathbf{G}(1, 2)$  and higher-order correlations. However, Eq. 2.52 can formally be recast into a one-particle equation by introducing the nonhermitian and nonlocal self-energy operator  $\tilde{\Sigma}(1, 2)$  according to

$$\tilde{\Sigma}(1, 2) = -i\hbar \int v_{ee}(1, 3) \mathbf{G}(1, 3^+, 4, 3^{++}) \mathbf{G}^{-1}(4, 2) d(3, 4), \quad (2.54)$$

encapsulating all interactions between an electron and its surrounding. Taking into account the inverse of the Green's function, defined by

$$\int \mathbf{G}(1, 3) \mathbf{G}^{-1}(3, 2) d(2) = \delta(1-2), \quad (2.55)$$

and explicitly splitting off the Hartree term from  $\tilde{\Sigma}$  via

$$\begin{aligned} \tilde{\Sigma}(1, 2) &= \Sigma_H(1, 2) + \Sigma(1, 2) \\ &= \delta(1-2) \underbrace{\int v_{ee}(1, 3) \rho(\mathbf{r}_3) d(3)}_{=v_H(\mathbf{r}_1)} + \Sigma(1, 2), \end{aligned} \quad (2.56)$$

Eq. 2.52 thus reads

$$\left( i\hbar \frac{\partial}{\partial t_1} - \underbrace{\mathbf{h}_0(\mathbf{r}_1) - v_H(\mathbf{r}_1)}_{=h_{0,H}(\mathbf{r}_1)} \right) \mathbf{G}(1, 2) - \int \Sigma(1, 3) \mathbf{G}(3, 2) d(3) = \delta(1-2). \quad (2.57)$$

The self-energy operator, just like the Green's function, depends only on the time difference of its arguments. It is therefore possible to Fourier transform Eq. 2.57 into frequency space (see Appendix A), yielding

$$(\hbar\omega - \mathbf{h}_{0,H}(\mathbf{r}_1)) \mathbf{G}(\mathbf{r}_1, \mathbf{r}_2, \omega) - \int \Sigma(\mathbf{r}_1, \mathbf{r}_3, \omega) \mathbf{G}(\mathbf{r}_3, \mathbf{r}_2, \omega) d\mathbf{r}_3 = \delta(\mathbf{r}_1 - \mathbf{r}_2). \quad (2.58)$$

<sup>9</sup>To simplify the notation, the abbreviation  $1 := (\mathbf{r}_1, t_1)$  for individual events in space time is used. Additionally, differentials and delta distributions are abbreviated as  $d(1) := d\mathbf{r}_1 dt_1$  and  $\delta(1-2) := \delta(\mathbf{r}_1 - \mathbf{r}_2) \delta(t_1 - t_2)$ .

Inserting the Lehmann representation 2.47 of the Green's function, multiplying both sides by an individual pole  $\hbar\omega - \epsilon_k$  and taking the limit  $\hbar\omega \rightarrow \epsilon_k$ , one finally arrives at the set of quasiparticle equations

$$\mathbf{h}_{0,\text{H}}(\mathbf{r})\phi_k(\mathbf{r}) + \int \Sigma(\mathbf{r}, \mathbf{r}', \epsilon_k/\hbar)\phi_k(\mathbf{r}') d\mathbf{r}' = \epsilon_k\phi_k(\mathbf{r}), \quad (2.59)$$

bearing a striking resemblance to the Kohn-Sham equations 2.14 and justifying the notion of  $\Sigma$  as a self-energy operator: Unlike the XC potential within the Kohn-Sham equation,  $\Sigma$  would exactly cancel the spurious self-interaction introduced by the Hartree potential for the true, interacting system. The energy-dependent self-energy operator thus fully determines the true quasiparticle energies  $\epsilon_k$  and wave functions  $\phi_k(\mathbf{r})$ . Due to  $\Sigma$  being nonhermitian and energy-dependent, the  $\{\phi_k(\mathbf{r})\}$  do not form a set of eigenfunctions of a single operator and are neither normalized nor orthonormal. They do, however, form a bi-orthogonal system

$$\langle \phi_m | \tilde{\phi}_n \rangle = \delta_{m,n}, \quad (2.60)$$

with  $\{\tilde{\phi}_i\}$  as the solution of the adjoint equation to 2.59 [77]. Additionally, the eigenvalues  $\epsilon_i$  are complex, with the imaginary part corresponding to the quasiparticle's lifetime. This lifetime thereby reflects the average time between scattering events of the quasiparticle between individual one-particle states.

## 2.2.2 Hedin's Equations and *GW* Approximation

In order to determine the self-energy operator and its connection to the Green's function, Eq. 2.58 is recast slightly to explicitly include the Green's function  $\mathbf{G}_0$  of particles interacting solely via the mean-field Hartree term  $\nu_{\text{H}}$ .  $\mathbf{G}_0$  is given by 2.47, with  $\phi_i^{N\pm 1}$  and  $\epsilon_i^{N\pm 1}$  fulfilling

$$\mathbf{h}_{0,\text{H}} |\phi_i^{N\pm 1}\rangle = \epsilon_i^{N\pm 1} |\phi_i^{N\pm 1}\rangle. \quad (2.61)$$

Using  $\mathbf{G}_0$ , the Green's function fulfills the Dyson equation

$$\mathbf{G}(1, 2) = \mathbf{G}_0(1, 2) + \int \mathbf{G}_0(1, 3)\Sigma(3, 4)\mathbf{G}(4, 2) d(3, 4)$$

(2.62)

in the time domain. Evidently, it is not possible to deduce the self energy via Eq. 2.62 alone.

One mechanism still missing in this description is a reduction of the effective Coulomb interaction between a quasiparticle and its surrounding due to screening effects. In 1965, Hedin proposed a scheme to incorporate screening into the self-energy concept by determining the response of the system to a time-dependent external potential, which is later set to 0 [78]. In this manner, it is possible to expand the self-energy operator in terms of the screened Coulomb potential

$$\mathbf{W}(1, 2) = \int \nu_{\text{ee}}(1, 3)\epsilon^{-1}(3, 2) d(3), \quad (2.63)$$

where the screening is encoded in the inverse dielectric function  $\epsilon^{-1}(1, 2)$ . It is connected to the irreducible polarizability  $\mathbf{P}$  via

$$\epsilon(1, 2) = \delta(1 - 2) - \int \nu_{\text{ee}}(1, 3)\mathbf{P}(3, 2) d(3). \quad (2.64)$$

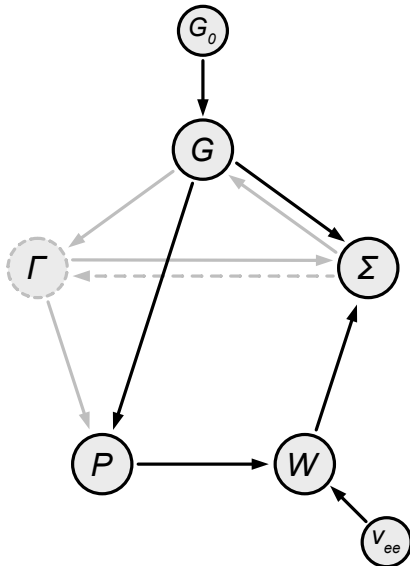


**Figure 2.1:** Schematic flowchart of the five operators  $G$ ,  $\Sigma$ ,  $W$ ,  $P$  and  $\Gamma$  in the Hedin's equations in its full form (black and gray arrows) and within the  $G_0W_0$  approximation (black arrows only). The scheme is initialized with the Green's function of independent particles  $G_0$ .

Hedin showed that the four operators  $G$ ,  $\Sigma$ ,  $W$  and  $P$  together with the three-point vertex function  $\Gamma(1, 2, 3)$  may be expressed in a closed set of equations.<sup>10</sup> Apart from the Dyson equation for  $G$  in 2.62, these equations read

$$\Sigma(1,2) = -i\hbar \int G(1,3)\Gamma(3,2,4)W(1^+,4) d(3,4), \quad (2.65)$$

$$W(1,2) = v_{ee}(1,2) + \int v_{ee}(1,3)P(3,4)W(4,2)d(3,4), \quad (2.66)$$

$$P(1,2) = i\hbar \int G(1,3)G(4,1^+) \Gamma(3,4,2) d(3,4) \quad (2.67)$$

$$\text{and } \Gamma(1, 2, 3) = -\delta(1-2)\delta(1-3)$$

$$+ \int \frac{\delta \Sigma(1,2)}{\delta G(4,5)} G(4,6)G(7,5)\Gamma(6,7,3) d(4,5,6,7). \quad (2.68)$$

These Hedin's equations are, in principle, an exact reformulation of the many-body problem and their self-consistent solution allows to determine the total energy as well as all one-particle and excitation properties of an interacting electronic system. In Fig. 2.1, the flowchart of the Hedin's equations is schematically depicted (gray and black arrows). In practice, one would take a single iteration of Hedin's equations, starting from a reasonable initial estimation of  $G$ . The most common choice is thereby  $G = G_0$ , immediately implying  $\Sigma = 0$  via Eq. 2.62 for the zeroth iteration. Inserting these conditions into the Hedin's

---

<sup>10</sup>For a thorough derivation of the Hedin's equations, the Reader is referred to various publications, including [37, 40, 76, 78, 79].

equations then yields

$$\Gamma(1, 2, 3) = -\delta(1-2)\delta(1-3), \quad (2.69)$$

$$P(1, 2) = -i\hbar G_0(1, 2)G_0(2, 1), \quad (2.70)$$

$$\text{and } \Sigma(1, 2) = i\hbar G_0(1, 2)W(1^+, 2). \quad (2.71)$$

The last expression for the self-energy operator in the time domain as the product between  $G$  and the screened Coulomb potential  $W$  thereby coins the  $GW$  approximation. Its flowchart is depicted in Fig. 2.1 (black arrows). For later use, we note that the principle shape of  $P$  in the original Hedin's equations 2.67 implies a correlated electron-hole propagation, coupled by the vertex function  $\Gamma$ . However, within the  $GW$  approximation, the two propagations are independent.<sup>11</sup>

The self-energy operator within  $GW$  enables a post-processing scheme to correct the one-particle energies  $\epsilon_i^{\text{DFT}}$  obtained from a subsequent DFT calculation to account for quasiparticle effects. Since (i) the one-particle wave functions on the DFT level  $\phi_i^{\text{DFT}}$  are known to match the quasiparticle ones very closely [67] and (ii) the XC potential  $v_{\text{xc}}$  can be assumed to already partly account for quasiparticle effects, the true quasiparticle energies  $\epsilon_i^{\text{QP}}$  may be expanded into a perturbation series

$$\epsilon_i^{\text{QP}} \approx \epsilon_i^{\text{DFT}} + \langle \phi_i^{\text{DFT}} | \Sigma(\epsilon_i^{\text{QP}}/\hbar) - v_{\text{xc}} | \phi_i^{\text{DFT}} \rangle. \quad (2.72)$$

In order to circumvent the evaluation the self-energy operator at the true quasiparticle energies,  $\Sigma$  is expanded around  $\epsilon_i^{\text{DFT}}$ ,

$$\Sigma(\epsilon_i^{\text{QP}}) \approx \Sigma(\epsilon_i^{\text{DFT}}) + (\epsilon_i^{\text{QP}} - \epsilon_i^{\text{DFT}}) \frac{\partial \Sigma(\omega)}{\partial \omega} \bigg|_{\epsilon_i^{\text{DFT}}/\hbar}, \quad (2.73)$$

yielding

$$\epsilon_i^{\text{QP}} = \epsilon_i^{\text{DFT}} + Z_i \langle \phi_i^{\text{DFT}} | \Sigma(\epsilon_i^{\text{DFT}}/\hbar) - v_{\text{xc}} | \phi_i^{\text{DFT}} \rangle, \quad (2.74)$$

with the renormalization constant  $Z_i = \left(1 - \langle \phi_i^{\text{DFT}} | \frac{\partial \Sigma(\omega)}{\partial \omega} \bigg|_{\epsilon_i^{\text{DFT}}/\hbar} | \phi_i^{\text{DFT}} \rangle\right)^{-1}$ .

The energy-dependent self-energy operator can be determined by taking the Fourier transformation of Eq. 2.71 into the frequency domain,

$$\Sigma(\mathbf{r}_1, \mathbf{r}_2, \omega) = \frac{i\hbar}{2\pi} \int G_0(\mathbf{r}_1, \mathbf{r}_2, \omega + \omega') W(\mathbf{r}_1, \mathbf{r}_2, \omega') e^{i\omega' \eta} d\omega' \quad \text{with } \eta \rightarrow 0^+. \quad (2.75)$$

The Green's function within this convolution may be constructed directly using Eq. 2.47 and the DFT solutions  $\epsilon_i^{\text{DFT}}$  and  $\phi_i^{\text{DFT}}$ . The screened Coulomb potential  $W$  on the other hand is determined via Eq. 2.63. Thereby, the dielectric function in Eq. 2.64 (whose frequency dependence entirely stems from the Fourier transform of  $P$ ) has to be numerically inverted for every individual frequency value, posing a large computational bottleneck. For this reason, this inversion step is sometimes skipped by assuming a model dielectric function (plasmon-pole model) [67, 80]. Finally,  $\Sigma$  is determined by performing the frequency integration in Eq. 2.75 as a contour integral in the complex plane [75, 76].

<sup>11</sup>For this reason, the relation in Eq. 2.70 is sometimes also referred to as the random-phase approximation [67]. In contrast, the origin of the random-phase approximation will later be discussed in terms of the polarizability  $\chi$  (Chapter 3).

A single iteration of the Hedin's equations within the  $GW$  approximation (single-shot  $GW$  or  $G_0W_0$ ) was shown to capture the biggest part of the quasiparticle correction to the fundamental band gap for a number of compounds [81]. Due to the perturbative nature of the correction scheme, the accuracy of the  $G_0W_0$  correction thereby depends on the accuracy of the preceding DFT calculation. In principle, the obtained quasiparticle energies can be used for further iterations of the Hedin's equations. Depending on the updating scheme, a number of (partially) self-consistent flavors are possible [82, 83], including the  $GW_0$  approximation, in which the screened Coulomb potential  $W$  is kept constant, while only  $\mathbf{G}$  and  $\Sigma$  are updated. This way, the most time-consuming step within  $GW$  (determining the screening) has to be performed only once, while self-consistency is achieved on the level of  $\mathbf{G}$ .

However, neither within  $GW_0$  nor within the fully self-consistent  $GW$  scheme, in which  $W$  is also updated, convergence of  $\mathbf{G}$  towards the exact Green's function can be expected, since the vertex function  $\Gamma$  is not updated accordingly, see Fig. 2.1. For this reason, iteration schemes beyond  $G_0W_0$  were found to even worsen the agreement with experimental data in a number of cases [81, 84].



# 3

## Theoretical spectroscopy

Optical spectroscopy provides a number of powerful methods to determine electronic and structural properties of solids as well as molecules. To this end, the interaction between light and matter is exploited by impinging electromagnetic radiation of a specific frequency, polarization and propagation direction onto a probe and measuring its material-specific response. Typical spectroscopic methods may be subdivided into several categories based on the respective fundamental processes acting on the involved light field, including:

- **Light absorption:** The intensity of radiation passing through a probe decreases based on the Beer–Lambert law, which relates the relative intensity drop to the frequency-dependent absorption coefficient  $\alpha(\omega)$  and the sample thickness. In the case of semiconductors and insulators, the absorption onset of  $\alpha(\omega)$  is a direct indicator for the optical band gap [85].
- **Light scattering:** This is the fundamental process behind Raman spectroscopy. Due to inelastic scattering between impinged photons and ionic vibrations (phonons) the photon may undergo a Stokes shift (shift towards higher frequency) or an anti-Stokes shift (towards lower frequency). The location and intensities of the Raman bands thereby give direct insights into the vibrational properties of matter (phonon dispersion, acoustics) and indirect insights into its structural character (atomic composition, defect concentrations).

In both cases, the material's fundamental response functions, i.e., the dielectric function (light absorption) and the differential Raman cross section (light scattering) are fundamentally governed by the electronic structure. This chapter therefore aims at elaborating how these two responses may be determined on the basis of DFT and quasiparticle calculations.

### 3.1 Dielectric Response Function

An external, time-dependent perturbation  $\Delta\nu_{\text{ext}}$  to a many-body electron system induces a variation in the electron density  $\Delta\rho$  according to<sup>1</sup>

$$\Delta\rho(1) = \int \chi(1, 2) \cdot \Delta\nu_{\text{ext}}(2) d(2). \quad (3.1)$$

The density response is thereby encoded in the nonlocal polarizability  $\chi$ . Within the DFT framework,  $\chi$  can be computed explicitly by considering the energy difference

$$\Delta E = E[\rho_0 + \Delta\rho] - E[\rho_0] \quad (3.2)$$

between the ground state and the perturbed system, with the DFT total energy functional  $E[\rho]$  given by Eq. 2.11. Expanding  $\Delta E$  around  $\rho_0$  to second order and applying the extremal condition  $\frac{\delta(\Delta E)}{\delta(\Delta\rho)} = 0$  then yields [86]

$$-\Delta\nu_{\text{ext}}(1) = \int \frac{\delta^2 F}{\delta\rho(1)\delta\rho(2)} \bigg|_{\rho_0} \cdot \Delta\rho(2) d(2), \quad (3.3)$$

implying the formal identity

$$\begin{aligned} \chi^{-1}(1, 2) &= -\frac{\delta^2 F}{\delta\rho(1)\delta\rho(2)} \bigg|_{\rho_0} \\ &= -\frac{\delta^2 T}{\delta\rho(1)\delta\rho(2)} \bigg|_{\rho_0} - \nu_{\text{ee}}(1, 2) - \underbrace{\frac{\delta^2 E_{\text{xc}}}{\delta\rho(1)\delta\rho(2)} \bigg|_{\rho_0}}_{=K_{\text{xc}}(1, 2)}, \end{aligned} \quad (3.4)$$

with  $F$  as the universal functional (see Eq. 2.7),  $K_{\text{xc}}$  as the XC kernel and  $\nu_{\text{ee}}$  as the instantaneous Coulomb interaction according to Eq. 2.52. On the other hand, the response to a change in the total effective potential (i.e., external perturbation and screening potential) is mediated by the polarizability of independent particles  $\chi^0$  via

$$\Delta\rho(1) = \int \chi^0(1, 2) \cdot \Delta\nu_{\text{eff}}(2) d(2), \quad (3.5)$$

$$\text{where } \Delta\nu_{\text{eff}}(1) = \Delta\nu_{\text{ext}}(1) + \int \{\nu_{\text{ee}}(1, 2) + K_{\text{xc}}(1, 2)\} \cdot \Delta\rho(2) d(2).$$

Solving for  $\chi^0$  and formal inversion yields

$$\begin{aligned} \{\chi^0\}^{-1}(1, 2) &= \frac{\delta\nu_{\text{eff}}(2)}{\delta\rho(1)} \\ &= \chi^{-1}(1, 2) + \nu_{\text{ee}}(1, 2) + K_{\text{xc}}(1, 2). \end{aligned} \quad (3.6)$$

---

<sup>1</sup>Individual events in space time are again abbreviated by the single numerical values 1 and 2.

Exploiting the definition 2.55 for the inverse of a two-point function, the connection between the two response functions takes the form of a Dyson equation

$$\chi(1, 2) = \chi^0(1, 2) + \int \chi^0(1, 3) \{v_{ee}(3, 4) + K_{xc}(3, 4)\} \chi(4, 2) d(3, 4). \quad (3.7)$$

Finally, the microscopic dielectric function  $\varepsilon$  relates  $\Delta v_{\text{eff}}$  and  $\Delta v_{\text{ext}}$  via

$$\begin{aligned} \varepsilon^{-1}(1, 2) &= \frac{\delta v_{\text{eff}}(2)}{\delta v_{\text{ext}}(1)} \\ &= \delta(1-2) + \int \{v_{ee}(1, 3) + K_{xc}(1, 3)\} \cdot \chi(3, 2) d(3). \end{aligned} \quad (3.8)$$

If the origin of the perturbation is assumed to be a test particle, the random-phase approximation (RPA) can be applied at this point by neglecting the XC kernel [87]. Within the RPA, Eqs. 3.7 and 3.8 allow to rewrite  $\varepsilon$  to be solely dependent on  $\chi^0$ , yielding <sup>2</sup>

$$\varepsilon(1, 2) = \delta(1-2) - \int v_{ee}(1, 3) \chi^0(3, 2) d(3). \quad (3.9)$$

### 3.1.1 The Independent-(Quasi-)Particle Approximation

The advantage of  $\varepsilon$  being entirely determined via the polarizability of independent particles is the fact that an explicit expression for  $\chi^0$  is known. Using first-order perturbation theory on the one-particle Kohn-Sham equations 2.14,  $\chi^0$  is given in frequency space by the Adler-Weis expression [88–90]

$$\chi^0(\mathbf{r}_1, \mathbf{r}_2, \omega) = 2 \sum_{i,j} (f_i - f_j) \frac{\phi_i^*(\mathbf{r}) \phi_j(\mathbf{r}) \phi_j^*(\mathbf{r}') \phi_i(\mathbf{r}')}{\epsilon_i - \epsilon_j - \hbar(\omega + i\eta)}, \quad \text{with } \eta \rightarrow 0^+, \quad (3.10)$$

or, via Fourier transformation into reciprocal space (see Appendix A),

$$\chi_{G, G'}^0(\mathbf{q}, \omega) = 2 \sum_{i,j} (f_i - f_j) \frac{(B_i^j(\mathbf{q} + \mathbf{G}))^* B_i^j(\mathbf{q} + \mathbf{G}')}{\epsilon_i - \epsilon_j - \hbar(\omega + i\eta)}, \quad (3.11)$$

$$\text{where } B_i^j(\mathbf{q} + \mathbf{G}) = \langle \phi_i | e^{i(\mathbf{q} + \mathbf{G}) \cdot \mathbf{r}} | \phi_j \rangle.$$

Note that  $\{\epsilon_i\}$  and  $\{|\phi_i\rangle\}$  refer to the quasiparticle one-electron energies and wave functions, respectively, as introduced in Sec. 2.2. In the following,  $i$  and  $j$  correspond to quantum numbers of a solid, i.e., band index  $c$  and  $v$  of the conduction and valence band and their respective wave vectors  $\mathbf{k}$  and  $\mathbf{k}'$ . For a semiconductor, this implies  $f_{c, \mathbf{k}} = 0$  and  $f_{v, \mathbf{k}'} = 1$ . Fourier transforming Eq. 3.9 into frequency and reciprocal space and inserting the Adler-Weis expression then yields

$$\begin{aligned} \varepsilon_{G, G'}(\mathbf{q}, \omega) &= \delta_{G, G'} - v_G(\mathbf{q}) \cdot \chi_{G, G'}^0(\mathbf{q}, \omega), \\ \text{where } v_G(\mathbf{q}) &= \frac{4\pi e^2}{|\mathbf{q} + \mathbf{G}|^2}. \end{aligned} \quad (3.12)$$

<sup>2</sup>Within the quasiparticle formulation, the irreducible polarization  $P$  and the polarizability  $\chi$  are sometimes used synonymously. However, in general, only the irreducible polarization for independent particles, as given by Eq. 2.70 within the  $GW$  approximation, and  $\chi^0$  are equal [38], making Eqs. 2.64 and 3.9 equivalent for the microscopic dielectric function.

If a given atomic system was spatially isotropic,  $\epsilon$  would only depend on the difference between atomic coordinates  $\mathbf{r}_1 - \mathbf{r}_2$  in real space, rendering its Fourier transform diagonal in  $\mathbf{G}$ . Anisotropies in a system due to its atomic structure give rise to nonvanishing off-diagonal elements  $\mathbf{G} \neq \mathbf{G}'$  in  $\epsilon_{\mathbf{G}, \mathbf{G}'}(\mathbf{q}, \omega)$ . These microscopic fluctuations in charge density and electric field are consequently called local-field effects.

Finally, the macroscopic dielectric function  $\epsilon_M(\omega)$  as the system's response to a macroscopic perturbation in the optical limit  $\mathbf{q} \rightarrow 0$  is given by [88, 89]

$$\epsilon_M(\omega) = \lim_{\mathbf{q} \rightarrow 0} \frac{1}{\epsilon_{\mathbf{G}, \mathbf{G}'}^{-1}(\mathbf{q}, \omega)} \Big|_{\mathbf{G} = \mathbf{G}' = 0}. \quad (3.13)$$

Neglecting local-field effects,  $\epsilon_M(\omega)$  is then equivalent to the head (  $\mathbf{G} = \mathbf{G}' = 0$  matrix element) of the microscopic dielectric function

$$\begin{aligned} \epsilon_M(\omega) &= \lim_{\mathbf{q} \rightarrow 0} \epsilon_{0,0}(\mathbf{q}, \omega) \\ &= 1 + \lim_{\mathbf{q} \rightarrow 0} \frac{4\pi e^2}{|\mathbf{q}|^2} \frac{2}{V} \sum_{c,v} \sum_{\mathbf{k}, \mathbf{k}'} \frac{\left| B_{c,k}^{v,k'}(\mathbf{q}) \right|^2}{\epsilon_{c,k} - \epsilon_{v,k'} - \hbar(\omega + i\eta)}, \end{aligned} \quad (3.14)$$

with  $V$  denoting the volume of the system's unit cell. The wave vectors  $\mathbf{k}$  and  $\mathbf{k}'$  within the Bloch integrals  $B_{c,k}^{v,k'}(\mathbf{q})$  are thereby not independent, since  $\mathbf{k}$  and  $\mathbf{k}'$  must differ by  $\mathbf{q}$  in order to fulfill momentum conservation. For  $\mathbf{q} = 0$  this corresponds to the limitation of pure vertical transitions of an electron between a valence and conduction state. A straight forward evaluation of the  $\mathbf{q} \rightarrow 0$  limit in Eq. 3.14 via the L'Hôpital's rule would introduce the dipole operator, which is linear in  $\mathbf{r}$  and therefore not well-defined for periodic boundary conditions [91]. Instead, the following identity is used

$$\begin{aligned} \lim_{\mathbf{q} \rightarrow 0} \frac{B_{c,k}^{v,k-\mathbf{q}}(\mathbf{q})}{\mathbf{q}} &= \lim_{\mathbf{q} \rightarrow 0} \frac{1}{\mathbf{q}} \frac{\langle \phi_{c,k} | [\mathbf{H}, e^{i\mathbf{q}\mathbf{r}}] | \phi_{v,k-\mathbf{q}} \rangle}{\epsilon_{c,k} - \epsilon_{v,k-\mathbf{q}}} \\ &= \frac{\hbar}{\epsilon_{c,k} - \epsilon_{v,k}} \cdot \langle \phi_{c,k} | \mathbf{e}_q \cdot \mathbf{v} | \phi_{v,k} \rangle, \end{aligned} \quad (3.15)$$

introducing the velocity operator  $\mathbf{v} = \frac{i}{\hbar} [\mathbf{H}, \mathbf{r}]$  and the unit vector  $\mathbf{e}_q = \frac{\mathbf{q}}{|\mathbf{q}|}$ , along which the  $\mathbf{q} \rightarrow 0$  limit is taken. The evaluation of the velocity operator in the quasiparticle case is thereby rather delicate, since the hamiltonian  $\mathbf{H}$  includes nonlocal contributions from the self-energy operator  $\Sigma$  (see Eq. 2.59), yielding [92]

$$\begin{aligned} \mathbf{v} &= \frac{\mathbf{p}}{m} + \frac{\partial \Sigma(\mathbf{r}, \mathbf{p})}{\partial \mathbf{p}}, \\ \text{where } \Sigma(\mathbf{r}, \mathbf{p}) &= \int \Sigma(\mathbf{r}, \mathbf{r}') e^{\frac{i}{\hbar}(\mathbf{r}' - \mathbf{r}) \cdot \mathbf{p}} d\mathbf{r}'. \end{aligned} \quad (3.16)$$

It is, however, possible to reformulate the problem of evaluating the matrix elements over  $\mathbf{v}$  in Eq. 3.15 to feature only the matrix elements over the much less problematic momentum operator  $\mathbf{p}$ . Taking advantage of the fact that the quasiparticle states  $\{|\phi_i\rangle\}$  are nearly identical to those obtained from Kohn-Sham theory  $\{|\phi_i^{KS}\rangle\}$ , the limit in Eq. 3.15 may be expressed via the Kohn-Sham hamiltonian (see 2.14) and the Kohn-Sham energy eigenvalues

$\{\epsilon_i^{\text{KS}}\}$ . In that case, the commutator equals  $\nu = \frac{p}{m}$ .<sup>3</sup> The matrix elements over  $\nu$  are thus obtained as rescaled matrix elements over  $p$

$$\langle \phi_{c,k} | \mathbf{e}_q \cdot \nu | \phi_{v,k} \rangle = C_{c,k}^{\nu,k} \cdot \langle \phi_{c,k} | \mathbf{e}_q \cdot \mathbf{p} | \phi_{v,k} \rangle, \\ \text{where } C_{c,k}^{\nu,k} = \frac{\epsilon_{c,k} - \epsilon_{v,k}}{\epsilon_{c,k}^{\text{KS}} - \epsilon_{v,k}^{\text{KS}}}. \quad (3.17)$$

Following Eq. 3.15, the macroscopic dielectric response can be understood as a dielectric matrix, with its anisotropy being encoded in the vector  $\mathbf{e}_q$ . In a cartesian base, with  $i, j \in \{x, y, z\}$ , the matrix elements  $\varepsilon_{i,j}(\omega)$  are given by

$$\varepsilon_{i,j}(\omega) = \delta_{i,j} + \frac{8\pi\hbar^2 e^2}{Vm^2} \sum_{c,v} \sum_{\mathbf{k}} \left( \frac{C_{c,k}^{\nu,k}}{\epsilon_{c,k} - \epsilon_{v,k}} \right)^2 \frac{\langle \phi_{c,k} | \mathbf{p}_i | \phi_{v,k} \rangle \cdot \langle \phi_{v,k} | \mathbf{p}_j | \phi_{c,k} \rangle}{\epsilon_{c,k} - \epsilon_{v,k} - \hbar(\omega + i\eta)}. \quad (3.18)$$

The elements of the momentum operator  $\mathbf{p}$  are thereby labeled  $\{\mathbf{p}_i\}$ . If the energy eigenvalues  $\{\epsilon_i\}$  are assumed to be the Kohn-Sham (quasiparticle) ones, the expression in Eq. 3.18 corresponds to the dielectric matrix within the independent-(quasi)particle approximation (I(Q)PA).

For a given orientation  $i, j$ , spectroscopic signatures of a system, in particular the complex refractive index  $n(\omega)$ , absorption coefficient  $\alpha(\omega)$  and reflectivity  $R(\omega)$ , can be obtained from the real and imaginary parts of  $\varepsilon(\omega)$  via

$$n(\omega) := n_1(\omega) + i n_2(\omega) \\ = \sqrt{\frac{|\varepsilon(\omega)| + \text{Re}\{\varepsilon(\omega)\}}{2}} + i \sqrt{\frac{|\varepsilon(\omega)| - \text{Re}\{\varepsilon(\omega)\}}{2}}, \quad (3.19)$$

$$\alpha(\omega) = \frac{2\omega}{c} \cdot n_2(\omega), \quad (3.20)$$

$$\text{and } R(\omega) = \frac{(n_1(\omega) - 1)^2 + n_2^2(\omega)}{(n_1(\omega) + 1)^2 + n_2^2(\omega)}. \quad (3.21)$$

### 3.1.2 Local-Field Effects

If local-field effects are to be included in  $\varepsilon_M(\omega)$ , the microscopic dielectric function  $\varepsilon_{G,G'}(\mathbf{q}, \omega)$  has to be inverted for every frequency  $\omega$  (see Eq. 3.13), posing a large numerical bottleneck. It was, however, shown that this inversion step can be skipped (at least in principle) by reformulating  $\varepsilon_M(\omega)$  as [38, 94]

$$\varepsilon_M(\omega) = 1 - \lim_{\mathbf{q} \rightarrow 0} \nu_0(\mathbf{q}) \cdot \bar{\mathbf{P}}_{0,0}(\mathbf{q}, \omega), \quad (3.22)$$

with the modified irreducible polarizability  $\bar{\mathbf{P}}_{G,G'}(\mathbf{q}, \omega)$  fulfilling the Dyson-like equation

$$\bar{\mathbf{P}}_{G,G'}(\mathbf{q}, \omega) = \mathbf{P}_{G,G'}(\mathbf{q}, \omega) + \sum_K \mathbf{P}_{G,K}(\mathbf{q}, \omega) \bar{\nu}_K(\mathbf{q}) \bar{\mathbf{P}}_{K,G'}(\mathbf{q}, \omega). \quad (3.23)$$

<sup>3</sup>Care has to be taken if the pseudopotential formalism is utilized, introducing nonlocal contributions to the hamiltonian also on the Kohn-Sham level. For a number of strongly bounded compounds (e.g., group-IV materials or diamond), these nonlocal contributions have been shown to lower the amplitude of  $\varepsilon_M(\omega)$  by 10 – 25 % [38, 93].

The static kernel is thereby given by the amputated Coulomb interaction, having the divergent  $\mathbf{G} = 0$  term explicitly removed

$$\bar{v}_G(\mathbf{q}) = \begin{cases} v_G(\mathbf{q}) & \text{if } \mathbf{G} \neq 0 \\ 0 & \text{if } \mathbf{G} = 0 \end{cases}. \quad (3.24)$$

For later use, we note that Eq. 3.23 corresponds formally to the matrix equation

$$\bar{\mathbf{P}} = \mathbf{P} + \mathbf{P} \bar{v} \bar{\mathbf{P}}. \quad (3.25)$$

## 3.2 Two-Particle Effects and the Bethe-Salpeter Equation

Despite the fact that quasiparticle effects within the  $GW$  approximation are known to accurately correct the band gap from Kohn-Sham theory, spectroscopic signatures within the IQPA have been shown to still feature large deviations compared to experimental data. In particular, a pronounced blueshift of the IQPA spectra with respect to the experimental ones is observed [92, 95, 96]. In addition, the IQPA tends to underestimate the overall absorption strength for low energies and overestimate it for higher energy regime [96].

As previously discussed, optical excitations induce vertical transitions of electrons from a valence into a conduction state, subsequently creating a hole with positive charge. Within the I(Q)PA, the propagation of electron and hole, as denoted by the irreducible polarizability  $\mathbf{P}$ , is thereby treated as uncorrelated (see Eq. 2.67). In reality, however, the formation of bound electron-hole pairs (excitons) and their respective excitonic states is accompanied by the existence of sharp, isolated absorption peaks below the absorption onset and thus by an overall redshift of the entire spectrum with respect to the I(Q)PA [37].

### 3.2.1 Generalization to Four-Point Operators

The incorporation of excitonic effects into the general dielectric response function 2.64 can be achieved by generalizing the two-point irreducible polarizability  $\mathbf{P}(1, 2)$  into the four-point form  $\mathbf{P}(1, 2, 3, 4)$ . To this end, an additional iteration of the vertex function  $\Gamma$  within the Hedin equations 2.68 beyond the  $GW$  approximation is carried out. With  $\Sigma(1, 2) = i\hbar G(1, 2)W(1^+, 2)$  it follows that

$$\frac{\delta \Sigma(1, 2)}{\delta \mathbf{G}(4, 5)} = i\hbar W(1^+, 2)\delta(1-4)\delta(2-5), \quad (3.26)$$

implying

$$\Gamma(1, 2, 3) = -\delta(1-2)\delta(1-3) + i\hbar W(1^+, 2) \cdot \int G(1, 6)G(7, 2)\Gamma(6, 7, 3)d(6, 7). \quad (3.27)$$

The integral in 3.27 can be identified as a generalization of the two-point irreducible polarizability  $\mathbf{P}(1, 2)$  in Eq. 2.67 into the three-point polarizability  $\mathbf{P}(1, 2, 3)$ . Indeed, the former is contained in the latter as a contraction according to  $\mathbf{P}(1, 2) = \mathbf{P}(1, 2, 2)$ . After multiplying both sides of 3.27 with  $i\hbar G(4, 1)G(2, 5)$ , integrating over 1 and 2 and renaming coordinates,  $\mathbf{P}(1, 2, 3)$  is given by the Dyson equation

$$\mathbf{P}(1, 2, 3) = -i\hbar G(1, 3)G(3, 2) + i\hbar \int G(1, 4)G(5, 2)W(4^+, 5)\mathbf{P}(4, 5, 3)d(4, 5). \quad (3.28)$$

With this definition, the four-point propagator  $P(1, 2, 3, 4)$  can be constructed, which again contains the two-point one via  $P(1, 2) = P(1, 1, 2, 2)$ , yielding [38]

$$P(1, 2, 3, 4) = P_0(1, 2, 3, 4) - \int P(1, 2, 5, 6)W(5, 6, 7, 8)P_0(7, 8, 3, 4)d(5, 6, 7, 8), \quad (3.29)$$

with  $P^0(1, 2, 3, 4) = -i\hbar G(1, 3)G(4, 2)$ ,  
and  $W(1, 2, 3, 4) = W(1, 2)\delta(1-3)\delta(2-4)$ .

This is equivalent to a matrix representation

$$\begin{aligned} P &= P^0 - PWP^0 \\ \Leftrightarrow P &= P^0(1 + WP^0)^{-1}. \end{aligned} \quad (3.30)$$

Finally, by inserting 3.30 into 3.25, we arrive at the Bethe-Salpeter equation (BSE) in real space

$$\bar{P}(1, 2, 3, 4) = P^0(1, 2, 3, 4) + \int P^0(1, 2, 5, 6)\Xi(5, 6, 7, 8)\bar{P}(7, 8, 3, 4)d(5, 6, 7, 8), \quad (3.31)$$

with the kernel

$$\Xi(1, 2, 3, 4) = \delta(1-2)\delta(3-4)v_{ee}(1, 3) - \delta(1-3)\delta(2-4)W(1^+, 2), \quad (3.32)$$

describing local-field effects (first part) and the electron-hole interaction (second part). Similar to the naked Coulomb interaction  $v_{ee}$ ,  $W$  is assumed to be static, with time dependence

$$W(1, 2) = W(\mathbf{r}_1, \mathbf{r}_2)\delta(t_1 - t_2). \quad (3.33)$$

### 3.2.2 The BSE Hamiltonian

In the next step, the BSE is transformed into a matrix representation by taking the transition matrix element of both sides in 3.31 between the Kohn-Sham states  $\langle \phi_{n_1} \phi_{n_2} |$  and  $| \phi_{n_3} \phi_{n_4} \rangle$ , assumed to be orthonormal and complete

$$\langle \phi_{n_i} | \phi_{n_j} \rangle = \delta_{n_i, n_j} \quad \text{and} \quad \sum_{n_i} |\phi_{n_i}\rangle \langle \phi_{n_i}| = 1. \quad (3.34)$$

Generalizing  $P$  in Eq. 2.70 into a four-point operator, an individual matrix element over  $P^0(1, 2, 3, 4)$  is given by<sup>4</sup>

$$\begin{aligned} P_{(n_1 n_2 n_3 n_4)}^0 &:= \langle \phi_{n_1} \phi_{n_2} | P^0(\mathbf{r}_1, \mathbf{r}_2, \mathbf{r}_3, \mathbf{r}_4) | \phi_{n_3} \phi_{n_4} \rangle \\ &= \int \sum_{n_1, n_2, n_3, n_4} (f_{n_2} - f_{n_1}) \frac{\phi_{n_1}^*(\mathbf{r}_1) \phi_{n_2}(\mathbf{r}_2) \phi_{n_3}(\mathbf{r}_3) \phi_{n_4}^*(\mathbf{r}_4)}{\epsilon_{n_2} - \epsilon_{n_1} - \hbar\omega - i\hbar\eta} d\mathbf{r}_1 d\mathbf{r}_2 d\mathbf{r}_3 d\mathbf{r}_4 \\ &= \frac{f_{n_2} - f_{n_1}}{\epsilon_{n_2} - \epsilon_{n_1} - \hbar\omega - i\hbar\eta} \delta_{n_1, n_3} \delta_{n_2, n_4} \quad \text{with} \quad \eta \rightarrow 0^+. \end{aligned} \quad (3.35)$$

<sup>4</sup>Implicitly, the BSE 3.31 is assumed to be Fourier transformed into frequency space. The explicit frequency-dependence of the operators is omitted to simplify the notation.

Again,  $\{\epsilon_{n_i}\}$  correspond to the quasiparticle energy eigenvalues and  $\{f_{n_i}\}$  to the occupation number of the respective states  $\{n_i\}$ . In the following, matrix elements over arbitrary operators will be abbreviated in a similar manner to  $\mathbf{P}^0$  in 3.35.

Inserting two complete sets of Kohn-Sham states into the right hand side of the BSE and regrouping of terms, we arrive at [37, 38]

$$\bar{P}_{(n_1 n_2 n_3 n_4)} = [\mathbf{H}^{\text{exc}} - \mathbf{1}\hbar\omega]_{(n_1 n_2 n_3 n_4)}^{-1} \cdot (f_{n_4} - f_{n_3}), \quad (3.36)$$

with  $\mathbf{1}$  as the identity operator. It is thus possible to obtain  $\bar{P}_{(n_1 n_2 n_3 n_4)}$  via an inversion of the excitonic hamiltonian  $\mathbf{H}^{\text{exc}}$  for each individual frequency  $\omega$ . The matrix elements of  $\mathbf{H}^{\text{exc}}$  are thereby

$$H_{(n_1 n_2 n_3 n_4)}^{\text{exc}} = (\epsilon_{n_1} - \epsilon_{n_2})\delta_{n_1, n_3}\delta_{n_2, n_4} + (f_{n_2} - f_{n_1})\Xi_{n_1 n_2 n_3 n_4}. \quad (3.37)$$

A straight forward inversion is highly challenging due to the large dimension and non-hermiticity of  $\mathbf{H}^{\text{exc}}$ . In more common approaches, the operator  $[\mathbf{H}^{\text{exc}} - \mathbf{1}\hbar\omega]^{-1}$  is instead expressed according to its spectral representation

$$[\mathbf{H}^{\text{exc}} - \mathbf{1}\hbar\omega]^{-1} = \sum_{\lambda, \lambda'} \frac{|\Psi_{\lambda}\rangle S_{\lambda, \lambda'}^{-1} \langle \Psi_{\lambda'}|}{E_{\lambda} - \hbar\omega}, \quad (3.38)$$

$$\text{where } \mathbf{H}^{\text{exc}} |\Psi_{\lambda}\rangle = E_{\lambda} |\Psi_{\lambda}\rangle \quad \text{and} \quad S_{\lambda, \lambda'} = \langle \Psi_{\lambda} | \Psi_{\lambda'}' \rangle,$$

with the eigenvalues  $\{E_{\lambda}\}$  and eigenstates  $\{\Psi_{\lambda}\}$  corresponding to the optical transition energies and excitonic amplitudes, respectively. The latter can be expressed in a base of Kohn-Sham electron-hole product states

$$\Psi_{\lambda}(\mathbf{r}_1, \mathbf{r}_2) = \sum_{n_1, n_2} A_{\lambda}^{n_1, n_2} \phi_{n_1}^*(\mathbf{r}_1) \phi_{n_2}(\mathbf{r}_2). \quad (3.39)$$

The eigenvalue problem in Eq. 3.38 for the excitonic hamilton operator  $\mathbf{H}^{\text{exc}}$  with Eigenstates  $|\Psi_{\lambda}\rangle$  is thus reformulated as an eigenvalue problem for the excitonic (or BSE) matrix  $H^{\text{exc}}$ , given by Eq. 3.37, with eigenvectors  $\{A_{\lambda}^{n_1, n_2}\}$ .

In practice, the diagonalization of  $H^{\text{exc}}$  causes the biggest computational load due to the unfavorable  $\mathcal{O}(N^3)$  scaling of traditional diagonalization schemes. In order to utilize the BSE scheme for nontrivial systems, some assumptions regarding the shape of  $H^{\text{exc}}$  have to be made. Fortunately, the complexity can be reduced considerably by a number of conditions. First, if the quantum numbers  $\{n_i\}$  are again interpreted as a combined index  $(n, \mathbf{k})$  of band number  $n$  and wave vector  $\mathbf{k}$  of a solid, only momentum-conserving, vertical transitions are considered. Additionally, only transition between empty conduction states ( $c$ ) and filled valence states ( $v$ ) contribute to  $\bar{P}$  due to the occupation factors in Eq. 3.36, reducing the rank of  $H^{\text{exc}}$  further by a factor of 2. Lastly, the resulting hamiltonian can be shown to separate into four blocks according to [37, 38]

$$H^{\text{exc}} = \begin{pmatrix} H^{\text{res}} & H^{\text{coup}} \\ -(H^{\text{coup}})^* & -(H^{\text{res}})^* \end{pmatrix}, \quad (3.40)$$

with the resonant part

$$H_{(vc\mathbf{k}), (v'c'\mathbf{k}')}^{\text{res}} = (\epsilon_{c, \mathbf{k}} - \epsilon_{v, \mathbf{k}})\delta_{v, v'}\delta_{c, c'}\delta_{\mathbf{k}, \mathbf{k}'} + \Xi_{(vc\mathbf{k}), (v'c'\mathbf{k}')}, \quad (3.41)$$

corresponding to the transitions at positive frequencies, and the coupling terms

$$H_{(vck),(v'c'k')}^{\text{coup}} = \Xi_{(vck),(c'v'k')}.$$
 (3.42)

For many bulk semiconductors, including elemental Si and C [97, 98] and the transition metal oxides MnO and NiO [37] the influence of the coupling terms on the dielectric response was shown to be small, justifying the Tamm-Dancoff approximation (TDA), stating  $H^{\text{coup}} = 0$ .<sup>5</sup> Applying the TDA, the rank of  $H^{\text{exc}}$  reduces by an additional factor of two and translates the diagonalization of the full BSE matrix into a diagonalization of the submatrix  $H^{\text{res}}$ .

Employing these approximations, the resonant part of the BSE matrix is given by the sum of three contributions corresponding to a diagonal part (diag), unscreened exchange (ux) and screened Coulomb interaction (sc). In the limit  $\mathbf{q} \rightarrow 0$ , these contributions read

$$\begin{aligned} H^{\text{res}} &= H^{\text{diag}} + H^{\text{ux}} + H^{\text{sc}}, \\ \text{with } H_{(vck),(v'c'k')}^{\text{diag}} &= (\epsilon_{c,k} - \epsilon_{v,k}) \delta_{v,v'} \delta_{c,c'} \delta_{k,k'}, \\ H_{(vck),(v'c'k')}^{\text{ux}} &= 2 \frac{4\pi e^2}{V} \sum_{G \neq 0} \frac{B_{c,k}^{v,k}(G) \left( B_{c',k'}^{v',k'}(G) \right)^*}{|G|^2}, \\ \text{and } H_{(vck),(v'c'k')}^{\text{sc}} &= -\frac{4\pi e^2}{V(2\pi)^6} \sum_{G,G'} B_{c,k}^{c',k'}(\mathbf{k} - \mathbf{k}' + \mathbf{G}) \left( B_{v,k}^{v',k'}(\mathbf{k} - \mathbf{k}' + \mathbf{G}') \right)^* \\ &\quad \cdot \mathbf{W}_{G,G'}(\mathbf{k} - \mathbf{k}'). \end{aligned} \quad (3.43)$$

It is thus possible to set up the BSE matrix using the quasiparticle energies  $\{\epsilon_{n,k}\}$  and screened Coulomb interaction  $\mathbf{W}_{G,G'}(\mathbf{q})$  obtained by a preceding  $GW$  calculation.

The principle workflow to determine the macroscopic dielectric function including local-field effects and excitonic contributions can thus be formulated in the following way: Solving the eigenvalue equation for the BSE matrix  $H^{\text{exc}}$ , the right hand side of Eq. 3.36 can be constructed according to the spectral representation 3.38. The irreducible polarizability in real space is subsequently reconstructed via

$$\bar{P}(\mathbf{r}_1, \mathbf{r}_2, \mathbf{r}_3, \mathbf{r}_4) = \sum_{n_1, n_2, n_3, n_4} \phi_{n_1}(\mathbf{r}_1) \phi_{n_2}^*(\mathbf{r}_2) \phi_{n_3}^*(\mathbf{r}_3) \phi_{n_4}(\mathbf{r}_4) \bar{P}_{n_1 n_2 n_3 n_4}. \quad (3.44)$$

Using Eq. 3.22 the macroscopic dielectric function then finally reads

$$\begin{aligned} \varepsilon_M(\omega) &= 1 - \lim_{\mathbf{q} \rightarrow 0} \nu_0(\mathbf{q}) \int e^{i\mathbf{q}\mathbf{r}_1} \bar{P}(\mathbf{r}_1, \mathbf{r}_1, \mathbf{r}_2, \mathbf{r}_2) e^{-i\mathbf{q}\mathbf{r}_2} d\mathbf{r}_1 d\mathbf{r}_2 \\ &= 1 + \frac{\hbar^2 e^2}{V} \sum_{\lambda} \left| \sum_{cvk} \frac{\langle \phi_{vk} | \mathbf{e}_q \mathbf{v} | \phi_{ck} \rangle}{\epsilon_{ck} - \epsilon_{vk}} A_{\lambda}^{ck, vk} \right|^2 \\ &\quad \cdot \left( \frac{1}{E_{\lambda} - \hbar\omega - i\hbar\eta} + \frac{1}{E_{\lambda} + \hbar\omega + i\hbar\eta} \right) \end{aligned} \quad (3.45)$$

<sup>5</sup>It should be pointed out that the validity of the TDA breaks down for strongly confined systems, e.g., molecules [99], and for describing plasmonic excitations [100].

### 3.3 Raman Cross Section

The Raman effect, corresponding to the inelastic scattering of monochromatic light in solids and molecular systems, was first observed experimentally by Raman in 1928 [101]. Besides the frequency  $\omega_0$  of the impinged radiation, the scattered light thereby contains additional side bands ( $\omega_0 \pm \omega_{\text{vib}}$ ) as a result of the coupling between light field and vibrational eigenmodes of the solid or molecule with frequency  $\omega_{\text{vib}}$ .

The probability for a scattering event to occur between the light field and a specific phonon mode with index  $v$  may be deduced using Fermi's Golden Rule by considering the external light field as a perturbation inducing a transition of an electron either (i) from the ground into an excited, virtual electronic state with a subsequent relaxation into a virtual phonon state (Stokes scattering) or (ii) from a virtual phonon into a virtual, excited electronic state with a subsequent relaxation into the electronic ground state (Anti-Stokes scattering). Using the scattering probability, the differential Raman cross section  $\frac{d\sigma^v}{d\Omega}$ , defined as the cross section at a scattering (solid) angle  $\Omega$ , can be constructed within the polarization theory of Placzek [26, 27], yielding, for Stokes scattering [102]

$$\frac{d\sigma^v}{d\Omega} = \frac{(\omega_0 - \omega_v)^4}{(4\pi)^2 c^4} |\mathbf{e}_i \cdot \mathbf{R}^v \cdot \mathbf{e}_s|^2 \frac{\hbar}{2\omega_v} (n_v + 1) \quad (3.46)$$

where  $R_{i,j}^v = \sum_{k,\beta} \frac{\partial \chi_{i,j}(\omega_0)}{\partial u_{k,\beta}} \cdot \frac{e_{k,\beta}^v}{\sqrt{m_k}}$ .

Here,  $\omega_v$  and  $n_v$  denote the vibrational frequency of the phonon with index  $v$  and its respective bosonic occupation factor  $n_v = \left( e^{\frac{\hbar\omega_v}{k_B T}} - 1 \right)^{-1}$ . The polarization directions of the incident and scattered light field are denoted as  $\mathbf{e}_i$  and  $\mathbf{e}_s$ , respectively. The electronic and ionic degrees of freedom and their coupling are encoded in the Raman susceptibility tensor  $\mathbf{R}^m$ . Essentially, it contains informations about (i) the change in polarizability  $\chi$  under the displacement  $u_{k,\beta}$  of an atom  $k$  along the direction  $\beta$  and (ii) the displacement  $e_{k,\beta}^v$  of the same atom along the same direction within the  $v$ -th phonon mode, normalized by its mass  $m_k$ . Only the case of nonresonant Raman scattering is considered, assuming the light frequency  $\omega_0$  and transitional frequencies between true electronic states to be well separated.

In the following, the ionic and electronic contribution to the differential Raman cross section and Raman susceptibility tensor 3.46 are discussed separately.

#### 3.3.1 Ionic Contribution

The ionic contribution to 3.46 is given by the phonon eigendisplacements  $\{e^v\}$  and vibrational frequencies  $\{\omega^v\}$  in the optical limit  $\mathbf{q} \rightarrow 0$ . Within the harmonic approximation, they are obtained as solutions of the generalized eigenvalue equation

$$\sum_{k',\beta'} \left( \Phi_{k,\beta}^{k',\beta'} - \omega_v^2 m_k \delta_{\beta,\beta'} \delta_{k,k'} \right) e_{k',\beta'}^v = 0, \quad (3.47)$$

with the entries of the force-constant matrix  $\Phi$

$$\Phi_{k,\beta}^{k',\beta'} = - \frac{\partial F_{k,\beta}}{\partial u_{k',\beta'}} = \frac{\partial^2 E_0}{\partial u_{k,\beta} \partial u_{k',\beta'}} \quad (3.48)$$

describing the force  $F_{k,\beta}$  acting on an atom  $k$  along  $\beta$ , if an atom  $k'$  is displaced along  $\beta'$ . The eigendisplacements are assumed to be normalized via the ionic mass  $m_k$  according to [103]

$$\sum_{k',\beta'} m_{k'} e_{k',\beta'}^v e_{k',\beta'}^w = \delta_{v,w}. \quad (3.49)$$

Conceptually, the simplest approach to set up the matrix  $\Phi$  is the frozen-phonon (FP) method, in which the derivatives  $\frac{\partial F_{k,\beta}}{\partial u_{k',\beta'}}$  are evaluated directly by means of finite differences: The ground-state energy and forces are determined for a number of distorted ionic geometries, in which each ion  $k'$  is displaced by a small amount  $u$  along the positive and negative cartesian directions  $\beta'$  and  $-\beta'$ , fixing the row  $(k, \beta)$  of  $\Phi$  according to

$$\Phi_{k,\beta}^{k',\beta'} \approx \frac{\frac{1}{2}(F_{k,\beta}(\beta') - F_{k,\beta}(-\beta'))}{u}. \quad (3.50)$$

While the FP method is easily implemented, its disadvantage lies in the number of total-energy calculations required to set up the force-constant matrix, scaling linearly with the number of atoms within the cell under consideration. Additionally, the FP method is intrinsically limited to the  $\Gamma$  point only, i.e., to phonon wave vectors  $\mathbf{q} = 0$ . Calculations of phonons at nonzero wave vectors (in particular phonons in the limit  $\mathbf{q} \rightarrow 0$ ) therefore require setting up and evaluating large repetitions of a unit cell (supercells), increasing the computational cost even further.

Alternatively, density-functional perturbation theory (DFPT) can be used to evaluate the second-order derivative of the ground-state energy in Eq. 3.48. In general, if the external potential  $v_{\text{ext}}$  is assumed to depend on a set  $\lambda = \{\lambda_i\}$  of external parameters (e.g., the ionic displacements  $\{u_{k,\beta}\}$ ),  $\lambda$  also uniquely defines the charge density  $\rho$  and ground-state energy  $E_0$ , according to the Hohenberg-Kohn theorems. The derivative of  $E_0$  with respect to two arbitrary parameters is then given by [104]

$$\frac{\partial^2 E_0}{\partial \lambda_i \partial \lambda_j} = \int \frac{\partial^2 v_{\text{ext}}(\mathbf{r})}{\partial \lambda_i \partial \lambda_j} \rho(\mathbf{r}) d\mathbf{r} + \int \frac{\partial \rho(\mathbf{r})}{\partial \lambda_i} \frac{\partial v_{\text{ext}}(\mathbf{r})}{\partial \lambda_j} d\mathbf{r}. \quad (3.51)$$

Evidently, the second derivative of the energy requires knowledge of only the first derivative of the charge density. This is a direct consequence of the  $(2n + 1)$  theorem, stating that the  $n$ -th derivative of a wave function (and therefore also the density) enables the evaluation of the energy derivative up to the order  $2n + 1$ . According to Eq. 2.8, the linear variation  $\Delta_\lambda \rho = \sum_j \frac{\partial \rho}{\partial \lambda_j} \Delta \lambda_j$  with respect to the perturbation  $\lambda$  can be expressed as

$$\Delta_\lambda \rho(\mathbf{r}) = \sum_v \phi_v(\mathbf{r}) \cdot \Delta_\lambda \phi_v^*(\mathbf{r}) + \text{c.c.}, \quad (3.52)$$

with c.c. denoting the complex conjugate and  $v$  running over all occupied states. The variation  $\Delta_\lambda \phi_v$  of the Kohn-Sham states is given by standard first-order perturbation theory, according to [104]

$$|\Delta_\lambda \phi_v\rangle = \sum_{m \neq v} \frac{\langle \phi_m | \Delta_\lambda v_{\text{eff}} | \phi_v \rangle}{\epsilon_v - \epsilon_m} |\phi_m\rangle, \quad (3.53)$$

$$\text{where } \Delta_\lambda v_{\text{eff}}(\mathbf{r}) = \Delta_\lambda v_{\text{ext}}(\mathbf{r}) + e^2 \int \frac{\Delta_\lambda \rho(\mathbf{r}')}{|\mathbf{r} - \mathbf{r}'|} d\mathbf{r}' + \frac{\delta v_{\text{xc}}[\rho]}{\delta \rho} \Delta_\lambda \rho(\mathbf{r}).$$

The density variation in Eq. 3.52 may thus be expressed as

$$\Delta_\lambda \rho(\mathbf{r}) = \sum_v \sum_{m \neq v} \phi_v^*(\mathbf{r}) \phi_m(\mathbf{r}) \frac{\langle \phi_m | \Delta_\lambda \nu_{\text{eff}} | \phi_v \rangle}{\epsilon_v - \epsilon_m} + c.c. \quad (3.54)$$

Note that all terms, for which both  $v$  and  $m$  denote occupied states, cancel. The variation of the density therefore only responds to perturbations  $\Delta_\lambda \nu_{\text{eff}}$ , which couple occupied and empty states [104], leaving the index  $m$  to run only over unoccupied conduction states  $c$ . Similar to the Kohn-Sham equations,  $\Delta_\lambda \rho$  can be solved self-consistently according to 3.52 and 3.53. It, however, requires the summation over an infinite number of unperturbed Kohn-Sham states in Eq. 3.52. This can be circumvented by applying the operator  $(\mathbf{H}_{\text{KS}} - \epsilon_v)$  to  $|\Delta_\lambda \phi_v\rangle$  in 3.53, yielding the linear equation

$$\begin{aligned} (\mathbf{H}_{\text{KS}} - \epsilon_v) |\Delta_\lambda \phi_v\rangle &= \sum_c \frac{(\mathbf{H}_{\text{KS}} - \epsilon_v) |\phi_c\rangle}{\epsilon_v - \epsilon_c} \langle \phi_c | \Delta_\lambda \nu_{\text{eff}} | \phi_v \rangle \\ &= - \sum_c |\phi_c\rangle \langle \phi_c | \Delta_\lambda \nu_{\text{eff}} | \phi_v \rangle \\ &= -(\mathbf{1} - \rho) \Delta_\lambda \nu_{\text{eff}} |\phi_v\rangle, \end{aligned} \quad (3.55)$$

where  $\mathbf{H}_{\text{KS}}$  corresponds to the Kohn-Sham hamiltonian and  $\rho = \sum_v |\phi_v\rangle \langle \phi_v|$  to the density operator, given by the projector on the subspace of occupied Kohn-Sham states. Since  $\epsilon_v$  is an eigenvalue of  $\mathbf{H}_{\text{KS}}$ , the operator on the left side of Eq. 3.55 has an eigenvalue of 0 and is hence not invertible. In practice, a small portion of  $\rho$  is therefore added to the operator. According to the previous discussion, the solution  $|\Delta_\lambda \phi_v\rangle$  is thereby not effected, since it is composed purely of unoccupied states.

Special care has to be taken regarding the aforementioned  $\mathbf{q} \rightarrow 0$  limit in 3.47 in the case of polar crystals. Due to the long-range nature of the Coulomb interaction, longitudinal optical phonons may thereby generate macroscopic electric fields, giving rise to additional forces on the ions and, thus, to an additional component in the force constant matrix 3.48. In this case, a nonanalytical and direction-dependent term  $\bar{\Phi}$  has to be added to  $\Phi$  with [105]

$$\bar{\Phi}_{k,\beta}^{k',\beta'}(\mathbf{q} \rightarrow 0) = \frac{4\pi}{V} \frac{\left( \sum_\gamma q_\gamma Z_{k,\gamma\beta}^* \right) \left( \sum_{\gamma'} q_{\gamma'} Z_{k',\gamma'\beta'}^* \right)}{\sum_{\mu,\nu} q_\mu \epsilon_{\mu,\nu}^\infty q_\nu}. \quad (3.56)$$

Here,  $\epsilon^\infty$  denotes the low-frequency limit of the macroscopic dielectric function 3.18 and

$$Z_{k,\gamma\beta}^* = V \frac{\partial P_\gamma}{\partial u_{k,\beta}} \bigg|_{\mathcal{E}=0} \quad (3.57)$$

the Born effective charge tensor, defined as the rate of change in the macroscopic polarization  $\mathbf{P}$  induced by an ionic displacement  $u_{k,\beta}$  at vanishing electric fields  $\mathcal{E}$ . Similar to  $\Phi$  and the electronic contribution to the Raman susceptibility tensor (see next section),  $Z^*$  can be evaluated via DFPT [105]. It serves as a fundamental quantity in lattice dynamics, governing the magnitude of splitting between longitudinal and transverse optical modes in the limit  $\mathbf{q} \rightarrow 0$  (LO-TO splitting).

### 3.3.2 Electronic contribution

In a similar manner to the ionic contribution, the electronic one, given by the derivative of the polarizability  $\chi$  with respect to the ionic displacements  $\mathbf{u}$ , can be evaluated using either a direct finite differences method or DFPT. Within the direct method, an electronic ground-state calculation is again performed for all distorted ionic geometries, in which each ion  $k'$  is displaced along the directions  $\beta'$  and  $-\beta'$  by an amount  $u$ . The ground-state energies and eigenstates for each geometry then fix the polarizability  $\chi \propto \varepsilon_M$  within the IPA via Eq. 3.18 and the derivative can be constructed in a similar manner to the force-constant matrix in Eq. 3.50. In principle, ionic and electronic contribution can be determined simultaneously within this method by evaluating forces as well as the dielectric function with the same electronic ground-state properties for every ionic step. For small systems, this approach has been successfully used to determine Raman spectra in good agreement with experimental data both in terms of peak position as well as relative peak heights [106, 107].

This method, however, is not followed in this thesis. Instead, a DFPT based approach by Lazzeri and Mauri [108, 109] is used to evaluate the electronic contribution. Thereby, the polarizability  $\chi$  is interpreted as the second derivative of the ground-state energy  $E_0$  with respect to an external electric field  $\mathcal{E}$ . Using the density operator  $\rho$ , the electronic contribution may be written as

$$\frac{\partial \chi_{i,j}}{\partial u_{k,\beta}} = \frac{\partial^3 E_0}{\partial \mathcal{E}_i \partial \mathcal{E}_j \partial u_{k,\beta}} = 2 \text{Tr} \left\{ \left( \frac{\partial^2 \rho}{\partial \mathcal{E}_i \partial \mathcal{E}_j} \right) \frac{\partial v_{\text{ext}}}{\partial u_{k,\beta}} \right\}, \quad (3.58)$$

with  $\text{Tr}\{\dots\} = \sum_v \langle \phi_v | \dots | \phi_v \rangle$  denoting the trace of an operator. The difficulty now lies in calculating the second derivative of the density operator with respect to the components of  $\mathcal{E}$ . A formalism to evaluate general (mixed) derivatives of  $\rho$  up to arbitrary order was introduced by Lazzeri and Mauri in 2003, stating, up to second order:

$$\begin{aligned} \frac{\partial \rho}{\partial \lambda} &= \sum_v \left| \mathbf{P} \frac{\partial \phi_v}{\partial \lambda} \right\rangle \langle \phi_v | + \text{c.c.} \\ \text{and} \quad \frac{\partial^2 \rho}{\partial \lambda \partial \mu} &= \sum_v \left( \left| \mathbf{P} \eta_v^{(\lambda,\mu)} \right\rangle \langle \phi_v | + \left| \mathbf{P} \frac{\partial \phi_v}{\partial \lambda} \right\rangle \left\langle \frac{\partial \phi_v}{\partial \mu} \mathbf{P} \right| \right. \\ &\quad \left. - \sum_{v'} \left| \phi_{v'} \right\rangle \left\langle \frac{\partial \phi_{v'}}{\partial \lambda} \mathbf{P} \right| \left\langle \mathbf{P} \frac{\partial \phi_v}{\partial \mu} \right\rangle \langle \phi_v | \right) + \text{c.c.}, \end{aligned} \quad (3.59)$$

where  $\mathbf{P} = \mathbf{1} - \rho$ .

Derivatives are taken with respect to arbitrary perturbations  $\lambda$  and  $\mu$ . The second derivatives of occupied Kohn-Sham states within the parallel-transport gauge are denoted with  $|\eta_v^{(\lambda,\mu)}\rangle$ . Using the terminology of Gonze, the parallel-transport gauge is thereby given by the condition [110]

$$\langle \phi_v | \eta_{v'}^{(i)} \rangle - \langle \eta_v^{(i)} | \phi_{v'} \rangle = 0. \quad (3.60)$$

In principle, the derivatives of the wave functions in 3.59 can be determined in a similar manner to 3.53. However, for electric-field perturbations, i.e.,  $v_{\text{ext}} \propto -\mathcal{E} \cdot \mathbf{r}$ , the expectation value over the position operator would have to be evaluated, which is not well defined for periodic boundary conditions. To circumvent this issue, the derivatives of the wave functions

are rewritten in a way to explicitly depend on commutators between the derivatives of the effective potential and the density operator, yielding

$$\begin{aligned} \left| \mathbf{P} \frac{\partial \phi_v}{\partial \lambda} \right\rangle &= \mathbf{G}_v \left[ \frac{\partial v_{\text{eff}}}{\partial \lambda}, \boldsymbol{\rho} \right] |\phi_v\rangle, \\ \text{and } \left| \mathbf{P} \eta_v^{(\lambda, \mu)} \right\rangle &= \mathbf{G}_v \left\{ \frac{\partial^2 v_{\text{eff}}}{\partial \lambda \partial \mu} + \left[ \frac{\partial v_{\text{eff}}}{\partial \lambda}, \frac{\partial \boldsymbol{\rho}}{\partial \mu} \right] + \left[ \frac{\partial v_{\text{eff}}}{\partial \mu}, \frac{\partial \boldsymbol{\rho}}{\partial \lambda} \right] \right\} |\phi_v\rangle, \end{aligned} \quad (3.61)$$

with the Green's function

$$\mathbf{G}_v = \sum_c \frac{|\phi_c\rangle \langle \phi_c|}{\epsilon_v - \epsilon_c} \quad (3.62)$$

projected on the empty states  $|\phi_c\rangle$ . Since  $\boldsymbol{\rho}$  and its derivatives are localized, the expectation values in 3.61 are well defined for periodic boundary conditions, even in the case of  $\frac{\partial v_{\text{eff}}}{\partial \lambda} \propto \mathbf{r}$ . It is thus possible to evaluate the second derivative in Eq. 3.58 by self-consistently solving equations 3.59 and 3.61.

# 4

## Ferroelectrics

All systems investigated within this thesis are members of the particular class of ferroelectric solids. In general, ferroelectrics can thereby be considered a subgroup of dielectrics which are characterized by the fact that an internal dipole moment within the material can be induced by applying an external electric field  $\mathcal{E}$ . In particular, ferroelectrics are a subgroup of polar dielectrics, i.e., materials whose net dipole moment (internal polarization)  $P$  is nonzero even in the absence of an electric field because the centers of positive and negative sublattice do not coincide [111]. In ferroelectrics, external electric fields cannot only change the magnitude of the internal polarization, but can also flip its orientation into two or more stable configurations. These new orientations thereby remain stable even after the electric field is removed, according to the ferroelectric hysteresis loop, see Fig. 4.1. Initially, the

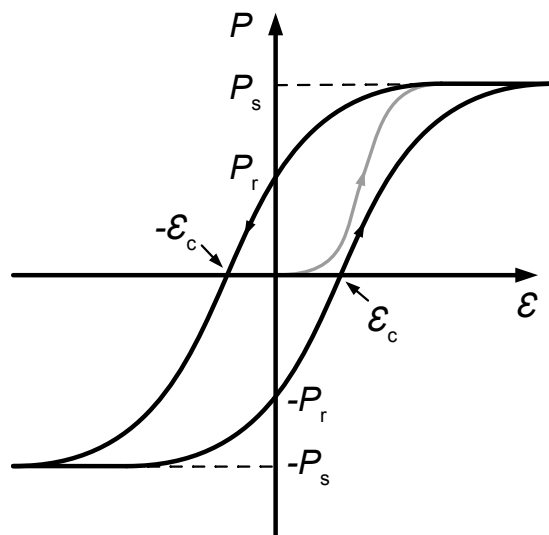


**Figure 4.1:** Schematic representation of the ferroelectric hysteresis loop in a plot of the polarization  $P$  versus the applied electric field  $\mathcal{E}$ . Values of the coercive field  $\mathcal{E}_c$ , remanent polarization  $P_r$  and saturation polarization  $P_s$  are indicated.

existing dipole moments within the material are aligned due to the applied field, raising the internal polarization from 0 to a saturation value  $P_s$  (gray line). Decreasing the electric field  $\mathcal{E}$  back to zero, a remanent polarization  $P_r$  remains in the material. Applying an electric field in the opposite direction, the polarization first reaches zero at the coercitive field  $-\mathcal{E}_c$  before again reaching its saturation value  $-P_s$ . A reversal of the applied field causes  $P$  to drop back to the remanent polarization  $-P_r$  for zero field, vanish for  $\mathcal{E} = \mathcal{E}_c$  and finally saturate at  $P_s$ .

## 4.1 Ferroelectric-Paraelectric Phase Transition

Apart from the naming, a number of properties in ferroelectrics bear resemblances to those within ferromagnetic solids. In particular, the existence of a material-specific critical temperature  $T_C$  (Curie temperature), above which the internal magnetization of a ferromagnetic material vanishes, is similarly found regarding the internal polarization within ferroelectrics. In analogy to the high and low temperature para and ferromagnetic phases, the  $P = 0$  phase is thereby called paraelectric.

Historically, phase transitions between para- and ferroelectric phase have been divided into two classes: order-disorder and displacive ones. Within an order-disorder phase transition, electric dipoles are present within the material even in its paraelectric phase. However, they are randomly oriented, therefore effectively averaging each other out. The amount of orientations thereby varies based on the given material and space group. A particular example for a ferroelectric possessing an order-disorder type transitions is  $\text{KH}_2\text{PO}_4$ , with its Curie temperature at 123 K. The transition occurs between the paraelectric  $\bar{4}2m$  and the ferroelectric  $mm2$  phases. Above  $T_C$ , hydrogen ions linking  $\text{PO}_4$  tetrahedra are delocalized between two equivalent positions. Below  $T_C$ , H localizes at one position randomly, giving rise to the distortion of  $\text{PO}_4$ , creating a spontaneous polarization. Since  $T_C$  is intrinsically tied to the probability of H hopping between the two positions, its value can be increased up to 20 K by substituting heavier Deuterium atoms for H [112–114].

In contrast, a displacive phase transition is characterized by the existence of electric dipoles only within the ferroelectric phase. Ferroelectric and paraelectric phase are linked by small, continuous atomic lattice displacements. The transition from ferroelectric to paraelectric phase is heralded by the existence of a soft mode. Close to  $T_c$ , the lattice deformation of this soft mode results in a lack of restoring force due to the deformation pointing away from a local energy maximum. The contribution of the soft mode to the total vibrational energy of a system within the harmonic approximation is thereby given by [115]

$$H_{\text{vib}} = \frac{1}{2} \sum_k \omega_k^2 \cdot Q_k^2, \quad (4.1)$$

with  $\omega_k$  as the vibrational frequency and  $Q_k$  as the normal mode displacement for wave vector  $k$ . Evidently, for  $H_{\text{vib}}$  to possess a local maximum at  $Q_k = 0$ , the frequency must amount to 0 or a complex value, implying a softening (shift to lower frequency) of the mode close to the transition temperature. Examples for displacive phase transitions include many perovskite oxides, i.e., materials with the general constitution formula  $\text{ABO}_3$ , with cations A and B. As the first experimental evidence for soft-mode behavior,  $\text{SrTiO}_3$  was found to undergo a displacive phase transition at 110 K from a tetragonal to a cubic phase [116–119]. Using Raman spectroscopy at different temperatures, the two lowest-frequency optical modes within

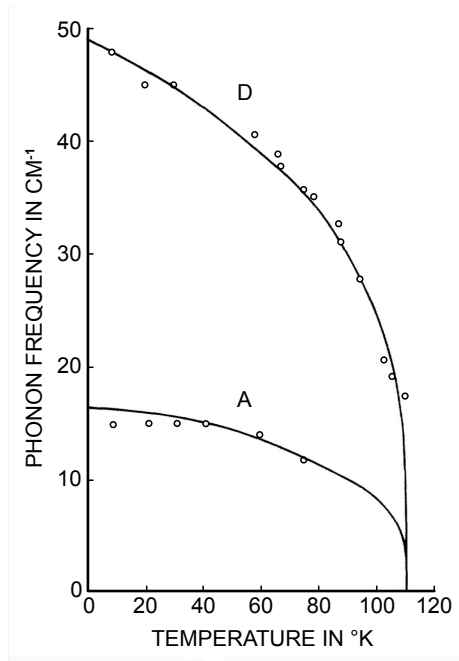


**Figure 4.2:** Temperature dependence of the two lowest-frequency modes A and D in tetragonal  $\text{SrTiO}_3$ . Figure adapted from Ref. [118].

the tetragonal phase were found to dramatically decrease in frequency when the temperature approaches the transition temperature from below, see Fig. 4.2. Microscopically, the reason for this softening was traced back to the condensation of a triply degenerate oxygen mode labeled  $\Gamma_{25}$  within the cubic phase. At wave vectors parallel to (111),  $\Gamma_{25}$  involves a clock- and anticlockwise rotation of individual oxygen cages around the  $z$  direction. This displacement condenses into a tetragonal structure below 110 K, in which  $\Gamma_{25}$  splits up into two individual modes (A and D in Fig. 4.2) located at the  $\Gamma$  point, being observable via Raman spectroscopy.

Apart from phase transitions of pure order-disorder and displacive type, paraelectric-ferroelectric phase transitions of mixed type are observed as well. One such case is  $\text{LiNbO}_3$ , whose crystal structure along the ferroelectric  $z$  axis is given by planes containing O and Li, with the Nb atoms being located in the center of the so formed  $\text{NbO}_6$  cages. For a long time, the nature of the paraelectric-ferroelectric phase transition, taking place at around 1480 K, has been the subject of debate. One reason for this unclarity is the fact that experimental studies have either confirmed [120, 121] or disproven [122] the existence of a soft mode in bulk  $\text{LiNbO}_3$ . In contrast, a clear picture could be obtained using molecular dynamics calculations [123–125]. The Li and Nb sublattices were thereby found to contribute differently to the full phase transition mechanism. Below the Curie temperature, the distribution of Li and Nb along the  $z$  direction is unimodal. Close to the Curie temperature, the distribution of Nb shifts continuously towards being localized exactly in the middle between two O planes, corresponding to a displacive-type phase transition. The Li sublattice, on the other hand, was found to shift towards a binodal distribution, located exactly within the O planes only on average, adding an additional order-disorder contribution to the full phase transition mechanism.

Another material exhibiting a mixed displacive and order-disorder type phase transition is Lithium heptagermanate  $\text{Li}_2\text{Ge}_7\text{O}_{15}$  (LGO), which is an example of a weak ferroelectric [126] due to its relatively small spontaneous polarization in the ferroelectric phase, in the order of  $0.02\text{--}0.03 \mu\text{C}/\text{cm}^2$  [127]. The crystal structure of LGO consists of  $\text{GeO}_4$  tetrahedra and  $\text{GeO}_6$  octahedra, linked by a mutual O atom. The resulting cavities are occupied by  $\text{Li}^+$  ions distributed among two nonequivalent sites, Li(1) and Li(2), differently coordinated with respect to neighboring O atoms [128]. At a temperature of 283.5 K, LGO undergoes a transition from its high temperature paraelectric phase (space group  $Pbcn$ ) to its low temperature ferroelectric phase (space group  $Pbc2_1$ ). During the phase transition, a soft mode, related to a rotation of the  $\text{GeO}_4$  tetrahedra, is observed experimentally [128, 129], indicating a displacive type of phase transition. However, due to its small oscillator strength, the contribution of the mode to the total dielectric constant is relatively low, hinting towards an additional phase transition mechanism [130]. This additional mechanism thereby involves the  $\text{Li}^+$  sublattice. The thermal displacement parameters of Li(1) and Li(2) (determined experimentally by neutron diffraction) are found to be equal in the low temperature ferroelectric phase. In the high energy paraelectric phase, however, the displacement parameters of Li(2) turn highly anisotropic, with its highest value along the  $x$  direction being almost one order of magnitude larger compared to Li(1) [128]. Therefore, the position of the Li(2) atom can be considered statistically distributed along the  $x$  channel, resulting to an order-disorder-type contribution to the phase transition.

## 4.2 Technological Applications of Ferroelectrics

Ferroelectrics are a material class evoking particular interest in numerous technological fields. In particular, their tunable internal polarization gives rise to many unique optical and electrical properties. These are exploited, for instance, in

- Acoustics: Acoustic resonators can be fabricated in the shape of multilayer thin film FBARs (ferroelectric bulk acoustic resonators) utilizing  $\text{BaTiO}_3\text{--SrTiO}_3$  mixed crystals (BSTO) as the key material. Here, the large electromechanical coupling of BSTO is exploited to make the resonance frequency of each individual layer tunable by the induced piezoelectric effect. Piezoelectrically inactive BSTO in its paraelectric phase is rendered piezoelectrically active by an electric field displacing the Ti/Sr ions along the polar axis, reminiscent to a paraelectric-ferroelectric phase transition. [131]
- Nonvolatile memory: Arrays of ferroelectric material can be used to store logical information encoded into their polarization state, akin to standard magnetic drives encoding information into their internal magnetization. Ferroelectric memory cells may be fabricated using doped hafnium oxide ( $\text{FE-HfO}_2$ ) either in a one-transistor (1T) or one-transistor-one-capacitor (1T-1C) architecture. [132]

Another technological sector exploiting ferroelectric properties in matter is linear and nonlinear optics, which shall be discussed in more detail in the following.

In the context of linear optics, electro-optic (EO) modulators belong to the most widespread applications. In an EO modulator, the EO effect alters the refractive index of a crystal under the influence of an external electric field, giving rise to a modulation of the phase, polarization or amplitude of impinged light. For this purpose, ferroelectric crystals are partic-

ularly suited, because the linear EO coefficient, governing the magnitude of the EO effect, is proportional to the dielectric constant and the spontaneous internal polarization [133–135]. For the perovskite-type ferroelectrics  $M\text{NbO}_3$  (with  $M=\text{K}, \text{Li}$ ), the strength of their respective EO coefficient is thereby related to their geometry: A displacement of the Nb atom in the center of the  $\text{O}_6$  octahedron, caused by a low frequency electric field, has been shown to induce a change in the crystals optical response [136].

Within nanophotonics, the miniaturization of EO modulators and their integration into single chips with a variety of different optical devices has been a key objective for the last decades. Thin films of  $\text{LiNbO}_3$  [137–139] emerged as standard material for this purpose due to their high modulation bandwidth in addition to low power consumption. Other ferroelectric oxides used for the fabrication of integrated thin film EO modulators include  $\text{LiTaO}_3$  [140],  $\text{BiFeO}_3$  [135] or  $\text{BaTiO}_3$  [141, 142], grown on top of Si-based substrates. As a key quantity for EO modulation, the EO coefficients of all four materials vary in a range between 12 pm/V ( $\text{BiFeO}_3$ ) and 730 pm/V ( $\text{BaTiO}_3$ ) [141]. In the case of  $\text{BaTiO}_3$ , even values in the order of 1300 pm/V for unclamped (stress-free) crystals have been observed [141]. Modulators based on these ferroelectrics, however, come with the drawback of possible deterioration due to the photorefractive effect [143] or a complete depoling of the crystal [144] if driven by too high electric fields. Higher robustness against large electric fields can be achieved by using thin films of lead-based ferroelectrics like lanthanum-modified lead zirconate titanate ( $\text{Pb}_{1-x}\text{La}_x[\text{Zr}_y\text{Ti}_{1-y}]_{1-x/4}\text{O}_3$ , PLZT). Large EO coefficients (120 pm/V – 340 pm/V) in addition to low propagation loss have been observed in photonic-integrated circuits based on PLZT [143, 145].

Apart from EO modulators, the portfolio of devices utilizing the linear-optical properties of ferroelectric materials additionally includes optical deflectors, shutter arrays or light valves [144]. Another technological task, well covered by the peculiar properties of ferroelectrics, is the generation of monochromatic light at wavelengths, previously out of scope with conventional radiation sources, via second-harmonic generation (SHG). This is partly due to a specific crystallographic requirement for SHG to take place in a material in the first place: the lack of an inversion center within the crystal. Due to the internal polarization, ferroelectric materials possess by definition, this requirement is naturally fulfilled.

During SHG in a nonlinear material, impinged light of frequency  $\omega$  (source) is partially converted to a frequency  $2\omega$  (signal) due to nonlinear interaction between light and matter. Ideally, the signal intensity should continuously increase along the propagation path. However, since both beams are subject to dispersion, their respective phase velocities  $v_p = \frac{c}{n}$  generally differ. Here  $c$  is the speed of light and  $n = n(\omega)$  the frequency-dependent refractive index. This velocity mismatch gives rise to a mismatch in phase, causing the signal intensity to drop to zero after propagating a distance  $l_c \propto (\Delta n)^{-1}$  (coherence length) due to destructive interference [146]. In order to maximize  $l_c$ , the difference in refractive indices  $\Delta n$  between source and signal should therefore be minimized, ideally fulfilling the phase-matching condition  $n(\omega) = n(2\omega)$ . Perfect phase matching thereby yields a quadratic increase in signal intensity along the propagation path [147]. Several phase-matching techniques can be employed, including birefringence phase matching [146, 148–150]. Here, the birefringence in a nonlinear material (i.e., anisotropy of its refractive index) is exploited to account for the phase mismatch by having source and signal beam differently polarized, either along the ordinary or the extraordinary axis of the nonlinear crystal. Depending on the specific technique, either critical or noncritical phase matching can be achieved. In

the case of critical phase matching, the beam's propagation direction is chosen specifically for the ordinary and extraordinary refractive index to fulfill the phase-matching condition. Because the direction has to be carefully adjusted, this technique is sensitive to variations of the propagation angle. On the other hand, noncritical phase matching can be achieved via the temperature dependence of both refractive indices [151]. Thereby, ordinary and extraordinary refractive indices are matched by adjusting the crystal's temperature, effectively dropping the need of highly accurate angular adjustment in the case of critical phase matching, but introducing the need of high temperature stabilization. Both techniques come with a number of drawbacks. First, the nonlinear crystal has to be birefringent by definition, effectively making birefringent phase matching inaccessible to isotropic materials with promisingly high SHG coefficients, including GaAs [152]. Secondly, the angular/thermal stability required for critical and noncritical phase matching limits the accessible wavelength interval [153]. Additionally, due to the fixed polarization configuration of source and signal the individual components of the nonlinear susceptibility may not be chosen independently.

A different way to partially overcome the problem of phase mismatch is to employ quasi-phasematching (QPM), a technique first proposed theoretically by Armstrong *et al.* in 1962 [154] and later realized experimentally in 1964 by Miller for ferroelectric BaTiO<sub>3</sub> [155]. The principle idea behind QPM is that a sign change in the SHG coefficient introduces a phase shift of  $\pi$  in the signal beam. Therefore, by periodically flipping the sign of the SHG coefficient along the propagation path with a period length  $l_C$ , the power flow from signal to source can be partially reverted, giving rise to a sub-quadratic increase in signal intensity [146, 147]. Because coherence lengths for typical SHG setups amount to a few  $\mu\text{m}$  [156], fabrication of such periodic structures for general nonlinear materials turned out to be highly technologically challenging. For ferroelectric crystals, however, the sign of the SHG coefficient is intrinsically tied to its polarization state [157]. QPM in ferroelectrics can therefore be realized by periodically switching the polarization state, creating a grating of differently polarized ferroelectric domains. Historically, several techniques have been utilized to pattern ferroelectric crystals in this way, including ion exchange [158] and dopant in-diffusion [157]. Notably, the only technique that has stood the test of time is periodic poling: By applying an electric field exceeding the coercitive field strength  $E_c$  antiparallel to the direction of ferroelectric polarization, a polarization inversion can be achieved.

Material systems used to create periodically poled SHG gratings include the previously mentioned crystals LiNbO<sub>3</sub> and LiTaO<sub>3</sub> [147, 157, 159–163]. Both materials show large nonlinear coefficients in addition to a broad transparency region, covering the entire range of visible wavelengths up to mid-infrared [162, 164]. However, their relatively large coercitive field strength, reaching 1.7–4 kV/mm in the case of stoichiometric and 21 kV/mm in the case of a (more common) congruent composition [165], renders the fabrication of periodically poled structures highly demanding [14]. Additionally, in the case of LN, a relatively low index contrast between the waveguide core region and cladding layers makes large device dimensions and large bending radii inevitable [159].

### 4.3 The Potassium Titanyl Phosphate Crystal Family

The ferroelectric potassium titanyl phosphate (KTiOPO<sub>4</sub>, KTP) is a member of the crystal family with general constitutional formula  $MTiOXO_4$ , where  $M = \{\text{K, Rb, Tl, Cs, NH}_4\}$  and  $X = \{\text{P, As}\}$ . Members of this family are isomorphic (i.e., possess the same crystal symmetry)

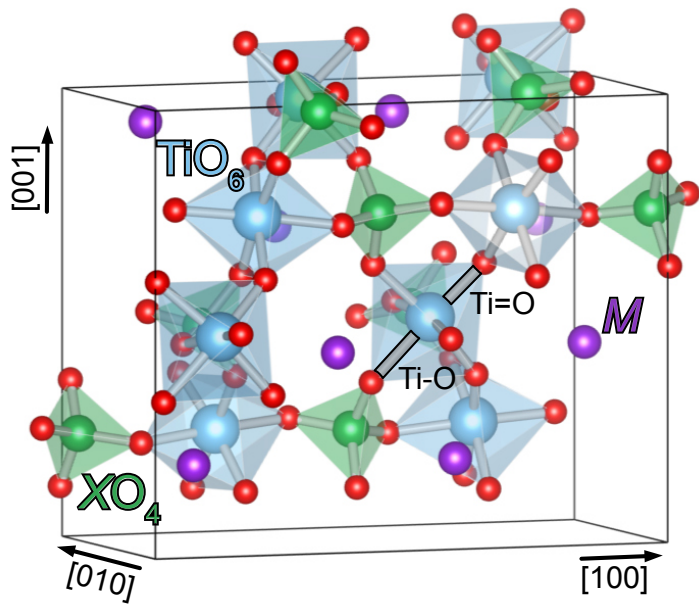


**Figure 4.3:** Orthorhombic unit cell of a general  $MTiOXO_4$  crystal family member. Long and short Ti–O bonds are indicated. Figure adapted from Ref. [171].

and are known to exhibit favorable optical properties, including high nonlinear coefficients and large transparency windows, rendering them particularly suited for applications in linear and nonlinear optics and photonics.

The technological potential of KTP remained unknown for a long time. The first preparation of KTP dates back to 1890, when Ouvrard synthesized it out of a flux containing  $TiO_2$ ,  $K_4P_2O_7$  and  $KP_3O_4$  [166]. KTP was rediscovered many decades later, in the 1970, during an era of high demand on materials with extraordinary nonlinear properties. In 1971, Masse and Grenier released a short report on the synthesis of three members of the KTP family, with  $X = P$  and  $M = \{K, Rb, Tl\}$  and the subsequent first experimental study regarding their crystallographic properties [167]. The crystal structure was found to be orthorhombic, with space group  $Pna2_1$ , which was later confirmed by other studies [7, 168, 169]. In 1976, the optical properties of mixed crystals between KTP and RTP have been reported for the first time by Zumsteg *et al.* [170]. It was found that phase-matching was possible for the entire transparency region of the material (350 – 4500 nm) and efficient frequency doubling could be achieved for radiation at 1060 nm wavelength. The origin for these properties as well as for the general ferroelectricity in KTP-type crystals can be traced back to the particular crystal structure, see Fig. 4.3. Since KTP-type crystals are isomorphic, this discussion will, for the sake of simplicity, be restrict to KTP only.

#### 4.3.1 Crystal structure

The unit cell of KTP is orthorhombic, with lattice constants  $a = 12.819 \text{ \AA}$ ,  $b = 6.399 \text{ \AA}$  and  $c = 10.584 \text{ \AA}$ , and contains 64 atoms in total [172]. Due to its  $Pna2_1$  space group, a total of four symmetry operations exist, mapping symmetry-equivalent atoms within the unit cell

onto each other. For reduced coordinates  $x$ ,  $y$  and  $z$ , these operations are <sup>1</sup>

$$\begin{aligned}
 (x, y, z) &\rightarrow (x, y, z) \quad (\text{Identity}) \\
 (x, y, z) &\rightarrow \left( \frac{1}{2} - x, \frac{1}{2} + y, \frac{1}{2} + z \right) \\
 (x, y, z) &\rightarrow \left( \frac{1}{2} + x, \frac{1}{2} - y, z \right) \\
 (x, y, z) &\rightarrow \left( 1 - x, 1 - y, \frac{1}{2} + z \right).
 \end{aligned} \tag{4.2}$$

It is therefore possible to characterize the crystal structure of KTP using only 16 irreducible atoms (two formula units of  $\text{KTiOPO}_4$ ), with the rest being given by the application of 4.2. Ti, P and O within a KTP unit cell are arranged into  $\text{TiO}_6$  octahedra and  $\text{PO}_4$  tetrahedra, linked by a mutual O atom. These polyhedra form alternating  $\text{TiO}_6\text{--PO}_4$  chains along the [100] and [010] direction, with the orientation of the polyhedra chains alternating along [001]. Along [011] and [011], KTP consists of helical  $\text{TiO}_6$  octahedra chains. Within  $\text{TiO}_6$ , the bond lengths between Ti and O are not identical. In particular, the formation of a very short  $\text{Ti=O}$  double bond (1.716 Å) and a very long  $\text{Ti--O}$  single bond (1.733 Å) are observed [172], slightly distorting the  $\text{TiO}_6$  octahedra, see Fig. 4.2. The cavities between the polyhedra strands are occupied by K ions at two nonequivalent positions, being 8- and 9-fold coordinated with respect to O. The K ions are thereby positively charged and only weakly bound to its surrounding  $\text{TiO}_6$  and  $\text{PO}_4$  polyhedra, giving rise to its overall large ionic mobility. Along the polar [001] direction, this mobility is thereby four orders of magnitude larger compared to [100] and [010] [168].

The 10 oxygen and each two K, Ti and P atoms within an irreducible KTP unit are usually subdivided into categories according to their respective coordination. In the case of K, the notation K(1) and K(2) type refer to ions of 8- and 9-fold coordination, respectively. For O, two possible coordinations exist, either bridging Ti and P or bridging two Ti atoms. The 8 O atoms of the former group are typically labeled O(1)–O(8), while the latter two O atoms are labeled O(9) and O(10). P and Ti can be classified according to the orientation of the respective polyhedra strand they build up: P(1) and Ti(1) refer to an orientation along [010], while P(2) and Ti(2) refer to [100]. In the case of Ti, another way of classification is thereby possible: If O atoms of type O(9) and O(10) within a  $\text{TiO}_6$  octahedron enclose a 90° angle with the central Ti atom, it is considered of Ti(1) type, otherwise, for a 180° angle, of Ti(2) type.

The relatively large nonlinear optical coefficients of KTP, ranging from  $d_{15} = 2.04 \text{ pm/V}$  to  $d_{33} = 18.5 \text{ pm/V}$  [173], were initially believed to arise mainly from the short  $\text{Ti--O}$  bond within the  $\text{TiO}_6$  octahedra [170]. However, the discovery of KTA possessing an overall even better nonlinear response put this assumption into question, since the bond distortion in  $\text{TiO}_6$  is present in both isomorphs [174, 175]. Consequently, P(As)–O and K–O bonds were found to be the main contribution to the optical nonlinearity in KTP (KTA) [175].

<sup>1</sup>Reduced coordinates  $(x_d, y_d, z_d)$  thereby refer to coordinates as multiples of the three lattice vectors  $\{\mathbf{a}_i\}$ . Cartesian coordinates  $(x_c, y_c, z_c)$  are obtained from the reduced ones via  $(x_c, y_c, z_c) = x_d \cdot \mathbf{a}_x + y_d \cdot \mathbf{a}_y + z_d \cdot \mathbf{a}_z$ .

### 4.3.2 Curie temperature and crystal growth

The internal polarization of KTP amounts to  $20.1 \mu\text{C}/\text{cm}^2$  [5, 176] and is oriented along the [001] direction. The microscopic origin of the internal polarization is thereby the displacement of Ti, P and K with respect to the O sublattice, which was determined by Bierlein and Arweiler using a simple point-charge model [177]. KTP was shown to undergo a phase transition into a higher-symmetry paraelectric phase with space group *Pnna* [178, 179]. The nature of this transition was originally believed to be purely displacive [180]. However, newer studies hinted towards a mixture between order-disorder and displacive type [181]. The displacive component involves a continuous displacement of the Ti atoms within  $\text{TiO}_6$  along the [001] direction, giving rise to the previously discussed short and long Ti–O bonds within the ferroelectric phase. The order-disorder component, on the other hand, involves the site splitting of the K sublattice [182]. Within the ferroelectric *Pna*<sub>2</sub><sub>1</sub> phase, each site K(1) and K(2) features a respective split site K(1)s and K(2)s, shifted along the polar [001] direction. At room temperature, the statistical occupation of these split sites amounts to around 10 %. However, within the paraelectric *Pnna* phase, K(1)s and K(2) (as well as K(2)s and K(1)) become crystallographically equivalent, giving rise to an equal distribution of K among all sites, effectively averaging out a statistical variation of displacements along [001]. While the Curie temperature was known to be relatively high ( $>800^\circ\text{C}$ ), the precise value of  $T_C$  has been reported with a considerable amount of scattering, ranging from  $892^\circ\text{C}$  to  $959^\circ\text{C}$ , depending on the utilized experimental technique [183]. It was shown by Angert *et al.* that  $T_C$  strongly depends on the KTP growth conditions [183, 184] and therefore reflects the challenging means to grow KTP in the first place.

At  $1172^\circ\text{C}$ , KTP melts incongruently, decomposing into liquid  $\text{KPO}_3$  and solid  $\text{TiO}_2$  [185]. Since the solid and melt thus contain different compositions, it is not possible to grow KTP using standard melt techniques, e.g., the Czochralski method. Instead, two different methods for growing KTP out of solutions are employed:

- Flux method: KTP crystalizes out of a KTP/flux solution at elevated temperatures and under atmospheric pressure. As fluxes, numerous compositions can be used, including phosphatic systems ( $\text{K}_4\text{P}_2\text{O}_7$ ,  $\text{K}_8\text{P}_6\text{O}_{19}$ , etc.), tungstates or halides [168]. Since congruent crystallization takes place only for very slow cooling rates of the solution, the overall growth process can take up to several months, depending on the desired size and quality of the crystal.
- Hydrothermal growth: An aqueous mixture containing titania and potassium phosphate is placed in a tube at high pressure with a temperature gradient between its ends and a seed crystal at the cooler side, enabling a slow crystallization.

Coming back to the dependence of the Curie temperature on the growth conditions, it was shown that  $T_C$  for flux grown KTP is proportional not only to the KTP concentration within the solution, but also to the K/P ration within the solvent [183, 184].

## 4.4 Polar Surfaces

Splitting a ferroelectric crystal perpendicular to the direction of internal polarization, two surfaces are created. Due to the presence of microscopic dipole moments between two

subsequent layers of the ferroelectric, these two surfaces are, in general, structurally as well as electronically not equivalent, i.e., both surfaces differ with respect to their polarity. In order to stabilize both surfaces, a depolarization field opposite to the internal polarization is built up, accompanied by a number of reconstruction mechanisms of the surface layers. The surface morphology as well as stoichiometry are thereby subject to change due to adsorption and desorption processes [186]. Theoretical modeling of a polar surface can, in principle, be

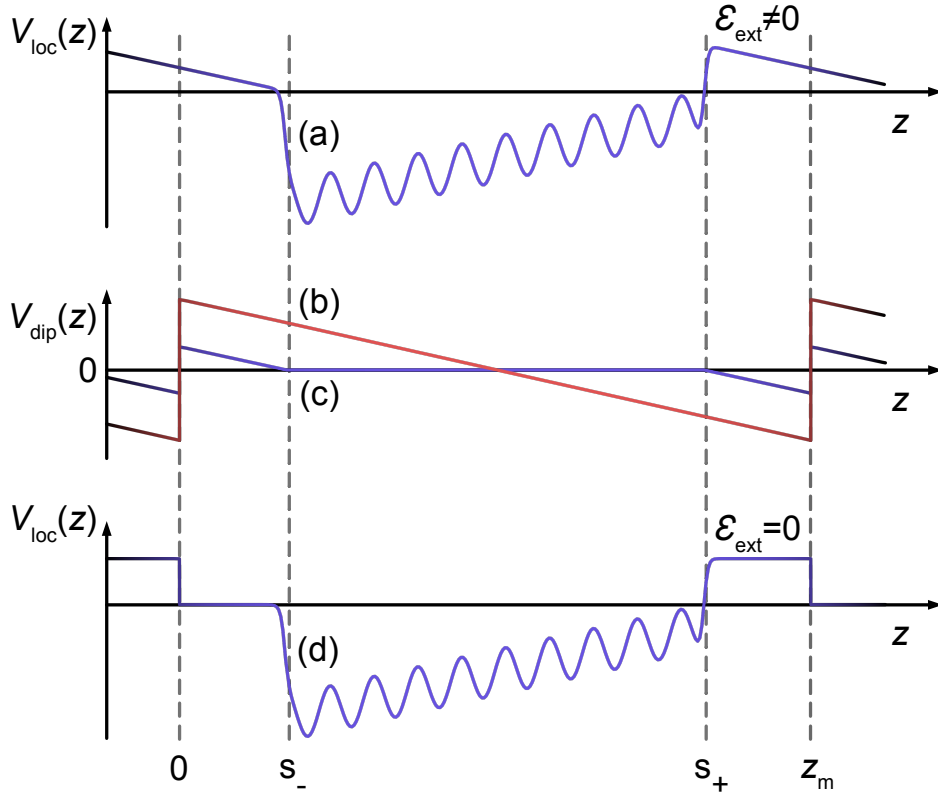


**Figure 4.4:** Schematic illustration of the plane averaged local potential  $V_{\text{loc}}(z)$  along the surface normal of a polar surface within a supercell of height  $z_m$  (a) before and (d) after the inclusion of a linear dipole correction  $V_{\text{dip}}(z)$ . The shape of  $V_{\text{dip}}(z)$  before and after self-consistent determination of the slab's charge density is depicted in (b) and (c), respectively. Within the vacuum region, inclusion of  $V_{\text{dip}}(z)$  leads to a perfect cancellation of the external electric field  $\mathcal{E}_{\text{ext}}$ . The position of the slab's outermost layers are indicated by  $s_{\pm}$ .

performed in a similar fashion to nonpolar surfaces using periodic boundary conditions. The surface is thereby built up in a slab geometry, consisting of several layers of the respective bulk material along the surface normal. In the following, this surface normal is assumed to be parallel to the  $z$  direction. Perpendicular to  $z$ , the material is left periodic according to the point group within the bulk, with a surface area of  $A$ . Along  $z$ , interaction between periodic images of the slab is prevented by including a vacuum region above the surface layer. If the end facets of the slab are not equivalent, the electrostatic interaction between them results in a spurious electric field  $\mathcal{E}_{\text{ext}}(z)$  within the vacuum region, given by a constant

slope in the plane averaged local electrostatic potential

$$V_{\text{loc}}(z) = \frac{1}{A} \int_A V_{\text{loc}}(\mathbf{r}) dx dy \quad (4.3)$$

along the  $z$  direction, see Fig. 4.4, (a). The total local potential  $V_{\text{loc}}(\mathbf{r})$  is thereby composed of

$$V_{\text{loc}}(\mathbf{r}) = V_{\text{ion}}(\mathbf{r}) + \int \frac{\rho(\mathbf{r}')}{|\mathbf{r}' - \mathbf{r}|} d\mathbf{r}' + V_{\text{xc}}(\mathbf{r}), \quad (4.4)$$

with the three contributions corresponding to the ionic potential, the Hartree potential and the local part of the XC potential, respectively. The external field originates from both end facets being differently terminated and, in the worst case, may result in a drift of electrons from one end facet to the other. Correction schemes to account for this effect have first been proposed by Neugebauer and Scheffler in 1992 [187]. The principle idea was later adopted and refined in a number of different publications [188–191]. Essentially, this dipole correction scheme entails including a constant electric field to the local potential along the  $z$  direction within the entire unit cell, see Fig. 4.4 (b). This electric field is modeled by a dipole potential  $V_{\text{dip}}(x)$  with constant slope, which, in order to satisfy periodic boundary conditions, features a jump within the vacuum region. This jump has practically no effect on the electronic states of the slab, because the wave functions decay exponentially outside the slab and should therefore ideally drop to zero in the vacuum region between the two end facets. If the supercell is considered to have a height of  $z_m$ ,  $V_{\text{dip}}(x)$  is given by [191]

$$V_{\text{dip}}(z) = -4\pi e m \left( \frac{z}{z_m} - \frac{1}{2} \right), \quad \text{where } z \in [0, z_m], \quad (4.5)$$

with the electron charge  $e$  and the surface dipole density

$$m = \int_0^{z_m} \rho(z') z' dz'. \quad (4.6)$$

Because  $m$  depends on the charge density of the system  $\rho(z)$ ,  $V_{\text{dip}}(z)$  is intrinsically a functional of  $\rho(z)$ . In the context of DFT calculations,  $V_{\text{dip}}(z)$  along with all other contributions to the total potential have therefore been determined self-consistently on the basis of  $\rho(z)$ . Iterating the dipole potential results in a separation of charge within the slab, leading to a screening of  $V_{\text{dip}}(z)$ , akin to the screening of an electric field within a metal (see Fig. 4.4 (c)). Within the vacuum region, the electric field induced by  $V_{\text{dip}}(z)$  prevails, cancelling  $\mathcal{E}_{\text{ext}}$ , see Fig. 4.4 (d).

Correcting the local potential this way has a number of implications. First, the total energy of the system is altered and now reads [191]

$$E_{\text{tot}} = E_{\text{tot}}^0 + \frac{2\pi A}{z_m} m^2, \quad (4.7)$$

where  $E_{\text{tot}}^0$  denotes the total energy without dipole corrections and  $A$  the surface area. Ionic forces are modified as well and take the form

$$\mathbf{F}_i = \mathbf{F}_i^0 - \frac{4\pi e Z_i}{z_m} m \cdot \mathbf{e}_z. \quad (4.8)$$

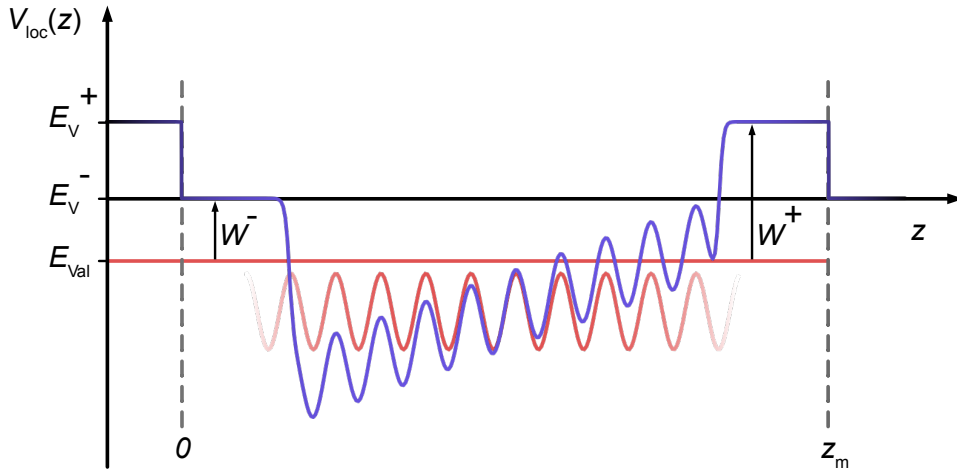


**Figure 4.5:** Planar averaged local potential  $V_{\text{loc}}(z)$  of a polar crystal along the polar axis within bulk (red) as well as within a dipole-corrected slab geometry (blue). The position of the valence band within the bulk material  $E_{\text{val}}$  as well as the vacuum levels of the positive and negative surface  $E_V^\pm$  determine the respective (nonequivalent) work functions  $W^+$  and  $W^-$ .

Again,  $F_i^0$  corresponds the force acting on the ion with label  $i$  without dipole corrections, with  $Z_i$  denoting its charge and  $\mathbf{e}_z$  the unit vector along the  $z$  direction.

Another consequence of introducing dipole corrections originates from the fact that vacuum levels  $E_V^\pm$  of both end facets (i.e., a constant level of  $V_{\text{loc}}(z)$  within the vacuum region) become well defined, allowing the assessment of surface related electronic quantities of each end facet individually. One of these quantities is the change in the surface dipole moment  $\Delta\phi_{\text{Dip}}$  as a consequence of the reconstruction of the surface. This relative change with respect to a reference surface is given by the difference between their vacuum levels. Dipole corrections additionally enable the evaluation of the work function  $W$ , defined as the minimal energy required to move an electron from a surface into the vacuum, infinitely far away from the surface. For an undoped insulator,  $W$  may be expressed as the energy difference between the highest valence state  $E_{\text{val}}$  within the bulk structure and the vacuum level [192]. Taking the center region of the slab as a reference, the local potentials of bulk and slab may be aligned (see Fig. 4.5) to determine the position of  $E_{\text{val}}$  with respect to the vacuum levels. The work functions of both surfaces thus read

$$W^+ = E_V^+ - E_{\text{val}} \quad \text{and} \quad W^- = E_V^- - E_{\text{val}}. \quad (4.9)$$

Given the previous definition of the induced surface dipole moment,  $W$  and  $\Delta\phi_{\text{Dip}}$  are not independent, but rather show a linear dependence  $W \sim \Delta\phi_{\text{Dip}}$ .

# 5

## Spectroscopic Signatures of KTP and Related Materials

In order to investigate the atomic origins of spectroscopic signatures of KTP, RTP and KTA, the methodologies introduced in Chapters 2 and 3 will be applied to all three materials on various levels of theory. The influence of quasiparticle and excitonic effects on their respective dielectric function  $\epsilon(\omega)$  shall be systematically investigated and discussed. Likewise, the respective phonon spectra and Raman cross sections shall, for the first time, be determined in a non-phenomenological way, giving insights into the atomic and vibrational origin to the most prominent Raman peaks.

This chapter is structured as following: In the first section, the focus lies on the investigation of electronic and optical properties of bulk KTP. The general methodology and computational parameters are introduced, followed by the results and discussion of structural parameters, the band structure and the dielectric function on various levels of theory. The basic characteristics of electronic states are discussed on the basis of the fundamental band gap and the orbital character of the valence band maximum (VBM) and conduction band minimum (CBM). In the second section, these results are compared to those of the related materials RTP and KTA. In particular, the difference in the onset of optical absorption is discussed with respect to the involved constituents and compared to experimental results. In the third section, the results regarding Raman cross sections of KTP, RTP and KTA are presented and discussed with respect to experimental spectra.

Parts of the results within this chapter have already been published, see Ref. [171] and [193].

### 5.1 Band Structure and Dielectric Function of KTP

#### 5.1.1 Methodology

In order to determine the ground-state properties of KTP, DFT calculations are performed using version 5.4.4 of the commercially available VIENNA AB INITIO SIMULATION PACKAGE (VASP) [194]. Being a plane-wave code, all electronic wave functions  $\phi_{n,k}(\mathbf{r})$  are thereby

expanded into a plane-wave basis set according to

$$\phi_{n,k}(\mathbf{r}) = \frac{1}{\sqrt{V}} \sum_{\mathbf{G}} c_{n,k}(\mathbf{G}) e^{i(\mathbf{k} + \mathbf{G}) \cdot \mathbf{r}}, \quad (5.1)$$

where  $c_{n,k}(\mathbf{G}) = \int \phi_{n,k}(\mathbf{r}') e^{-i(\mathbf{k} + \mathbf{G}) \cdot \mathbf{r}'} d\mathbf{r}'$ .

The number of plane waves is truncated using a single parameter, the energy cutoff  $E_{\text{cut}}$ , according to the condition that only plane waves with kinetic energy lower than  $E_{\text{cut}}$  are included in the basis set, i.e.,

$$\frac{\hbar^2 |\mathbf{k} + \mathbf{G}|^2}{2m} < E_{\text{cut}}. \quad (5.2)$$

An energy cutoff of 500 eV is used. This value was tested with respect to the convergence of the fundamental band gap of KTP at the  $\Gamma$  point and leads to an error below 10 meV. The same criterion is utilized to test the  $\mathbf{k}$ -point mesh used to sample the Brillouin zone. A regular,  $\Gamma$ -centered  $2 \times 4 \times 2$  mesh is thereby found to be sufficiently large.

Electronic exchange and correlation effects are taken into account using the GGA, as parametrized within the PBEsol functional, see Sec. 2.1.4. Additionally, the projector-augmented-wave (PAW) method is used to account for electron-ion interaction [195]. Regarding the individual constituents of KTP, only a subset of electrons of each atomic species are treated as valence electrons, with the rest being frozen and accounted for within the pseudopotential formalism. In addition to all open shells,  $\text{K}_{3p}$ ,  $\text{Ti}_{4s}$ ,  $\text{P}_{3s}$  and  $\text{O}_{2s}$  orbitals are thereby considered valence states.

In the first step, the ground-state geometry, band structure and dielectric function of KTP are determined on the level of standard DFT. To this end, ions as well as lattice constants are structurally relaxed until the maximum force acting on each atom falls below a threshold of 0.01 eV/Å. Using the ground-state geometry, electronic eigenvalues are extracted along the path  $\Gamma \rightarrow \text{Y} \rightarrow \text{T} \rightarrow \text{Z} \rightarrow \Gamma$ , see Fig. 5.1. On the basis of the band structure, the dielectric function is determined using the IPA (see Sec. 3.1.1).

In the second step, QP effects on the band structure as well as the dielectric function are investigated. To this end, the self-energy operator  $\Sigma(\mathbf{r}, \mathbf{r}'; \omega)$ , as introduced in Sec. 2.2, is determined using the  $G_0W_0$  approximation from the convolution of the single-particle

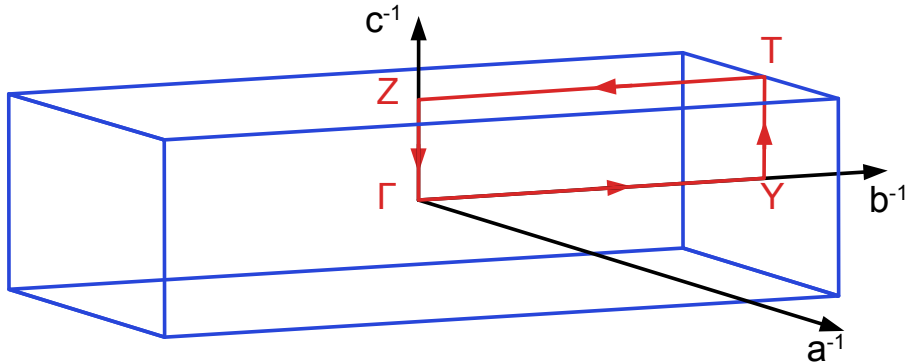


**Figure 5.1:** Outline of the first Brillouin zone of KTP along with high-symmetry points. The  $\mathbf{k}$ -point path used for the band-structure calculations is indicated by red arrows. Figure adapted from Ref. [171].

Green's function  $G$  and the screened Coulomb interaction  $W$ , as implemented by Shishkin and Kresse [196]. The QP shift for each single-particle energy eigenvalue obtained from the prior DFT calculation is subsequently calculated from  $\Sigma$  in a perturbative manner according to Eq. 2.74. The response function  $\chi^0$ , which directly enters the dielectric function  $\epsilon$  in Eq. 3.12 and indirectly the screened Coulomb interaction  $W$  via Eq. 2.63, is set up using an energy cutoff of 300 eV and a total of 1800 states. Again, this ensures numerical convergence of the quasiparticle energies better than 10 meV. The same  $2 \times 4 \times 2$   $k$ -point mesh, which was used to determine the electronic ground state within the previous DFT step, is used to evaluate the QP shifts within the  $GW$  calculation. Due to the large size of the KTP unit cell, this relatively low density thereby suffices for the direct band gap to converge within 10 meV. Finally, the dielectric function within the IQPA is obtained from the QP energies using Eq. 3.18.

The electron-hole interaction and local-field effects are taken into account in the third step by solving the BSE (see Sec. 3.2), using the QP energies and screened Coulomb interaction obtained from the previous  $GW$  calculation. In order to set up the BSE hamiltonian in Eq. 3.43, a total of 184 bands are used, subdivided into 64 valence and 120 conduction bands.

### 5.1.2 Structural Properties

Within DFT-PBESol, the lattice constants of KTP amount to  $a = 12.860 \text{ \AA}$ ,  $b = 6.432 \text{ \AA}$ , and  $c = 10.599 \text{ \AA}$ , which deviate by less than 0.4 % from the respective experimental X-ray diffraction data [167, 178, 197–200]. Regarding the lengths of the longest Ti–O single and shortest Ti=O double bond, values of  $2.12 \text{ \AA}$  and  $1.78 \text{ \AA}$  are obtained, respectively, with a mean Ti–O bond length of  $1.97 \text{ \AA}$ . These values are in good agreement with respective measured bond lengths of  $2.15 \text{ \AA}$ ,  $1.72 \text{ \AA}$  and  $1.97 \text{ \AA}$  [178]. In Tab. 5.1, the reduced coordinates of the 16 non-symmetry-equivalent atoms within a KTP unit are compiled along with their deviations from experimental values [172]. PBESol is found to yield atomic coordinates very close to those found by the experiment, with an average deviation of  $1.6 \cdot 10^{-3}$  and a maximum deviation of  $10^{-2}$ . For comparison, KTP lattice constants within PBE are found to overestimate the experimental ones by as much as 1.5 %, with the average and maximum deviation in atomic coordinates amounting to  $2 \cdot 10^{-3}$  and  $10^{-2}$ , respectively. Within LDA, the situation additionally worsens, with an underestimation in lattice constants up to 1.9 % and deviations in atomic coordinates similar to PBE.

### 5.1.3 Electronic Properties

The electronic band structure of KTP is calculated along the path shown in Fig. 5.1 using the relaxed ground-state structure. In Fig. 5.2 (lhs), the band structure on the DFT level is depicted.

The obtained band gap of KTP amounts to 2.97 eV, which is in close agreement with earlier theoretical studies by Lowther *et al.* [201]. While the CBM is located at the  $\Gamma$  point, the highest occupied state at  $\Gamma$  lies marginally below the VBM at the T point, separated by 28 meV, rendering the band gap slightly indirect. A minor increase of the band gap to 3.1 eV is found upon treating the  $\text{Ti}_{3p}$  orbitals as valence states (mandating an increase of the energy cutoff to 800 eV). This effect, however, is neglected in the following, as an in-

**Table 5.1:** Reduced coordinates of non-symmetry-equivalent atoms of KTP as obtained within DFT-PBEsol. The deviation with respect to single-crystal X-ray diffraction (XRD) data [172] is given in brackets. Coordinates  $x$ ,  $y$ , and  $z$  are assumed to be aligned along the [100], [010], and [001] directions, respectively (see Fig. 4.3).

	Direction		
	$x$	$y$	$z$
K(1)	0.375 [-0.003]	0.779 [-0.002]	0.690 [+0.002]
K(2)	0.108 [+0.003]	0.699 [±0]	0.936 [+0.003]
Ti(1)	0.373 [±0]	0.500 [±0]	0.991 [-0.009]
Ti(2)	0.245 [-0.002]	0.260 [-0.01]	0.742 [-0.006]
P(1)	0.498 [±0]	0.339 [+0.003]	0.738 [-0.002]
P(2)	0.180 [-0.001]	0.504 [+0.002]	0.487 [±0]
O(1)	0.486 [±0]	0.489 [+0.002]	0.849 [-0.001]
O(2)	0.510 [±0]	0.467 [+0.001]	0.615 [-0.002]
O(3)	0.401 [+0.001]	0.199 [±0]	0.720 [-0.001]
O(4)	0.594 [+0.001]	0.196 [+0.003]	0.760 [+0.001]
O(5)	0.111 [-0.002]	0.314 [+0.003]	0.459 [±0]
O(6)	0.112 [+0.001]	0.696 [+0.004]	0.513 [+0.001]
O(7)	0.253 [±0]	0.538 [+0.002]	0.372 [±0]
O(8)	0.252 [-0.001]	0.465 [+0.003]	0.602 [+0.001]
O(9)	0.223 [-0.002]	0.966 [+0.001]	0.358 [+0.002]
O(10)	0.224 [+0.001]	0.051 [+0.01]	0.612 [+0.002]

crease of the cutoff energy by such an amount would render all subsequent GW calculations computationally unfeasible.

A number of experimental and theoretical studies have estimated the value of the fundamental band gap of KTP. Regarding the reported experimental values concluded from optical absorption, a considerable spread can be made out, ranging from 3.2 eV to 3.8 eV [200, 202–205]. An even larger spread is found for values predicted from DFT calculations. Depending on the choice of the XC functional, band gaps between 3.0 eV and 4.0 eV are reported [200, 201, 206, 207]. The largest reported value of 4.9 eV stems from an early empirical tight-binding calculation [208]. In this context, a band gap of 2.97 eV, as obtained in the present study, evidently underestimates the reported experimental estimations. However, the measured values must be taken with caution, as they are concluded from optical absorption spectra and therefore substantially affected by excitonic effects. The seemingly good overlap between the measured and calculated band gaps in literature may thus result from an error cancellation between excitonic binding energy (experiment) and neglected electronic self energy (DFT).

The orbital characters of all bands can be analyzed using the orbital-decomposed (or

partial) density of states (PDOS), as shown in Fig. 5.2. The single-particle wave functions of each state are thereby projected onto atomic orbitals of the involved atoms, with the value of this projection governing the contribution of each state to the PDOS. For the largest part, valence and conduction bands are formed by  $O_{2p}$  and  $Ti_{3d}$  orbitals, respectively, which is also evident from the charge density of the VBM and CBM depicted in Fig. 5.3. Low energy optical absorption in KTP can therefore be considered to arise mainly from transitions between  $O_{2p}$  and  $Ti_{3d}$ , not involving P and K. In the past, spin-orbit coupling (SOC) has been shown to induce a momentum-dependent splitting of spin bands (Rashba effect) not only for surfaces and interfaces, but also for non-centrosymmetric bulk semiconductors, e.g., BiTeI [209]. It is therefore possible for the combined effect of SOC and the Coulomb-potential asymmetry related to the ferroelectricity in KTP to induce a similar splitting, reducing the band gap and creating a Rashba-like spin texture of the electronic structure. For this reason, the influence of SOC on the band gap is explored using the VASP implementation [210]. Within the valence and conduction bands, a SOC induced splitting is observed only for states close to the T point, amounting to 7 and 8 meV. Additionally, the size as well as the character of the band gap are unaffected, with the VBM and the CBM remaining at the T and  $\Gamma$  point, respectively. For KTP, the influence of SOC can thus be considered negligible.

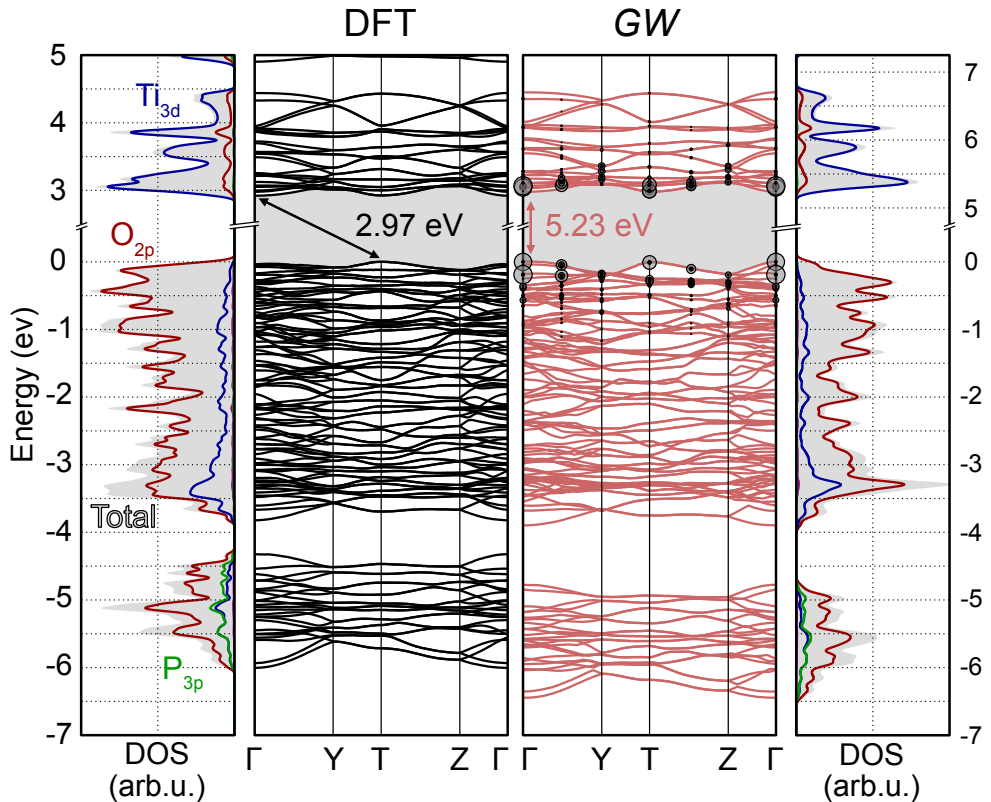


**Figure 5.2:** KTP band structures and PDOS as calculated within DFT-PBEsol (lhs) and *GW* (rhs). Energies of all states refer to the respective VBM. Relative contributions of transitions between valence and conduction bands to the first bright exciton at 4 eV are marked by circles in the *GW* band structure. The radii of the circles thereby indicate the contribution  $A_{\lambda}^{ck, vk}$  of the electron-hole pair at that  $k$  point to the excitonic wave function, see Eq. 3.39. Figure adapted from Ref. [171].

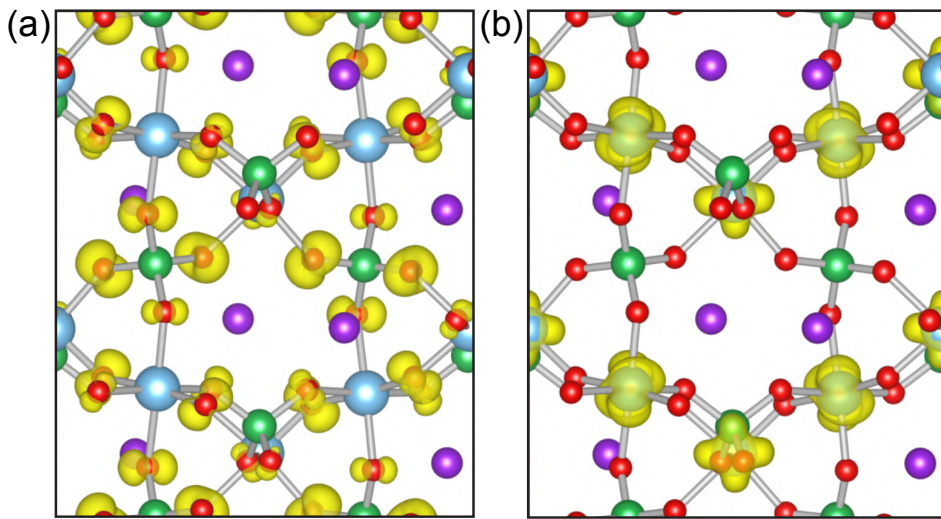


**Figure 5.3:** Calculated orbital character of (a) the VBM and (b) the CBM in KTP. Color coding follows Fig. 4.3. Figure adapted from Ref. [171].

As stated in Sec. 2.1.6, the fundamental band gap is usually underestimated within standard DFT Kohn-Sham theory. In order to correct this underestimation,  $GW$  quasiparticle calculations are performed. The QP shifts  $\epsilon_i^{\text{QP}} - \epsilon_i^{\text{DFT}}$  for each Kohn-Sham state  $i$  as a function of  $\epsilon_i^{\text{DFT}}$  are depicted in Fig. 5.4. As expected, valence and conduction states experience a negative and positive shift, respectively. This leads to an increased separation between VBM and CBM and thus to a widening of the band gap. Additionally, the magnitude of the QP shift tends to be larger for more localized orbitals ( $\text{Ti}_{3d}$  and  $\text{K}_{3p}$ ). Qualitatively, this can be understood from the self-energy operator  $\Sigma$  correcting the previously discussed spurious self-interaction of an electron with itself: An electron within an orbital of limited spatial spread experiences larger confinement and self-interaction, resulting in a larger QP shift within  $GW$ . A comparison between QP shifts of individual  $\mathbf{k}$  points (gray dots in 5.4) and their average value (red dots) additionally indicates that the QP shift depends much more on the orbital character of a state than the respective  $\mathbf{k}$  point. For  $\text{O}_{2p}$  and  $\text{Ti}_{3d}$  states around the fundamental gap, the spread in shifts amounts to around 0.2 eV and 0.05 eV, respectively (see inset in Fig. 5.4). For this reason, the QP shifts for each  $\mathbf{k}$  point along the path in Fig. 5.1 are determined using linear interpolation between  $\mathbf{k}$  points of the used  $2 \times 4 \times 2$  grid and subsequently added to the Kohn-Sham states to acquire the band structure within the  $GW$  approximation in Fig. 5.2 (rhs).

Unsurprisingly, valence and conduction states are shifted essentially dispersionless to lower and higher energies, respectively. For all states close to the band gap, the respective shifts amount to  $-0.6$  eV and  $1.7$  eV, resulting in a widening of the electronic band gap to  $5.23$  eV. In addition, the VBM is observed to switch from  $\text{T}$  to  $\Gamma$ , being  $8$  meV above the highest occupied state at  $\text{T}$ . Since all states are assumed to have equal orbital character in DFT and  $GW$ , no significant change in the shape of the PDOS is found. The obtained band gap value of  $5.23$  eV is expected to represent a lower bound to the transport gap of the real system, as (i) self-consistent  $GW$  calculations have frequently reported to yield larger QP gaps compared to those from  $G_0W_0$  [211, 212] and (ii) the inclusion of  $\text{Ti}_{3p}$  orbitals as valence states is expected to further increase the gap.

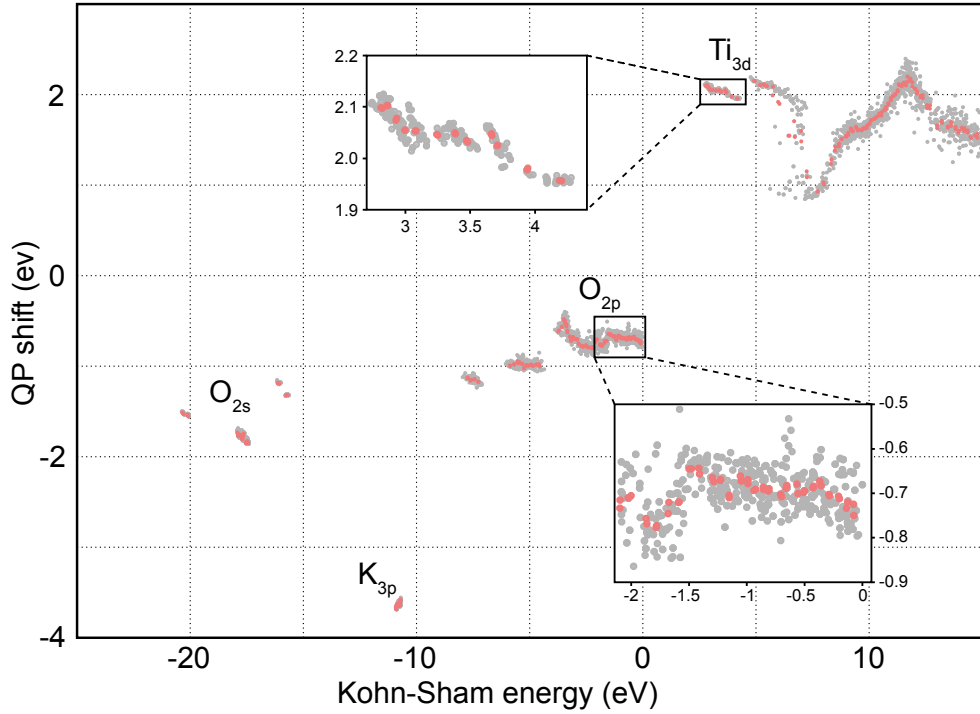


**Figure 5.4:** QP shifts of Kohn-Sham states in KTP. Gray dots refer to states located at individual  $\mathbf{k}$  points of the  $2 \times 4 \times 2$  grid, while red dots indicate the average over all  $\mathbf{k}$  points. Text refers to the orbital character of each group of states.

### 5.1.4 Linear Optical Properties

The frequency-dependent dielectric function on the IPA and IQPA levels of theory is calculated from the electronic structure obtained from the previous DFT-PBEsol and *GW* calculations. In Fig. 5.5 (lhs), the imaginary parts of the diagonal components  $(x,x)$ ,  $(y,y)$  and  $(z,z)$  are depicted. A polarization-dependent modulation in lineshape of the optical absorption onset is observed. In the low energy regime (below 4 eV on the IPA level), two distinct peaks can be identified in the imaginary parts of  $\epsilon_{xx}$  and  $\epsilon_{zz}$  (labeled  $p_1$  and  $p_2$ ), while a weak shoulder and only one pronounced peak characterize  $\epsilon_{yy}$ . In addition, a peak of relatively low intensity at 6 eV (labeled  $p_3$ ) can be observed within all three polarizations. In order to determine the origin of the three peaks  $p_1$ – $p_3$ , oscillator strengths of each transition between valence and conduction states (i.e., momentum matrix elements in Eq. 3.18) are analyzed. In Fig. 5.5 (rhs), oscillator strengths of transitions below 7 eV are color coded within the DFT band structure. Thereby, the strength in red coloring of a valence state is proportional to the accumulated oscillator strengths of transitions into every conduction band (color coding of conduction bands is defined in a similar manner). Evidently, optical absorption is governed by transitions from  $O_{2p}$  states up to 1 eV below the VBM into  $Ti_{3d}$  states up to 6 eV above the CBM. In particular, the absorption onset leading to  $p_1$  originates from transitions between states close to the VBM and CBM. Transitions from states within about 1 eV below the VBM to the CBM, and states about 2 eV above the CBM give rise to the  $p_2$  and  $p_3$  peak, respectively. The strong optical anisotropy of KTP can thus be related to the particular geometry of the  $TiO_6$  octahedra, which lifts the degeneracy of the  $O_{2p}$  states.

To test this assumption, the octahedra are symmetrized by enforcing an additional trans-

lational symmetry along the [100] direction, allowing for a bisection of the KTP lattice constant  $a$ , see Fig. 5.6. The artificial, partially symmetrized KTP cell obtained in this manner is tetragonal, with identical lattice constants  $a$  and  $b$ . This more symmetric configuration indeed results in (i) a vanishing splitting between the  $p_1$  and  $p_2$  peaks within all three diagonal components and (ii) the dielectric function of the  $(x,x)$  and  $(y,y)$  polarization to become identical (see dashed lines in Fig. 5.5). However, the anisotropy between  $(x,x)/(y,y)$  and  $(z,z)$  polarization remains, as the density of  $\text{TiO}_6$  octahedra along the respective directions differs. Similar observations were made earlier for bismuth titanate ( $\text{Bi}_4\text{Ti}_3\text{O}_{12}$ ) [213].

The calculated IPA spectra can be directly compared to previous results on the same level of theory [200, 207]. Both studies report DFT calculations within the GGA using the relativistic full-potential linearized augmented-plane-wave method (FP-LAPW), but arrive at somewhat different results: Reshak *et al.* [200], utilizing the Engel-Vosko GGA functional [214], find a sharply peaked absorption onset, which is followed by a weak shoulder and a minor peak for  $\epsilon_{xx}/\epsilon_{yy}$  and  $\epsilon_{zz}$ , respectively. In contrast, the more recent calculations by Ghoohestani *et al.*, utilizing PBEsol and a modified Becke-Johnson functional [215], predict an absorption onset characterized by a minor shoulder followed by a major peak for  $\epsilon_{xx}$  and  $\epsilon_{zz}$ . In the case of  $\epsilon_{yy}$ , a single peak is predicted. The findings of Ghoohestani *et al.* are essentially reproduced by the present IPA calculations regarding the line shapes and peak positions as well as the relative peak heights.

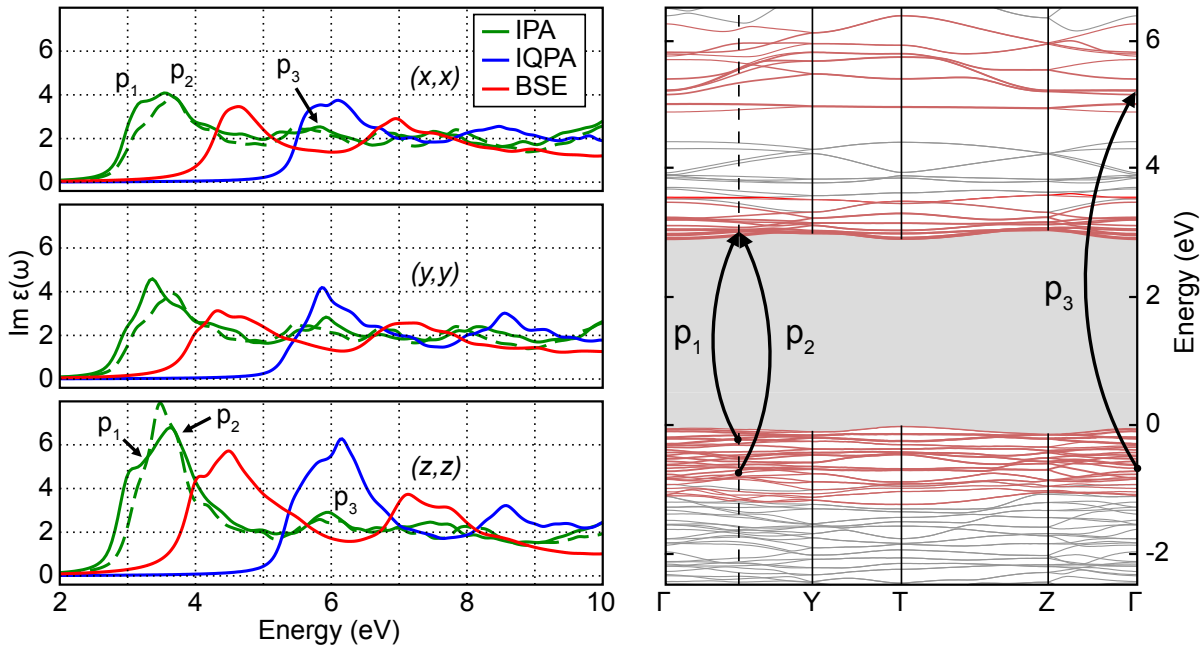


**Figure 5.5:** Left: Imaginary part of the diagonal components of the KTP dielectric function calculated on the level of IPA, IQPA and BSE. Dashed curves refer to the IPA spectra of an artificially symmetrized structure (see text). Right: Transition characteristics for optical absorption below 7 eV on IPA level. Transitions between red valence and conduction bands show largest oscillator strengths. Arrows additionally highlight single transitions with the highest contribution to the individual peaks  $p_1$ – $p_3$ . Figure adapted from Ref. [171].

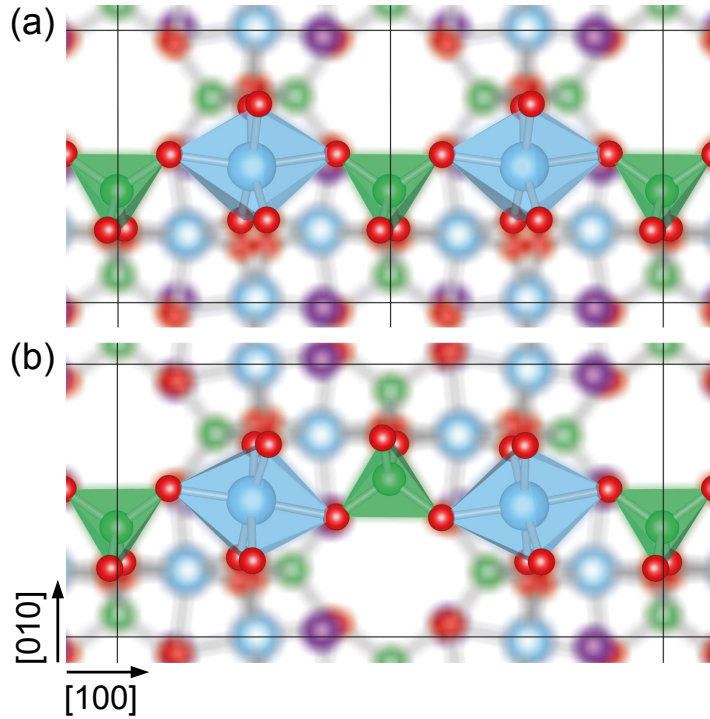


**Figure 5.6:** Atomic geometry of  $\text{TiO}_6\text{--PO}_4$  polyhedra strands (a) within an artificial, partially symmetrized structure of KTP with a tetragonal unit cell and (b) within orthorhombic bulk KTP. Color coding of the atoms follows Fig. 4.3. Unit cell boundaries are depicted in black. Figure adapted from Ref. [171].

The inclusion of quasiparticle effects within the IQPA leads to a spectral blueshift of all spectra by more than 2 eV, as shown by the blue lines in Fig. 5.5. Apart from the peak  $p_1$  losing intensity within  $(y,y)$  and  $(z,z)$  polarization, no overall modification of the lineshapes takes place.

A redshift by about 1.5 eV results from the inclusion of excitonic and local-field effects in the optical response upon solving the BSE, see the red lines in Fig. 5.5. Additionally, the  $p_2$  peak in  $(y,y)$  and  $(z,z)$  polarization sharpens again if excitonic effects are included. Evidently, electron-hole interaction partially compensates the quasiparticle effects in the KTP optical response. Using the definition of the two-particle excitonic wave function in Eq. 3.39, the localization in  $\mathbf{k}$  space of the energetically lowest absorption peak with significant oscillator strength (bright exciton) can be analyzed. The first bright exciton is thereby located at around 4 eV. In the  $GW$  band structure in Fig. 5.2, the coefficients  $A_{\lambda}^{ck,vk}$  are plotted as circles for each pair of valence and conduction state, with the respective radii being proportional to the absolute value  $|A_{\lambda}^{ck,vk}|$ . Apparently, the exciton is delocalized in  $\mathbf{k}$  space, with most of the excitonic weight centered at  $\Gamma$ . This, in turn, hints towards a strong localization of the exciton in real space, which is in good agreement with Ghoohestani *et al.* [216]: If the position of the hole is fixed at a  $\text{O}_{2p}$  orbital, the electron is located at the  $\text{Ti}_{3d}$  orbitals of the adjacent Ti atoms.

Experimental studies regarding the linear optical spectrum of KTP are very scarce. In Fig. 5.7 the measured average reflectivity reported by Reshak *et al.* [200] is compared with the average reflectivity obtained from the dielectric function (according to Eq. 3.21) calcu-

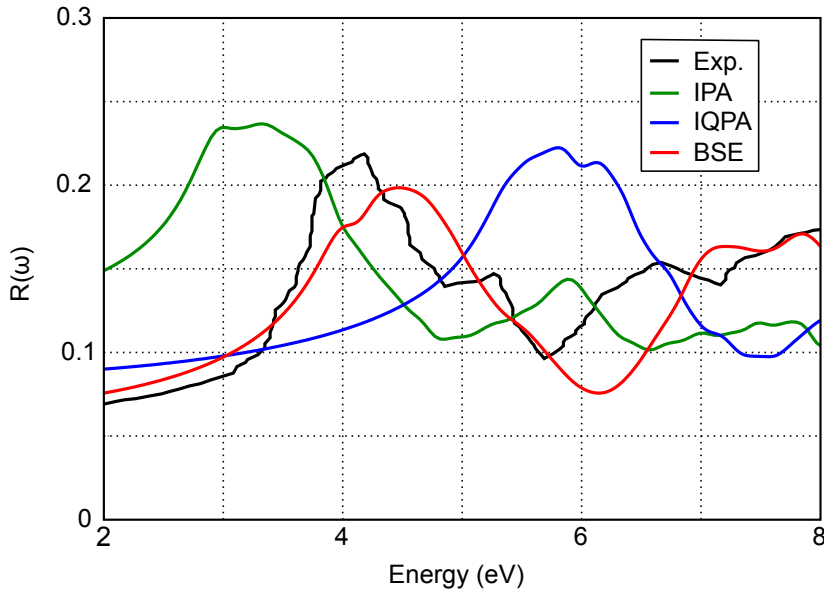


**Figure 5.7:** Average reflectivity (see Eq. 3.21) of KTP calculated on the IPA, IQPA and BSE levels of theory in comparison to experimental data (black line) [200]. Figure adapted from Ref. [171].

lated on the IPA, IQPA, and BSE levels of theory. Clearly, the reflectivity onset calculated within IPA drastically underestimates the experimental findings. This is evidence for the occurrence of large self-energy effects neglected in previous electronic-structure calculations for KTP. On the other hand, the reflectivity obtained from the quasiparticle band structure in the *GW* approximation overestimates the optical transition energies by more than 1 eV. Only the inclusion of electron-hole attraction effects within the BSE leads to a roughly correct alignment with the measured data on the energy axis. The comparison between experiment and theory in Fig. 5.7 thus clearly demonstrates the importance of many-body effects for the KTP excited-state properties.

It has to be said that the quantitative agreement between the measured reflectivity and the BSE calculations is clearly not perfect. The onset of the measured reflectivity is underestimated in magnitude and overestimated in energy. The second pronounced reflectivity peak measured at about 5.3 eV is visible only as a weak shoulder in the BSE spectrum. These deviations may be attributed to a number of reasons. For one, the present calculations neglect zero-point motion and thermal lattice vibrations that are known to lower optical transition energies and may partially explain the blueshift of the BSE spectrum in comparison to the measured data [211]. Moreover, KTP crystals grown by the traditional flux method, such as used in Ref. [200], solidify in a broad homogeneity range, which may not reflect the stoichiometric composition. In particular, the potassium and titanium content is known to deviate from bulk stoichiometry within a few atomic percent [7, 217]. The remaining discrepancies between experiment and theory may at least partially be related to point defects and stoichiometry deviations which were neglected in the present calculations. In fact, defect states are expected to redistribute oscillator strengths and are hence a plausible explanation for some deviations between the BSE results and experiments.

## 5.2 Comparison to KTA and RTP

In the next step, the effects of anion substitution on the electronic and linear optical properties of KTP are investigated. To this end, P and K are replaced by As and Rb, yielding bulk KTA and RTP, respectively. Band structures and dielectric functions of KTA and RTP are determined subsequently using the same general methodology and computational parameters as for KTP, described in Sec. 5.1.1. In particular, the PBEsol functional is utilized, along with identical cutoff energies (500 eV) and  $k$ -point densities ( $2 \times 4 \times 2$ ). In KTA and RTP,  $\text{As}_{4s}$  and  $\text{Rb}_{4p}$  orbitals are treated as valence states, respectively (in addition to all open shells).

Using these settings, the equilibrium lattice constants of RTP and KTA were found to be  $a = 12.986 \text{ \AA}$ ,  $b = 6.521 \text{ \AA}$ ,  $c = 10.568 \text{ \AA}$  and  $a = 13.181 \text{ \AA}$ ,  $b = 6.607 \text{ \AA}$ ,  $c = 10.791 \text{ \AA}$ , respectively. Similar to KTP, a maximum deviation of around 0.5 % compared to experimental values is found [7]. The mean Ti–O bond lengths in RTP and KTA amount to  $1.977 \text{ \AA}$  and  $1.973 \text{ \AA}$ , respectively, and compare favorably with respective measured values, amounting to  $1.979 \text{ \AA}$  and  $1.966 \text{ \AA}$  [178]. The mean bond length in KTP is almost identical ( $1.970 \text{ \AA}$ ). This indicates that an indirect influence of the different covalent radii of K/Rb and P/As on the  $\text{TiO}_6$  substructure via a change in lattice constants is almost negligible. A similar effect was found experimentally for pressure induced structural changes in KTP by Allan *et al.* [197]: Up to pressure values of 5 GPa, the biggest portion of cell volume reduction was compensated by a shrinkage of the K cages, while the remaining structural motifs ( $\text{PO}_4$  and  $\text{TiO}_6$  polyhedra) remain nearly unchanged in size and shape.

### 5.2.1 Band Structure

The electronic band structures of RTP and KTA on DFT and  $GW$  levels of theory are depicted in Fig. 5.8 (lhs) and (rhs), respectively. On the DFT level, the direct band gaps at  $\Gamma$  amount to 2.96 eV for RTP and 2.98 eV for KTA. The respective KTP band gap of 2.97 eV is very similar and falls in between these two values. This is a direct consequence of the nearly identical Ti–O bond lengths of all three materials, as the orbital character of valence- and conduction-band edges is dominated by  $\text{O}_{2p}$  and  $\text{Ti}_{3d}$  states in KTA, RTP and KTP (see the PDOS in Figs. 5.8 and 5.2). In the case of KTA, however, an additional small contribution of  $\text{As}_{4p}$  orbitals to the valence and conduction states can be made out in the PDOS. In a previous study on KTA, using full potential linearized augmented plane wave (FP-LAPW) calculations, Khyzhun *et al.* observed a similar contribution [218]. Its influence on the dielectric function is discussed in Sec. 5.2.2.

Self-energy effects are found to widen the band gap of RTP and KTA by more than 2 eV, yielding a respective quasiparticle band gap of 5.30 eV and 5.24 eV. These values, again, are very close to the quasiparticle gap in KTP (5.23 eV). On the DFT as well as  $GW$  level, the fundamental band gap in KTA is found to be direct at  $\Gamma$ . In RTP, however, the VBM experiences a shift from  $\Gamma$  to T if self-energy effects are included, while the CBM remains at  $\Gamma$ . The fundamental gap in RTP is thus rendered indirect within  $GW$ . Interestingly, this corresponds to the opposite ordering within KTP, where the VBM shifts from T to  $\Gamma$ . This suggests that close to the band edges, the band structure details of the KTP family materials depend more sensitively on the alkali-metal species than on the group-V atom.

The effect, however, is small, since the relative positions of the highest valence-band states at  $\Gamma$  and T differ by less than 20 meV. Additionally, the data should be interpreted

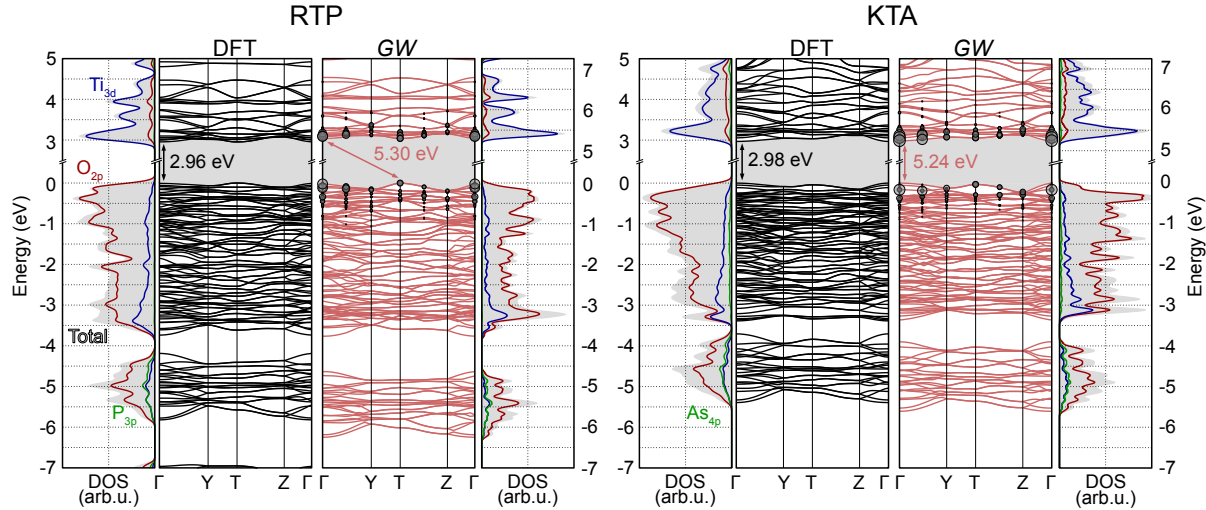


**Figure 5.8:** Comparison of the band structures and PDOS of RTP (lhs) and KTA (rhs) calculated on the DFT and *GW* levels of theory. Relative contributions of transitions between valence and conduction bands to the first optical absorption peak are indicated by circles within the *GW* band structure. The radii of the circles are proportional to the contribution of the electron-hole pair at the respective  $k$  point to the first excitonic wave function. Figure adapted from Ref. [193].

with caution, as the energy differences are below the numerical accuracy of the present calculations. While the quasiparticle corrections considerably widen the band gaps, the dispersion of the electron bands of all three KTP family materials is affected only slightly.

### 5.2.2 Dielectric Function

The differences in the orbital character of valence and conduction states as well as the fundamental band gap are expected to alter the dielectric functions of RTP and KTA with respect to KTP. Their respective imaginary parts for the diagonal polarization configurations  $(x,x)$ ,  $(y,y)$ , and  $(z,z)$  on the IPA, IQPA, and BSE levels of theory are depicted in Fig. 5.9. For comparison, the IPA and BSE spectra of KTP are included as well. In general, the observations within KTP regarding the overall shift of absorption onsets after the inclusion of quasiparticle and excitonic effects also hold for RTP and KTA: Large quasiparticle shifts, equal to the *GW* quasiparticle shifts, cause a spectral blueshift of all spectra and are partially compensated by large excitonic binding energies, redshifting the spectra by about 1 eV.

In particular, the lineshapes of RTP and KTP are nearly identical in the low energy region, with a slightly higher absorption onset in the case of RTP. As expected from the quasiparticle gaps of all three materials, the occupation of the alkali sites effects the dielectric function onset only weakly. To estimate the total shift in the onset induced by K (Rb) vacancies, the dielectric function is calculated for an artificial structure of KTA (RTP), in which all K (Rb) atoms are removed. On the IPA level, all polarization configurations experience a blueshift of 0.12 eV – 0.19 eV with respect to the bulk spectra. This blueshift additionally reduces to 0.07 eV – 0.1 eV on the BSE level. For defect densities of up to 10% [220], the influence of K and Rb defects on the low energy regime of the dielectric function can thus be considered negligible.

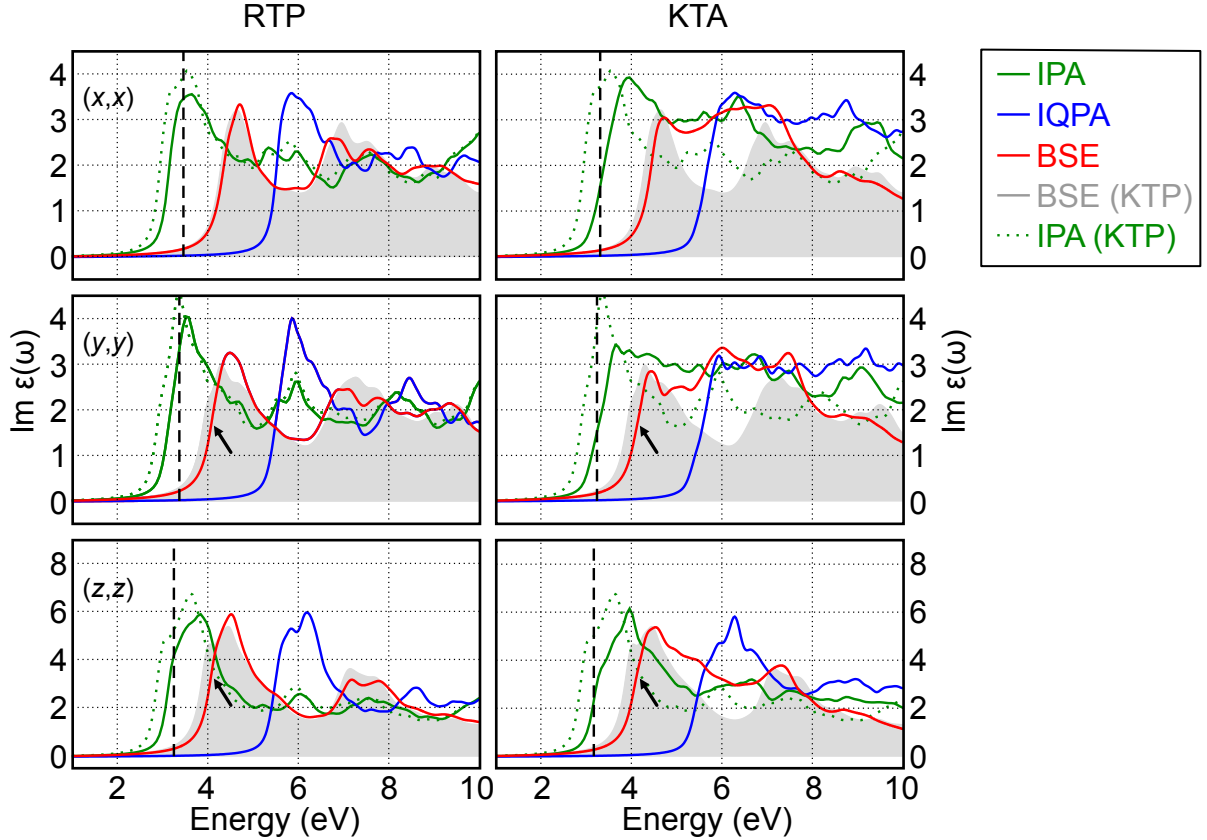


**Figure 5.9:** Dielectric functions of RTP (lhs) and KTA (rhs) calculated on the IPA, IQPA, and BSE levels of theory. For comparison, the results for KTP (see Fig. 5.5) are additionally included. The first bright exciton of both systems corresponds to a very weak shoulder in the respective BSE spectrum and is marked by an arrow. Vertical dashed lines indicate the positions of experimental absorption onsets measured by Hansson *et al.* [219]. Figure adapted from Ref. [193].

For photon energies about 2 eV above the absorption onset, the dielectric function of KTA differs substantially compared to those of KTP and RTP. Especially within the  $(x,x)$  and  $(y,y)$  polarization configurations, the optical absorption of KTA in that particular region is much stronger. This increase in optical absorption can be explained by analyzing the transition characteristics of prominent absorption peaks within the  $(x,x)$  configuration at around 6.3 eV on the IPA level of theory. The additional absorption in KTA is found to stem from transitions between valence states of pure  $O_{2p}$  character and conduction states involving both  $Ti_{3d}$  and hybrid  $O_{2p}/As_{4d}$  orbitals, as illustrated by the respective charge densities depicted in Fig. 5.10. As previously discussed, this particular hybrid character of the conduction states is only observed in KTA, whereas the corresponding states in KTP and RTP are of pure  $Ti_{3d}$  character. The absorption characteristics for high-energy photons are thus significantly affected by the choice of group-V atom.

As previously mentioned, the inclusion of excitonic effects causes a redshift in all spectra. The magnitude of this shift thereby equals to the binding energy of the first bright exciton. For both materials, the first bright exciton thereby corresponds to a very weak shoulder at about 4.1 eV in the BSE spectrum (see arrows in Fig. 5.9). The contribution of electron-

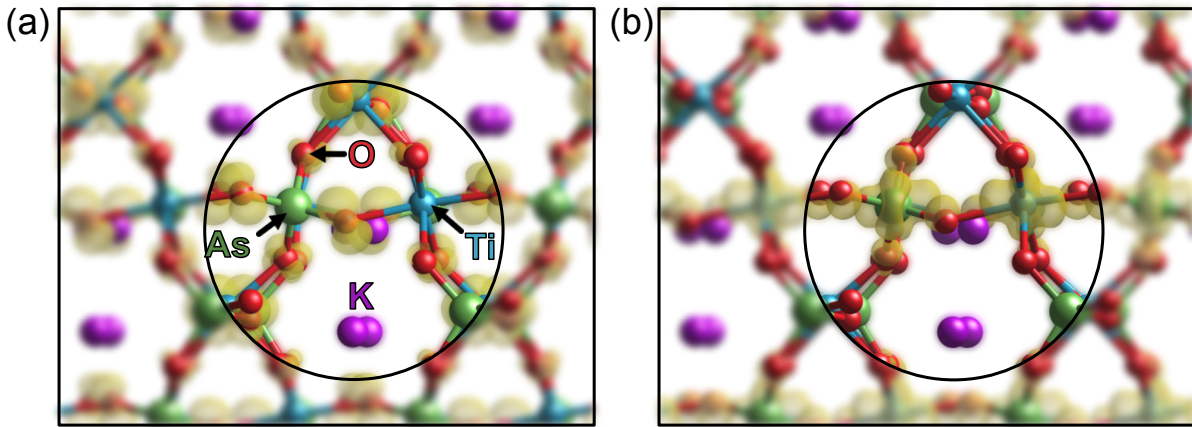


**Figure 5.10:** Transitions between the valence and conduction-band state related to (a)  $O_{2p}$  and (b)  $Ti_{3d} - O_{2p}/As_{4p}$  orbitals, respectively, give rise to the absorption peak at 6.3 eV within the IPA level of theory for  $(x, x)$  polarization in KTA. Figure adapted from Ref. [193].

hole pairs ( $ck, v\mathbf{k}$ ) to the wave function of the first bright exciton can be analyzed via the magnitude of the coefficients  $A_{\lambda}^{ck, v\mathbf{k}}$ , see circles in Fig. 5.8. Similar to KTP, the exciton is found to be essentially delocalized in  $\mathbf{k}$  space, with the largest share stemming from states close to  $\Gamma$ .

By evaluating the shift along the energy axis between the onsets of the optical absorption calculated on the BSE and IQPA levels of theory, average binding energies of 1.38 eV and 1.51 eV for the first bright excitons in RTP and KTA are determined, respectively. The binding energy of 1.47 eV in KTP is thereby very close to the value in KTA. Compared to the respective binding energies of RTP and KTP obtained by Ghoohestani *et al.*, amounting to 0.82 eV and 0.84 eV, a large overestimation is found. This apparent discrepancy, however, stems from the fact that Ghoohestani *et al.* interpret the difference between the first main peak in the BSE spectrum and the minimum band gap of the quasiparticle band structure as the exciton binding energy. This leads to an underestimation, because the resonances in the BSE spectrum are not compared with their actual counterparts in the IQPA, but rather to the energy of a direct transition between the VBM and the CBM, disregarding the oscillator strengths.

The onset of the optical absorption is found to depend on the particular material composition as well as the polarization configuration. The onsets are thereby determined by a linear extrapolation of the first absorption peaks onto the energy axis and are listed in Tab. 5.2 for RTP and KTA (with the respective values of KTP additionally listed for reference). On the BSE level of theory, the onset is found to be the lowest for  $(z, z)$  and highest for  $(x, x)$  polarization, irrespective of the material. Additionally, with the exception of  $(z, z)$ , the onset position is found to decrease when going from KTA via RTP to KTP. This differs from the experimentally observed ordering KTP > RTP > KTA [219]. In addition, the reported position of the absorption onsets (see dashed lines in Fig. 5.9) differ by up to 26 % compared to the present results. However, these observations should be taken with caution, since (i) the energy differences within the present calculations are below the numerical accuracy and (ii) the experimental results are affected by a number of uncertainties. First of all poor sample

**Table 5.2:** Absorption onsets (in eV) of KTA and RTP calculated on the IPA, IQPA, and BSE levels of theory. For comparison, calculated values for KTP as well as experimental data are provided.

Material	Theory			Experiment	
	IPA	IQPA	BSE	Ref. [219]	Ref. [202]
KTA	( $x,x$ )	2.98	5.33	4.15	3.29
	( $y,y$ )	2.90	5.27	3.80	3.22
	( $z,z$ )	2.83	5.17	3.74	3.15
RTP	( $x,x$ )	2.81	5.30	4.04	3.44
	( $y,y$ )	2.85	5.25	3.79	3.35
	( $z,z$ )	2.79	5.23	3.77	3.22
KTP	( $x,x$ )	2.79	5.27	3.99	3.52
	( $y,y$ )	2.79	5.26	3.62	3.45
	( $z,z$ )	2.70	5.09	3.59	3.39

quality may influence the shape and onset position for all KTP related materials [219]. Indeed, for flux-grown KTP, Mangin *et al.* found a sharp increase of optical absorption for all polarizations already at 2.95 eV [221], whereas no such increase is found for any sample (flux-grown and hydrothermally grown) reported by Hansson *et al.*. Lastly, the methods to determine the position of the onset differ, with the experimental values being assigned to the energy, at which the optical absorption reaches an arbitrary cutoff value of  $2 \text{ cm}^{-1}$ . A different method to determine the fundamental absorption edge of flux-grown KTP was used by Dudelzak *et al.* [202]. By fitting the low energy regime of the absorption spectrum to the Urbach tail

$$\alpha(E, T) = \alpha_0 e^{-\sigma \frac{E_0 - E}{k_B T}} \quad (5.3)$$

for various temperatures  $T$ , the positions  $E_0$  of absorption onsets were concluded to be 4.3 eV, 4.1 eV and 3.98 eV for  $(x,x)$ ,  $(y,y)$  and  $(z,z)$  polarization, respectively. Evidently, these values are considerably larger than the data reported in Refs. [219, 221].

## 5.3 Raman Cross Sections

The focus of this last section lies on the investigation of vibrational fingerprints of KTP and related materials. For this purpose, Raman spectra of KTP, RTP and KTA are calculated using DFPT routines (see Sec. 3.3), as implemented in the QUANTUM ESPRESSO software package [222]. A comparison to experimental spectra is carried out using data from Rüsing [223] obtained by a confocal  $\mu$ -Raman setup in backscattering geometry<sup>1</sup>.

As previously discussed in the introduction (Chapter 1), a detailed analysis of Raman spectra may provide in-depth insight into the local material properties in the vicinity of structural perturbations, e.g., in the form of ferroelectric domain walls. However, any in-depth interpretation of spectral changes is challenging. This is especially true for the KTP family, as their Raman spectra are very complex and only partly understood due to the 64 atoms per unit cell giving rise to a total of 189 vibrational degrees of freedom. Additionally, due to the low symmetry in the system, all 189 vibrational modes are nondegenerate and Raman active. Using group theory, the phonons can be further differentiated into 4 different symmetry groups of 48 phonons of  $A_1$ , 47 of  $A_2$ , 47 of  $B_1$ , and 47 of  $B_2$  types, respectively. The symmetry species of a given phonon mode is thereby encoded using Mulliken symbols [225]. Consequently,  $A_1$  ( $A_2$ ) denotes modes, which are symmetric with respect to the principle axis of symmetry and symmetric (antisymmetric) with respect to a rotational axis or mirror plane perpendicular to the principle axis. Similarly,  $B_1$  and  $B_2$  modes are anti-symmetric with respect to the principle axis. Within backscattering geometry, no mixing between phonon branches (symmetry species and LO/TO character) occurs, see Tab. 5.3. For this reason, a particular phonon branch can be accessed individually by the scattering geometry.

So far, no full theoretical prediction of the Raman spectra or  $\Gamma$ -point phonon frequencies for any member of the KTP-family exists. The main spectral features have been explained in

<sup>1</sup>In order to denote a particular Raman-scattering geometry, the porto notation  $\mathbf{k}_i(\mathbf{e}_i, \mathbf{e}_s)\mathbf{k}_s$  is used in the following [224]. For the incident beam, the direction of propagation and polarization is thereby indicated by  $\mathbf{k}_i$  and  $\mathbf{e}_i$ , respectively. Similarly, the scattered light beam is characterized by  $\mathbf{k}_s$  and  $\mathbf{e}_s$ . A backscattering geometry therefore implies  $\mathbf{k}_i \parallel \mathbf{k}_s$ . Directions of propagation and polarization are always chosen along the three cartesian axes  $x$ ,  $y$  and  $z$ . In the case of theoretical Raman spectra, the directions of propagation are not explicitly considered and therefore omitted in the notation.

terms of the vibrational eigenmodes of idealized substructures of the crystal, most prominently the  $\text{TiO}_6$  octahedron and the  $\text{PO}_4$  or  $\text{AsO}_4$  tetrahedron, respectively. Here, the eigenfrequencies and selection rules of these substructures have been calculated. This approach allows, for example, to understand that the high-frequency phonons in the  $> 800 \text{ cm}^{-1}$  range are mostly governed by eigenmodes of the  $\text{PO}_4$  or  $\text{AsO}_4$  tetrahedra, while many dominating peaks in the lower frequency range are associated with eigenmodes of the  $\text{TiO}_6$  octahedron. However, any further predictions based on this approach are limited, as the actual structures of the octahedra and tetrahedra within the real crystal structure differ from their ideal counterparts, which leads to lifted degeneracy of modes or altered selection rules compared to the idealized structure.

For this reason, *ab initio* DFPT calculations of the complete Raman spectrum are performed for KTP, RTP and KTA and systematically compared to experimental results. In the past, this approach was already successfully applied to lithium niobate and lithium tantalate, allowing for an unambiguous phonon assignment [106].

### 5.3.1 Computational Method

Similar to the methodology elaborated in Sec. 5.1.1, ground-state properties of KTP, RTP and KTA are determined using DFT routines, as implemented in the QUANTUM ESPRESSO software package (version 6.3) [222]. The Perdew-Zunger (PZ) parametrization of the LDA (see Sec. 2.1.3) is thereby used to account for electronic exchange and correlation [47]. Norm-conserving pseudopotentials within the PZ formulation are used to model the electron-ion interaction. In addition to all open shells, atomic orbitals  $\text{P}_{3s}$ ,  $\text{O}_{2s}$  and  $\text{As}_{4s}$  have been treated as valence states. In case of Ti, a modified electron configuration was assumed, with the 3d and 4s shell being occupied by 3 and 1 electron, respectively. Electronic wave functions were expanded into plane waves up to a cutoff energy of 100 Ry, ensuring convergence of Raman spectra regarding peak positions and heights. Integration over the Brillouin zone has been carried out using a regular  $2 \times 4 \times 2$   $\mathbf{k}$ -point mesh.

Since Raman spectra are known to be very sensitive to lattice distortions, lattice constants of all three materials are kept constant at their respective experimental values [7] instead of the LDA ones (overestimations of up to 2 % are observed).

For all three materials, structural relaxation via a quasi-newtonian algorithm was performed until residual forces and total energy changes fell below threshold values of  $10^{-4} \text{ Ry/bohr}$  and  $10^{-8} \text{ Ry}$ , respectively. Subsequent calculation of the phonon modes and Raman cross sections are carried out using DFPT routines, as described in Sec. 3.3. We restrict this study on the investigation of TO phonons by evaluating the third-order Raman tensor at the  $\Gamma$  point only, neglecting the influence of long-range electric fields via the non-analytical term 3.56 when setting up the force constant matrix. As previously discussed, the assignment of individual modes in the Raman spectra remains unaffected by this approach, because no mixing between LO and TO phonon branches occurs within the space group  $Pna2_1$ , see Tab. 5.3.

### 5.3.2 Phonon Modes

In the first step, the distribution of phonon frequencies and displacement patterns of all three materials are analyzed by evaluating the atomically resolved phononic DOS. To this

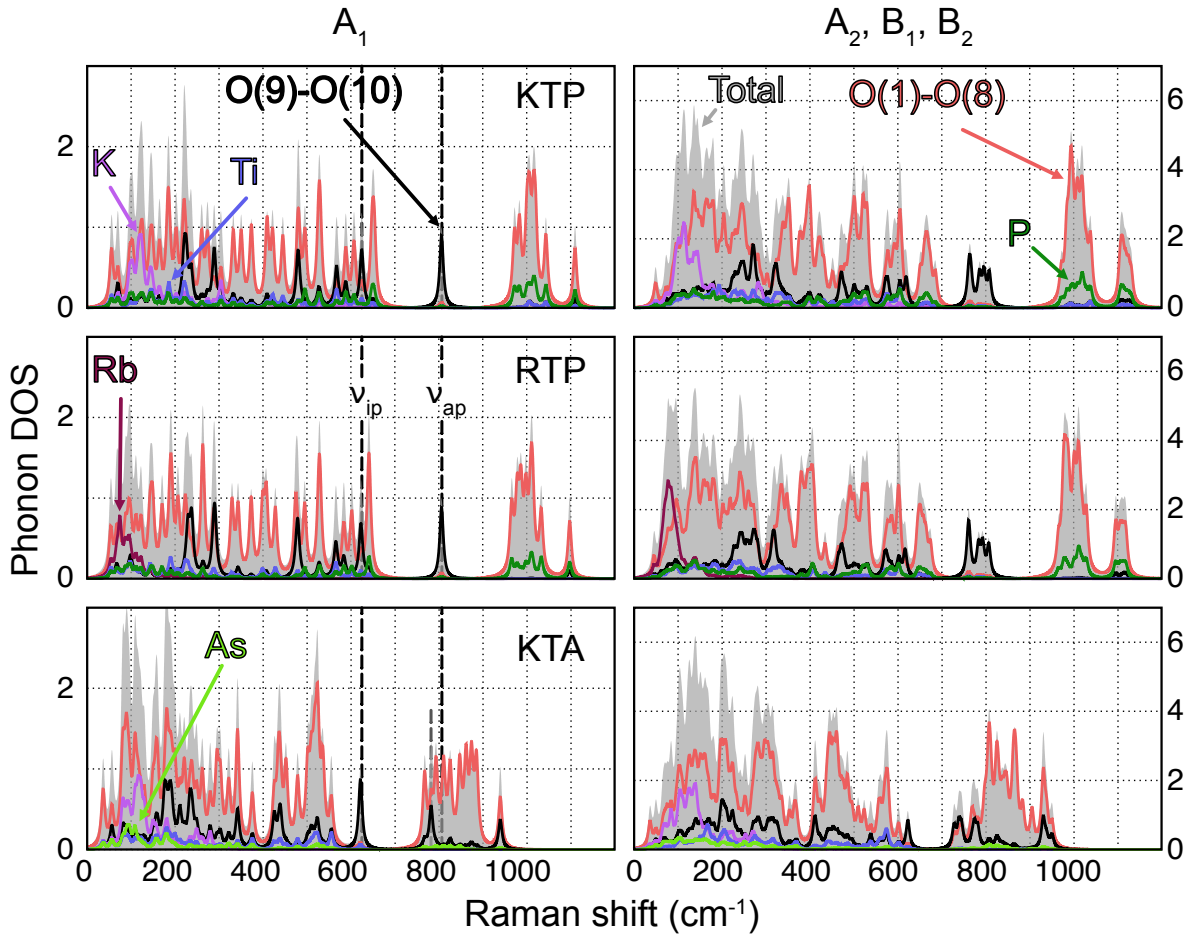


**Figure 5.11:** Atomically resolved phononic DOS for all  $A_1$  (lhs) and  $A_2, B_1$  and  $B_2$  (rhs) type phonons of KTP, RTP and KTA.  $O(1)-O(8)$  and  $O(9)-O(10)$  thereby refer to O atoms in a P–O–Ti and Ti–O–Ti coordination, respectively. The position of the most prominent  $O(9)$  and  $O(10)$  type phonons with  $A_1$  symmetry, labeled  $\nu_{ip}$  and  $\nu_{ap}$ , are indicated by dashed lines. Note the redshift in the position of  $\nu_{ap}$  for KTA with respect to KTP/RTP.

end, the displacement patterns of all respective 189 phonon modes are first projected onto each of the 64 atoms within the unit cell. For a given mode, the contributions of individual Ti, P (As) and K (Rb) atoms are summed up to acquire the entire contribution of the atomic species to the phonon mode. In the case of O, contributions of P–Ti coordinated  $O(1)-O(8)$  and Ti–Ti coordinated  $O(9)-O(10)$  ions are analyzed individually. The phononic DOS is then modeled by lorentzian functions with an arbitrary line width of  $10\text{ cm}^{-1}$ , which are centered at the individual phonon frequencies  $\omega$  and whose heights correspond to each respective atomic species contribution.

In Fig. 5.11, the atomically resolved phononic DOS of KTP, RTP and KTA are depicted. Since the main diagonal components ( $x,x$ ), ( $y,y$ ) and ( $z,z$ ) only feature phonons of  $A_1$  symmetry (see Tab. 5.3),  $A_1$  phonons are displayed separately. A number of common features in the phononic DOS of all three materials can be made out. For one, each spectrum can be roughly subdivided into the following intervals of different atomic contributions:

- Vibrations featuring displacements of the heavy alkali atoms K (Rb) with respect to the surrounding  $\text{PO}_4$  ( $\text{AsO}_4$ ) and  $\text{TiO}_6$  polyhedra are found predominantly in the low frequency regime ( $< 300 \text{ cm}^{-1}$ )
- Owing to their relatively large force constants due to higher bond strength and overall lower masses, P–O type vibrations are localized essentially at frequencies upwards of  $950 \text{ cm}^{-1}$
- Since As has a much higher mass compared to P, As–O type vibrations possess much lower force constants and are thus localized at frequencies close to the K and Rb regime
- Vibrations involving Ti are found in a broad frequency range below around  $650 \text{ cm}^{-1}$

Additionally, in the case of KTP and RTP, a broad gap between  $650 \text{ cm}^{-1}$  and  $950 \text{ cm}^{-1}$  can be made out in the phononic DOS, occupied exclusively by phonons of O(9) and O(10) type character. The sublattice of O(9) and O(10) type atoms takes a special role in the phononic DOS, since its chemical environment is identical in KTP, RTP and KTA. Vibrations of predominantly O(9) and O(10) character should therefore be found at virtually equal frequencies for all three materials. This observation especially holds for phonons in the middle of the gap region, at around  $800 \text{ cm}^{-1}$ . Even in the phononic DOS of KTA, in which the gap region is superimposed by high frequency vibrations of O(1)–O(8) type, phonons of O(9) and O(10) type experience only a relatively small frequency shift compared to KTP and RTP. Out of those phonons, only a single one (in the following labeled  $\nu_{\text{ap}}$ ) is of  $A_1$  symmetry, located at  $806 \text{ cm}^{-1}$  (KTP and RTP) and  $782 \text{ cm}^{-1}$  (KTA). Its displacement pattern in the case of KTP is displayed in Fig. 5.12, with the respective displacement patterns in RTP and KTA being nearly identical. The induced distortion of the  $\text{TiO}_6$  octahedra is found to depend on their orientation, i.e., if neighboring octahedra are linked in a cis or trans manner. In the

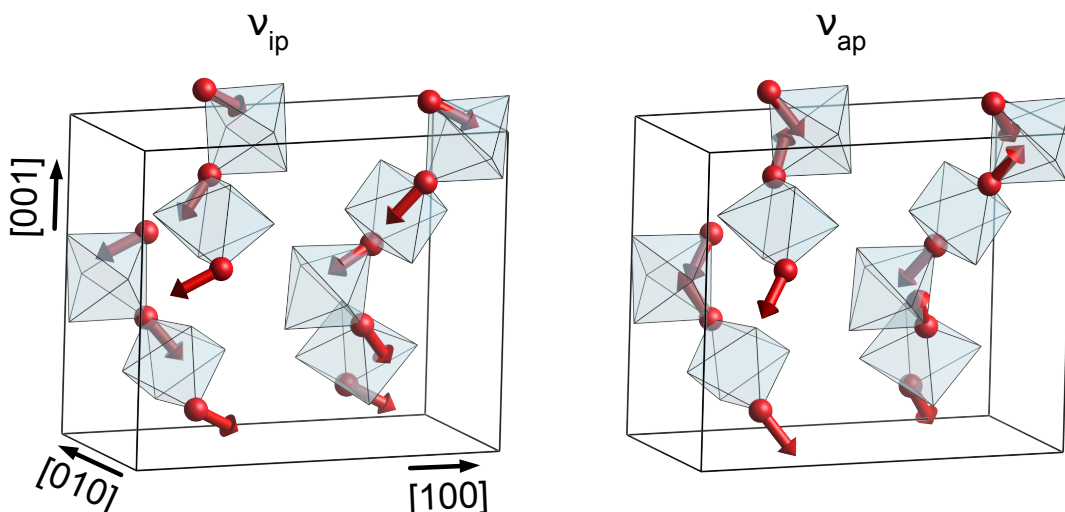


**Figure 5.12:** Displacement pattern of the modes  $\nu_{\text{ip}}$  and  $\nu_{\text{ap}}$  in KTP, located at  $622 \text{ cm}^{-1}$  and  $806 \text{ cm}^{-1}$ , respectively. For visualization sake, only Ti octahedra as well as O atoms of type O(9) and O(10) are displayed.

case of octahedra oriented along the  $x$  direction (trans type linking),  $\nu_{ap}$  induces an anti-phase stretch/compression along the [011] and [01̄] directions, while octahedra oriented along  $y$  (cis type linking) experience predominantly an anti-phase stretch/compression of a single octahedron edge along [001]. In addition to  $\nu_{ap}$ , the O(9)–O(10) type mode  $\nu_{ip}$  located at  $622\text{ cm}^{-1}$  is expected to play an important role in the interpretation of the Raman spectra of all three materials, since both modes are easily separated from the remaining phonon bands. Unlike  $\nu_{ap}$ , the displacement pattern of  $\nu_{ip}$  thereby features an in-phase distortion of the  $\text{TiO}_6$  octahedra, see Fig. 5.12.

In their pioneering work, Kugel *et al.* mapped the entire phonon spectrum of KTP, obtained by infrared and Raman spectroscopy, onto the vibrational eigenmodes of the  $\text{PO}_4$  and  $\text{TiO}_6$  substructures [25]. A comparison between the spectra of KTP and RTP thereby indicated the existence of external lattice modes (involving the displacement of K and Rb) below  $200\text{ cm}^{-1}$ . Additionally, based on calculated frequencies of the internal vibrations in  $\text{PO}_4$ , Raman bands in the high-frequency regime could be mapped to two triply degenerate  $\text{PO}_4$  vibrational modes in the range between  $950\text{ cm}^{-1}$  and  $1100\text{ cm}^{-1}$ . In the present study, these two mappings are essentially confirmed. In order to complete the internal mode analysis in KTP, the remaining Raman bands have been assigned to (i) internal  $\text{TiO}_6$  modes and (ii) collective modes involving displacements of the entire  $\text{TiO}_6$  substructure with respect to the rest of the crystal as well as individual components of a breathing mode within  $\text{TiO}_6$ . This assignment thereby stands on a phenological footing and is based on similarities regarding mode distributions in KTP, RTP and  $\text{BaTiO}_3$ . It ultimately leads to the conclusion that Raman bands of highest intensity are related to anti-phase vibrations involving the long and short Ti–O bonds in  $\text{TiO}_6$ . For KTP vibrations of this character can be identified in the present phonon spectrum as an amalgamation of modes with various symmetries around  $\nu_{ap}$  and  $\nu_{ip}$ . For this reason, the hypothesis by Kugel *et al.* may be extended: Phonon modes of O(9) and O(10) character in general should be responsible for the most prominent Raman peaks. Regarding  $A_1$ -type phonons, observable within the main diagonal components ( $x,x$ ), ( $y,y$ ) and ( $z,z$ ), this further underlines the important role of the modes  $\nu_{ap}$  and  $\nu_{ip}$ .

### 5.3.3 Raman Spectra

In the next step, this presumed prominent role of O(9) and O(10) modes is further analyzed by calculating the Raman cross sections of all modes for all three materials. The experimental spectra were captured at room temperature, hence the temperature in the occupation factor in Eq. 3.46 is set to 300 K. Calculated spectra are obtained by introducing an artificial lorentzian broadening of  $10\text{ cm}^{-1}$  around the respective phonon frequency.

As a first benchmark test, the tensor elements  $|\mathbf{e}_i \cdot \mathbf{R}^\nu \cdot \mathbf{e}_s|^2$  of phonons  $\nu$  with the highest calculated Raman cross section per polarization configuration ( $s,i$ ) are compared with experimental data. Since all three materials are members of the same space group and relative intensities of tensor elements should therefore be similar, we restrict this analysis to KTP only. According to Tab. 5.3,  $A_2$ -TO phonons in ( $x,y$ ) and  $A_1$ -TO phonons in ( $z,z$ ) polarization show the lowest and highest intensities, respectively, separated by a factor of about 26. With respect to ( $z,z$ ),  $A_1$ -TO phonons within the other two main diagonal components ( $x,x$ ) and ( $y,y$ ) show weaker intensities, at around 16 and 43 %, respectively. Similar observations have been made by Kugel *et al.* [25]. This is expectable, as the largest change in polarizability occurs along  $z$  as the direction of internal polarization [223]. The

**Table 5.3:** Raman selection rules for crystals of space group  $Pna2_1$  in backscattering geometry. In addition, experimental and calculated intensities of the respective phonon branches in KTP, normalized to  $A_2$ -TO, are displayed [223].

Scattering geometry	Observable phonon branch	Relative intensity (Experimental)	Relative intensity (Calculated)
$y(x, x)\bar{y}$	$A_1$ -TO	4.2	8.1
$z(x, x)\bar{z}$	$A_1$ -LO	1.8	-
$x(y, y)\bar{x}$	$A_1$ -TO	11.2	12.7
$z(y, y)\bar{z}$	$A_1$ -LO	9.0	-
$x(z, z)\bar{x}$	$A_1$ -TO	26.3	31.9
$y(z, z)\bar{y}$	$A_1$ -TO	26.3	31.9
$z(x, y)\bar{z}$	$A_2$ -TO	1.0	1.0
$y(x, z)\bar{y}$	$B_1$ -TO	1.9	2.2
$x(y, z)\bar{x}$	$B_2$ -TO	10.2	9.3

experimental trends regarding relative intensities within different scattering geometries are generally well reproduced by the present calculations. As the only exception, the Raman scattering within  $(x, x)$  polarization is predicted at about twice the intensity with respect to the experimental data. This might be a consequence of the Raman spectrum of KTP in  $(x, x)$  polarization being essentially governed by a single high intensity peak at  $530\text{ cm}^{-1}$ , related to a  $\text{PO}_4$ -type vibration, see Fig. 5.11 and 5.13. An uncertainty in peak height of this mode would therefore predominantly affect the relative intensity in  $(x, x)$ . In fact, if the mode of the second-highest intensity was chosen as a reference, the relative intensity would drop to 4.57, which is much closer to the experimental value.

Next, experimental and calculated Raman spectra of all three materials are directly compared. To this end, the spectra of all polarization configurations and materials are normalized to the highest intensity. The comparison of main- and off-diagonal components is depicted in Fig. 5.13 and 5.14, respectively.

While the frequency range, in which Raman-active modes are detected in the experiment, is qualitatively reproduced by the present theoretical spectra, the overall agreement regarding mode position and peak height is rather unsatisfying for a number of reasons. For one, unlike within the experimental spectra, most high intensity peaks are found in the low-frequency regime around and below  $200\text{ cm}^{-1}$ , involving K- and Rb-type vibrations. In particular, the modes of highest intensity for nearly all off-diagonal and the  $(z, z)$  component fall into this frequency range. A noticeable difference between the spectra of KTP/KTA and RTP is thereby observed, related to the admixture of K and Rb into the modes in the low-frequency regime. For this reason, in the case of RTP, the influence of the utilized pseudopotential on the overall shape of the spectra is analyzed by testing a modified pseudopotential including the  $\text{Rb}_{4p}$  orbitals as valence states. However, apart from a very tiny blueshift of modes related to O, no significant difference in Raman intensity of the low frequency part of the RTP spectrum is observed.

In comparison, the high frequency regime around and above  $1000\text{ cm}^{-1}$ , involving vi-

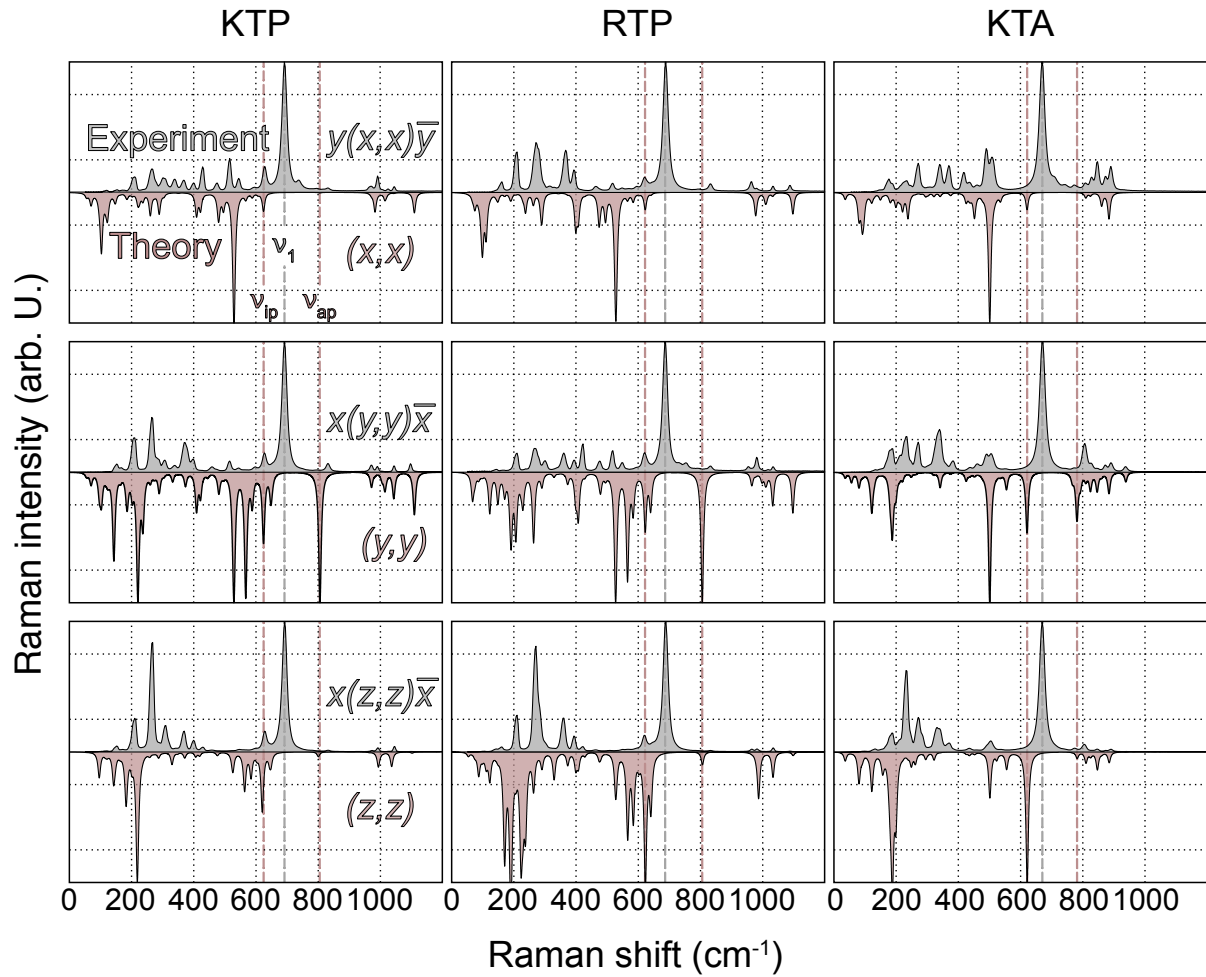


**Figure 5.13:** Experimental (gray) and theoretical (red) Raman spectra of KTP, RTP and KTA in the polarization configurations  $(x, x)$ ,  $(y, y)$  and  $(z, z)$ . The peak heights in all spectra are normalized to the mode of highest intensity. Positions of O(9)–O(10) related modes  $\nu_{ip}$  and  $\nu_{ap}$ , as well as the mode  $\nu_1$  of highest experimental Raman intensity, are indicated by dashed lines. Experimental spectra from Ref. [223].

brations of  $\text{PO}_4$  and  $\text{AsO}_4$ , shows an overall much better agreement with the experimental spectra. Especially for the main diagonal components, peak positions and relative intensities are reproduced favorably. This discrepancy in agreement with the experiment is a consequence of the fact that modes involving  $\text{PO}_4/\text{AsO}_4$  are nearly decoupled from the remaining lattice, as stated by Kugel *et al.* [25].

The biggest discrepancy between calculated and experimental spectra is observed in the mid-frequency regime, in particular regarding the experimentally detected mode of highest Raman intensity. Using the notation of Kugel *et al.*, this mode shall be labeled  $\nu_1$  and is found at  $692 \text{ cm}^{-1}$  (KTP),  $690 \text{ cm}^{-1}$  (RTP) and  $670 \text{ cm}^{-1}$  (KTA) for the  $A_1$ -TO phonon branch within all three possible polarization configurations. All three frequencies fall into the before mentioned gap region within the phononic DOS, so no direct assignment to calculated phonon modes based on the frequency and peak height can be made. In the vicinity of the

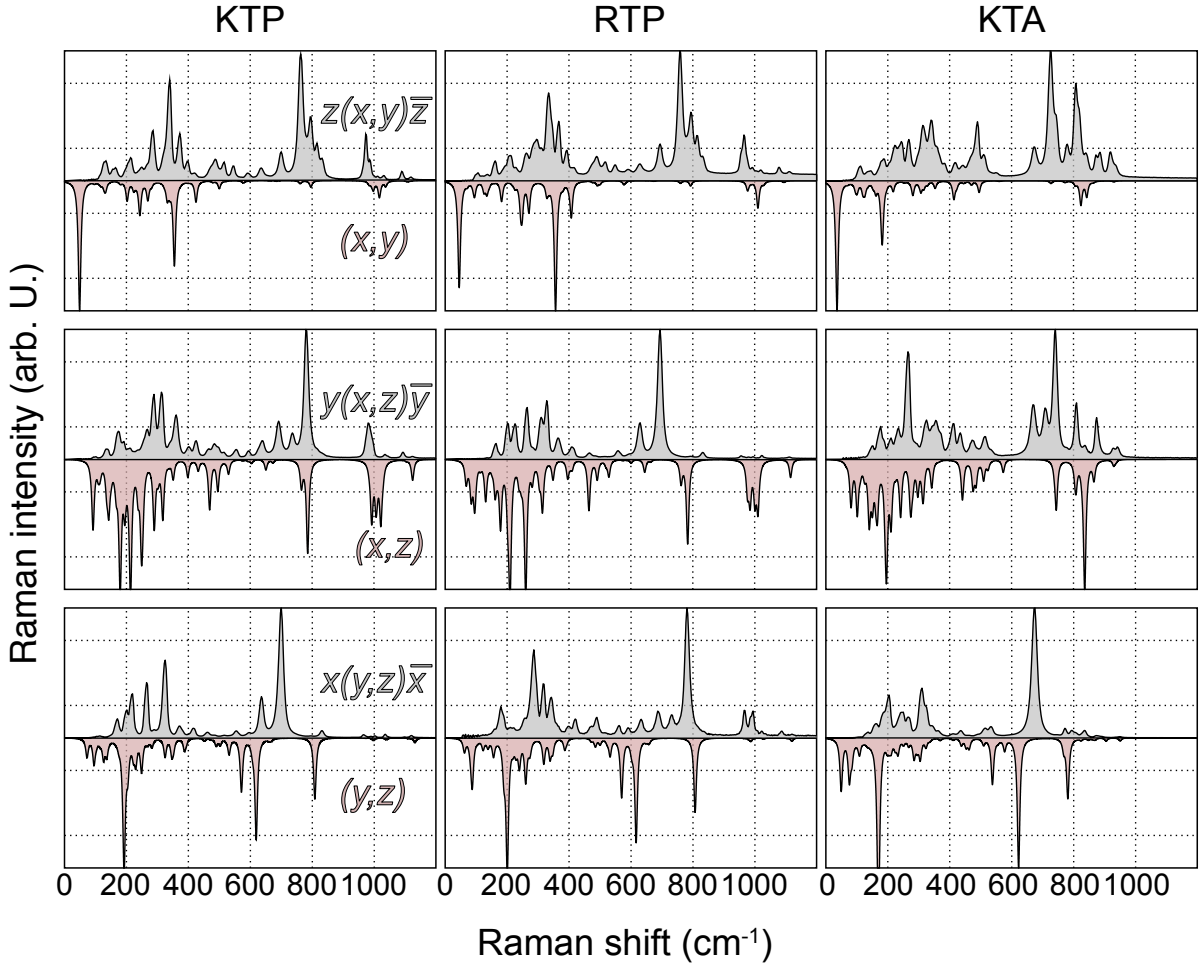


**Figure 5.14:** Experimental (gray) and theoretical (red) Raman spectra of KTP, RTP and KTA in the polarization configurations  $(x, y)$ ,  $(x, z)$  and  $(y, z)$ . The peak heights in all spectra are normalized to the mode of highest intensity. Experimental spectra from Ref. [223].

gap region, however, only a few modes with nonzero Raman intensity within any polarization configuration are observed, in particular the previously discussed modes  $\nu_{\text{ip}}$  and  $\nu_{\text{ap}}$ . Since LDA is known to overestimate vibrational frequencies, an assignment to  $\nu_{\text{ap}}$  appears to be more likely, albeit a difference in frequency of around  $100 \text{ cm}^{-1}$ . This difference is partially explainable by the utilized pseudopotential and lattice constants, as the frequency of  $\nu_{\text{ap}}$  in KTP is found to decrease by around  $20 \text{ cm}^{-1}$  if the phonon spectrum is calculated using PBEsol and relaxed lattice constants. Further evidence for  $\nu_1$  being associated with  $\nu_{\text{ap}}$  is the frequency difference between its value in KTP/RTP and KTA, as the experimentally detected difference of  $20 \text{ cm}^{-1}$  is identical to the one seen for  $\nu_{\text{ap}}$ .

This mode assignment, however, is not supported by the Raman intensity of  $\nu_{\text{ap}}$ . Unlike the highest-intensity peak in the experimental spectra, the peak height of  $\nu_{\text{ap}}$  is found to be highly anisotropic: For all three materials, it is largest for  $(y, y)$  polarization and almost zero for  $(x, x)$ , see Fig. 5.13. A similar observation can be made for  $\nu_{\text{it}}$ , having highest and lowest intensity for  $(z, z)$  and  $(x, x)$  polarization, respectively. The origin of this dissimilarity between experimental and calculated spectra is not fully clear. In order to rule out a strong

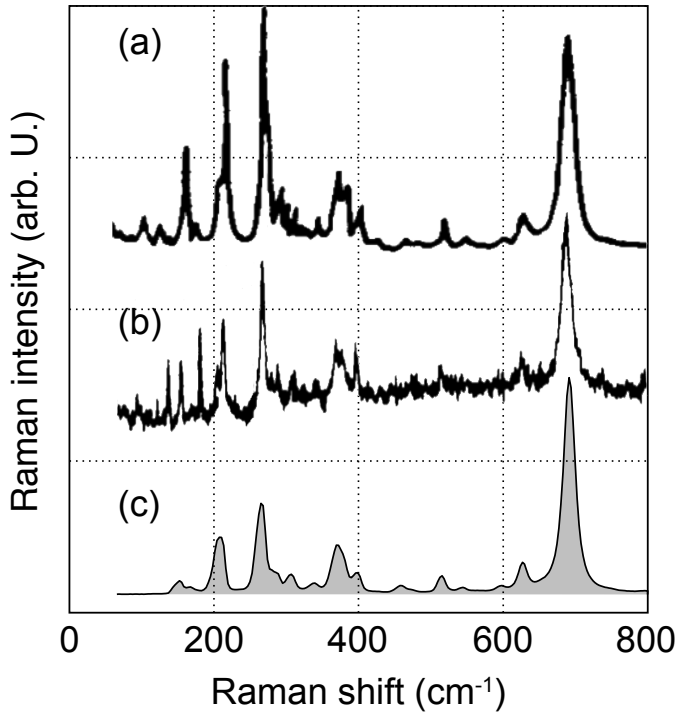


**Figure 5.15:** Experimental room-temperature Raman spectra of KTP for  $x(y,y)\bar{x}$  polarization, as obtained by (a) Voronko *et al.*, (b) Kugel *et al.* and (c) Rüsing [223]. Graphs in (a) and (b) adapted from Refs. [231] and [25], respectively.

link between the observed dissimilarity and the utilized DFPT methodology, Raman spectra of all three materials are calculated again within the VASP program package, using finite-difference routines (see Sec. 3.3) and the same computational settings/atomic geometries as described in Sec. 5.1 and 5.2. As expected, all spectra experience a blueshift of up to  $40\text{ cm}^{-1}$  due to the changes in lattice constants and pseudopotential. The general trend regarding the mid-frequency regime, however, does not change. For one, the modes  $\nu_{\text{ip}}$  and  $\nu_{\text{ap}}$  are found below and above  $\nu_1$ , respectively. In addition, the Raman intensity of both modes is nearly zero for  $(x,x)$  polarization, with the intensity of modes  $\nu_{\text{ip}}$  and  $\nu_{\text{ap}}$  being highest for  $(z,z)$  and  $(y,y)$ , respectively. The discrepancy between experimental and calculated spectra is therefore not mainly related to the used methodology.

It should be noted that the dissimilarities in peak heights within the low- and mid-frequency regime are not independent, as a reduction in relative intensity for the low-frequency part would naturally lead to an increase in the mid-frequency part and vice versa. As previously discussed, all three materials are prone to K and Rb deficiencies, which are expected to influence the low-frequency regime of the respective spectra, as observed by a number of experimental Raman studies [25, 223, 226–231]. Exemplarily, this is illustrated for the  $x(y,y)\bar{x}$  polarization of KTP in Fig. 5.15. The three experimental spectra from Voronko *et al.* [231], Kugel *et al.* [25] and Rüsing [223] were thereby obtained under room temperature conditions. Above  $350\text{ cm}^{-1}$ , the amount of detected peaks as well as relative intensities does not change between the three spectra. In the low-frequency part, however, the spectra differ noticeably. In particular, the intensity of a prominent peak at  $265\text{ cm}^{-1}$

shows a considerable spread, being either much stronger or weaker compared to  $\nu_1$ . For this reason, the nonstoichiometry of the utilized crystals in general and alkali-atom deficiency in particular are expected to at least partially explain the observed discrepancies between experimental and calculated spectra.

## 5.4 Conclusions

For the three materials KTP, RTP and KTA, spectroscopic signatures in the form of optical response functions and differential Raman cross sections have been determined on the footing of DFT ground and excited-state calculations.

Calculations of band structures and dielectric functions were carried out on various levels of theory, stepwise including the influence of quasiparticle and excitonic effects. In the present work, the electronic transport gap of KTP is shown to be much larger than concluded from previous experimental and theoretical studies. Its lower bound, as determined on the *GW* level of theory, can be expected to be about 5.23 eV. Additionally, the optical band gap is shown to be affected by a large exciton binding energy, amounting to about 1.5 eV. Overall, the calculated reflectivity spectrum on the BSE level of theory is found to be in good agreement with experimental data [200]. This demonstrates the crucial importance of many-body effects on the excited-state properties of KTP. In addition, the present study demonstrates the sensitivity of the optical response of KTP with respect to its structural details. In particular, the optical anisotropy and peak splitting of the absorption onset is shown to be caused by the orientation and arrangement of the  $\text{TiO}_6$  octahedra within the unit cell.

A similar trend regarding band structures and optical response functions is observed for the isomorphic ferroelectrics RTP and KTA, with their respective transport band gaps predicted at 5.30 eV and 5.24 eV. The shape and position of the band edges are found to be more sensitive to an exchange of the alkali-metal ion than of the group-V atom. The optical absorption is affected by strong exciton binding energies of 1.38 eV for RTP and 1.51 eV for KTA. The first bright exciton in all three materials is found to arise from transitions involving essentially the entire Brillouin zone, with the largest share coming from the  $\Gamma$  point. The stronger optical absorption of KTA compared to RTP and KTP for high-energy photons is related to transitions involving empty  $\text{As}_{4p}$  orbitals. The optical absorption onset depends on both, the material and the polarization. It is predicted here to occur first for the  $(z,z)$  polarization in RTP and last for the  $(x,x)$  polarization in KTA.

Calculations of phonon spectra and Raman cross sections of all three materials were performed using DFPT routines. The phonon spectra were thereby found to be subdivided into a number of regions with varying vibrational character, confirming the prior mapping by Kugel *et al.* [25]. Owing to their high mass, the low frequency part of all spectra is dominated by vibrations of the respective alkali atom K and Rb, with additional contributions of As in the case of KTA. Phonons of P-type character, on the other hand, are found predominantly in the high frequency part. A broad gap region in the mid-frequency regime, populated nearly exclusively by phonons of O(9) and O(10) character, could be made out around  $800 \text{ cm}^{-1}$  (KTP/RTP) and  $650 \text{ cm}^{-1}$  (KTA). Two of these O(9)–O(10)-type phonons exhibit  $A_1$  symmetry and show only a slight frequency shift among the three materials, namely mode  $\nu_{\text{ip}}$  at around  $620 \text{ cm}^{-1}$ , involving an in-phase distortion of the  $\text{TiO}_6$  octahedra along

[001] and mode  $\nu_{\text{ap}}$  at around  $800\text{ cm}^{-1}$ , distorting the  $\text{TiO}_6$  substructure in an anti-phase manner. Taking into the account the conclusion of Kugel *et al.*, after which phonons of largest Raman cross section should involve a distortion of the long and short bonds within  $\text{TiO}_6$ , modes  $\nu_{\text{ip}}$  and  $\nu_{\text{ap}}$  are expected to feature the highest intensities in the Raman spectra of all three materials within the main diagonal components. To assert these assumptions, Raman spectra for all three materials were calculated and compared to experimental data by Rüsing [223]. This comparison, however, revealed a number of dissimilarities regarding position and height of individual Raman signals. While the relative intensities of the highest peaks within different polarization configurations are well reproduced, no conclusive matching between experimental and calculated high-intensity peaks could be made. In particular, the experimental  $A_1$ -type mode  $\nu_1$  of highest intensity for all three materials is located directly within the calculated gap region, preventing a direct, frequency-based mode assignment. Additionally, all calculated modes in the vicinity of the gap region (modes  $\nu_{\text{ip}}$  and  $\nu_{\text{ap}}$  in particular) are found to feature a pronounced modulation of peak height with respect to the polarization configuration, which is not seen in the experiment. Nonetheless, a number of arguments can be made for an assignment between  $\nu_1$  and  $\nu_{\text{ap}}$ . (i) The blueshift of  $\nu_{\text{ap}}$  with respect to  $\nu_1$  is partially explainable by the use of the PZ-LDA functional, (ii) both modes feature the same redshift of about  $20\text{ cm}^{-1}$  between materials KTP/RTP and KTA and (iii) the relative peak heights between  $\nu_1$  and low-frequency modes are known to be affected significantly by the density of K vacancies, partially explaining the dissimilarities regarding experimental and calculated peak heights. In order to verify this mapping, however, argument (iii) should be further quantified by analyzing the Raman signatures of nonstoichiometric KTP, RTP and KTA.

# 6

## Surface Reconstructions

In the previous chapter, the focus was laid specifically on the determination of spectroscopic signatures of KTP, RTP and KTA in their respective bulk phases. While most spectroscopic methods are used to assess the bulk quantities of the three materials, the particular reconstruction of a given surfaces may have an influence on the optical spectra due to the formation of surface states. Understanding the reconstruction mechanisms for a given surface therefore plays an important role in estimating its influence on electronic and optical properties of the respective bulk material.

In this chapter, findings regarding the modeling of KTP Z and Y-cut surfaces as well as the determination of the thermodynamically most stable reconstructions and their role in the formation of surface states are summarized. While a qualitative difference between equivalent surfaces of KTP and RTP/KTA due to the inclusion different atomic species is possible, the general conclusions of this study is expected to remain valid for all members of the KTP crystal family.

The outline of this chapter is the following: First, the general methodology to determine KTP surface phase diagrams is introduced. Next, KTP Z cut and Y cut are discussed separately, beginning with an outline of the general modeling of both surfaces, followed by the results regarding phase diagrams and surface states.

Parts of the results within this chapter have already been published, see Ref. [232].

### 6.1 General Methodology

At its core, the general methodology used in this chapter follows closely the approach to calculate optical and electronical properties of KTP type crystals in Chapter 5. Thereby, the total energy of a given surface is determined using DFT routines implemented in the VASP program package [194]. Again, the electronic XC energy is calculated within the GGA using PAW potentials [195] and the PBEsol functional [55].

In the following, each KTP surface is considered to be in contact with a reservoir of all four atomic species building up the bulk material, i.e., K, P, Ti and O. This reservoir allows for the exchange of atoms onto and away from the surface, making the particular number  $N_i$  of atoms of species  $i$  a variable quantity. Because the DFT total energy  $E_{\text{DFT}}(\{N_i\})$  depends

on the number of atoms in a given unit cell,  $E_{\text{DFT}}$  is not a good choice to directly assess the stability of a surface being subject to changes in its stoichiometry. In order to account for varying surface stoichiometries, the surface energy  $\gamma(p, T, \{\mu_i\})$ , defined as

$$\gamma(p, T, \{\mu_i\}) = \frac{1}{A} \left( G(p, T, \{N_i\}) - \sum_i N_i \cdot \mu_i \right), \quad (6.1)$$

is used instead. Here,  $A$  denotes the surface area of the given unit cell and  $G(p, T, \{N_i\})$  the Gibbs free energy. The surface- and Gibbs free energy are functions of the chemical potentials  $\{\mu_i\}$  of each atomic species  $i$ , reflecting different chemical environments in the form of a higher or lower energetic cost to remove an atom from a reservoir and adding it to the system or vice versa. At a given temperature and pressure, a high or low value of  $\mu_i$  corresponds to an environment enriched or depleted of atoms of species  $i$ , respectively. For a specific chemical environment, given by the values of the set  $\{\mu_i\}$ , a surface is considered stable, if it minimizes  $\gamma(p, T, \{\mu_i\})$  at a fixed temperature  $T$  and pressure  $p$  [233]. The Gibbs free energy is related to the Helmholtz free energy  $F(V, T, \{N_i\})$  via the Legendre transformation

$$G(p, T, \{N_i\}) = F(V, T, \{N_i\}) + pV. \quad (6.2)$$

For most solids, the influence of pressure variations to the surface energy (i.e., the term  $pV$ ) can thereby be neglected. In fact, a change in surface stoichiometry  $\Delta N$  introduces an energy variation of the form  $\Delta N \cdot pV_{\text{at}}$ , with  $V_{\text{at}}$  being a characteristic atomic volume [233]. For normal pressures  $p = 10^5 \text{ Pa}$  and typical volumes in the order of  $V_{\text{at}} \approx (2 \text{ \AA})^3$  this contribution amounts to less than 0.005 meV per atom, which is very close to the numerical precision used in this work and is thus considered negligibly small.

The Gibbs free energy in Eq. 6.1 may therefore be replaced by  $F(V, T, \{N_i\})$ . Applying a Legendre transformation, the relation between  $F(V, T, \{N_i\})$  and the internal energy  $U(V, S, \{N_i\})$  reads

$$F(V, T, \{N_i\}) = U(V, S, \{N_i\}) - TS. \quad (6.3)$$

The entropy term  $TS$  includes all contributions from lattice vibrations and is generally too large to be neglected [233]. However, a large compensation to this term can be assumed by considering the equipartition theorem, stating that each ionic degree of freedom contributes equally to the internal energy by a factor of  $k_B T$

$$U(V, S, \{N_i\}) = E(\{N_i\}) + 3k_B T \sum_i N_i. \quad (6.4)$$

Here,  $E(\{N_i\})$  denotes the total energy of the system at  $T = 0 \text{ K}$  and  $k_B$  the Boltzmann constant. In the classical limit, the last terms in Eqs. 6.3 and 6.4 nearly cancel [233]. The Helmholtz free energy can therefore be approximated by the zero-temperature total energy as the leading term in the internal energy. Thus, the surface energy is in the following evaluated as

$$\gamma(\{\mu_i\}) = \frac{1}{A} \left( E(\{N_i\}) - \sum_i N_i \cdot \mu_i \right). \quad (6.5)$$

This expression enables the estimation of the stability of a given surface directly via the total energy  $E$  obtained by DFT calculations on a surface slab containing  $\{N_i\}$  atoms of the element  $i$ .

Until now, the accessible phase space, given by the respective ranges of the chemical potentials  $\{\mu_i\}$ , has been considered arbitrary. However, in order to ensure the stability of bulk KTP, a number of constraints for  $\{\mu_i\}$  have to be met. For the sake of readability, we change the variables from bare chemical potentials to the respective variations with respect to their bulk phase:

$$\Delta\mu_i := \mu_i - \mu_i^{\text{bulk}}. \quad (6.6)$$

For potassium, a number of experimental bulk phases have been reported, showing only small differences in formation energy [234]. As the reference bulk phase for K in this study, the bcc structure with space group  $Im\bar{3}m$  is chosen [235]. The chemical potential is determined by the total DFT energy per atom after structural relaxation and amounts to  $\mu_K^{\text{bulk}} = -1.11$  eV (see Tab. B.1 in Appendix B). Similarly, the bulk phases of Ti and P are chosen as hcp titanium [236] and black phosphorus [237], respectively, and amount to  $\mu_{\text{Ti}}^{\text{bulk}} = -8.31$  eV and  $\mu_{\text{P}}^{\text{bulk}} = -5.78$  eV. In the case of O, solid phases are reported only for low temperatures and high pressure environments [238], making molecular  $\text{O}_2$  the most reasonable choice as a reference system.  $\text{O}_2$  is modeled by two O atoms within a cubic supercell of side length 15 Å and yields a chemical potential (i.e., total energy per O atom) of  $\mu_{\text{O}}^{\text{bulk}} = -4.57$  eV<sup>1</sup>.

As a first constraint to  $\{\Delta\mu_i\}$ , the potentials may not be varied independently. In order for all elements added to the surface via the respective reservoir to form the bulk phase of KTP, the condition

$$\Delta\mu_{\text{K}} + \Delta\mu_{\text{Ti}} + \Delta\mu_{\text{P}} + 5\Delta\mu_{\text{O}} = \Delta H_{\text{KTP}}^f \quad (6.7)$$

must hold, with the heat of formation of KTP

$$\Delta H_{\text{KTP}}^f = \mu_{\text{KTP}}^{\text{bulk}} - \mu_{\text{K}}^{\text{bulk}} - \mu_{\text{Ti}}^{\text{bulk}} - \mu_{\text{P}}^{\text{bulk}} - 5\mu_{\text{O}}^{\text{bulk}}. \quad (6.8)$$

Similar to the chemical potential of each element's bulk phase,  $\mu_{\text{KTP}}^{\text{bulk}}$  is determined as the DFT total energy per formula unit of  $\text{KTiOPO}_4$ . Assuming Eq. 6.7, the dimensionality of the phase space  $\{\Delta\mu_i\}$  is reduced to 3, allowing it to be visualized as a tetrahedral phase diagram, see Fig. 6.1, upper part. Each point within the tetrahedron fulfills Eq. 6.7, i.e., the sum of its coordinates, stoichiometrically weighted by the molecular formula of KTP ( $\text{KTiOPO}_4$ ), sums up to the constant value  $\Delta H_{\text{KTP}}^f$ .

As a second constraint, the accessible ranges of all chemical potentials may be further narrowed down. If  $\mu_i$  was larger than  $\mu_i^{\text{bulk}}$ , desorption of the element  $i$  away from the surface and formation of its respective bulk phase would occur, giving rise to the condition  $\Delta\mu_i \leq 0$ . Inserting this upper bound for three out of the four elements into Eq. 6.7 additionally provides a lower bound, given by  $\Delta H_{\text{KTP}}^f$ . In total, the chemical potentials are bound by

$$\begin{aligned} \Delta H_{\text{KTP}}^f \leq \Delta\mu_i \leq 0, \quad \text{with } i \in \{\text{K, Ti, P}\}, \\ \text{and } \Delta H_{\text{KTP}}^f \leq 5 \cdot \Delta\mu_{\text{O}} \leq 0. \end{aligned} \quad (6.9)$$

The final constraint is derived from the assertion that no segregation of the involved elements into different bi- or triatomic phases should occur. If  $\text{A}_\alpha\text{B}_\beta\text{C}_\gamma$  labels such a phase with

<sup>1</sup>In order to keep the notation consistent,  $\mu_{\text{O}}^{\text{bulk}}$  will, in the following, refer to the chemical potential of oxygen in its molecular  $\text{O}_2$  phase.

respective elements  $\{A, B, C\}$  and stoichiometric coefficients  $\{\alpha, \beta, \gamma\}$ , the final condition reads

$$\alpha \cdot \Delta\mu_A + \beta \cdot \Delta\mu_B + \gamma \cdot \Delta\mu_C \leq \Delta H_{A_\alpha B_\beta C_\gamma}^f, \quad (6.10)$$

with the formation enthalpy given by

$$\Delta H_{A_\alpha B_\beta C_\gamma}^f = \mu_{A_\alpha B_\beta C_\gamma}^{\text{bulk}} - \alpha \cdot \mu_A^{\text{bulk}} - \beta \cdot \mu_B^{\text{bulk}} - \gamma \cdot \mu_C^{\text{bulk}}. \quad (6.11)$$

For a specific phase  $A_\alpha B_\beta C_\gamma$ , Eq. 6.10 partitions the available phase space into a region, in which bulk KTP is stable and another one, in which the phase  $A_\alpha B_\beta C_\gamma$  is formed instead (see binodal curves in Fig. 6.1). In case of the elements K, Ti, P and O, a vast number of stable bi and triatomic phases exists. In order to take into account as many of these phases as possible, structural data from the Materials Project database is used [234]. All bi- and triatomic phases containing the constituents of KTP that are reported stable against decomposition have thereby been considered, amounting to 33 compounds in total (see Tab. B.1

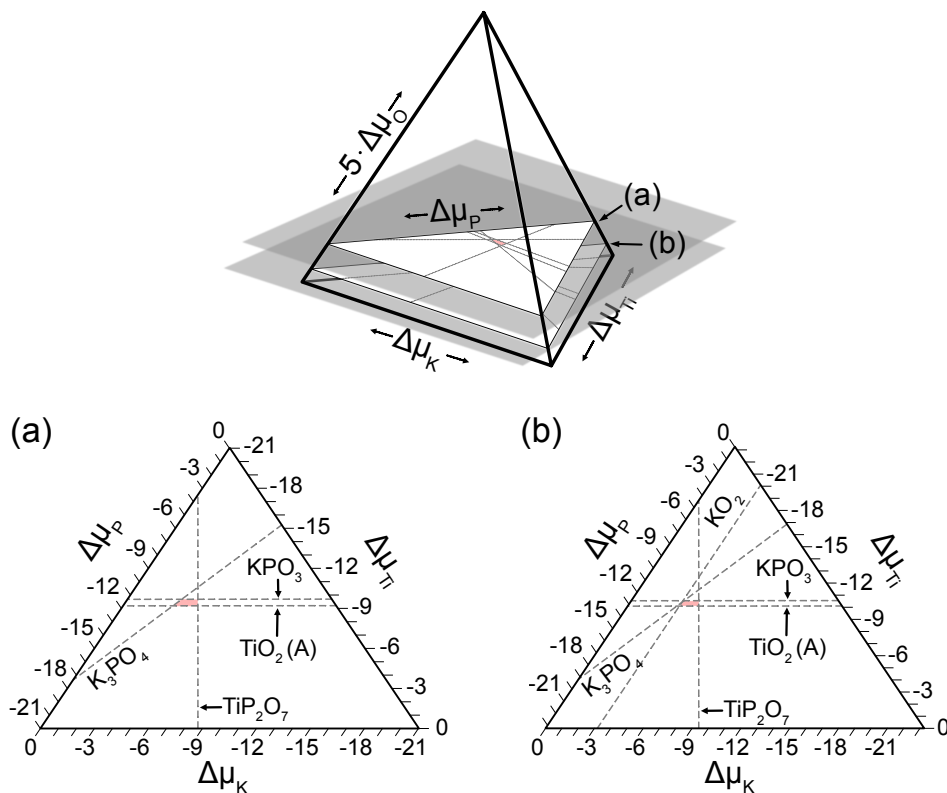


**Figure 6.1:** The full phase space  $\{\Delta\mu_K, \Delta\mu_{\text{Ti}}, \Delta\mu_P, 5 \cdot \Delta\mu_O\}$  for KTP formation under the restrictions imposed by Eqs. 6.7 and 6.9 is given by a tetrahedron (upper part). Fixing the value of  $\Delta\mu_O$  reduces the phase space to three variables, making it possible to visualize it within a ternary phase diagram. (a) Phase diagram under UHV conditions, i.e.,  $\Delta\mu_O = -0.71$  eV, (b) phase diagram under atmospheric pressure, i.e.,  $\Delta\mu_O = -0.27$  eV. Binodal curves between KTP and a different phase, directly enclosing the red KTP stability region, are visualized by dashed lines.  $\text{TiO}_2$  (A) thereby abbreviates the Anatase phase of  $\text{TiO}_2$ . All chemical potential variations are given in eV

in Appendix B). The intersection of all binodal planes partitioning the phase diagram according to Eq. 6.10 encloses the bulk KTP stability region. In order to identify the stable surface terminations of KTP within this stability region, a two-dimensional visualization of the full phase space is required. To this end, the chemical potential of O will, in the following, be considered fixed. This restriction may be represented as a slice through the entire tetrahedral phase space (see Fig. 6.1 (a) and (b)), yielding a ternary phase diagram with the chemical potentials of the three remaining elements  $i=\{K, Ti, P\}$  as variables, bound by

$$0 \leq \Delta\mu_i \leq \Delta H_{\text{KTP}}^f - 5 \cdot \Delta\mu_O. \quad (6.12)$$

A specific value for  $\Delta\mu_O$  at typical experimental conditions may be deduced by approximating the oxygen reservoir  $O_2$  as an ideal gas. In this case, the relation between the chemical potential, partial pressure  $p$  and temperature  $T$  is given by [239]

$$\Delta\mu_O = \frac{k_B T}{2} \left( \ln\left(\frac{p\lambda^3}{k_B T}\right) - \ln(Z_{\text{rot}}) - \ln(Z_{\text{vib}}) \right), \quad (6.13)$$

with  $\lambda = \sqrt{\frac{2\pi\hbar^2}{mk_B T}}$  as the de-Broglie wavelength of an  $O_2$  molecule with mass  $m$  and  $Z_{\text{rot}}$  and  $Z_{\text{vib}}$  as the respective rotational and vibrational partition functions. In the case of a homonuclear diatomic molecule, the latter two expressions read

$$Z_{\text{rot}} = \frac{k_B T I}{\hbar^2} \quad (6.14)$$

$$\text{and } Z_{\text{vib}} = \frac{1}{1 - e^{\frac{\hbar\omega}{k_B T}}}. \quad (6.15)$$

The moment of inertia and the frequency of the stretching mode of  $O_2$  are denoted by  $I$  and  $\omega$ , respectively.

At ultra-high vacuum (UHV) conditions ( $p = 10^{-10}$  Pa and  $T = 300$  K), the chemical potential of O amounts to  $\Delta\mu_O = -0.71$  eV. Taking this value as constant, the lower bound to the chemical potentials of the three remaining elements increases to  $\Delta H_{\text{KTP}}^f - 5 \cdot \Delta\mu_O \approx -21$  eV. The ternary phase diagram under this condition is depicted in Fig. 6.1 (a). Compared to the size of the entire phase space, the stability region for bulk KTP is given by a small subspace, bound by the binodal curves of four different phases. These phases are:

- Tripotassium phosphate ( $K_3PO_4$ ) for very K-rich conditions. Similar to KTP,  $K_3PO_4$  undergoes a phase transition at a temperature of 550°C, with its lower temperature phase belonging to the orthorhombic  $Pnma$  space group [240].
- Potassium phosphate ( $KPO_3$ ) for environments with  $\Delta\mu_{\text{Ti}} = 9.7$  eV. As a side product from the dehydration of  $KH_2PO_4$ , this compound has been shown to be polymorphic, with three phases being stable for different temperature ranges [241]. At room temperature, the monoclinic (C) phase with space group  $P2_1/c$  is most stable, as it has been determined via X-ray diffraction [242].
- Titanium dioxide in its anatase phase ( $TiO_2$  (A)) for environments of  $\Delta\mu_{\text{Ti}} = 9.18$  eV. Several polymorphs of  $TiO_2$  are known, with the naturally occurring anatase (space group  $I4_1/amd$ ), rutile ( $P4_2/mmm$ ) and brookite ( $Pbca$ ) phases being the most prominent. Anatase and brookite are thereby shown to undergo a phase transition into the

rutile phase at elevated temperatures [243]. All three phases are energetically nearly degenerate in this work, with the formation energy of anatase being only 50 meV below that of rutile, see Tab. B.1.

- Titanium pyrophosphate ( $\text{TiP}_2\text{O}_7$ ) for environments of high to moderate P enrichment. This compound crystallizes in a cubic unit cell with space group  $\text{Pa}\bar{3}$  [244]. A different phase (space group  $\text{P}2_1/c$ ) is listed in the Material Project database as energetically slightly more favorable [234]. However, in our calculations, both phases are energetically nearly degenerate. The existence of a  $3\times3\times3$  superstructure has been reported [245, 246]. In this work, however, this phase is not considered, because (i) no large difference in formation enthalpy with respect to the  $\text{P}2_1/c$  phase is expected and (ii) the large size of the unit cell (108 formula units, 1080 atoms) prevents a straight forward determination of the ground-state geometry.

By increasing the pressure from UHV to atmospheric (ATM) conditions ( $p = 10^5 \text{ Pa}$ ), the chemical potential of oxygen decreases to a value of  $\Delta\mu_{\text{O}} = -0.27 \text{ eV}$ . The overall position and size of the KTP stability region is effected only slightly, as depicted in Fig. 6.1 (b). Additionally, the concurring phases enclosing the stability region do not change, with the exception of an additional small border between KTP and the phase  $\text{KO}_2$  emerging. This compound has been shown to undergo multiple crystallographic and magnetic phase transitions in a temperature region between 4.2 and 400 K [247–249]. Close to room temperature, a structure of space group  $I_4/mmm$  as well as an incommensurable superstructure have shown to be most stable [249].

## 6.2 Z Cut

Z-cut surfaces are modeled using periodic repetitions of the KTP bulk unit cell along the  $z$  direction. Along  $z$ , KTP may be thought of as assembled of alternating  $\text{K}_2\text{Ti}_2\text{P}_2\text{O}_4$  and  $\text{O}_6$  layers, see Fig. 6.2. These layers can be further differentiated by the orientation of the constituent  $\text{TiO}_6$  and  $\text{PO}_4$  polyhedra. They are connected by a common O atom and form chain structures parallel to either the  $x$  direction (Fig. 6.2 d) or the  $y$  direction (Fig. 6.2 c). Accordingly, we discriminate between  $\text{K}_2\text{Ti}_2\text{P}_2\text{O}_4$  (x) and (y) layers.  $\text{O}_6$  layers following an x- or y-type layer will also be distinguished separately as  $\text{O}_6$  ( $x_{\text{O}}$ ) and ( $y_{\text{O}}$ ), respectively. Regarding the stacking order, both the positive and negative  $z$  direction are indistinguishable, since the character of ( $x_{\text{O}}$ ) and ( $y_{\text{O}}$ ) type layers switch when going from one orientation to another.

However, the polar character of the Z-cut surface is reflected structurally by a strong shift of the  $\text{K}^+$  ions along the surface normal as well as by a pronounced buckling of the  $\text{TiO}_6$  octahedra. Taking the position of P as a reference, Ti atoms show only a small displacement along the positive  $z$  direction, amounting to  $0.05 \text{ \AA}$  for both, x- and y-type layers. The four O atoms within each individual layer can be split into two non-symmetry-equivalent groups occupying different positions along  $z$ . In the case of x-type layers, two O atoms show a displacement of  $-0.19 \text{ \AA}$ , while the remaining two are displaced by  $+0.24 \text{ \AA}$  with respect to P. For y-type layers, the displacement is larger, with  $-0.3 \text{ \AA}$  and  $+0.27 \text{ \AA}$ . Evidently, the displacements of O in x- and y-type layers nearly cancel out. The existence of a microscopic dipole moment along  $z$  may therefore solely be attributed to a nearly rigid displacement of

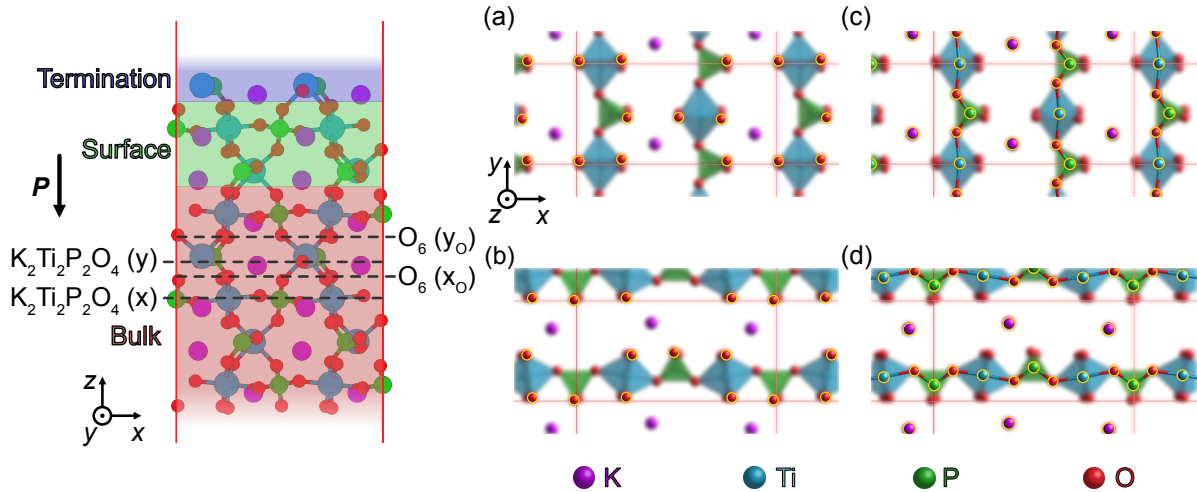


**Figure 6.2:** Left: Stacking sequence of  $\text{K}_2\text{Ti}_2\text{P}_2\text{O}_4$  and  $\text{O}_6$  layers in Z-cut KTP. Bulk layers remain fixed during relaxation and all four surface layers as well as the termination atoms are free to relax. The direction of the internal polarization  $\mathbf{P}$  is indicated by a black arrow. Right: Atomic geometries of the four bulk cuts (a)  $\text{O}_6(y_O)$ , (b)  $\text{O}_6(x_O)$ , (c)  $\text{K}_2\text{Ti}_2\text{P}_2\text{O}_4(y)$  and (d)  $\text{K}_2\text{Ti}_2\text{P}_2\text{O}_4(x)$ . In yellow, surface atoms are highlighted. Figure adapted from Ref. [232].

the  $\text{K}^+$  sublattice. This displacement amounts to  $-0.5 \text{ \AA}$  (x-type) and  $-0.55 \text{ \AA}$  (y-type). In total, all microscopic dipole moments sum up to a macroscopic polarization oriented along the negative  $z$  direction (see Fig. 6.2). On average, the variation in  $z$  position within  $x_O$  and  $y_O$  layers is smaller, amounting to  $\pm 0.07 \text{ \AA}$  and  $\pm 0.12 \text{ \AA}$ , respectively.

### 6.2.1 Structural Modelling

In order to model Z-cut surfaces in a slab geometry, four regions have to be taken into account (see Fig. 6.2): (i) A number of KTP layers with atoms frozen onto their respective bulk positions (bulk region), emulating a semi-infinite substrate, (ii) several KTP layers with atoms being free to relax (surface region) on top of the bulk region, (iii) a termination layer, reflecting various (not necessarily stoichiometric) surface reconstructions, and (iv) a vacuum layer, preventing spurious interactions between the positive and negative surface due to periodic boundary conditions.

The number of considered bulk layers is chosen under the condition of the bulk layer yielding an averaged local electrostatic potential of the same shape as in bulk KTP (see Fig. 6.3). This condition is found to be met for 11 layers. Half a KTP unit cell (i.e., four total layers) is chosen to build up the surface region. Due to the electrostatic interaction between both end facets, an external electric field would, in principle, be present within the vacuum region regardless of its thickness, see Fig. 6.3 (a). In order to compensate for this effect, dipole corrections along the  $z$  direction are utilized, as discussed in Sec. 4.4. Accordingly, the height of the vacuum layer is chosen to be large enough to feature a region of constant local potential if dipole corrections are switched on, see 6.3 (b). A height of  $15 \text{ \AA}$  is thereby found to be sufficient to fulfill this criterion for arbitrary terminations. The

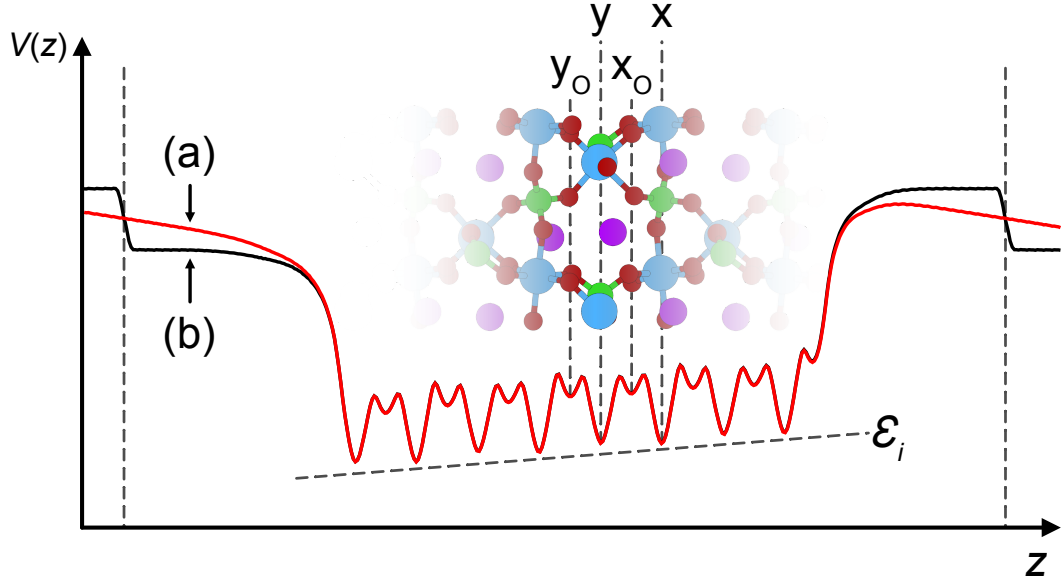


**Figure 6.3:** Planar averaged local potential  $V(z)$  along the  $z$  direction of an unreconstructed Z-cut surface with  $y_o$ - (right) and  $x$ -type (left) termination. Local minima within  $V(z)$  correspond to individual  $x$ ,  $y$ ,  $x_o$  and  $y_o$  layers, as depicted in the inset. Electrostatic interactions between the positive and negative termination give rise to an artificial external electric field within the vacuum region (a), compensated by the inclusion of dipole corrections (b). In both cases, an internal electric field  $\epsilon_i$  within the material prevails. Color coding of the atoms within the inset follows Fig. 6.2.

$k$ -point density in the  $x$ - $y$  plane is chosen to be identical to bulk KTP as  $2 \times 4$  points. The large height of the slab allows for the use of a single  $k$  point along the  $z$  direction. Ionic relaxation of surface and termination layers is performed until the force acting on each atom is smaller than  $0.01 \text{ eV}/\text{\AA}$ .

The facet opposite to the investigated surface is always chosen to be of  $y_o$ -type. This  $y_o$ -type termination consists of two O atoms bound covalently to P and four O atoms with highly ionic bonds to Ti. The remaining dangling bonds introduce spurious metallic states within the band gap of the slab. In the spirit of conventional surface modeling, these dangling bonds would be saturated using one (pseudo) H atom per bond [250]. Unfortunately, the ionic nature of the Ti–O bonds renders this saturation method not practical. However, since the surface energy of this  $y_o$ -type facet is the same for all slabs modeling a specific cut, energetic differences between different terminations remain unaffected by the existence of these unpassivated dangling bonds, yielding reasonable predictions regarding the relative stability of a given termination.

The entire phase space, which has to be investigated, is given by all possible surface stoichiometries, ionically relaxed for all possible starting geometries. Naturally, to cover as much of the phase space as possible, an infinite amount of surface relaxations would have to be performed, posing an insurmountable computational task. The complexity of the problem must therefore be reduced by a number of assumptions. First, the number of surface atoms per unit cell of a specific species is assumed to be limited by its respective number within a given termination layer. For  $x_o$  and  $y_o$ -type layers, this condition limits the

number of terminations to be considered to the set  $\{O_\alpha\}$  with  $\alpha \in \{1, \dots, 6\}$ . Consequently, terminations investigated for x and y-type layers correspond to stoichiometries of the form  $\{K_\alpha Ti_\beta P_\gamma O_\delta\}$  with  $\alpha, \beta, \gamma \in \{0, 1, 2\}$  and  $\delta \in \{0, \dots, 4\}$ . Under this assumption, 564 terminations remain to be modeled. As a second consideration, surface atoms are assumed to prefer relaxation sites close to the minima within their respective potential energy surface (PES) for adsorption onto an unreconstructed surface of a given termination layer. For all KTP constituents and termination layers, these PES are depicted in Figs. C.1 – C.3.<sup>2</sup> A number of conclusions can be drawn from the PES of each constituent regarding its energetically preferred starting position. In the case of K, the PES of all four investigated terminations shows a very flat energetical landscape bearing no significant difference between  $x_0$  and  $y_0$ -type layers. In general, adsorption onto the  $Z^+$  surface turns out to be more favorable, with two distinct local maxima appearing on  $Z^-$ , located at the respective bulk positions of K within the underlying x and y-type layers. This preference is due to the K sublattice being shifted towards the negative  $z$  direction, as previously discussed, rendering the nominal charge of  $Z^+$  slightly more positive compared to  $Z^-$ . The starting position of K is therefore chosen close to the bulk position of the respective layer. A small, random shift is introduced in order to prevent the ion to be stuck in a local minimum. For P and Ti, adsorption sites maximizing the number of saturated O dangling bonds are preferred. This is achieved for sites in the vicinity of an underlying Ti atom, see Fig. C.2 and C.4. Adsorption onto diffusion channels of K along  $z$ , on the other hand, are highly unfavored. In general, adsorption sites corresponding to the bulk positions within the respective layer are found to be relatively favorable as well. A similar preference is found for O on  $x_0$  and  $y_0$  layers, see Fig. C.3. In order to determine each constituent's starting position for a given stoichiometry, the following method is used: All termination atoms are initially placed at their respective bulk positions, randomly displaced by a small shift. Next, the positions of two atoms are switched to be on top of the underlying Ti atom. Which atoms are switched is thereby determined by the adsorption energy of the global minimum within the respective PES. While Ti and P show a similar adsorption energy minimum of  $-9$  eV and  $-8$  eV, respectively, adsorption of O onto the same site only amounts to  $-5$  eV. The hierarchy of switched atoms therefore reads  $Ti \rightarrow P \rightarrow O$ . In the exemplary case of a  $TiP_2O_4$  termination on a  $x_0$ -type layer, the Ti atom as well as one of the P atoms would be placed onto a site of an underlying Ti atom, while all other atoms would remain at their respective bulk position. Regarding the starting position of O within a termination layer of  $x_0$  or  $y_0$  type the situation is more straight forward. According to the PES in Fig. C.3, adsorption onto sites apart from the bulk positions is highly unfavored, with potential barriers being as high as 10 eV. These bulk positions either passivate underlying Ti or P, with adsorption onto P sites being energetically favored by about 0.5 eV. For  $x_0$ - and  $y_0$  layers, O is therefore placed at randomly displaced bulk positions, with adsorption sites on top of P being occupied first.

Since the opposite face of a given termination is not passivated, surface states of  $Z^+$  and  $Z^-$  are expected to appear simultaneously within the KTP band gap. Additionally, due to the internal electric field within the bulk region, surface states of  $Z^+$  and  $Z^-$  experience a nonequivalent shift, further convoluting the overall band structure. In order to identify surface states belonging to only one of the two facets, the wave functions of each state are projected onto the atomic orbitals of every atom within the cell. A surface state can then be identified by a larger projection value for atoms within the first surface layers.

<sup>2</sup>Details about the computational method utilized to obtained each PES are summarized in Appendix C.

## 6.2.2 Results

Phase diagrams of  $Z^+$  and  $Z^-$  surfaces for two different chemical potentials of O under ATM and UHV conditions are shown in Fig. 6.4. Both cuts show a large variety of stable terminations regardless of  $\Delta\mu_O$  within the entire phase space. Bulk terminated  $K_2Ti_2P_2O_4$  and  $O_6$  surfaces are thereby found to be stable at no point.

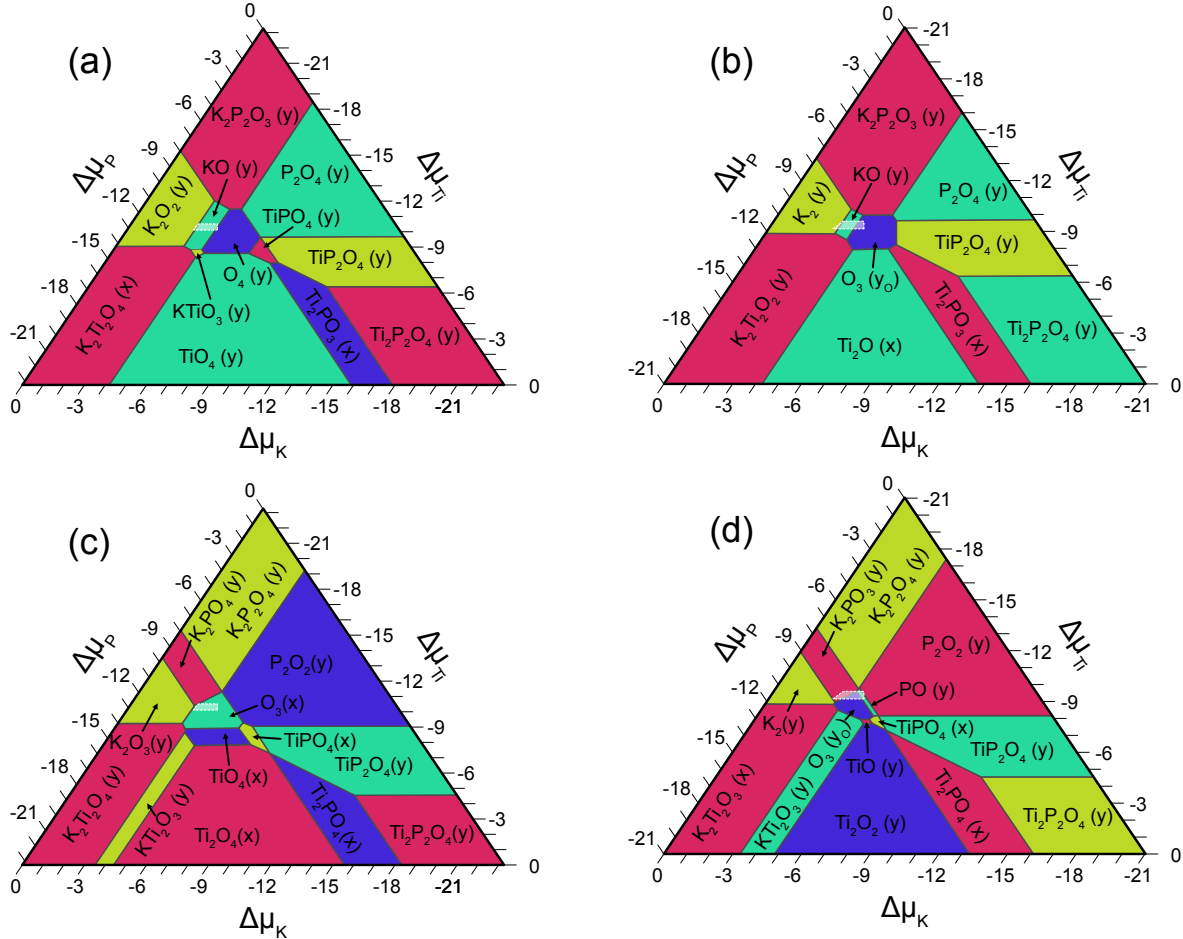


**Figure 6.4:** Phase diagrams of KTP Z-cut surfaces. Stoichiometries of the most stable terminations along with their respective layer type are indicated. (a) and (b) refer to  $Z^+$ , (c) and (d) to  $Z^-$  surfaces. Two different environments governing the value of  $\Delta\mu_O$  are assumed: ATM conditions, yielding  $\Delta\mu_O = -0.27$  eV in case of (a) and (c), UHV conditions, yielding  $\Delta\mu_O = -0.71$  eV in case of (b) and (d). The stability region for KTP formation is indicated in white. Chemical potential variations are given in eV. Coloring of each region serves only as a visual separation of regions with different terminations. Figure adapted from Ref. [232]

As a general trend,  $x_O$ - and  $y_O$ -type terminations are found to be stable only for intermediate values of  $\Delta\mu_K$ ,  $\Delta\mu_{Ti}$  and  $\Delta\mu_P$ . This may be explained by the large number of O, P and Ti dangling bonds introduced via  $x$  and  $y$ -type layers not being adequately passivated solely by O. Furthermore, the differences in surface energy between equal terminations of  $x$  and

$y$  type as well as  $x_O$  and  $y_O$  type are very small, on average amounting to a few 100 meV. Additionally, the differences between the energetically most favored terminations at each point are found to be very small, with energetic differences amounting to the same typical order of a few 100 meV. For this reason, stoichiometries of experimentally observed surfaces can be expected to be prone to temperature variations as well as kinetic effects.

By changing the chemical environment from ATM to UHV conditions, terminations with lower O content are expected to become more stable for both surfaces. Taking the entire phase space into account, this behavior is indeed observed, with  $K_2(y)$ , the only termination not involving O, being solely stable for UHV conditions. Furthermore, this effect is found within the respective stability regions for high O coverage. On  $Z^+$ , a small region of stable  $O_4(y)$  for ATM conditions becomes unstable for UHV, giving rise to a region of stable  $O_3(y_O)$ , which, considering the underlying  $y$ -type layer, features a much smaller O content on the surface. A similar effect is found for  $Z^-$ , with  $O_3(x)$  being exchanged for  $O_3(y_O)$ .

In total, five stable phases are found to exist on both cuts within the stability region. The relaxed structures of each phase are depicted in Fig. 6.5 and 6.6 for  $Z^+$  and  $Z^-$ , respectively. With the exception of  $K_2(y)$ , all stable reconstructions consist of at least one O atom per unit cell, while no stable termination featuring Ti is found. This indicates a high O coverage, as well as a depletion of Ti on Z-cut surfaces for common chemical environments. A number of common structural motifs for stable reconstructions on either surface may be identified. First, structural relaxation is mainly limited to the outermost 2–3 layers, reflecting a weaker coupling between layers along the  $z$  direction, compared to  $x$  and  $y$ . Additionally, for  $O_3(y_O)$  as the only stable  $y_O$ -type termination, the fourfold coordination of the underlying P is highly preserved by the terminating O, while out of the four total dangling bonds of the underlying two Ti atoms, only one is saturated. The preservation of the  $PO_4$  structure is also observed within the termination layer for all reconstructions featuring terminating P as well as O, see  $PO(y)$ ,  $P_2O_2(y)$  and  $K_2PO_3(y)$  on  $Z^-$ . For high O coverages, the formation of  $O_2$  dimers is observed, see  $O_4(y)$  on  $Z^+$  and  $O_3(x)$  on  $Z^-$ . This formation is accompanied by a strong distortion of  $TiO_6$  octahedra and  $PO_4$  tetrahedra of the underlying layer, forming additional O–O bonds. Additionally, an increase in unsaturated O bonds due to a higher O coverage causes a stronger outward relaxation of K atoms, both within the terminating layer as well as within the bulk, due to the Coulomb attraction between O and  $K^+$ .

Apart from those common structural motifs, stable terminations on  $Z^+$  and  $Z^-$  show pronounced differences, as expected for nonequivalent faces of a polar surface. Reconstructions on  $Z^+$  and  $Z^-$  featuring the same stoichiometry are found for no point within the stability region. Stoichiometrically,  $Z^+$  is more likely to reconstruct incorporating K, while the only stable terminations featuring P are found on  $Z^-$ . This may again be attributed to the polarity of either face, preferring adsorption of atoms either in a nominally positive or negative charge state. On average, O coverage is slightly higher for the  $Z^-$  surface.

While no experimental study directed towards resolving specific differences in the reconstructions of  $Z^+$  and  $Z^-$  has yet been published, Atuchin *et al.* [34, 35] have addressed the overall structure and morphology of the (011) and (001) crystal faces. Using X-ray photoelectron spectroscopy (XPS), reflection high-energy electron diffraction (RHEED) and atomic force microscopy (AFM), the as-grown (001) face was determined to be covered by an amorphous layer depleted of the most volatile elements P and K for temperatures above 650°C. This layer was shown to be composed of the anatase phase of  $TiO_2$ . Considering the full phase diagram for KTP formation in Fig. 6.1, this amorphous layer would thus trans-

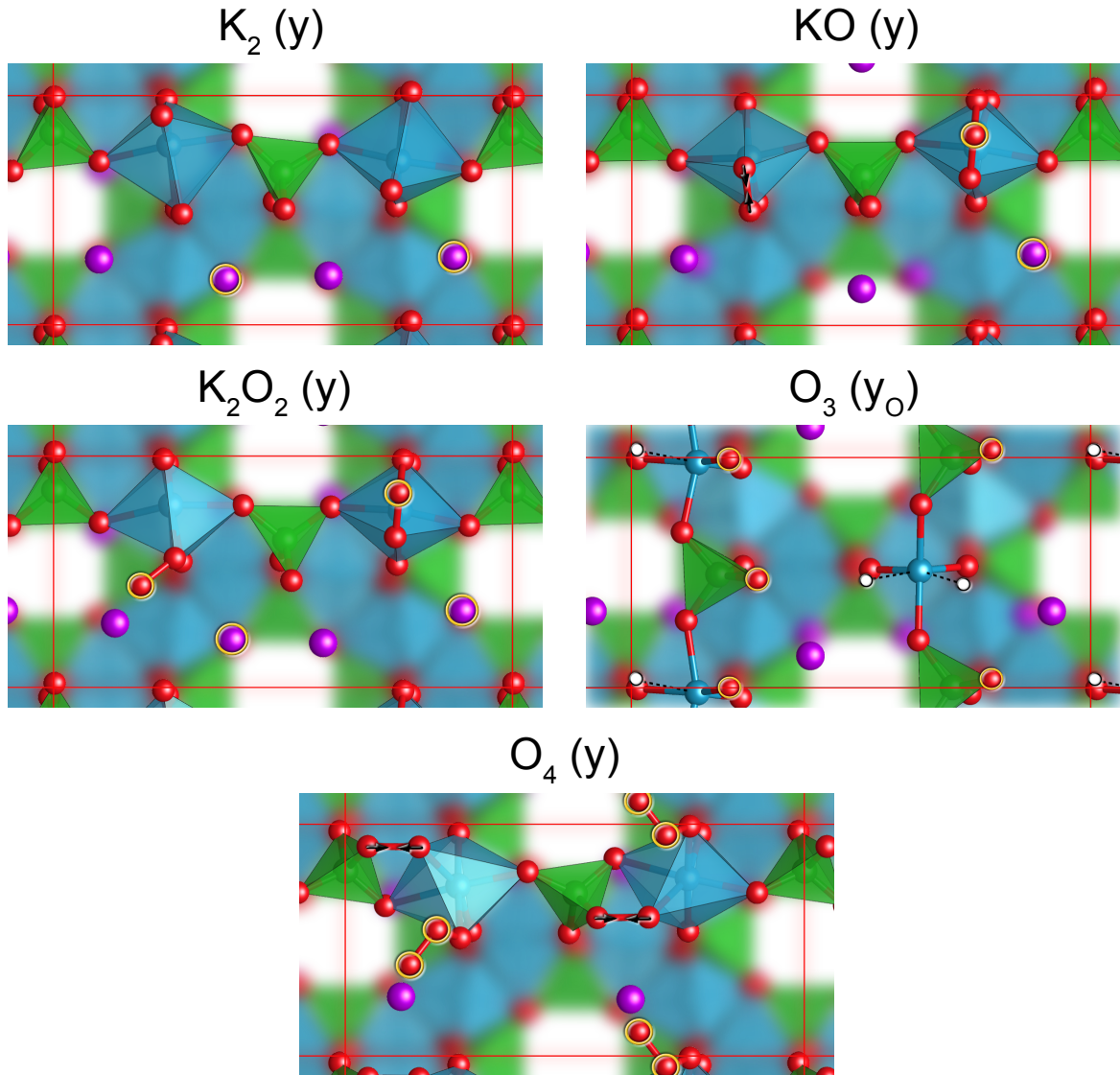


**Figure 6.5:** Atomic structure of the five stable terminations on the KTP  $Z^+$  surface, see Fig. 6.4. Surface atoms of the outermost layer are highlighted in yellow and unreconstructed KTP is depicted with blurry polyhedra. Arrows indicate pronounced rearrangements of O atoms (compared to the bulk cut) due to structural relaxation. Expected positions of O within bulk cut forming  $\text{TiO}_6$  octahedra are highlighted with white circles and indicate unsaturated Ti dangling bonds. Color coding of the atoms follows Fig. 6.2.

late to a chemical environment with  $\Delta\mu_{\text{Ti}} < -9$  eV, which favors decomposition of KTP into  $\text{TiO}_2$  (A),  $\text{P}_2\text{O}_5$  and  $\text{K}_2\text{O}$ . Mechanical polishing and subsequent  $\text{Ar}^+$  bombardment led to a removal of the amorphous layer. XPS data of the polished surface revealed a relative element content very close to bulk KTP. Thus, the polished (001) face of KTP is suggested to be terminated essentially bulk-like, at variance to our calculated stable terminations, which clearly differ stoichiometrically from bulk cut for both end facet. However, a comparison between these findings is not directly possible. The previously mentioned high sensibility

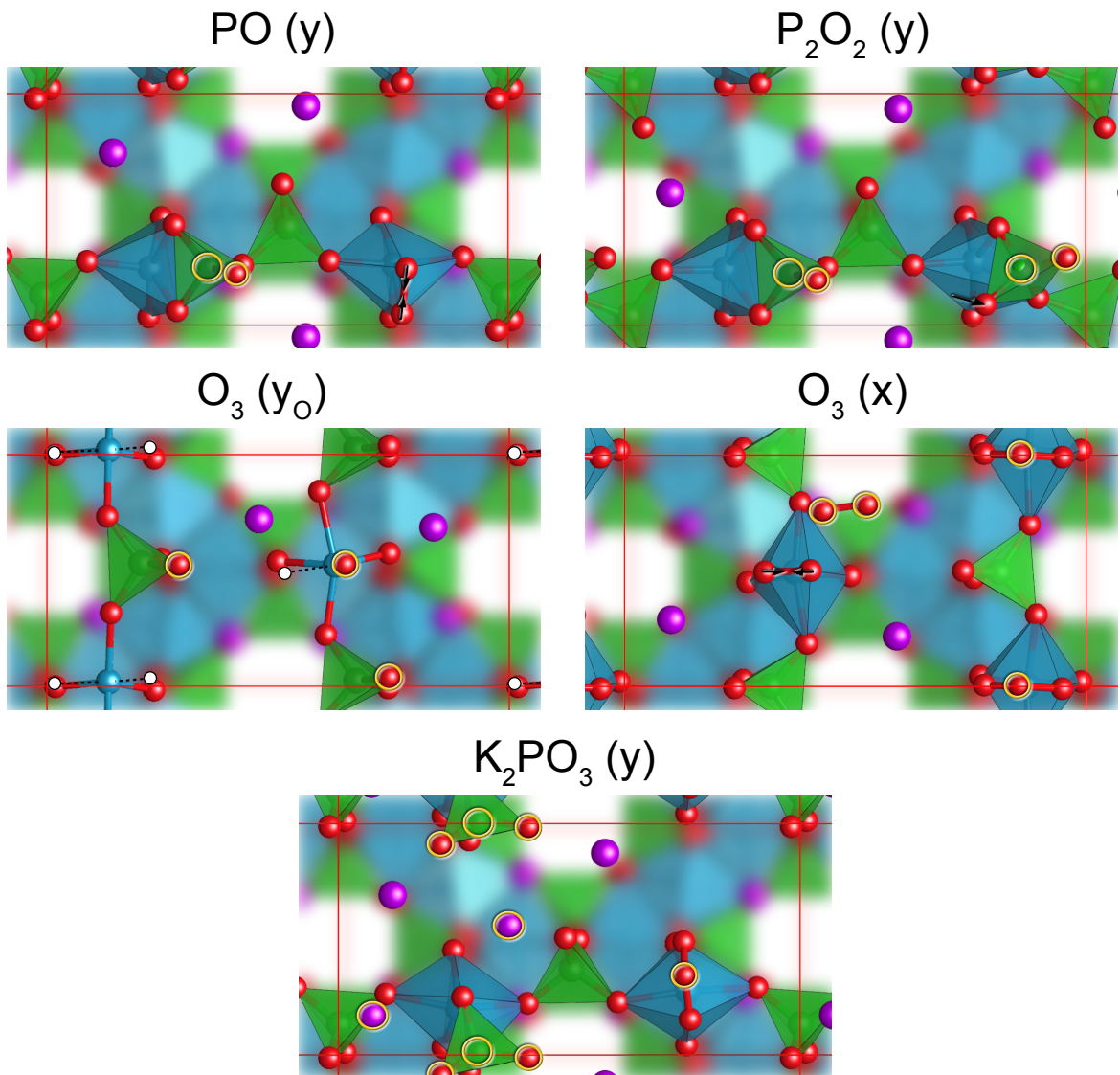


**Figure 6.6:** Atomic structure of the five stable terminations on the KTP  $Z^-$  surface. Symbol and color coding follows Fig. 6.5.

of the Z-cut terminations to external perturbations would result in the mechanical polishing driving the system away from the thermodynamical equilibrium and thus to highly different stable terminations.

The changes in surface stoichiometry, re-bonding processes and structural modifications accompanying the KTP surface formation naturally have an effect on the surface band structure. Due to the general enrichment of O on  $Z^+$  and  $Z^-$ , dangling bond states related to  $O_{2p}$  orbitals are expected to appear within the KTP bulk band gap region. Indeed, the band gap of all stable terminations is found to be much smaller than in bulk KTP due to occupied O states being pushed above the VBM and, in case of some terminations, due to unoccupied Ti states being pushed below the CBM. This shift is exemplarily illustrated with the surface band structures of KO (y) on  $Z^+$  and  $O_3$  ( $y_O$ ) on  $Z^-$  in Fig. 6.7. Out of every state within the band structure, the depicted surface states thereby feature the largest projection of their

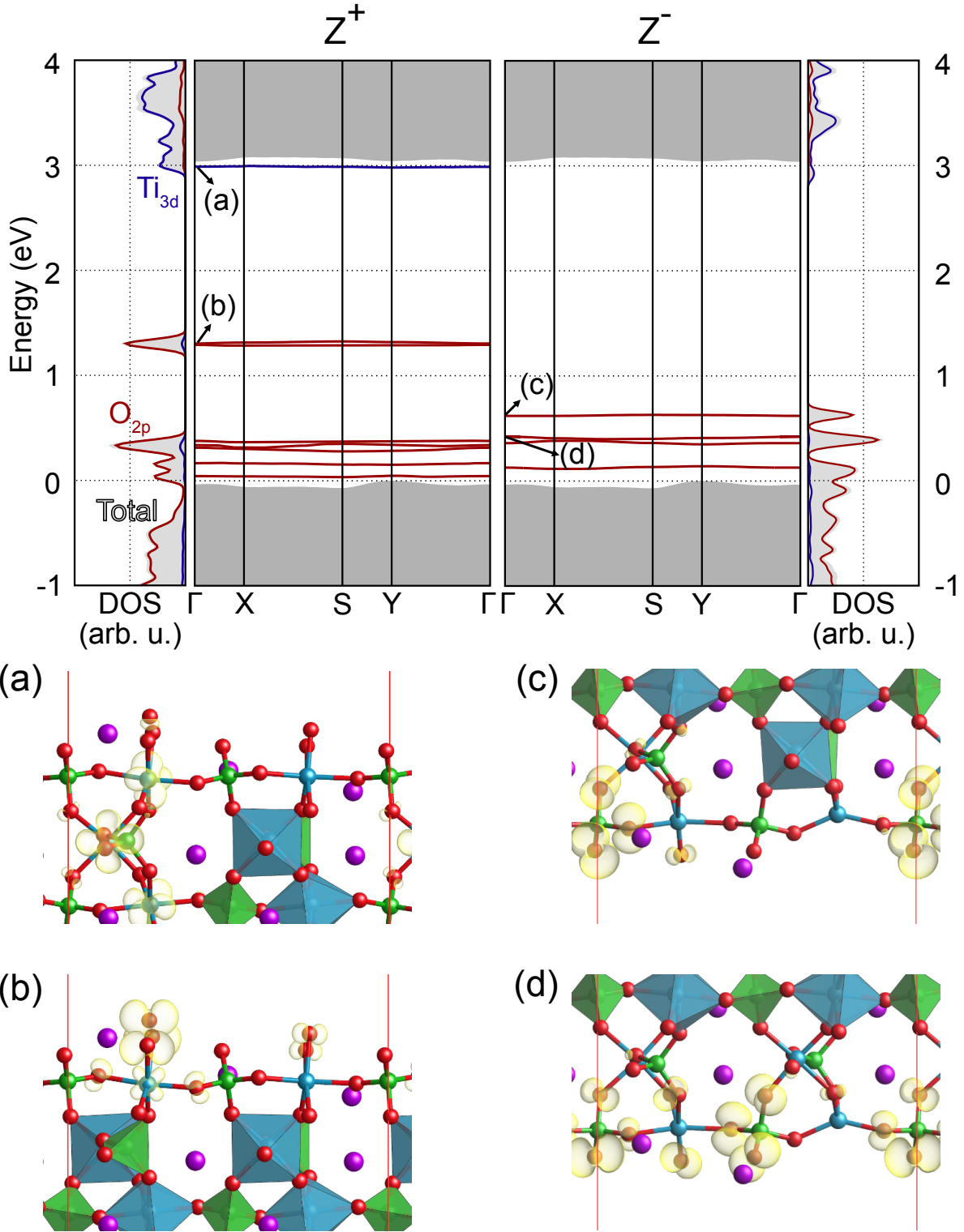


**Figure 6.7:** Top: Localized surface states of the KO(y) termination on  $Z^+$  and of  $O_3$  ( $y_0$ ) on  $Z^-$ . Blue  $Ti_{3d}$  states are empty and red  $O_{2p}$  states are occupied (with the exception of two fractionally filled  $O_{2p}$  states labeled (b)). Shaded areas correspond to the KTP bulk band structure. Bottom: Charge densities of  $Ti_{3d}$  and  $O_{2p}$  related surface states are depicted in (a) – (d). Figure adapted from Ref. [232].

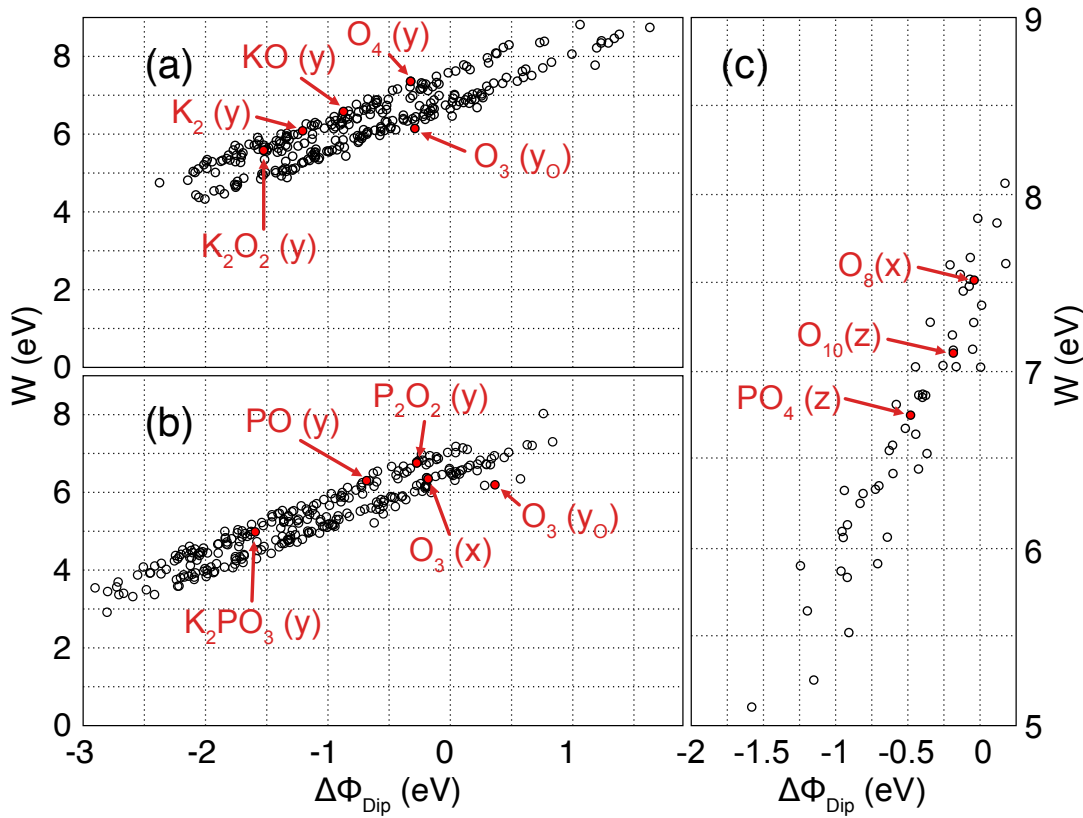


**Figure 6.8:** Work functions  $W$  and the relative change of the surface dipole  $\Delta\Phi_{\text{Dip}}$  (see text) of all investigated terminations on (a)  $Z^+$ , (b)  $Z^-$  and (c)  $Y$ -cut surfaces. In red, stable surfaces are highlighted. Figure adapted from Ref. [232].

wave function onto atomic orbitals of atoms within the outermost four layers. As expected, surface states within the band gap show almost no dispersion and are related entirely to  $O_{2p}$  and  $Ti_{3d}$  states. At least one occupied O state is found for all stable terminations on  $Z^+$  and  $Z^-$ , with some terminations additionally forming partially filled O states (see  $KO(y)$  on  $Z^+$  in Fig. 6.7). However, no general rule between the given surface stoichiometry and the number or character of surface states can be identified. While an increase in O content increases the number of states in most cases, several exceptions to this rule can be identified. In the case of  $O_4(y)$  on  $Z^+$ , as the termination with the highest amount of O, this trend is even reversed, with only three surface states existing within the bulk band gap.

As a possible indicator for the stability of a given surface, the work function  $W$  and induced surface dipole moment  $\Delta\Phi_{\text{Dip}}$  is investigated using the methodology described in Sec. 4.4. The induced surface dipole moment is thereby determined with respect to the unreconstructed  $K_2Ti_2P_2O_4(y)$  termination. In Fig. 6.8 (a) and (b),  $W$  is depicted over  $\Delta\Phi_{\text{Dip}}$  for each investigated termination on both cuts. For both  $Z^+$  and  $Z^-$ , the previously discussed linear relationship between  $W$  and  $\Delta\Phi_{\text{Dip}}$  evidently holds, with a slope of one. The apparent shift between  $x/x_0$  and  $y/y_0$  type terminations stems from using a single reference value for the surface dipole moment of all four types. In general, terminations on the  $Z^+$  cut show a larger value of the work function compared to  $Z^-$ , reflecting the fact that the nominal surface charge is positive on  $Z^+$  and negative on  $Z^-$ . A similar difference

in the work function of opposite facets was found for the (0001) surface of  $\text{LiNbO}_3$ : Values of 6.2 eV and 4.6 eV were reported for the positive and negative facet, respectively [251]. A proposed trend for stable polar surfaces to minimize both the work function as well as the induced surface dipole [186], as qualitatively observed on the LN (1̄100) surface, is not observed for KTP Z-cut surfaces. On both facets, the values of  $W$  and  $\Delta\phi_{\text{Dip}}$  for every stable termination scatter in a range of about 2 eV.

### 6.3 Y Cut

The Y-cut surface of KTP is modeled in a similar fashion to Z cut via a slab geometry consisting of periodic repetitions of bulk KTP along the  $y$  direction. Along  $y$ , bulk KTP is composed of alternating layers with stoichiometries  $\text{Ti}_2\text{P}_2\text{O}_{12}$  and  $\text{K}_4\text{Ti}_2\text{P}_2\text{O}_6$ . Apart from the stoichiometry, both layers differ with respect to the orientation of the Ti–O–P chain structure, see Fig. 6.9 (a) and (b). According to the orientation,  $\text{K}_2\text{Ti}_2\text{P}_2\text{O}_6$  and  $\text{Ti}_2\text{P}_2\text{O}_{12}$  will, in the following, be referred to as x and y-type layer, respectively. Unlike for KTP Z cut, the displacement of K atoms along the surface normal with respect to the height of the x-type layer is symmetric. Considering an additional symmetric displacement of Ti, P and O for each layer, the Y-cut surface is therefore not polar, making the top and bottom facet structurally equivalent.

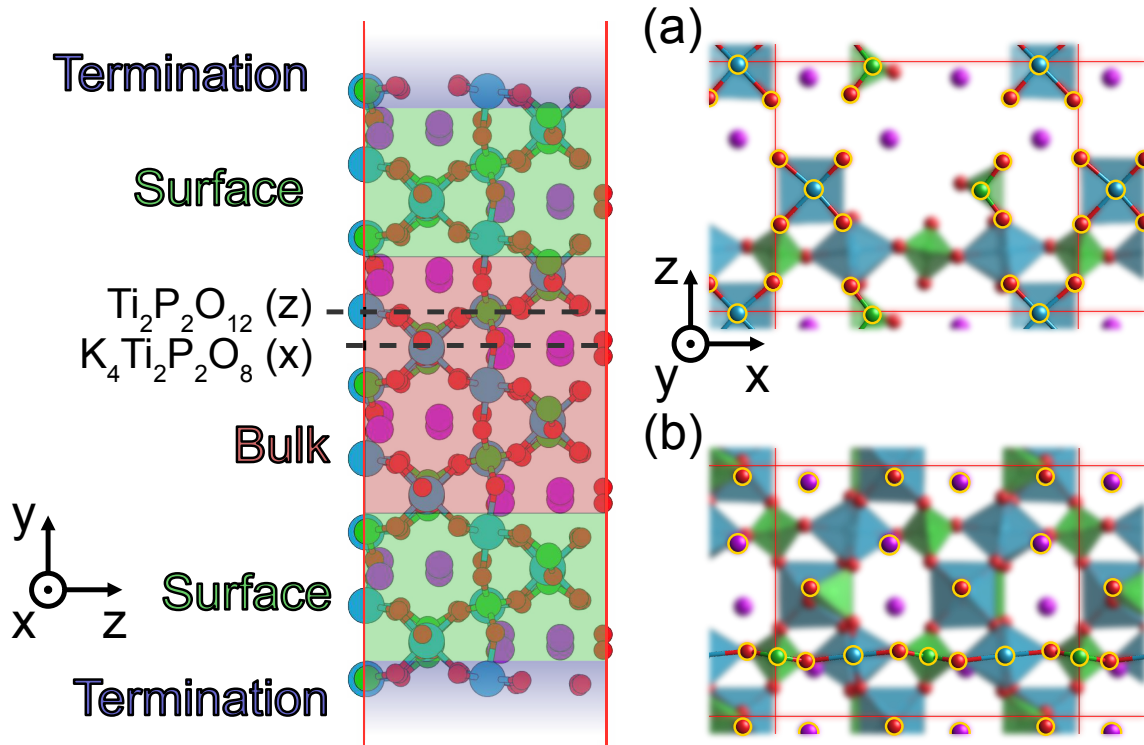


**Figure 6.9:** Left: Stacking sequence of  $\text{Ti}_2\text{P}_2\text{O}_{12}$  and  $\text{K}_4\text{Ti}_2\text{P}_2\text{O}_6$  layers in Y-cut KTP. Bulk layers remain fixed during relaxation and all four surface layers as well as the termination atoms are free to relax. The color coding follows Fig. 6.2. Right: Atomic geometries of the two bulk cuts (a)  $\text{Ti}_2\text{P}_2\text{O}_{12}$  (z) and (b)  $\text{K}_4\text{Ti}_2\text{P}_2\text{O}_6$  (x). In yellow, surface atoms are highlighted. Figure adapted from Ref. [232].

### 6.3.1 Structural Modelling

Due to the nonpolar nature of Y cut, the slab used to model different surface terminations may be constructed symmetrically along the  $y$  direction, see Fig. 6.9 (lhs). The bulk and surface regions thereby contain 7 and 4 layers, respectively. Compared to Z cut, the  $k$ -point density in the  $x$ - $z$  plane is reduced to  $2 \times 2$  due to the larger lattice constant along  $z$ . Apart from that, all numerical parameters are identical to those for the investigation of Z cut.

In order to consider every possible stoichiometry for the termination layer up to the bulk-cut stoichiometry, a total of 522 layers with structural formulae  $K_\alpha Ti_\beta P_\gamma O_\delta$  and  $Ti_\beta P_\gamma O_\epsilon$  would have to be modeled ( $\alpha \in \{0, \dots, 4\}$ ,  $\beta \in \{0, 1, 2\}$ ,  $\gamma \in \{0, 1, 2\}$ ,  $\delta \in \{0, \dots, 8\}$  and  $\epsilon \in \{0, \dots, 12\}$ ). However, taking into account the results obtained for the Z-cut surface, stable terminations are expected to be enriched in O. Therefore, only a smaller subset of the entire phase space is taken into account. In particular, we will focus on terminations likely to saturate the dangling bonds of x and z-type bulk cut, i.e., rich in O and P. In total, 56 terminations for x and z-type layers are investigated, see Tab. 6.1. Only a small number of Ti-rich terminations will be taken into account, since the large amount of dangling bonds introduced by each Ti atom in the termination layer can not be adequately saturated, as seen for the most stable surfaces on Z cut. Additionally, enrichment of K is only taken into account for a few number of x-type terminations. However, the general chemical trend for stable Y-cut surfaces is expected to be well captured by the given choice of stoichiometries.

The starting positions of each atom within the termination layer is chosen by similar arguments as for Z cut. In particular, P, Ti and K atoms are placed close to their respective, randomly displaced bulk positions. Starting positions of O are chosen based on the amount of P and Ti within the termination layer. Taking an O atom within a x-type layer as an exemplary case, four starting positions for this atom are considered, in which it saturates a dangling bond related to (i) an underlying P atom (threefold coordinated), (ii) an underlying Ti atom (fivefold coordinated), (iii) a P atom within the termination layer already twofold coordinated to the underlying layer or (iv) a P atom within the termination layer

**Table 6.1:** Investigated terminations on the KTP Y-cut surface for x and z-type layers.

x-type			z-type		
K	$O_3$	$P_2O_8$	O	$O_{12}$	$TiO_5$
$K_2$	$O_4$	Ti	$O_2$	P	$Ti_2$
$K_2Ti_2P_2$	$O_8$	$Ti_2$	$O_3$	$PO_2$	$Ti_2O_6$
$K_2Ti_2P_2O_8$	P	$Ti_2P_2$	$O_4$	$PO_3$	$Ti_2O_8$
$K_3Ti_2P_2O_8$	PO	$Ti_2P_2O_8$	$O_5$	$PO_4$	$Ti_2O_{10}$
$K_4$	$PO_2$		$O_6$	$P_2$	$Ti_2P_2$
$K_4Ti_2P_2$	$PO_3$		$O_7$	$P_2O_4$	$Ti_2P_2O_{12}$
$K_4Ti_2P_2O_8$	$PO_4$		$O_8$	$P_2O_6$	
$KTi_2P_2O_8$	$P_2$		$O_9$	Ti	
O	$P_2O_2$		$O_{10}$	$TiO_3$	
$O_2$	$P_2O_4$		$O_{11}$	$TiO_4$	

not coordinated at all. Tests with a  $P_2O_2$  (x) termination show that the total energy is minimized, if the two O atoms within the termination layer are placed in a way to fulfill cases (iii) and (iv). On the other hand, case (ii) is found to be energetically highly unfavorable. For this reason, O atoms are, in the following, positioned according to the following priority ranking. First, dangling bonds of P atoms within the termination layer are saturated. Next, the saturation of underlying P atoms is ensured. If more O atoms are left, they are placed in a way to saturate underlying Ti. Lastly, all remaining O atoms are placed at their respective bulk positions.

### 6.3.2 Results

The surface phase diagrams of KTP Y cut for ATM and UHV conditions are depicted in Fig. 6.10 (a) and (b), respectively. By considering only a small subset of all possible surface stoichiometries, both phase diagrams are much less clustered compared to Z cut. One general chemical trend is evidently fulfilled: An increase in chemical potential variation  $\Delta\mu_i$  leads to stable terminations being richer of element  $i$ . In particular, the abundance of O on all stable terminations within the stability regions increases noticeably upon going from UHV to ATM conditions. In total, three terminations fall within the KTP bulk stability region:  $O_{10}$  (z) and  $O_8$  (x) for ATM and  $PO_4$  (z) for UHV conditions. Due to the particular choice of atomic starting positions and structural reconstruction, all three terminations share the preservation of the fourfold coordination of P within the surface layers, see Fig. 6.11.

Additionally, under ATM conditions, the stable  $O_{10}$  (z) and  $O_8$  (x) terminations arrange in a way to form  $O_2$  dimers on the surface. A strong relaxation of O within the underlying

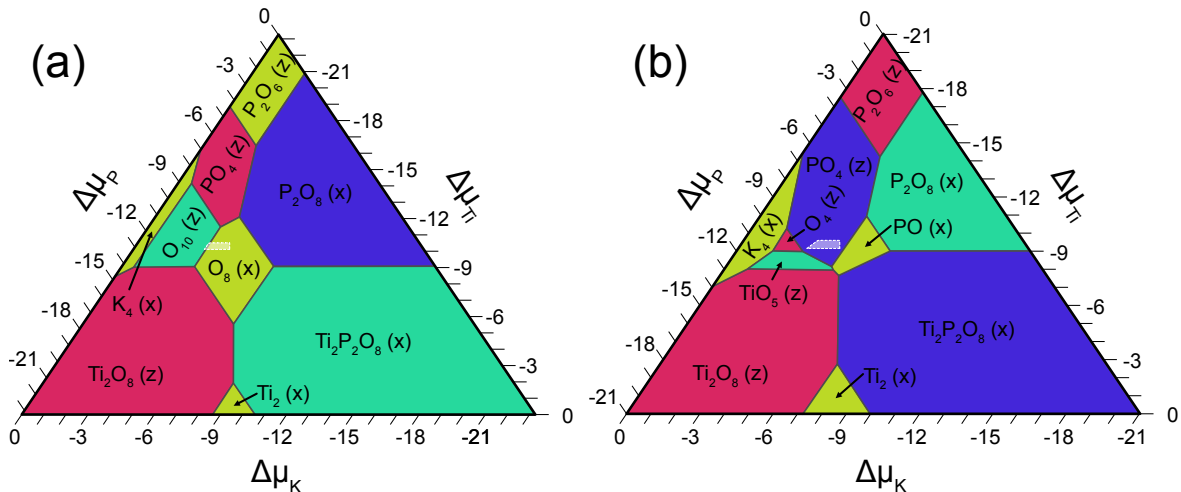


**Figure 6.10:** Phase diagrams of KTP Y cut for different values of  $\Delta\mu_O$ : ATM conditions ( $\Delta\mu_O = -0.27$  eV) in (a) and UHV conditions ( $\Delta\mu_O = -0.71$  eV) in (b). Stoichiometries of most stable terminations are indicated along their respective layer type. The stability region for KTP formation is indicated in white. Chemical potential variations are given in eV. Coloring of each region serves only as a visual separation of regions with different terminations. Figure adapted from Ref. [232].

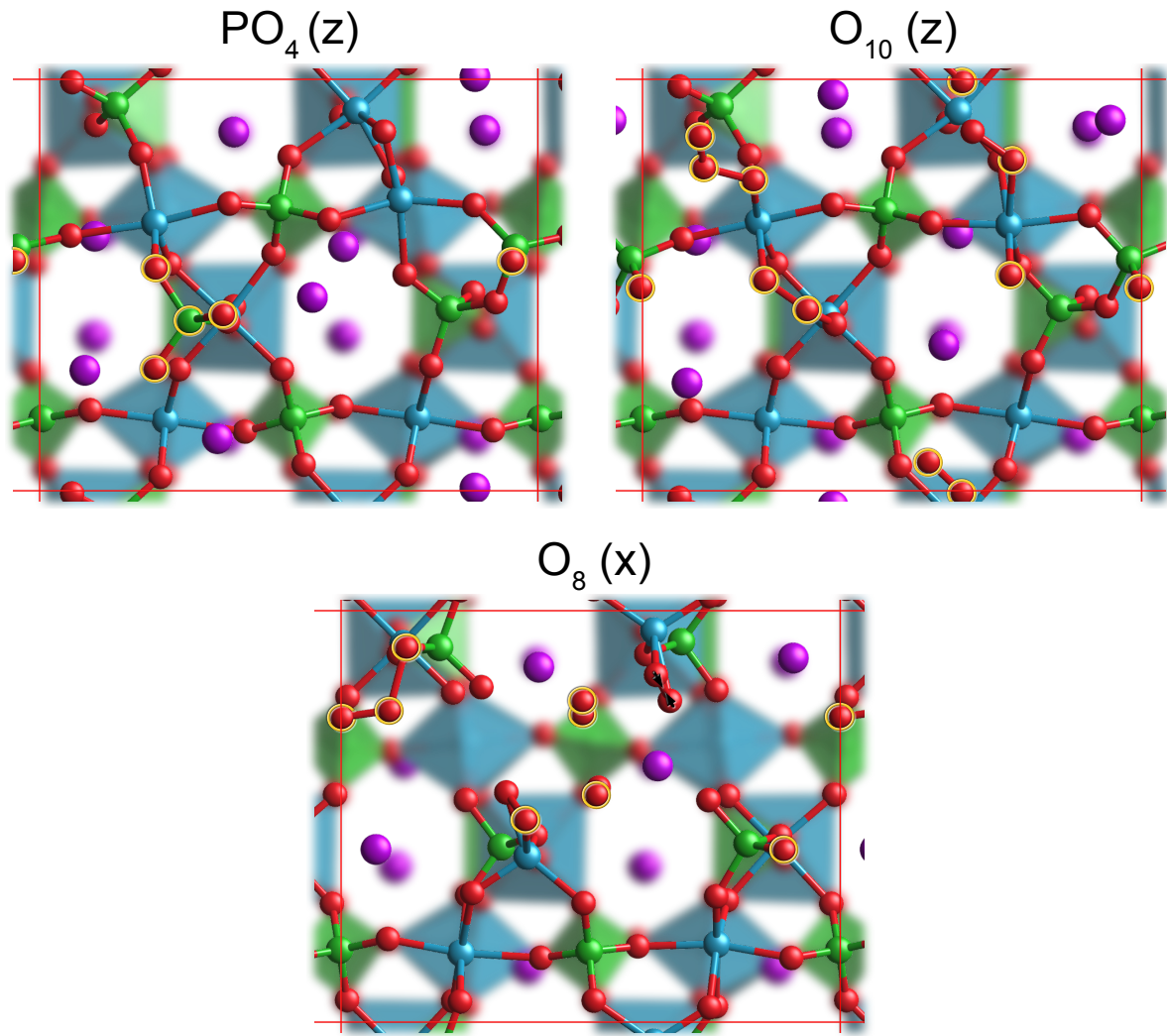


**Figure 6.11:** Atomic structure of the three stable terminations on the KTP Y-cut surface. Symbol coding follows Fig. 6.5.

layer is also observed, with two O atoms adjacent to fivefold terminated Ti forming a dimer bond, as seen for  $O_8$  (x). This tendency goes in line with the findings for Z cut, where the formation of  $O_2$  dimers was observed for O-rich conditions, see  $O_4$  (y) in Fig. 6.5.

The abundance of O on the surface is reflected in occupied  $O_{2p}$  states appearing above the VBM within the band gap of bulk KTP, as shown for  $PO_4$  (z) in Fig. 6.12. Their presence leads to a noticeable shrinkage of the band gap. In the case of  $PO_4$  (z), this shrinkage leaves a band gap of 2.3 eV, i.e., only about 75 % of its value in bulk KTP. Due to the higher number of O dangling bonds for  $O_{10}$  (z) and  $O_8$  (x) terminations, more surface states are present within their respective band structure, shrinking the band gap even further, down to values as low as 0.2 eV.

Similar to Z cut, a clear correlation between the stability of a given termination, its work function and its induced surface dipole (with respect to an unreconstructed surface with z-type termination layer) cannot be found, see Fig. 6.8 (c). Although all three stable terminations share a high value of  $\Delta\Phi_{Dip}$  and  $W$ , this is most likely related to the relatively

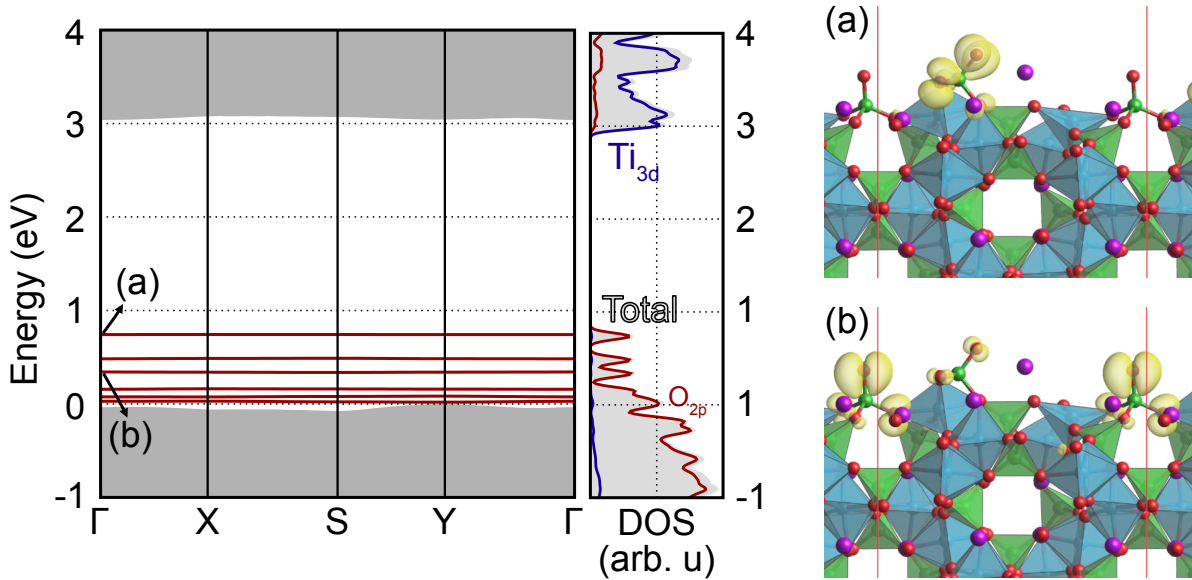


**Figure 6.12:** Left: Localized occupied surface states of the  $\text{PO}_4(\text{z})$  termination on KTP Y cut. Shaded areas correspond to the KTP bulk band structure. Right: Charge densities of two prominent surface states related to  $\text{O}_{2\text{p}}$  are depicted in (a) and (b). Figure adapted from Ref. [232].

small sample size of investigated stoichiometries. On average, stable terminations on Y cut show a slightly higher work function compared to those on Z cut.

## 6.4 Conclusions

For KTP Z and Y-cut surfaces, phase diagrams have been determined on the basis of *ab initio* total-energy calculations under the assumption of an O rich environment under UHV and ATM conditions. A number of stable terminations with different stoichiometries could be identified for both cuts, depending on the chemical potentials of all constituents. Energetically stable terminations for an individual cut vary only slightly in formation energy, hinting towards a strong influence of thermal and kinetic effects on the surface reconstructions. A number of common structural and electronic features are identified to characterize stable terminations on both cuts. For one, a depletion of Ti and abundance of O is found in the case of virtually all stable terminations within the stability region for KTP formation. This indicates that dangling bonds arising from O, P and Ti on the surface are more likely to be saturated by O rather than Ti. Additionally, all stable terminations have a tendency to preserve a fourfold coordination of P within the surface layers. The enrichment in O leads to occupied  $\text{O}_{2\text{p}}$  states being lifted above the VBM of bulk KTP, resulting in a noticeable shrinking of the fundamental band gap. A correlation between the stability of a termination, its work function and its induced surface dipole could not be found for either cut.

While Z and Y cut share similar surface motifs, a number of differences between the  $\text{Z}^+$  and  $\text{Z}^-$  facet could be made out. For one, both facets share no identical stable termination for any point within the phase diagram. Additionally, due to the polar nature of KTP Z cut, stable terminations on  $\text{Z}^+$  are found, on average, to feature a higher content of K. For the

same reason, terminations on  $Z^-$  are found to be more O rich compared to  $Z^+$ .

Two words of caution, however, have to be added regarding the interpretation of these results. First, the assumption of molecular  $O_2$  being the O reservoir renders only a tiny region of the entire four-dimensional phase space accessible. It would therefore be reasonable to assume the abundance of O within stable terminations to be a result of  $\Delta\mu_O$  being close to 0. However, increasing its value for  $Z^+$  and  $Z^-$  results in an overall stabilization of the  $O_3$  (y) termination within the KTP stability region. This suggests the O enrichment to be a universal feature for stable terminations in arbitrary chemical environments within the entire stability region. Second, the presence of four constituents on the surface renders the available phase space for surface formation insurmountably large, both in terms of stoichiometry and actual surface geometry. Having made the previously mentioned assumptions regarding the starting geometry for structural relaxation it is unclear, if the true energetic minimum for a given stoichiometry is truly captured. To our knowledge, no general rule exists to characterize stable polar surfaces involving covalent as well as ionic bonds, akin to the electron counting rule for low-index surfaces of semiconductors [252, 253]. The overall stability of a given surface reconstruction is therefore particularly difficult to assess based on the geometry alone. The present study therefore primarily serves as a first estimation regarding the stoichiometry of stable KTP Z and Y-cut surfaces and is expected to give an insight into the influence of reconstruction geometries on the formation of electronic surface states.



# 7

## Summary

On the footing of ground and excited-state DFT calculations, the ferroelectric material KTP and its isomorphs RTP and KTA have been characterized and systematically compared based on their spectroscopic signatures, in particular their linear optical response and Raman cross section. In addition, the influence of the chemical environment on the morphology and electronic structure for the technologically most important [010] and [001] faces of KTP was investigated.

In conclusion, the three main questions driving this thesis, as introduced in Chapter 1, may be addressed in the following way:

### 1. What is the true dielectric response function of KTP, RTP and KTA?

The dielectric function of all three materials was determined on the IPA, IQPA and BSE levels of theory, stepwise including quasiparticle and excitonic effects. On the IPA level, the dielectric function's low-energy regime was found to be essentially composed of a small number of peaks at around 3 eV, originating from transition between  $O_{2p}$  valence and  $Ti_{3d}$  conduction states. Apart from a small rigid redshift, the dielectric functions of KTP and RTP on the IPA level are nearly identical, reflecting the fact that optical absorption is governed by the Ti and O sublattice, with the alcali atom having only an indirect influence via a change in lattice constant. In KTA, on the other hand, optical absorption in the mid-energy region at around 6 eV is higher compared to KTP and RTP due to an admixture of  $As_{4p}$  orbitals to the conduction states. The anisotropy of the dielectric functions could be traced back to (i) a pronounced distortion of  $PO_4$  and  $TiO_6$  polyhedra along the  $x$  direction compared to  $y$  and (ii) a difference in  $TiO_6$  density along  $z$  compared to  $x$  and  $y$ .

The transport gaps, as indicators for the onset of the dielectric function, were shown to be affected significantly by quasiparticle effects, introducing a dispersionless widening of around 2.3 eV compared to the gap within DFT-PBEsol. For KTP, RTP and KTA, the lower bound of the transport gap was predicted at 5.23 eV, 5.30 eV and 5.24 eV, respectively. Consequently, quasiparticle effect were found to introduce a rigid blueshift of all spectra by around 2.3 eV.

Including excitonic effects by solving the BSE, all spectra were redshifted again by an amount corresponding to the binding energy of the respective first bright exciton. For KTP, RTP and KTA, this binding energy was evaluated as 1.47 eV, 1.38 eV and 1.51 eV, respectively. A comparison of the theoretical data for KTP with experimental data [200] revealed an overall satisfying reproduction of the reflectivity onset and line shape on the BSE level of theory.

For the first time, the importance of quasiparticle and excitonic effects on the dielectric response of members of the KTP family was demonstrated. The overall good reproduction of the absorption onset on the independent-particle level, as frequently seen in literature, could thus be explained by a partial error cancellation between the large exciton binding energy and the electronic self energy.

## 2. What is the correct assignment between phonon modes and observed Raman bands in bulk KTP, RTP and KTA?

Phonon spectra and Raman cross sections of KTP, RTP and KTA were calculated using DFPT routines. A subdivision of the phononic DOS into regions of modes with predominantly K/Rb, P and As-type displacement patterns could be made out, in accordance to the prior phenomenological mapping by Kugel *et al.* [25]. In addition, all three materials were found to possess a gap region around  $800\text{ cm}^{-1}$  (KTP and RTP) and  $650\text{ cm}^{-1}$  (KTA), populated predominantly by phonons involving the displacement of the O(9) and O(10) sublattice. In particular, two of these modes exhibit  $A_1$  symmetry and are thus detectable within the main diagonal polarization configurations ( $x, x$ ), ( $y, y$ ) and ( $z, z$ ): Modes  $\nu_{\text{ip}}$  and  $\nu_{\text{ap}}$  at around  $620\text{ cm}^{-1}$  and  $800\text{ cm}^{-1}$ , respectively, involving an in-phase and anti-phase distortion of the  $\text{TiO}_6$  cage along [001]. In accordance with the results of Kugel *et al.*, both modes are expected to feature high Raman intensities and thus enable a mapping between experimental Raman bands and calculated phonon modes.

This assumption, however, is only partially supported by a comparison between calculated and experimental [223] Raman spectra of all three materials. In particular, the highest experimental  $A_1$ -type peak  $\nu_1$ , located at around  $690\text{ cm}^{-1}$  (KTP and RTP) and  $670\text{ cm}^{-1}$  (KTA), can not be directly mapped to any calculated phonon mode. A frequency-based mapping between  $\nu_1$  and  $\nu_{\text{ap}}$  is supported by the fact that an observed discrepancy in frequency is partially explainable by the utilized PZ-LDA functional. The calculated Raman intensity of the mode  $\nu_{\text{ap}}$ , however, is observed to be highly anisotropic, being highest within ( $y, y$ ) polarization and nearly vanishing within ( $x, x$ ). This is in stark contrast to the experimentally observed Raman intensity of mode  $\nu_1$ , which dominates the spectra for all materials and polarization configuration.

As the origin of this discrepancy remains unknown, additional mappings between experimental Raman peaks and calculated phonon modes are not expected to give further meaningful insights. It is argued, however, that the existence of K and Rb vacancies is partially responsible for a relative intensity shift between low and mid-frequency Raman peaks. For this reason, future theoretical evaluation of Raman spectra of nonstoichiometric KTP, RTP and KTA is expected to at least partially close the observed discrepancy and provide means for further analyses.

---

**3. What are the thermodynamically most stable reconstructions of [010] and [001] surfaces of KTP?**

Using slab geometries, more than 600 surface terminations of varying stoichiometries have been modeled for the KTP Z cut and Y cut surface. The phase diagrams in dependence of the chemical potential of all constituents revealed a number of similarities between thermodynamically most stable terminations on both cuts: (i) Stable terminations for nearly all chemical environments within the KTP stability region feature an abundance of O and depletion of Ti, (ii) the fourfold coordination of underlying P is highly preserved for virtually all stable terminations and (iii) no correlation between the stability of a given surface and its respective work function and induced surface dipole is observed. The abundance of O is thereby found to introduce occupied surface states above the bulk VBM, leading to a noticeable shrinkage of the bulk band gap.

For KTP Z cut, the two facets of opposite polarity,  $Z^+$  and  $Z^-$ , are structurally not equivalent, rendering their respective stable terminations to be of higher K and O content. Overall, the energetical landscape within the phase diagram of Z-cut KTP is found to be relatively flat, making stable terminations on Z-cut surfaces prone to thermal and kinetic effects.

Due to the high complexity of the KTP termination layers on Z cut and Y cut, only a very small region of the full phase space could be accessed by the present study. In particular, by far not all possible surface stoichiometries and starting positions could be captured, owing to the high number of constituents and relatively large surface unit cell. The present findings may thus be regarded as a first estimate of stoichiometric trends on the technologically most important facets of KTP as well as their role in the modulation of the surface band gaps.



# Bibliography

- [1] M. Zhu *et al.*, [Polarization dependent ferroelectric photovoltaic effects in BFTO/CuO thin films](#), Applied Physics Letters **111**, 032901 (2017).
- [2] A. Lipatov *et al.*, [Polarization-Dependent Electronic Transport in Graphene/Pb\(Zr,Ti\)O<sub>3</sub> Ferroelectric Field-Effect Transistors](#), Advanced Electronic Materials **3**, 1700020 (2017).
- [3] L. K. Cheng and J. D. Bierlein, [KTP and isomorphs-recent progress in device and material development](#), Ferroelectrics **142**, 209 (1993).
- [4] Y. S. Liu, D. Dentz and R. Belt, [High-average-power intracavity second-harmonic generation using KTiOPO<sub>4</sub> in an acousto-optically Q-switched Nd:YAG laser oscillator at 5 kHz](#), Optics Letters **9**, 76 (1984).
- [5] G. Rosenman, A. Skliar, M. Oron and M. Katz, [Polarization reversal in KTiOPO<sub>4</sub> crystals](#), Journal of Physics D: Applied Physics **30**, 277 (1997).
- [6] M. Roth, N. Angert and M. Tseitlin, [Potassium titanyl phosphate \(KTP\) - an oxide of choice for nonlinear optical and electro-optic devices](#), in Proc. second Israeli-Russian Binational Workshop, Pages 223–235, Jerusalem, Tel-Aviv, 2003.
- [7] M. Roth, [Stoichiometry and Domain Structure of KTP-Type Nonlinear Optical Crystals](#) (Springer Berlin Heidelberg, Berlin, Heidelberg, 2010), Chap. 20, Pages 691–723.
- [8] Y. Yamamoto, S. Yamaguchi, K. Suzuki and N. Yamada, [Second-harmonic generation in a waveguide with domain-inverted regions like periodic lens sequence on z-face KTiOPO<sub>4</sub> crystal](#), Applied Physics Letters **65**, 938 (1994).
- [9] A. Zukauskas, V. Pasiskevicius, F. Laurell and C. Canalias, [Periodically Poled KTiOAsO<sub>4</sub> for Second Harmonic Generation in the Green Region](#), in CLEO: 2013, Page CW3B.3, Optical Society of America, 2013.
- [10] H. Karlsson, F. Laurell and L. K. Cheng, [Periodic poling of RbTiOPO<sub>4</sub> for quasi-phase matched blue light generation](#), Applied Physics Letters **74**, 1519 (1999).
- [11] A. Fragemann *et al.*, [Frequency converters from visible to mid-infrared with periodically poled RbTiOPO<sub>4</sub>](#), Applied Physics Letters **83**, 3090 (2003).

- [12] C. Eigner *et al.*, [Periodically poled ridge waveguides in KTP for second harmonic generation in the UV regime](#), *Optics express* **26**, 28827 (2018).
- [13] Q. Chen and W. P. Risk, [Periodic poling of KTiOPO<sub>4</sub> using an applied electric field](#), *Electronics Letters* **30**, 1516 (1994).
- [14] V. Y. Shur, E. V. Pelegova, A. R. Akhmatkhanov and I. S. Baturin, [Periodically poled crystals of KTP family: a review](#), *Ferroelectrics* **496**, 49 (2016).
- [15] M. J. Jongerius, R. J. Bolt and N. A. Sweep, [Blue second-harmonic generation in waveguides fabricated in undoped and scandium-doped KTiOPO<sub>4</sub>](#), *Journal of Applied Physics* **75**, 3316 (1998).
- [16] M. Rüsing *et al.*, [Imaging of 180° ferroelectric domain walls in uniaxial ferroelectrics by confocal Raman spectroscopy: Unraveling the contrast mechanism](#), *Physical Review Materials* **2**, 103801 (2018).
- [17] M. Rüsing *et al.*, [Identification of ferroelectric domain structure sensitive phonon modes in potassium titanyl phosphate: A fundamental study](#), *Journal of Applied Physics* **119**, 044103 (2016).
- [18] P. Hohenberg and W. Kohn, [Inhomogeneous Electron Gas](#), *Physical Review* **136**, B864 (1964).
- [19] W. Kohn and L. J. Sham, [Self-Consistent Equations Including Exchange and Correlation Effects](#), *Physical Review* **140**, 1133 (1965).
- [20] I. N. Yakovkin and P. A. Dowben, [The problem of the band gap in LDA calculations](#), *Surface Review and Letters* **14**, 481 (2007).
- [21] J. P. Perdew, [Density functional theory and the band gap problem](#), *International Journal of Quantum Chemistry* **28**, 497 (1985).
- [22] W. Ku and A. G. Eguiluz, [Band-Gap Problem in Semiconductors Revisited: Effects of Core States and Many-Body Self-Consistency](#), *Physical Review Letters* **89**, 126401 (2002).
- [23] A. Riefer, S. Sanna, A. Schindlmayr and W. G. Schmidt, [Optical response of stoichiometric and congruent lithium niobate from first-principles calculations](#), *Physical Review B* **87**, 195208 (2013).
- [24] F. Schmidt *et al.*, [Quasiparticle and excitonic effects in the optical response of KNbO<sub>3</sub>](#), *Physical Review Materials* **3**, 054401 (2019).
- [25] G. E. Kugel *et al.*, [The vibrational spectrum of a KTiOPO<sub>4</sub> single crystal studied by Raman and infrared reflectivity spectroscopy](#), *Journal of Physics C: Solid State Physics* **21**, 5565 (1988).
- [26] G. Placzek and E. Teller, [Die Rotationsstruktur der Ramanbanden mehratomiger Moleküle](#), *Zeitschrift für Physik* **81**, 209 (1933).

- [27] G. Placzek, *Handbuch der Radiologie* Vol. 6 (Akademische Verlagsgesellschaft m.b.H Leipzig, 1934).
- [28] G. Liu *et al.*, Removal of nitrate by photocatalytic denitrification using nonlinear optical material, *Environmental Science & Technology* **50**, 11218 (2016).
- [29] C. Dues, W. G. Schmidt and S. Sanna, Water splitting reaction at polar lithium niobate surfaces, *ACS Publications* **4**, 3850 (2019).
- [30] G. Namkoong *et al.*, III-nitride integration on ferroelectric materials of lithium niobate by molecular beam epitaxy, *Applied Physics Letters* **87**, 171107 (2005).
- [31] Y. Tsuchiya *et al.*, Effects of low-temperature-grown buffers on pulsed-laser deposition of GaN on LiNbO<sub>3</sub>, *Journal of Vacuum Science & Technology A: Vacuum, Surfaces, and Films* **24**, 2021 (2006).
- [32] S. V. Levchenko and A. M. Rappe, Influence of ferroelectric polarization on the equilibrium stoichiometry of lithium niobate (0001) surfaces, *Physical Review Letters* **100**, 256101 (2008).
- [33] S. Sanna and W. G. Schmidt, Lithium niobate X-cut, Y-cut, and Z-cut surfaces from *ab initio* theory, *Physical Review B* **81**, 214116 (2010).
- [34] V. V. Atuchin *et al.*, Study of KTiOPO<sub>4</sub> surface by x-ray photoelectron spectroscopy and reflection high-energy electron diffraction, *Surface and Interface Analysis* **34**, 320 (2002).
- [35] V. V. Atuchin *et al.*, Formation of TiO<sub>2</sub> and KTiOPO<sub>4</sub> nanoclusters on the (001) surface of KTiOPO<sub>4</sub> crystal upon annealing, *Journal of Structural Chemistry* **45**, S84 (2004).
- [36] G. Czycholl, *Theoretische Festkörperphysik* Vol. 3 (Springer-Verlag, 2015).
- [37] C. Rödl, *Elektronische und exzitonische Anregungen in magnetischen Isolatoren*, PhD Thesis, Friedrich-Schiller-Universität Jena, Jena, 2009.
- [38] S. Albrecht, Optical absorption spectra of semiconductors and insulators: *ab initio* calculation of many-body effects, PhD Thesis, École polytechnique, 1999.
- [39] M. Lewin, E. H. Lieb and R. Seiringer, Universal Functionals in Density Functional Theory, arXiv, 2019, 1912.10424.
- [40] R. M. Martin, L. Reining and D. M. Ceperley, *Interacting Electrons* (Cambridge University Press, 2016).
- [41] F. Aryasetiawan and O. Gunnarsson, The GW method, *Reports on Progress in Physics* **61**, 237 (1997).
- [42] M. Levy, Electron densities in search of Hamiltonians, *Physical Review A (General Physics)* **26**, 1200 (1982).
- [43] J. C. Slater and K. H. Johnson, Self-Consistent-Field  $X_\alpha$  Cluster Method for Polyatomic Molecules and Solids, *Physical Review B* **5**, 844 (1972).

- [44] D. M. Ceperley and B. J. Alder, [Ground State of the Electron Gas by a Stochastic Method](#), Physical Review Letters **45**, 566 (1980).
- [45] S. H. Vosko, L. Wilk and M. Nusair, [Accurate spin-dependent electron liquid correlation energies for local spin density calculations: a critical analysis](#), Canadian Journal of Physics **58**, 1200 (1980).
- [46] J. P. Perdew and Y. Wang, [Accurate and simple analytic representation of the electron-gas correlation energy](#), Physical Review B **45**, 13244 (1992).
- [47] J. P. Perdew and A. Zunger, [Self-interaction correction to density-functional approximations for many-electron systems](#), Physical Review B **23**, 5048 (1981).
- [48] J. P. Perdew and K. Schmidt, [Jacob's ladder of density functional approximations for the exchange-correlation energy](#), AIP Conference Proceedings **577**, 1 (2001).
- [49] A. van de Walle and G. Ceder, [Correcting overbinding in local-density-approximation calculations](#), Physical Review B **59**, 14992 (1999).
- [50] J. C. Grossman, L. Mitas and K. Raghavachari, [Structure and Stability of Molecular Carbon: Importance of Electron Correlation](#), Physical Review Letters **75**, 3870 (1995).
- [51] J. P. Perdew, K. Burke and M. Ernzerhof, [Generalized Gradient Approximation Made Simple](#), Physical Review Letters **77**, 3865 (1996).
- [52] N. Mardirossian and M. Head-Gordon, [Thirty years of density functional theory in computational chemistry: an overview and extensive assessment of 200 density functionals](#), Molecular Physics **115**, 2315 (2017).
- [53] V. N. Staroverov, G. E. Scuseria, J. Tao and J. P. Perdew, [Tests of a ladder of density functionals for bulk solids and surfaces](#), Physical Review B **69**, 075102 (2004).
- [54] J. P. Perdew, K. Burke and M. Ernzerhof, [Perdew, Burke, and Ernzerhof Reply](#):, Physical Review Letters **80**, 891 (1998).
- [55] J. P. Perdew *et al.*, [Restoring the density-gradient expansion for exchange in solids and surfaces](#), Physical Review Letters **100**, 136406 (2008).
- [56] A. Ambrosetti and P. L. Silvestrelli, [Cohesive properties of noble metals by van der Waals-corrected density functional theory: Au, Ag, and Cu as case studies](#), Physical Review B **94**, 045124 (2016).
- [57] J. Schmidt *et al.*, [A dataset of 175k stable and metastable materials calculated with the PBEsol and SCAN functionals](#), Scientific Data **9**, 1 (2022).
- [58] G. I. Csonka *et al.*, [Assessing the performance of recent density functionals for bulk solids](#), Physical Review B **79**, 155107 (2009).
- [59] P. Pulay, [Ab initio calculation of force constants and equilibrium geometries in polyatomic molecules. I. Theory](#), Molecular Physics **17**, 197 (1969).

- [60] Á. Ruiz-Serrano, N. D. M. Hine and C. K. Skylaris, [Pulay forces from localized orbitals optimized in situ using a psinc basis set](#), The Journal of Chemical Physics **136**, 234101 (2012).
- [61] A. C. Hurley, [The Electrostatic Calculation of Molecular Energies. I. Methods of Calculating Molecular Energies](#), in Proceedings of the Royal Society of London. Series A Vol. 226, Pages 170–178, 1954.
- [62] M. Di Ventra and S. T. Pantelides, [Hellmann-Feynman theorem and the definition of forces in quantum time-dependent and transport problems](#), Physical Review B **61**, 16207 (2000).
- [63] D. M. Wood and A. Zunger, [A new method for diagonalising large matrices](#), Journal of Physics A: Mathematical and General **18**, 1343 (1985).
- [64] P. Pulay, [Convergence Acceleration of Iterative Sequences. The Case of SCF Iteration](#), Chemical Physics Letters **73**, 393 (1980).
- [65] J. R. Shewchuk, [An introduction to the Conjugate Gradient Method Without the Agonizing Pain](#), Pittsburgh, 1994.
- [66] J. P. Perdew, R. G. Parr, L. Levy and J. L. Balduz, [Density-Functional Theory for Fractional Particle Number: Derivative Discontinuities of the Energy](#), Physical Review Letters **49**, 1691 (1982).
- [67] M. S. Hybertsen and S. G. Louie, [Electron correlation in semiconductors and insulators: Band gaps and quasiparticle energies](#), Physical Review B **34**, 5390 (1986).
- [68] W. E. Pickett, [Electronic structure of the high-temperature oxide superconductors](#), Reviews of Modern Physics **61**, 433 (1989).
- [69] C. E. Ekuma, M. Jarrell, J. Moreno and D. Bagayoko, [Re-examining the electronic structure of germanium: A first-principle study](#), Surface Science **377**, 2172 (2013).
- [70] B. Baumeier, [Self-interaction corrections to density-functional theory for solids, surfaces and nanotubes](#), PhD Thesis, Westfälische Wilhelms-Universität Münster, 2009.
- [71] O. Gunnarsson, B. I. Lundqvist and J. W. Wilkins, [Contribution to the cohesive energy of simple metals: Spin-dependent effect](#), Physical Review B **10**, 1319 (1974).
- [72] P. Mori-Sánchez, A. J. Cohen and W. Yang, [Discontinuous nature of the exchange-correlation functional in strongly correlated systems.](#), Physical Review Letters **102**, 066403 (2009).
- [73] W. Kohn, [Discontinuity of the exchange-correlation potential from a density-functional viewpoint](#), Physical Review B **33**, 4331 (1986).
- [74] J. F. Janak, [Proof that  \$\partial E/\partial n\_i = \epsilon\$  in density-functional theory](#), Physical Review B **18**, 7165 (1978).
- [75] R. W. Godby, M. Schlüter and L. J. Sham, [Self-energy operators and exchange-correlation potentials in semiconductors](#), Physical Review B **37**, 10159 (1988).

- [76] C. Friedrich and A. Schindlmayr, [Many-Body Perturbation Theory: The GW Approximation](#), in Computational Nanoscience: Do It Yourself! Vol. 31, Chap. 12, Pages 335–355, NIC, 2006.
- [77] A. J. Layzer, [Properties of the One-Particle Green's Function for Nonuniform Many-Fermion Systems](#), Physical Review **129**, 897 (1963).
- [78] L. Hedin, [New Method for Calculating the One-Particle Green's Function with Application to the Electron-Gas Problem](#), Physical Review **139**, 796 (1965).
- [79] S. Wippermann, [Understanding Substrate-supported Atomic-scale Nanowires from Ab Initio Theory](#), PhD Thesis, Universität Paderborn, Paderborn, 2010.
- [80] F. Bechstedt, R. Del Sole, G. Cappellini and L. Reining, [An efficient method for calculating quasiparticle energies in semiconductors](#), Solid State Communications **84**, 765 (1992).
- [81] F. Fuchs *et al.*, [Quasiparticle band structure based on a generalized Kohn-Sham scheme](#), Physical Review B **76**, 115109 (2007).
- [82] F. Kaplan, [Quasiparticle Self-Consistent GW-Approximation for Molecules : Calculation of Single-Particle Excitation Energies for Molecules](#), PhD Thesis, Karlsruher Institut für Technologie (KIT), Karlsruhe, 2015.
- [83] U. von Barth and B. Holm, [Self-consistent  \$GW\_0\$  results for the electron gas: Fixed screened potential  \$W\_0\$  within the random-phase approximation](#), Physical Review B **54**, 8411 (1996).
- [84] G. Onida, L. Reining and A. Rubio, [Electronic excitations: density-functional versus many-body Green's-function approaches](#), Reviews of Modern Physics **74**, 601 (2002).
- [85] A. Dolgonos, T. O. Mason and K. R. Poeppelmeier, [Direct optical band gap measurement in polycrystalline semiconductors: A critical look at the Tauc method](#), Journal of Solid State Chemistry **240**, 43 (2016).
- [86] H. Wendel and R. M. Martin, [Theory of structural properties of covalent semiconductors](#), Physical Review B **19**, 5251 (1979).
- [87] M. S. Hybertsen and S. G. Louie, [Ab initio static dielectric matrices from the density-functional approach. I. Formulation and application to semiconductors and insulators](#), Physical Review B **35**, 5585 (1987).
- [88] S. L. Adler, [Quantum Theory of the Dielectric Constant in Real Solids](#), Physical Review **126**, 413 (1962).
- [89] N. Wiser, [Dielectric Constant with Local Field Effects Included](#), Physical Review **129**, 62 (1963).
- [90] H. Ehrenreich and M. H. Cohen, [Self-Consistent Field Approach to the Many-Electron Problem](#), Physical Review **115**, 786 (1959).

- [91] W. A. Wheeler, L. K. Wagner and T. L. Hughes, [Many-body electric multipole operators in extended systems](#), Physical Review B **100**, 245135 (2019).
- [92] R. Del Sole and R. Girlanda, [Optical properties of semiconductors within the independent-quasiparticle approximation](#), Physical Review B **48**, 11789 (1993).
- [93] B. Adolph *et al.*, [Nonlocality and many-body effects in the optical properties of semiconductors](#), Physical Review B **53**, 9797 (1996).
- [94] W. Hanke and L. J. Sham, [Local-field and excitonic effects in the optical spectrum of a covalent crystal](#), Physical Review B **12**, 4501 (1975).
- [95] G. Onida *et al.*, [Ab Initio Calculations of the Quasiparticle and Absorption Spectra of Clusters: The Sodium Tetramer](#), Physical Review Letters **75**, 818 (1995).
- [96] M. Rohlfing and S. G. Louie, [Electron-Hole Excitations in Semiconductors and Insulators](#), Physical Review Letters **81**, 2312 (1998).
- [97] S. Albrecht, L. Reining, R. Del Sole and G. Onida, [Ab initio Calculation of Excitonic Effects in the Optical Spectra of Semiconductors](#), Physical Review Letters **80**, 4510 (1998).
- [98] T. Sander, E. Maggio and G. Kresse, [Beyond the Tamm-Danoff approximation for extended systems using exact diagonalization](#), Physical Review B **92**, 045209 (2015).
- [99] M. Grüning, A. Marini and X. Gonze, [Exciton-plasmon states in nanoscale materials: breakdown of the Tamm–Danoff approximation](#), Chemistry of Materials **9**, 2820 (2009).
- [100] V. Olevano and L. Reining, [Excitonic effects on the silicon plasmon resonance.](#), Physical Review Letters **86**, 5962 (2001).
- [101] C. V. Raman, [A new radiation](#), Indian Journal of Physics **2**, 387 (1928).
- [102] S. Neufeld, [Parameterfreie Simulation von Gitterschwingungen und Ramanstreuung substratgestützter Goldnanodrähte](#), Master thesis, Paderborn, 2015.
- [103] M. Veithen, X. Gonze and P. Ghosez, [Nonlinear optical susceptibilities, Raman efficiencies, and electro-optic tensors from first-principles density functional perturbation theory](#), Physical Review B **71**, 125107 (2005).
- [104] S. Baroni, S. de Gironcoli, A. Dal Corso and P. Giannozzi, [Phonons and related crystal properties from density-functional perturbation theory](#), Reviews of Modern Physics **73**, 515 (2001).
- [105] X. Gonze and C. Lee, [Dynamical matrices, Born effective charges, dielectric permittivity tensors, and interatomic force constants from density-functional perturbation theory](#), Physical Review B **55**, 10355 (1997).
- [106] S. Sanna *et al.*, [Raman scattering efficiency in  \$\text{LiTaO}\_3\$  and  \$\text{LiNbO}\_3\$  crystals](#), Physical Review B **91**, 224302 (2015).

- [107] P. Umari, A. Pasquarello and A. Dal Corso, [Raman scattering intensities in  \$\alpha\$ -quartz: A first-principles investigation](#), *Physical Review B* **63**, 094305 (2001).
- [108] M. Lazzeri and F. Mauri, [First-Principles Calculation of Vibrational Raman Spectra in Large Systems: Signature of Small Rings in Crystalline  \$\text{SiO}\_2\$](#) , *Physical Review Letters* **90**, 036401 (2003).
- [109] M. Lazzeri and F. Mauri, [High-order density-matrix perturbation theory](#), *Physical Review B* **68**, 161101 (2003).
- [110] X. Gonze, [Adiabatic density-functional perturbation theory](#), *Physical Review A* **52**, 1096 (1995).
- [111] J. D. Patterson and B. C. Bailey, [Dielectrics and Ferroelectrics](#) (Springer International Publishing, Cham, 2018), Pages 613–648.
- [112] R. Whatmore, [Ferroelectric Materials](#) (Springer International Publishing, 2017), Pages 589–614.
- [113] T. C. Upadhyay, R. S. Bhandari and B. S. Semwal, [Dielectric properties of KDP-type ferroelectric crystals in the presence of external electric field](#), *Pramana* **67**, 547 (2006).
- [114] D. S. Bystrov and E. A. Popova, [The molecular aspect of ferroelectricity in KDP crystals](#), *Ferroelectric* **72**, 147 (1987).
- [115] M. T. Dove, [Theory of displacive phase transitions in minerals](#), *American Mineralogist* **82**, 213 (1997).
- [116] R. A. Cowley, [Lattice Dynamics and Phase Transitions of Strontium Titanate](#), *Physical Review* **134**, A981 (1964).
- [117] G. Shirane and Y. Yamada, [Lattice-Dynamical Study of the 110°K Phase Transition in  \$\text{SrTiO}\_3\$](#) , *Physical Review* **177**, 858 (1969).
- [118] P. A. Fleury, J. F. Scott and J. M. Worlock, [Soft Phonon Modes and the 110°K Phase Transition in  \$\text{SrTiO}\_3\$](#) , *Physical Review Letters* **21**, 16 (1968).
- [119] S. A. Hayward and E. H. H. Salje, [Cubic-tetragonal phase transition in  \$\text{SrTiO}\_3\$  revisited: Landau theory and transition mechanism](#), *Phase Transitions* **68**, 501 (1999).
- [120] W. D. Johnston Jr. and I. P. Kaminow, [Temperature Dependence of Raman and Rayleigh Scattering in  \$\text{LiNbO}\_3\$  and  \$\text{LiTaO}\_3\$](#) , *Physical Review* **168**, 1045 (1968).
- [121] J. L. Servoin and F. Gervais, [Soft vibrational mode in  \$\text{LiNbO}\_3\$  and  \$\text{LiTaO}\_3\$](#) , *Solid State Communications* **31**, 387 (1979).
- [122] S. Kojima, [Order-disorder nature of ferroelectric phase transition in stoichiometric  \$\text{LiNbO}\_3\$  Crystals](#), *Ferroelectrics* **223**, 63 (1998).
- [123] S. R. Phillpot and V. Gopalan, [Coupled displacive and order-disorder dynamics in  \$\text{LiNbO}\_3\$  by molecular-dynamics simulation](#), *Applied Physics Letters* **84**, 1916 (2004), <https://doi.org/10.1063/1.1669063>.

- [124] D. Lee *et al.*, **Structure and energetics of ferroelectric domain walls in  $\text{LiNbO}_3$  from atomic-level simulations**, *Physical Review B* **82**, 014104 (2010).
- [125] S. Sanna and W. G. Schmidt, **Ferroelectric Phase Transition in  $\text{LiNbO}_3$ : Insights From Molecular Dynamics**, *IEEE Transactions on Ultrasonics, Ferroelectrics, and Frequency Control* **59**, 1925 (2012).
- [126] A. K. Tagantsev, **Weak ferroelectrics**, *Ferroelectrics* **79**, 57 (1988).
- [127] A. Y. Kudzin, M. D. Volnianskii and I. A. Bsoul, **Ferroelectric properties of lithium heptagermanate crystal  $\text{Li}_2\text{Ge}_7\text{O}_{15}$ (LGO) in the vicinity of phase transition**, *Ferroelectrics* **215**, 23 (1998).
- [128] Y. Iwata *et al.*, **Neutron Diffraction Study of Structural Phase Transition in Ferroelectric  $\text{Li}_2\text{Ge}_7\text{O}_{15}$** , *Journal of the Physical Society of Japan* **56**, 2420 (1987).
- [129] K. Krec and W. Steiner, **Ferroelectric phase transition in  $\text{Li}_2\text{Ge}_7\text{O}_{15}$  investigated by Mössbauer diffraction**, *Acta Crystallographica Section A* **49** (1993).
- [130] M. Wada, K. Fujita, A. Sawada and Y. Ishibashi, **Soft Mode in the Ferroelectric Phase Transition of  $\text{Li}_2\text{Ge}_7\text{O}_{15}$** , *Japanese Journal of Applied Physics* **24**, 488 (1985).
- [131] S. V. Ptashnik *et al.*, **Ferroelectric thin film acoustic devices with electrical multiband switching ability**, *Scientific Reports* **7**, 1 (2017).
- [132] S. Mueller *et al.*, **Next-generation ferroelectric memories based on FE- $\text{HfO}_2$** , in 2015 Joint IEEE International Symposium on the Applications of Ferroelectric (ISAF), International Symposium on Integrated Functionalities (ISIF), and Piezoelectric Force Microscopy Workshop (PFM), Pages 233–236, 2015.
- [133] P. Günter, **Electro-optical effects in ferroelectrics**, *Ferroelectrics* **74**, 305 (1987).
- [134] B. Zwicker and P. Scherrer, **Elektrooptische Eigenschaften der seignette-elektrischen Kristalle  $\text{KH}_2\text{PO}_4$  und  $\text{KD}_2\text{PO}_4$** , *Helvetica Physica Acta* **17**, 346 (1944).
- [135] M. Zhu *et al.*, **Ferroelectric  $\text{BiFeO}_3$  thin-film optical modulators**, *Applied Physics Letters* **108**, 233502 (2016), <https://doi.org/10.1063/1.4953201>.
- [136] X. Y. Meng, Z. Z. Wang, Y. Zhu and C. T. Chen, **Mechanism of the electro-optic effect in the perovskite-type ferroelectric  $\text{KNbO}_3$  and  $\text{LiNbO}_3$** , *Journal of Applied Physics* **101**, 103506 (2007).
- [137] J. Chiles *et al.*, **Heterogeneous lithium niobate photonics on silicon substrates**, *Optics express* **21**, 25573 (2013).
- [138] M. Zhang *et al.*, **Integrated lithium niobate electro-optic modulators: when performance meets scalability**, *Optica* **8**, 652 (2021).
- [139] D. Sando *et al.*, **Epitaxial ferroelectric oxide thin films for optical applications**, *Applied Physics Reviews* **5**, 041108 (2018).

- [140] M. R. Biazzo, [Fabrication of a lithium tantalate temperature-stabilized optical modulator](#), *Applied Optics* **10**, 1016 (1971).
- [141] A. Karvounis *et al.*, [Barium Titanate Nanostructures and Thin Films for Photonics](#), *Advanced Optical Materials* **8**, 2001249 (2020).
- [142] C. Xiong *et al.*, [Active Silicon Integrated Nanophotonics: Ferroelectric BaTiO<sub>3</sub> Devices](#), *Nano Letters* **14**, 1419 (2014).
- [143] S. Abe *et al.*, [Photonic integration based on a ferroelectric thin-film platform](#), *Scientific Reports* **9**, 1 (2019).
- [144] L. K. Anderson, [Optical applications of ferroelectrics](#), *Ferroelectrics* **7**, 55 (1974).
- [145] M. M. Zhu, Z. H. Du and J. Ma, [Optical and electro-optic properties of micrometric thick lead zirconate titanate films on \(Pb<sub>0.86</sub>,La<sub>0.14</sub>\)TiO<sub>3</sub>/glass](#), *Journal of Applied Physics* **106**, 023113 (2009), <https://doi.org/10.1063/1.3176897>.
- [146] S. A. Denev *et al.*, [Probing Ferroelectrics Using Optical Second Harmonic Generation](#), *Journal of the American Ceramic Society* **94**, 2699 (2011).
- [147] D. S. Hum and M. M. Fejer, [Quasi-phasematching](#), *Comptes Rendus Physique* **8**, 180 (2007).
- [148] J. A. Giordmaine, [Mixing of Light Beams in Crystals](#), *Physical Review Letters* **8**, 19 (1962).
- [149] P. A. Franken and J. F. Ward, [Optical Harmonics and Nonlinear Phenomena](#), *Reviews of Modern Physics* **35**, 23 (1963).
- [150] J. Q. Yao and T. S. Fahlen, [Calculations of optimum phase match parameters for the biaxial crystal KTiOPO<sub>4</sub>](#), *Journal of Applied Physics* **55**, 65 (1984).
- [151] C. Langrock, D. S. Hum, E. Diamanti and M. Charbonneau-Lefort, [Non-critical Phase Matched SHG of a DPSS Nd: YAG Laser in MgO: LiNbO<sub>3</sub>](#), *IEEE Journal of Selected Topics in Quantum Electronics* **20**, 101 (2002).
- [152] B. Zhang *et al.*, [Anomalously Strong Second-Harmonic Generation in GaAs Nanowires via Crystal-Structure Engineering](#), *Advanced Functional Materials* , 2104671 (2021).
- [153] E. G. Víllora, H. Ishibashi, K. Sumiya and K. Shimamura, [Birefringent- and quasi phase-matching with BaMgF<sub>4</sub> for vacuum-UV/UV and mid-IR all solid-state lasers](#), *Optics express* **17**, 12362 (2009).
- [154] J. A. Armstrong, N. Bloembergen, J. Ducuing and P. S. Pershan, [Interactions between Light Waves in a Nonlinear Dielectric](#), *Physical Review* **127**, 1918 (1962).
- [155] R. C. Miller, [Optical Harmonic Generation in Single Crystal BaTiO<sub>3</sub>](#), *Physical Review* **134**, A1313 (1964).

[156] M. M. Fejer, G. A. Magel, D. H. Jundt and R. L. Byer, **Quasi-Phase-Matched Second Harmonic Generation: Tuning and Tolerances**, IEEE Journal of Quantum Electronics **28**, 2631 (1992).

[157] E. J. Lim, M. M. Fejer and R. L. Byer, **Second-harmonic generation of green light in periodically poled planar lithium niobate waveguide**, Electronics Letters **25**, 174 (1989).

[158] C. J. Van der Poel, J. D. Bierlein, J. B. Brown and S. Colak, **Efficient type I blue second-harmonic generation in periodically segmented  $KTiOPO_4$  waveguides**, Applied Physics Letters **57**, 2074 (1998).

[159] C. Wang *et al.*, **Second harmonic generation in nano-structured thin-film lithium niobate waveguides**, Optics express **25**, 6963 (2017).

[160] M. Houé and P. D. Townsend, **An introduction to methods of periodic poling for second-harmonic generation**, Journal of Physics D: Applied Physics **28**, 1747 (1995).

[161] L. Li *et al.*, **Tunable violet radiation in a quasi-phase-matched periodically poled stoichiometric lithium tantalate waveguide by direct femtosecond laser writing**, Results in Physics **19**, 103373 (2020).

[162] J. P. Meyn *et al.*, **Fabrication of periodically poled lithium tantalate for UV generation with diode lasers**, Applied Physics B **73**, 111 (2001).

[163] V. Y. Shur, **Domain engineering in lithium niobate and lithium tantalate: domain wall motion**, Ferroelectrics **340**, 3 (2006).

[164] A. Boes *et al.*, **Efficient second harmonic generation in lithium niobate on insulator waveguides and its pitfalls**, Journal of Physics: Photonics **3**, 012008 (2021).

[165] S. Ganesamoorthy *et al.*, **A comparative study on the domain switching characteristics of near stoichiometric lithium niobate and lithium tantalate single crystals**, Materials Science and Engineering: B **120**, 125 (2005).

[166] M. L. Ouvrard, **Recherches sur les phosphate double de titane, d'étain et de cuivre**, Comptes Rendus **111**, 177 (1890).

[167] R. Masse and J. C. Grenier, **Etude des monophosphates du type  $M^I Ti OPO_4$  avec  $M^I = K, Rb$  et  $Tl$** , Bulletin de Minéralogie **94**, 437 (1971).

[168] J. D. Bierlein and H. Vanherzeele, **Potassium titanyl phosphate: properties and new applications**, Journal of the Optical Society of America B: Optical Physics **6**, 622 (1989).

[169] N. I. Sorokina and V. I. Voronkova, **Structure and properties of crystals in the potassium titanyl phosphate family: A review**, Crystallography Reports **52**, 80 (2007).

[170] F. C. Zumsteg, J. D. Bierlein and T. E. Gier,  **$K_x Rb_{1-x} TiOPO_4$ : A new nonlinear optical material**, Journal of Applied Physics **47**, 4980 (1976).

[171] S. Neufeld *et al.*, **Potassium titanyl phosphate (KTP) quasiparticle energies and optical response**, Journal of Physics: Materials **2**, 045003 (2019).

[172] P. A. Thomas, A. M. Glazer and B. E. Watts, [Crystal structure and nonlinear optical properties of  \$\text{KSnOPO}\_4\$  and their comparison with  \$\text{KTiOPO}\_4\$](#) , *Acta Crystallographica Section B* **46**, 333 (1990).

[173] H. Vanherzeele and J. D. Bierlein, [Magnitude of the nonlinear-optical coefficients of  \$\text{KTiOPO}\_4\$](#) , *Optics Letters* **17**, 982 (1992).

[174] S. C. Mayo *et al.*, [Structure and non-linear optical properties of  \$\text{KTiOAsO}\_4\$](#) , *Acta Crystallographica Section B: Structural Science* **50**, 655 (1994).

[175] D. Xue and S. Zhang, [The origin of nonlinearity in  \$\text{KTiOPO}\_4\$](#) , *Applied Physics Letters* **70**, 943 (1997).

[176] G. Rosenman *et al.*, [Low temperature periodic electrical poling of flux-grown  \$\text{KTiOPO}\_4\$  and isomorphic crystals](#), *Applied Physics Letters* **73**, 3650 (1998).

[177] J. D. Bierlein and C. B. Arweiler, [Electro-optic and dielectric properties of  \$\text{KTiOPO}\_4\$](#) , *Applied Physics Letters* **49**, 917 (1986).

[178] P. A. Thomas, S. C. Mayo and B. E. Watts, [Crystal structures of  \$\text{RbTiOAsO}\_4\$ ,  \$\text{KTiO}\(\text{P}\_{0.58}\text{As}\_{0.42}\)\text{O}\_4\$ ,  \$\text{RbTiOPO}\_4\$  and  \$\(\text{Rb}\_{0.465}\text{K}\_{0.535}\)\text{TiOPO}\_4\$ , and analysis of pseudosymmetry in crystals of the  \$\text{KTiOPO}\_4\$  family](#), *Acta Crystallographica Section B: Structural Science* **48**, 401 (1992).

[179] M. R. Katkova, S. S. Nosov, E. V. Chuprunov and E. L. Belokoneva, [Pseudosymmetry and ferroelectric phase transitions in the KTP structure type](#), *Crystallography Reports* **45**, 647 (2000).

[180] V. K. Yanovskii and V. I. Voronkova, [Ferroelectric Phase Transitions and Properties of Crystals of the  \$\text{KTiOPO}\_4\$  Family](#), *physica status solidi (a)* **93**, 665 (1980).

[181] M. Yashima and T. Komatsu, [Order-disorder and displacive components in the ferroelectric-paraelectric phase transition of potassium titanyl phosphate  \$\text{KTiOPO}\_4\$](#) , *Chemical Communications* **0**, 1070 (2009).

[182] S. T. Norberg and N. Ishizawa, [K-site splitting in  \$\text{KTiOPO}\_4\$  at room temperature](#), *Acta Crystallographica Section C: Crystal Structure Communications* **61**, i99 (2005).

[183] N. Angert, M. Tseitlin, E. Yashchin and M. Roth, [Ferroelectric phase transition temperatures of  \$\text{KTiOPO}\_4\$  crystals grown from self-fluxes](#), *Applied Physics Letters* **67**, 1941 (1995).

[184] M. N. Satyanarayan, A. Deepthy and H. L. Bhat, [Potassium Titanyl Phosphate and Its Isomorphs: Growth, Properties, and Applications](#), *Critical Reviews in Solid State and Materials Sciences* **24**, 103 (1999).

[185] M. E. Hagerman, V. L. Kozhevnikov and K. R. Poeppelmeier, [High-temperature decomposition of potassium titanyl phosphate,  \$\text{KTiOPO}\_4\$](#) , *Chemistry of Materials* **5**, 1211 (1993).

- [186] S. Sanna and W. G. Schmidt, [LiNbO<sub>3</sub> surfaces from a microscopic perspective](#), Journal of Physics: Condensed Matter **29**, 413001 (2017).
- [187] J. Neugebauer and M. Scheffler, [Adsorbate-substrate and adsorbate-adsorbate interactions of Na and K adlayers on Al\(111\)](#), Physical Review B **46**, 16067 (1992).
- [188] G. Makov and M. C. Payne, [Periodic boundary conditions in ab initio calculations](#), Physical review. B, Condensed matter **51**, 4014 (1995).
- [189] L. Bengtsson, [Dipole correction for surface supercell calculations](#), Physical Review B **59**, 12301 (1999).
- [190] B. Meyer and D. Vanderbilt, [Ab initio study of BaTiO<sub>3</sub> and PbTiO<sub>3</sub> surfaces in external electric fields](#), Physical Review B **63**, 205426 (2001).
- [191] L. Yu *et al.*, [Equivalence of dipole correction and Coulomb cutoff techniques in supercell calculations](#), Physical Review B **77**, 245102 (2008).
- [192] C. J. Fall, N. Binggeli and A. Baldereschi, [Deriving accurate work functions from thin-slab calculations](#), Journal of Physics: Condensed Matter **11**, 2689 (1999).
- [193] S. Neufeld, A. Schindlmayr and W. G. Schmidt, [Quasiparticle energies and optical response of RbTiOPO<sub>4</sub> and KTiOAsO<sub>4</sub>](#), Journal of Physics: Materials **5**, 015002 (2021).
- [194] G. Kresse and J. Furthmüller, [Efficient iterative schemes for ab initio total-energy calculations using a plane-wave basis set](#), Physical Review B **54**, 11169 (1996).
- [195] G. Kresse and D. Joubert, [From ultrasoft pseudopotentials to the projector augmented-wave method](#), Physical Review B **59**, 1758 (1999).
- [196] M. Shishkin and G. Kresse, [Implementation and performance of the frequency-dependent GW method within the PAW framework](#), Physical Review B **74**, 035101 (2006).
- [197] D. R. Allan, J. S. Loveday, R. J. Nelmes and P. A. Thomas, [A high-pressure structural study of potassium titanyl phosphate \(KTP\) up to 5 GPa](#), Journal of Physics: Condensed Matter **4**, 2747 (1992).
- [198] M. E. Hagerman and K. R. Poeppelmeier, [Review of the Structure and Processing-Defect-Property Relationships of Potassium Titanyl Phosphate: A Strategy for Novel Thin-Film Photonic Devices](#), Chemistry of Materials **7**, 602 (1995).
- [199] S. T. Norberg, P. A. Thomas and M. G. Tucker, [A neutron total scattering study of local coordination in KTiOPO<sub>4</sub> from room temperature to 900 °C](#), Journal of Physics: Condensed Matter **23**, 175401 (2011).
- [200] A. H. Reshak, A. V. Kityk and S. Auluck, [Investigation of the linear and nonlinear optical susceptibilities of KTiOPO<sub>4</sub> single crystals: Theory and experiment](#), Journal of Physical Chemistry B **114**, 16705 (2010).

- [201] J. E. Lowther, P. Manyum and S. Suebka, [Electronic and structural properties of orthorhombic  \$KTiOPO\_4\$  and related isomorphic materials](#), *physica status solidi (b)* **242**, 1392 (2005).
- [202] A. Dudelzak *et al.*, [Anisotropic fundamental absorption edge of  \$KTiOPO\_4\$  crystals](#), *Journal of Applied Physics* **87**, 2110 (2000).
- [203] M. Sheik-Bahae, D. C. Hitchings and E. W. Hagan, D. j. Van Stryland, [Dispersion of bound electron nonlinear refraction in solids](#), *IEEE Journal of Quantum Electronics* **27**, 1296 (1991).
- [204] H. P. Li, C. H. Kam, Y. L. Lam and W. Ji, [Femtosecond Z-scan measurements of nonlinear refraction in nonlinear optical crystals](#), *Optical Materials* **15**, 237 (2001).
- [205] R. DeSalvo *et al.*, [Infrared to ultraviolet measurements of two-photon absorption and  \$n\_2\$  in wide bandgap solids](#), *IEEE Journal of Quantum Electronics* **32**, 1324 (1996).
- [206] Y. Zhang *et al.*, [Mechanism of hydrogen treatment in  \$KTiOPO\_4\$  crystals at high temperature: experimental and first-principles studies](#), *CrystEngComm* **17**, 3793 (2015).
- [207] M. Ghohestani, A. Arab, S. J. Hashemifar and H. Sadeghi, [Ab-initio investigation of Rb substitution in KTP single crystal](#), *Journal of Applied Physics* **123**, 015702 (2018).
- [208] W.-Y. Ching and Y.-N. Xu, [Band structure and linear optical properties of  \$KTiOPO\_4\$](#) , *Physical Review B* **44**, 5332 (1991).
- [209] K. Ishizaka *et al.*, [Giant Rashba-type spin splitting in bulk BiTeI](#), *Nature materials* **10**, 521 (2011).
- [210] S. Steiner, S. Khmelevskyi, M. Marsmann and G. Kresse, [Calculation of the magnetic anisotropy with projected-augmented-wave methodology and the case study of disordered  \$Fe\_{1-x}Co\_x\$  alloys](#), *Physical Review B* **93**, 224425 (2016).
- [211] A. Riefer *et al.*, [LiNbO<sub>3</sub> electronic structure: Many-body interactions, spin-orbit coupling, and thermal effects](#), *Physical Review B* **93**, 075205 (2016).
- [212] A. Riefer *et al.*, [Zn-VI quasiparticle gaps and optical spectra from many-body calculations](#), *Journal of Physics: Condensed Matter* **29**, 215702 (2017).
- [213] A. Roy, R. Prasad, S. Auluck and A. Garg, [Optical anisotropy in bismuth titanate: An experimental and theoretical study](#), *Journal of Applied Physics* **115**, 133509 (2014).
- [214] E. Engel and S. H. Vosko, [Exact exchange-only potentials and the virial relation as microscopic criteria for generalized gradient approximations](#), *Physical Review B* **47**, 13164 (1993).
- [215] A. D. Becke and E. R. Johnson, [A simple effective potential for exchange](#), *The Journal of Chemical Physics* **124**, 221101 (2006).
- [216] M. Ghohestani, S. J. Hashemifar and A. Arab, [Linear and nonlinear optical properties of  \$RbTiOPO\_4\$ - \$KTiOPO\_4\$  alloys studied from first principles](#), *Journal of Applied Physics* **128**, 125707 (2020).

[217] M. Roth, N. Angert and M. Tseitlin, *Growth-dependent properties of KTP crystals and PPKTP structures*, Journal of Materials Science: Materials in Electronics **12**, 429 (2001).

[218] O. Y. Khyzhun *et al.*, *Electronic structure of KTiOAsO<sub>4</sub>: A comparative study by the full potential linearized augmented plane wave method, X-ray emission spectroscopy and X-ray photoelectron spectroscopy*, Journal of Alloys and Compounds **477**, 768 (2009).

[219] G. Hansson, H. Karlsson, S. Wang and F. Laurell, *Transmission measurements in KTP and isomorphic compounds*, Applied Optics **39**, 5058 (2000).

[220] M. J. Martín *et al.*, *Thermal reduction of KTiOPO<sub>4</sub> single crystals*, Journal of Applied Physics **76**, 7510 (1994).

[221] J. Mangin, A. Khodjaoui and G. Marnier, *Optical Absorption of KTP Single Crystals*, physica status solidi (a) **120**, K111 (1990).

[222] P. Giannozzi *et al.*, *QUANTUM ESPRESSO: a modular and open-source software project for quantum simulations of materials*, Journal of Physics: Condensed Matter **21**, 395502 (2009).

[223] M. Rüsing, *In depth Raman analysis of the ferroelectrics KTiOPO<sub>4</sub> and LiNbO<sub>3</sub>*, PhD Thesis, Universität Paderborn, Paderborn, 2018.

[224] T. C. Damen, S. P. Porto and B. Tell, *Raman Effect in Zinc Oxide*, Physical Review **142**, 570 (1966).

[225] R. S. Mulliken, *Report on Notation for the Spectra of Polyatomic Molecules*, The Journal of Chemical Physics **23**, 1997 (1955).

[226] S.-I. Furusawa *et al.*, *Raman Scattering Study of KTiOPO<sub>4</sub> (KTP) Single Crystal*, Journal of the Physical Society of Japan **60**, 2470 (1991).

[227] C. S. Tu *et al.*, *Temperature dependent Raman scattering in KTiOPO<sub>4</sub> and KTiOAsO<sub>4</sub> single crystals*, Journal of Applied Physics **79**, 3235 (1998).

[228] G. H. Watson, *Polarized Raman spectra of KTiOAsO<sub>4</sub> and isomorphic nonlinear-optical crystals*, Journal of Raman Spectroscopy **22**, 705 (1991).

[229] G. A. Massey, T. M. Loehr, L. J. Willis and J. C. Johnson, *Raman and electrooptic properties of potassium titanate phosphate*, Applied Optics **19**, 4136 (1980).

[230] B. Mohamadou *et al.*, *High-temperature vibrational spectra, relaxation and ionic conductivity effects in KTiOPO<sub>4</sub>*, Journal of Physics: Condensed Matter **3**, 9489 (1991).

[231] Y. K. Voronko *et al.*, *Raman scattering study of phase transformations in KTiOPO<sub>4</sub>*, Soviet physics, Solid state **31**, 1736 (1989).

[232] S. Neufeld, A. Bocchini and W. G. Schmidt, *Potassium titanyl phosphate Z- and Y-cut surfaces from density-functional theory*, Physical Review Materials **5**, 064407 (2021).

[233] F. Bechstedt, [Principles of Surface Physics](#) Vol. 57 (Springer Berlin Heidelberg, 2003).

[234] A. Jain *et al.*, [Commentary: The Materials Project: A materials genome approach to accelerating materials innovation](#), *APL Materials* **1**, 011002 (2013).

[235] L. G. Liu, [Compression and polymorphism of potassium to 400 kbar](#), *Journal of Physics and Chemistry of Solids* **47**, 1067 (1986).

[236] P. D. Hao *et al.*, [Anisotropic elastic and thermodynamic properties of the HCP-Titanium and the FCC-Titanium structure under different pressures](#), *Journal of Materials Research and Technology* **9**, 3488 (2020).

[237] Y. Du, C. Ouyang, S. Shi and M. Lei, [Ab initio studies on atomic and electronic structures of black phosphorus](#), *Journal of Applied Physics* **107**, 093718 (2010).

[238] Y. A. Freiman and H. J. Jodl, [Solid oxygen](#), *Physics Reports* **401**, 1 (2004).

[239] C. G. Van de Walle and J. Neugebauer, [First-principles surface phase diagram for hydrogen on GaN surfaces](#)., *Physical Review Letters* **88**, 066103 (2002).

[240] V. I. Voronin *et al.*, [Crystal structure of the low-temperature form of K<sub>3</sub>PO<sub>4</sub>](#), *Inorganic Materials* **42**, 908 (2006).

[241] E. Thilo and K. Dostól, [Kondensierte Kaliumarsenate und Kaliumarsenatophosphate und ihre Beziehungen zu verschiedenen Formen des Kaliumpolyphosphates](#), *Zeitschrift für anorganische und allgemeine Chemie* **298**, 100 (1959).

[242] K. H. Jost, [Die Struktur des Kaliumpolyphosphats \(KPO<sub>3</sub>\)<sub>x</sub>](#), *Acta Crystallographica* **16**, 623 (1963).

[243] M. Song, Z. Lu and D. Li, [Phase transformations among TiO<sub>2</sub> polymorphs](#), *Nanoscale* **12**, 23183 (2020).

[244] G. R. Levi and G. Peyronel, [Struttura Cristallografica del Gruppo Isomorfo \(Si<sup>4+</sup>, Ti<sup>4+</sup>, Zr<sup>4+</sup>, Sn<sup>4+</sup>, Hf<sup>4+</sup>\) P<sub>2</sub>O<sub>7</sub>](#), *Zeitschrift für Kristallographie* **92**, 190 (1935).

[245] S. T. Norberg, G. Svensson and J. Albertsson, [A TiP<sub>2</sub>O<sub>7</sub> superstructure](#), *Acta Crystallographica Section C* **57**, 225 (2001).

[246] J. Sanz *et al.*, [Structural Disorder in the Cubic 3 × 3 × Superstructure of TiP<sub>2</sub>O<sub>7</sub>. XRD and NMR Study](#), *Chemistry of Materials* **9**, 996 (1997).

[247] A. Helms and W. Klemm, [Die Struktur der sogenannten „Alkalitetroxyde“](#), *Zeitschrift für anorganische und allgemeine Chemie* **241**, 97 (1939).

[248] S. C. Abrahams and J. Kalnajs, [The Crystal Structure of  \$\alpha\$ -Potassium Superoxide\\*](#), *Acta Crystallographica* **8**, 503 (1955).

[249] M. Ziegler, H. R. Meister and W. Käenzig, [Zur Struktur von KO<sub>2</sub> in der Phase IV](#), *Helvetica Physica Acta* **48** (1975).

- [250] S. B. Zhang and S. H. Wei, *Surface energy and the common dangling bond rule for semiconductors.*, Physical Review Letters **92**, 086102 (2004).
- [251] W. C. Yang, B. J. Rodriguez, A. Gruverman and R. J. Nemanich, *Polarization-dependent electron affinity of LiNbO<sub>3</sub> surfaces*, Applied Physics Letters **85**, 2316 (2004).
- [252] S. Mirbt, N. Moll, A. Kley and J. D. Joannopoulos, *A general rule for surface reconstructions of III–V semiconductors*, Surface Science **422**, L177 (1999).
- [253] M. D. Pashley, *Electron counting model and its application to island structures on molecular-beam epitaxy grown GaAs(001) and ZnSe(001).*, Physical Review B **40**, 10481 (1989).
- [254] K. Momma and F. Izumi, *VESTA 3 for three-dimensional visualization of crystal, volumetric and morphology data*, Journal of Applied Crystallography **44**, 1272 (2011).
- [255] W. Humphrey, A. Dalke and K. Schulten, *VMD: Visual molecular dynamics*, Journal of Molecular Graphics **14**, 33 (1996).



# List of Figures

2.1	Schematic flowchart of the Hedin's equations in its full form and within the <i>GW</i> approximation. . . . .	19
4.1	Schematic representation of the ferroelectric hysteresis loop. . . . .	37
4.2	Temperature dependence of the two lowest-frequency modes A and D in cubic $\text{SrTiO}_3$ . . . . .	39
4.3	Orthorhombic unit cell of $MTi\text{OXO}_4$ type crystals. . . . .	43
4.4	Schematic illustration of the plane averaged local potential along the surface normal of a polar surface. An additional contribution to the potential corresponding to a dipole correction layer cancels the spurious external electric field. . . . .	46
4.5	Planar averaged local potential of a polar crystal along the polar axis within bulk as well as within a dipole-corrected slab geometry. . . . .	48
5.1	Outline of the first Brillouin zone of KTP along with high-symmetry points. .	50
5.2	KTP band structures and PDOS as calculated within DFT-PBEsol and <i>GW</i> . .	53
5.3	Calculated orbital character of VBM and CBM states in KTP . . . . .	54
5.4	Quasiparticle shifts of Kohn-Sham states in KTP . . . . .	55
5.5	Imaginary part of the diagonal components of the KTP dielectric function calculated on the IPA, IQPA and BSE level of theory. . . . .	56
5.6	Geometry of $\text{TiO}_6\text{--PO}_4$ polyhedra strands within an artificial, partially symmetrized structure of KTP with smaller, tetragonal unit cell and within orthorhombic bulk KTP . . . . .	57
5.7	Average reflectivity of KTP calculated on the IPA, IQPA and BSE levels of theory in comparison to experimental data. . . . .	58
5.8	Comparison of the band structures and PDOS of RTP and KTA calculated on the DFT and <i>GW</i> levels of theory. . . . .	60
5.9	Dielectric functions of RTP and KTA calculated on IPA, IQPA, and BSE levels of theory. For comparison, KTP spectra as well as experimentally determined absorption onsets are also included. . . . .	61
5.10	Charge densities of the $\text{O}_{2p}$ valence and $\text{Ti}_{3d} - \text{O}_{2p}/\text{As}_{4p}$ conduction-band state of the transition giving rise to the absorption peak at 6.3 eV within the IPA for $(x,x)$ polarization in KTA. . . . .	62

5.11 Atomically resolved phononic DOS for all $A_1$ , $A_2$ , $B_1$ and $B_2$ type phonons of KTP, RTP and KTA. . . . .	66
5.12 Displacement pattern of the modes $\nu_{ip}$ and $\nu_{ap}$ in KTP. . . . .	67
5.13 Experimental and theoretical Raman spectra of KTP, RTP and KTA in the polarization configurations $(x, x)$ , $(y, y)$ and $(z, z)$ . The peak heights in all spectra are normalized to the mode of highest intensity. . . . .	70
5.14 Experimental and theoretical Raman spectra of KTP, RTP and KTA in the polarization configurations $(x, y)$ , $(x, z)$ and $(y, z)$ . The peak heights in all spectra are normalized to the mode of highest intensity. . . . .	71
5.15 Experimental room-temperature Raman spectra of KTP for $x(y, y)\bar{x}$ polarization, as obtained by Voronko <i>et al.</i> , Kugel <i>et al.</i> and Rüsing. . . . .	72
6.1 Tetrahedral phase diagram for KTP formation. Two slices, corresponding to trigonal phase diagrams with high and low chemical potential of oxygen, are depicted, along with binodal curves between KTP and concurring phases. . . . .	78
6.2 Stacking sequence of $K_2Ti_2P_2O_4$ and $O_6$ layers in Z-cut KTP. Atomic arrangement of bulk-cut $O_6$ ( $x_O$ and $y_O$ ) and $K_2Ti_2P_2O_4$ ( $x$ and $y$ ) terminations are highlighted. . . . .	81
6.3 Planar averaged local potential along the $z$ direction of an unreconstructed Z-cut surface with $y_O$ - and x-type termination on either end facet. . . . .	82
6.4 Phase diagrams of KTP $Z^+$ and $Z^-$ surfaces for different values of $\Delta\mu_O$ . . . . .	84
6.5 Atomic structure of stable terminations on the KTP $Z^+$ surface. . . . .	86
6.6 Atomic structure of stable terminations on the KTP $Z^-$ surface. . . . .	87
6.7 Surface band structure of $KO(y)$ on $Z^+$ and of $O_3(y_O)$ on $Z^-$ , along with charge densities of localized surface states. . . . .	88
6.8 Work functions and relative change of the surface dipole of all investigated terminations for KTP $Z^+$ , $Z^-$ and Y-cut surfaces. . . . .	89
6.9 Stacking sequence of $Ti_2P_2O_{12}$ and $K_4Ti_2P_2O_6$ layers in Y-cut KTP. Additionally, the atomic arrangement of bulk-cut terminations of all four layer types is depicted. . . . .	90
6.10 Phase diagram of KTP Y cut for different values of $\Delta\mu_O$ . . . . .	92
6.11 Atomic structure of stable terminations on the KTP Y-cut surface. . . . .	93
6.12 Surface band structure of the $PO_4(z)$ termination on KTP Y cut. . . . .	94
C.1 Potential energy surfaces for adsorption of K on all layers of KTP Z cut. . . . .	128
C.2 Potential energy surfaces for adsorption of Ti on all layers of KTP Z cut. . . . .	128
C.3 Potential energy surfaces for adsorption of O on all layers of KTP Z cut. . . . .	129
C.4 Potential energy surfaces for adsorption of P on all layers of KTP Z cut. . . . .	130

# List of Tables

5.1	Reduced coordinates of non-symmetry-equivalent atoms of KTP as obtained within DFT-PBEsol. The deviation with respect to single-crystal X-ray diffraction (XRD) data is given in brackets. Coordinates $x$ , $y$ , and $z$ are assumed to be aligned along the [100], [010], and [001] directions, respectively. . . . .	52
5.2	Absorption onsets of KTA and RTP calculated on the IPA, IQPA, and BSE levels of theory. For comparison, calculated values for KTP as well as experimental data are provided. . . . .	63
5.3	Raman selection rules for crystals of space group $Pna2_1$ in backscattering geometry. In addition, experimental and calculated intensities of the respective phonon branches in KTP, normalized to $A_2$ -TO, are displayed. . . . .	69
6.1	Investigated terminations on the KTP Y-cut surface for x and z-type layers. . .	91
B.1	Calculated bulk chemical potentials and formation enthalpies of all investigated phases within PBEsol, along with their respective space groups. Phases enclosing the KTP stability region under UHV as well as ATM conditions for oxygen are highlighted; KTP is highlighted in bold. . . . .	126



# Lattice Vectors and Fourier Transformations

A

All investigated systems in this thesis are assumed to be perfect crystalline solids. Such a solid is thereby characterized by a discrete translational invariance, and therefore fully described by two sets: (i) The set of all atomic coordinates within a single unit cell (atomic base) and (ii) the set of all lattice vectors

$$\mathbf{R}_n = n_1 \mathbf{a}_1 + n_2 \mathbf{a}_2 + n_3 \mathbf{a}_3 \quad ; \quad n_1, n_2, n_3 \in \mathbb{Z}, \quad (\text{A.1})$$

with  $n = (n_1, n_2, n_3)$  as a macro index and  $\{\mathbf{a}_i\}$  as the three unit cell vectors. The periodic repetition of a unit cell along the vectors  $\{\mathbf{a}_i\}$  is again a unit cell (with rescaled unit cell vectors) and therefore not unique. A unit cell containing exactly a single lattice point  $\mathbf{R}_n$  thereby called a primitive cell. In that context, the Wigner-Seitz cell can be defined as the set of all points in real space closer to a given lattice point than to any other one. Closely related to the set of lattice vectors is the reciprocal lattice, which is characterized by all reciprocal lattice vectors  $\mathbf{G}_m$  fulfilling

$$\mathbf{G}_m \cdot \mathbf{R}_n = 2\pi k \quad ; \quad k \in \mathbb{Z}. \quad (\text{A.2})$$

Again,  $m = (m_1, m_2, m_3)$  denotes a macro index. Similar to the unit cell vectors  $\{\mathbf{a}_i\}$  spanning the lattice in real space, the reciprocal space is spanned by the reciprocal unit cell vectors  $\{\mathbf{b}_i\}$ , with

$$\mathbf{G}_m = m_1 \mathbf{b}_1 + m_2 \mathbf{b}_2 + m_3 \mathbf{b}_3 \quad ; \quad m_1, m_2, m_3 \in \mathbb{Z}. \quad (\text{A.3})$$

The equivalent to a Wigner-Seitz cell in reciprocal space is called the (first) Brillouin zone, defined by all reciprocal vectors  $\mathbf{q}$  closer to the origin  $\mathbf{G}_0 = 0$  than to any other reciprocal lattice vector. This is equivalent to the condition

$$\forall m \in \mathbb{Z}^3 : \mathbf{G}_m \cdot \mathbf{q} \leq \frac{|\mathbf{G}_m|^2}{2}. \quad (\text{A.4})$$

Functions defined in reciprocal space (e.g., the energy eigenvalues  $\epsilon_n(\mathbf{q})$ ) are normally evaluated and displayed solely within the first Brillouin zone. Within it, high-symmetry points are typically labeled with special indices. For all lattices, the central point  $\mathbf{k} = 0$  thereby

resembles the  $\Gamma$  point. In the case of an orthorhombic unit cell, the Brillouin zone is again orthorhombic (see Fig. 5.1), with special points  $Z = (0, 0, \frac{1}{2})$ ,  $Y = (0, \frac{1}{2}, 0)$  and  $T = (\frac{1}{2}, \frac{1}{2}, 0)$  in units of the reciprocal lattice constants.

Any local function  $f(\mathbf{r})$  can be written via its Fourier transform  $\tilde{f}(\mathbf{q} + \mathbf{G})$  as

$$f(\mathbf{r}) = \frac{1}{(2\pi)^3} \sum_{\mathbf{G}} \int_{BZ} e^{i(\mathbf{q} + \mathbf{G}) \cdot \mathbf{r}} \tilde{f}(\mathbf{q} + \mathbf{G}) d\mathbf{q}. \quad (A.5)$$

The sum over  $\mathbf{G}$  covers all reciprocal lattice vectors while the integral over  $\mathbf{q}$  is limited to the first Brillouin zone. Consequently, the inverse Fourier transform is then

$$\tilde{f}(\mathbf{q} + \mathbf{G}) = \int e^{-i(\mathbf{q} + \mathbf{G}) \cdot \mathbf{r}} f(\mathbf{r}) d\mathbf{r}. \quad (A.6)$$

In the case of lattice periodic functions  $f(\mathbf{r}) = f(\mathbf{r} + \mathbf{R})$ , Eq. A.6 simplifies to

$$\tilde{f}(\mathbf{q} + \mathbf{G}) = \delta(\mathbf{q}) \cdot \tilde{f}(\mathbf{G}) := \tilde{f}_G, \quad (A.7)$$

transforming  $f(\mathbf{r})$  in Eq. A.5 into a simple Fourier decomposition in the reciprocal lattice vectors  $\{\mathbf{G}\}$ . Similarly, an arbitrary nonlocal function  $f(\mathbf{r}, \mathbf{r}')$  of two variables transforms according to [37]

$$f(\mathbf{r}, \mathbf{r}') = \frac{1}{(2\pi)^6} \sum_{\mathbf{G}, \mathbf{G}'} \int \int e^{i(\mathbf{q} + \mathbf{G}) \cdot \mathbf{r}} \tilde{f}(\mathbf{q} + \mathbf{G}, \mathbf{q}' + \mathbf{G}') e^{-i(\mathbf{q}' + \mathbf{G}') \cdot \mathbf{r}'} d\mathbf{q}' d\mathbf{q}$$

and  $\tilde{f}(\mathbf{q} + \mathbf{G}, \mathbf{q}' + \mathbf{G}') = \int \int e^{-i(\mathbf{q}' + \mathbf{G}') \cdot \mathbf{r}'} f(\mathbf{r}, \mathbf{r}') e^{i(\mathbf{q} + \mathbf{G}) \cdot \mathbf{r}} d\mathbf{r}' d\mathbf{r}$ .

$$(A.8)$$

Again, if the function is periodic in both arguments, the simplification

$$\tilde{f}(\mathbf{q} + \mathbf{G}, \mathbf{q}' + \mathbf{G}') = \delta(\mathbf{q} - \mathbf{q}') \cdot \tilde{f}(\mathbf{q}, \mathbf{G}, \mathbf{G}') := \tilde{f}_{G, G'}(\mathbf{q}) \quad (A.9)$$

holds. The rightmost expressions in A.7 and A.9 are sometimes used as abbreviations akin to matrix notations in  $\mathbf{G}$ .

In time and frequency space, similar relations hold, with the convention

$$f(\omega) = \frac{1}{2\pi} \int e^{i\omega t} \tilde{f}(t) dt \quad \text{and} \quad \tilde{f}(t) = \int e^{-i\omega t} f(\omega) d\omega. \quad (A.10)$$

At several points within this thesis, a Fourier transformation is carried out over the product of two functions  $h(t) = f(t) \cdot g(t)$  by applying the convolution theorem

$$\tilde{h}(\omega) = \int \tilde{f}(\omega') \cdot \tilde{g}(\omega - \omega') d\omega', \quad (A.11)$$

stating that the Fourier transform of a product function is given by the respective convolution and vice versa.

# B

## Investigated K-Ti-P-O Phases

In order to consider the maximum possible number of bi- and triatomic phases containing the constituents of KTP to determine the stability region for bulk KTP formation, the Materials Project database is used [234]. Focussing on all compounds listed as stable against decomposition, the 33 phases listed in Tab. B.1 are investigated, in addition to the bulk phase of  $\text{KTiOPO}_4$  and the bulk phases of elemental K, Ti and P. The oxygen reservoir is assumed to be  $\text{O}_2$ , modeled by two oxygen atoms within a cubic unit cell with a lattice constant of 15 Å. Using the same methodology as for bulk KTP, each phase is relaxed using the VASP program package [194], PAW potentials [195], the PBEsol functional [55], 500 eV plane-wave cut-off energy and a force threshold of 0.01 eV/Å for structural relaxation. The  $\mathbf{k}$ -point grid is adjusted based on the size of each individual unit cell to ensure numerical convergence of the total ground-state energy. The chemical potential  $\mu^{\text{bulk}}$  of each bulk compound then amounts to the total energy per formula unit. Using the bulk chemical potentials of the four constituents of KTP, the heat of formation  $\Delta H^f$  of every compound  $\text{A}_\alpha\text{B}_\beta\text{C}_\gamma$  is determined via

$$\Delta H_{\text{A}_\alpha\text{B}_\beta\text{C}_\gamma}^f = \mu_{\text{A}_\alpha\text{B}_\beta\text{C}_\gamma}^{\text{bulk}} - \alpha \cdot \mu_{\text{A}}^{\text{bulk}} - \beta \cdot \mu_{\text{B}}^{\text{bulk}} - \gamma \cdot \mu_{\text{C}}^{\text{bulk}},$$

with  $\alpha$ ,  $\beta$  and  $\gamma$  as the stoichiometric coefficients of the elements A, B and C, respectively.

**Table B.1:** Calculated bulk chemical potentials and formation enthalpies of all investigated phases within PBEsol, along with their respective space groups, according to [234]. Phases enclosing the KTP stability region under UHV as well as ATM conditions for oxygen (see Fig. 6.1) are highlighted in red; KTP is highlighted in bold.

System	Space group	$\mu^{\text{bulk}} / \text{eV}$	$\Delta H^f / \text{eV}$	System	Space group	$\mu^{\text{bulk}} / \text{eV}$	$\Delta H^f / \text{eV}$
K	$Im\bar{3}m$	-1.11	0	P	$Cmce$	-5.78	0
<b>KO<sub>2</sub></b>	<b><math>I4/mmm</math></b>	<b>-13.94</b>	<b>-3.68</b>	P <sub>2</sub> O <sub>5</sub>	$Fdd2$	-51.65	-17.20
KP	$P2_12_12_1$	-7.70	-0.81	Ti	$P6_3/mmc$	-8.31	0
KP <sub>15</sub>	$P\bar{1}$	-89.12	-1.31	TiO	$P\bar{6}2m$	-18.39	-5.51
<b>KPO<sub>3</sub></b>	<b><math>P2_1/c</math></b>	<b>-34.06</b>	<b>-13.44</b>	<b>TiO<sub>2</sub>(Anatase)</b>	<b><math>I4_1/amd</math></b>	<b>-28.01</b>	<b>-10.55</b>
<b>KTiOPO<sub>4</sub></b>	$Pnma$	<b>-62.68</b>	<b>-24.50</b>	TiO <sub>2</sub> (Brookite)	$Pbca$	-27.99	-10.53
K <sub>2</sub> O	$Fm\bar{3}m$	-10.52	-3.72	TiO <sub>2</sub> (Rutile)	$P4_2/mmm$	-27.95	-10.50
K <sub>2</sub> O <sub>2</sub>	$Cmce$	-16.88	-5.51	TiP	$P6_3/mmc$	-16.61	-2.51
K <sub>2</sub> P <sub>3</sub>	$Fmmm$	-21.59	-2.02	Ti <sub>2</sub> P	$Pnma$	-22.70	-2.83
K <sub>2</sub> TiO <sub>3</sub>	$Cmcm$	-40.84	-16.59	<b>TiP<sub>2</sub>O<sub>7</sub></b>	<b><math>P2_1/c</math></b>	<b>-81.34</b>	<b>-29.43</b>
K <sub>2</sub> Ti <sub>6</sub> O <sub>13</sub>	$C2/m$	-180.06	-68.52	Ti <sub>2</sub> O	$P\bar{3}m1$	-27.54	-6.35
K <sub>3</sub> P <sub>11</sub>	$Pbcn$	-70.83	-3.92	Ti <sub>2</sub> O <sub>3</sub>	$R\bar{3}c$	-47.16	-16.82
<b>K<sub>3</sub>PO<sub>4</sub></b>	<b><math>Pnma</math></b>	<b>-47.73</b>	<b>-20.32</b>	Ti <sub>2</sub> P	$P\bar{6}2m$	-25.83	-3.43
K <sub>3</sub> Ti <sub>8</sub> O <sub>17</sub>	$P\bar{1}$	-240.63	-93.07	Ti <sub>3</sub> O	$P\bar{3}1c$	-36.05	-6.55
K <sub>4</sub> P <sub>2</sub> O <sub>7</sub>	$P6_3/mmc$	-81.91	-33.88	Ti <sub>3</sub> O <sub>5</sub>	$C2/m$	-61.13	-6.71
K <sub>4</sub> P <sub>3</sub>	$Cmcm$	-24.32	-2.53	Ti <sub>3</sub> P	$P4_2/n$	-34.39	-3.68
K <sub>4</sub> TiO <sub>4</sub>	$P\bar{1}$	-52.33	-21.28	Ti <sub>5</sub> (PO <sub>5</sub> ) <sub>4</sub>	$P2_12_12_1$	-237.67	-81.60
K <sub>6</sub> Ti <sub>2</sub> O <sub>7</sub>	$P2_1/c$	-93.19	-37.89	Ti <sub>5</sub> P <sub>2</sub> O	$C2/m$	-79.28	-13.29
O	-	-4.57	0	Ti <sub>7</sub> P <sub>4</sub>	$C2/m$	-94.65	-13.35

# Potential Energy Surfaces on KTP Z Cut

C

A potential energy surface (PES) maps the energy gain/loss from introducing an atom or molecule to a surface onto individual adsorption sites. For KTP Z-cut surfaces, a number of potentially different PES for elemental adsorption can be distinguished by the atomic species adsorbed, the type of termination layer as well as the polarity of the surface ( $Z^+$  and  $Z^-$ ). To obtain the PES for each case, the adsorbant is placed at individual points in the  $x$ - $y$ -plane, 2 Å above the termination layer of the unreconstructed surface. The positions of all atoms are fixed except of the adsorbant, which is free to relax along the  $z$  direction. Similar to the methodology behind surface relaxation covered in Sec. 6.2.1, dipole corrections are used to account for the spurious electric field between both end facets within the vacuum region and the adsorbant is relaxed until the total force acting on it falls below a threshold of 0.01 eV/Å. The adsorption energy  $E_{\text{ad}}(x, y)$  of an atom  $i$  at the site  $(x, y)$  is then determined by evaluating

$$E_{\text{ad}}(x, y) = E_{\text{tot}}(x, y) - E_0 - \mu_i^{\text{bulk}},$$

with  $E_0$  and  $\mu_i^{\text{bulk}}$  denoting the energy of the clean slab and the chemical potential of the element in its bulk phase, respectively.

For a constant  $z$  coordinate, two space group operations of KTP prevail:

$$\begin{aligned} (x, y, z) &\rightarrow \text{Identity} \\ \left(\frac{1}{2} + x, \frac{1}{2} - y, z\right) &\rightarrow \text{Glide plane perpendicular to } y. \end{aligned}$$

The second operation thereby halves the necessary number of sites to be investigated to cover the entire surface unit, since a site with  $x > \frac{1}{2}$  is equivalent to a different site with  $x \leq \frac{1}{2}$ . In total, the PES were constructed using an equidistant mesh of 16 sites, see white dots in Fig. C.1. A continuous mapping of the adsorption energy is finally realized by interpolating between adsorption sites.

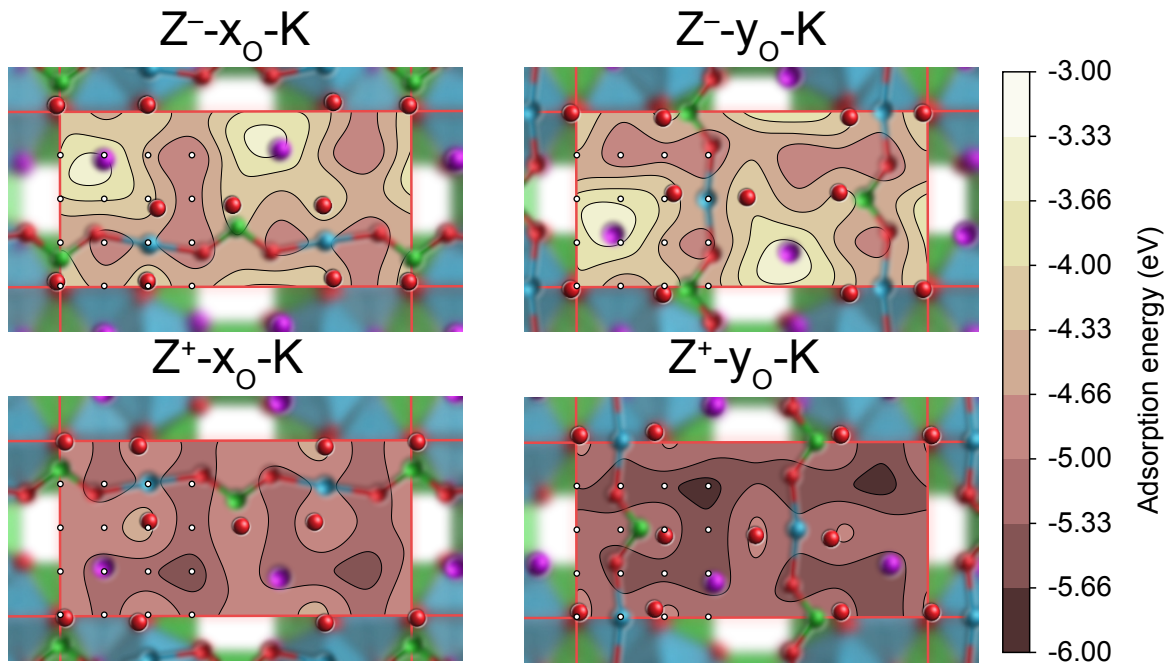


**Figure C.1:** PES for the adsorption of a single K atom on all layers of the positive ( $Z^+$ ) and negative ( $Z^-$ ) KTP Z-cut surface. Sharp and blurry atoms depict atoms within the outermost layer ( $x_O$  and  $y_O$ ) and the layer beneath it ( $x$  and  $y$ ), respectively. Color coding of all atoms follows Fig. 6.2. White dots indicate the 16 investigated adsorption sites. The remaining data of the PES are obtained by interpolation and application of symmetry operations.

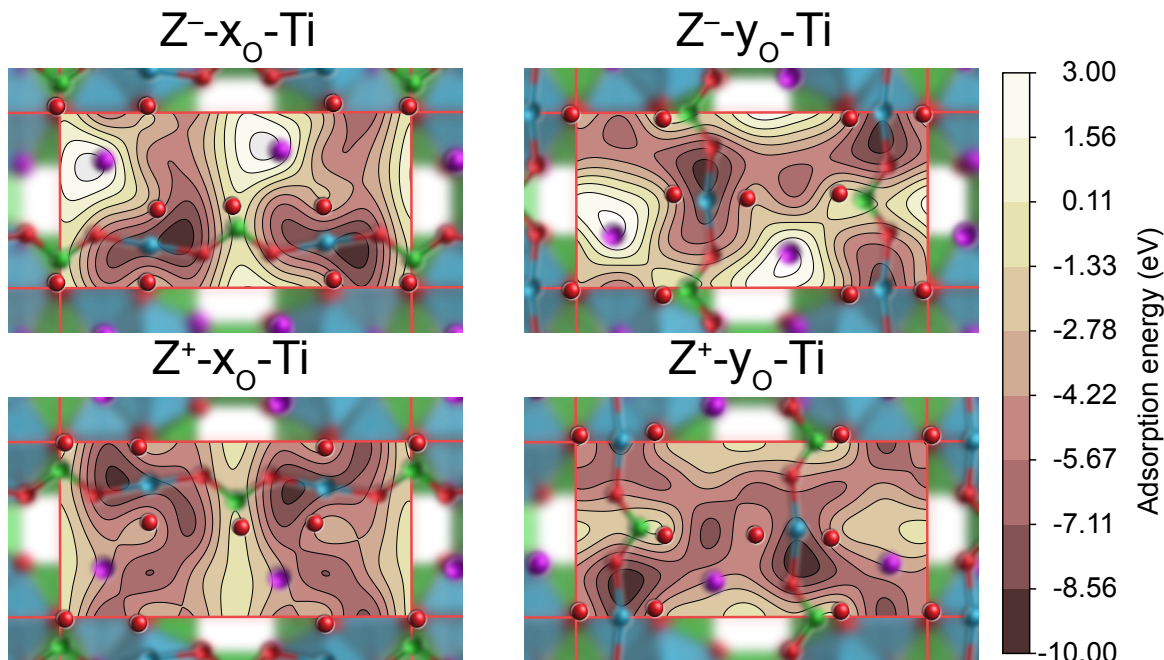


**Figure C.2:** PES for the adsorption of a single Ti atom on all layers of the positive ( $Z^+$ ) and negative ( $Z^-$ ) KTP Z-cut surface. Color coding of all atoms follows Fig. 6.2.

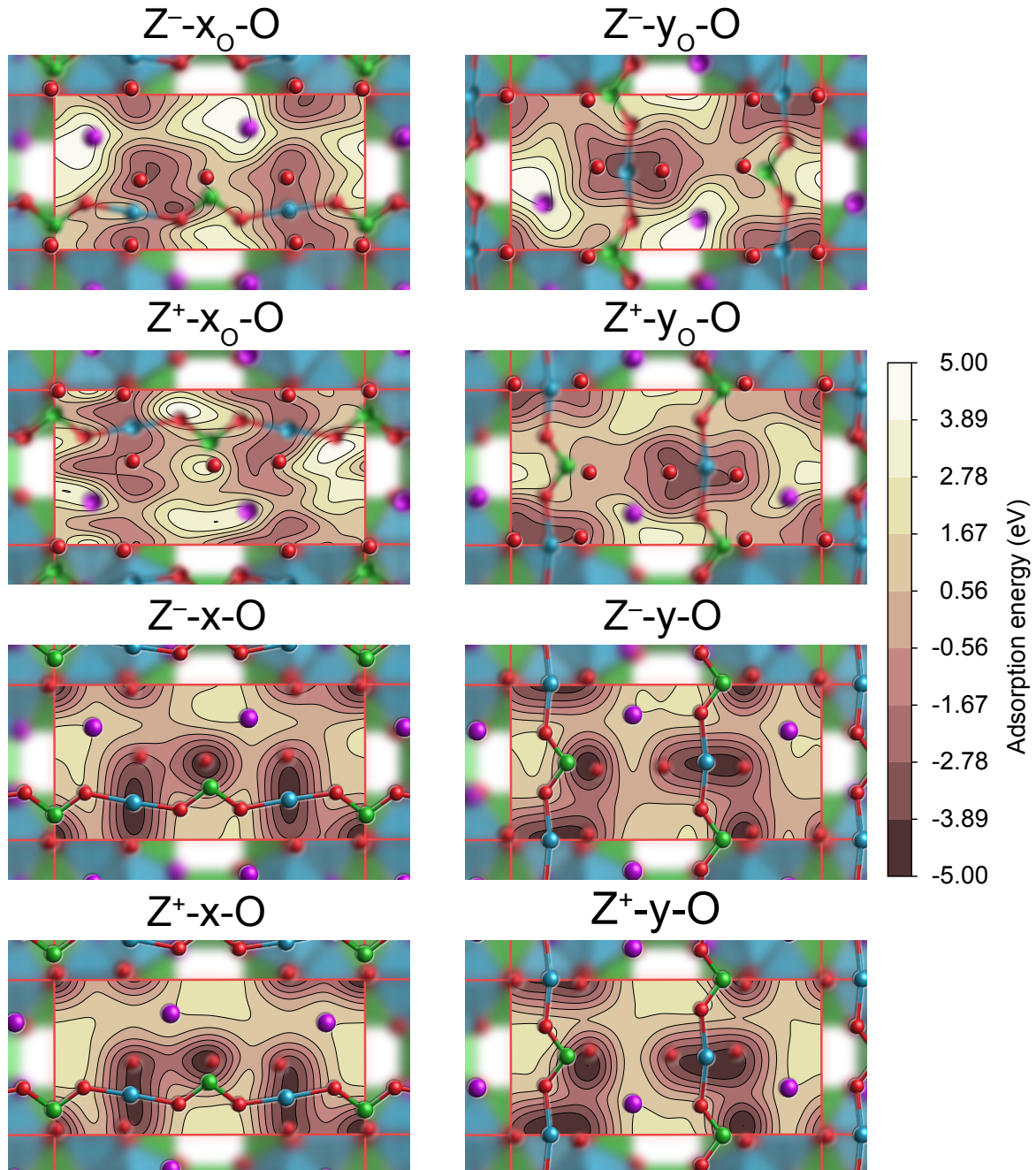


**Figure C.3:** PES for the adsorption of a single O atom on all layers of the positive ( $Z^+$ ) and negative ( $Z^-$ ) KTP Z-cut surface. Color coding of all atoms follows Fig. 6.2.

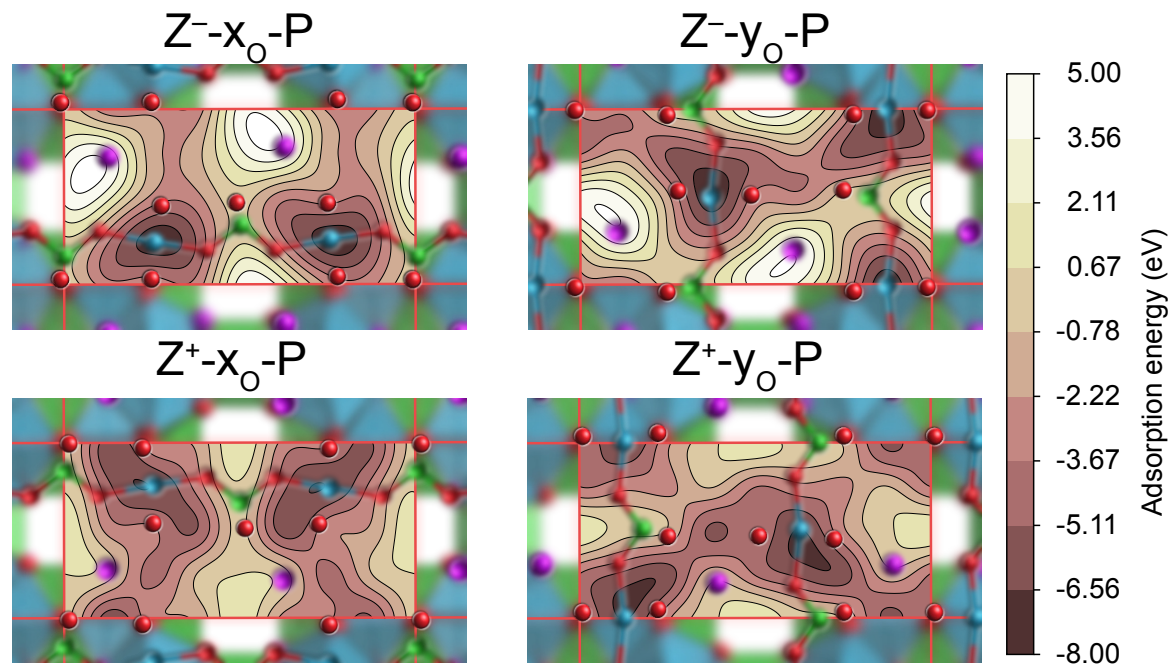


**Figure C.4:** PES for the adsorption of a single P atom on all layers of the positive ( $Z^+$ ) and negative ( $Z^-$ ) KTP Z-cut surface. Color coding of all atoms follows Fig. 6.2.

# Scientific Publications

D

## Publications related to KTP, RTP and KTA

1. A. Bocchini, **S. Neufeld**, U. Gerstmann and W. G. Schmidt, [Oxygen and potassium vacancies in KTP calculated from first principles](#), Journal of Physics: Condensed Matter **31**, 385401 (2019)
2. **S. Neufeld**, A. Bocchini, U. Gerstmann, A. Schindlmayr and W. G. Schmidt, [Potassium titanyl phosphate \(KTP\) quasiparticle energies and optical response](#), Journal of Physics: Materials **2**, 045003 (2019)
3. **S. Neufeld**, A. Bocchini, W. G. Schmidt, [Potassium titanyl phosphate Z- and Y-cut surfaces from density-functional theory](#), Physical Review Materials **5**, 064407 (2021).
4. **S. Neufeld**, A. Schindlmayr, W. G. Schmidt, [Quasiparticle energies and optical response of RbTiOPO<sub>4</sub> and KTiOAsO<sub>4</sub>](#), Journal of Physics: Materials **5**, 015002 (2022)

## Other publications

1. S. Sanna, A. Riefer, **S. Neufeld**, W. G. Schmidt, G. Berth, M. Rüsing, A. Widhalm, A. Zrenner, [Vibrational Fingerprints of LiNbO<sub>3</sub>-LiTaO<sub>3</sub> Mixed Crystals](#), Ferroelectrics **447**, 63–68 (2013)
2. S. Sanna, **S. Neufeld**, M. Rüsing, G. Berth, A. Zrenner, W. G. Schmidt, [Raman scattering efficiency in LiTaO<sub>3</sub> and LiNbO<sub>3</sub> crystals](#), Physical Review B **91**, 224302 (2015)
3. M. Rüsing, S. Sanna, **S. Neufeld**, G. Berth, W. G. Schmidt, A. Zrenner, H. Yu, Y. Wang and H. Zhang, [Vibrational properties of LiNb<sub>1-x</sub>Ta<sub>x</sub>O<sub>3</sub> mixed crystals](#), Physical Review B **93**, 184305 (2016)

4. M. Liebhaber, B. Halbig, U. Bass, J. Geurts, **S. Neufeld**, S. Sanna, W. G. Schmidt, E. Speiser, J. Räthel, S. Chandola and N. Esser, **Vibration eigenmodes of the Au-(5x2)/Si(111) surface studied by Raman spectroscopy and first-principles calculations**, *Physical Review B* **94**, 235304 (2016)
5. F. Edler, I. Miccoli, J. P. Stöckmann, H. Pfnür, C. Braun, **S. Neufeld**, S. Sanna, W. G. Schmidt and C. Tegenkamp, **Tuning the conductivity along atomic chains by selective chemisorption**, *Physical Review B* **95**, 125409 (2017)
6. B. Halbig, M. Liebhaber, U. Bass, J. Geurts, E. Speiser, J. Räthel, S. Chandola, N. Esser, M. Krenz, **S. Neufeld**, W. G. Schmidt and S. Sanna, **Vibrational properties of the Au-( $\sqrt{3}\times\sqrt{3}$ )/Si(111) surface reconstruction**, *Physical Review B* **97**, 035412 (2018)
7. M. Rüsing, **S. Neufeld**, J. Brockmeier, C. Eigner, P. Mackwitz, K. Spychala, C. Silberhorn, W. G. Schmidt, G. Berth, A. Zrenner and S. Sanna, **Imaging of 180° ferroelectric domain walls in uniaxial ferroelectrics by confocal Raman spectroscopy: Unraveling the contrast mechanism**, *Physical Review Materials* **2**, 103801 (2018)
8. C. Braun, **S. Neufeld**, U. Gerstmann, S. Sanna, J. Plaickner, E. Speiser, N. Esser and W. G. Schmidt, **Vibration-Driven Self-Doping of Dangling-Bond Wires on Si(553)-Au Surfaces**, *Physical Review Letters* **124**, 146802 (2020)
9. L. J. Glahn, I. A. Ruiz Alvarado, **S. Neufeld**, M. A. Zare Pour, A. Paszuk, D. Osthimer, S. Shekarabi, O. Romanyuk, D. C. Moritz, J. P. Hofmann, W. Jaegermann, T. Hannappel and W. G. Schmidt, **Clean and Hydrogen-Adsorbed AlInP(001) Surfaces: Structures and Electronic Properties**, *Physica Status Solidi B: Basic Solid State Physics*, 2200308 (2022)

## Conference Proceedings

1. S. Sanna, A. Riefer, **S. Neufeld**, W. G. Schmidt, G. Berth, A. Widhalm, A. Zrenner, **Vibrational fingerprints of LiNbO<sub>3</sub>-LiTaO<sub>3</sub> mixed crystals**, *Applications of Ferroelectrics, 2012 International Symp Piezoresponse Force Microscopy and Nanoscale Phenomena in Polar Materials (ISAF/ECAPD/PFM)* IEEE Conference Publications (2012)
2. S. Sanna, U. Gerstmann, E. Rauls, Y. Li, M. Landmann, A. Riefer, M. Rohrmüller, N. J. Vollmers, M. Witte, R. Hölscher, A. Lücke, C. Braun, **S. Neufeld**, K. Holtgrewe, W. G. Schmidt, **Surface Charge of Clean LiNbO<sub>3</sub> Z-Cut Surfaces**, *High Performance Computing in Science and Engineering '14*, Springer International Publishing Switzerland, 163–178 (2015)
3. A. Lücke, U. Gerstmann, S. Sanna, M. Landmann, A. Riefer, M. Rohrmüller, N. J. Vollmers, M. Witte, E. Rauls, R. Hölscher, C. Braun, **S. Neufeld**, K. Holtgrewe, W. G. Schmidt, **Solving the Scattering Problem for the P3HT On-Chain Charge Transport**, *High Performance Computing in Science and Engineering '15*, Springer International Publishing Switzerland, 155–170 (2016)

4. S. Sanna, C. Dues, U. Gerstmann, E. Rauls, D. Nozaki, A. Riefer, M. Landmann, M. Rohrmüller, N. J. Vollmers, R. Hölscher, A. Lücke, C. Braun, **S. Neufeld**, K. Holtgrewe, W. G. Schmidt, [Submonolayer Rare Earth Silicide Thin Films on the Si\(111\) Surface](#), High Performance Computing in Science and Engineering '16, Springer International Publishing AG, 163–175 (2016)
5. A. Lücke, T. Biktagirov, A. Riefer, M. Landmann, M. Rohrmüller, C. Braun, **S. Neufeld**, U. Gerstmann, W. G. Schmidt, [Photo-Excited Surface Dynamics from Massively Parallel Constrained-DFT Calculations](#), High Performance Computing in Science and Engineering '17, Springer International Publishing AG, 157–168 (2017)
6. T. Biktagirov, C. Braun, **S. Neufeld**, U. Gerstmann, W. G. Schmidt, [Accurate and Efficient Spin-Spin Zero-Field Splitting Calculations for Extended Periodic Systems](#), High Performance Computing in Science and Engineering '18, Springer International Publishing AG, 131–140 (2019)



# Danksagung

Damit wären wir schon am Ende angelangt. Die letzten Zeilen dieser Arbeit seien all jenen Menschen gewidmet, die mich auf dem Weg begleitet, unterstützt, inspiriert haben und an meiner Seite standen, auch wenn Dinge nicht ganz nach Plan verliefen.

Zunächst wäre da natürlich mein Professor, Wolf Gero Schmidt, zu nennen. Vielen dank für die Möglichkeit, seit meiner Zeit als Bachelorstudent innerhalb deiner Arbeitsgruppe mitwirken zu können. Du gabst mir die nötige Freiheit, meinen eigenen wissenschaftlichen Weg gehen zu können, warst aber nichtsdestotrotz jederzeit zur Stelle, den richtigen Impuls zu setzen wenn Dinge ins Leere zu drifteten drohten.

In eine ähnliche Kerbe schlägt auch das Dankeschön für Professor Simone Sanna. Du hast mich sogar noch länger begleitet, seit den Tagen des mathematischen Vorkurses, über meine Bachelor- und Masterzeit. *Voglio ringraziarti per tutto ciò che mi hai insegnato.*

Im Laufe der Jahre hatte ich die Gelegenheit, viele Menschen Kollegen und Büronachbarn nennen zu dürfen. Seien es Momente der Zerstreuung während der Mittagspause oder die Arbeit betreffende Fragen: zu jeder Zeit konnte ich mich darauf verlassen, dass ein offenes Ohr nur wenige Schritte entfernt ist. Azahel und Christian, euch gilt ein besonderer Dank, denn bessere Büronachbarn konnte ich mir nicht wünschen. Für das Korrekturlesen meiner Arbeit möchte ich Agnieszka ein großes *dziękuję* aussprechen. Sabuhi, Uwe, Hazem, Max, vielen Dank für die zahlreichen schönen Gespräche und gemeinsamen Momente auf diversen Konferenzen. Nicht vergessen möchte ich natürlich Simone Lange. Vielen Dank, dass du bei Weitem mehr bist als bloß unsere Sekretärin, du bist der Kleber, der die theoretische Physik seit jeher zusammen hält.

Meinen Freunden und meiner Familie gilt ein ganz besonderer Dank für ihren immer-währenden Rückhalt in guten und in schweren Zeiten. Anna, nie werde ich unsere Gespräche und deine guten Ratschläge vergessen. Allen meinen Kommilitonen, allen voran Thomas, Dennis, Franziska, Michael und Andreas möchte ich dafür danken unser Studium nie langweilig werden zu lassen. Jedes Treffen mit euch zeigt mir, dass uns auch heute noch die Erinnerung an die gemeinsame Zeit verbindet, auch wenn wir nach dem Master teils sehr unterschiedliche Pfade eingeschlagen sind.

Мама и папа, благодарить вас слов не хватит. Мой путь был длиннее чем я сначала думал, но в конце концов мы дошли вместе. Я горжусь вам и надеюсь, что вы гордитесь мной тоже.

Der Person, die mir wahrlich am nächsten steht und einen beträchtlichen Anteil zum Erhalt meiner geistigen Gesundheit während des gesamten Schreibprozesses ausgemacht hat, ist meine Freundin Adriana. Deine verständnisvolle Art, dein Humor (und nicht zuletzt

deine Kochkünste) haben bereits mehr dunkle Tage erhellt, als man zählen kann. *Grazie mille tesoro mio!*